Hossein Ehya

A Novel Health Monitoring System for Synchronous Generators using Magnetic Signatures

NTNU
Norwegian University of
Science and Technology

Hossein Ehya

A Novel Health Monitoring System for Synchronous Generators using Magnetic Signatures

Thesis for the Degree of Philosophiae Doctor

Trondheim, October 2022

Norwegian University of Science and Technology
Faculty of Information Technology and Electrical Engineering
Department of Electric Power Engineering

NTNU
Norwegian University of
Science and Technology

Preface

The thesis is submitted in partial fulfillment of the requirements of the degree of Philosophiae doctor (Ph.D.) at the Norwegian University of Science and Technology (NTNU) in Trondheim. The presented research was carried out at the Department of Electric Power Engineering between November 2018 and July 2022. The Ph.D. research was directed by Prof. Arne Nysveen as the main supervisor and Prof. Robert Nilssen as a co-supervisor.

Acknowledgements

My Ph.D. journey comes to its end. It was completely different from my what I expected. I always thought that Ph.D. life would be tough and I would have to read boring papers and solve sophisticated problems and finally write papers and thesis to get rid of my Ph.D. tasks. However, it turned out to be fun and full of joy. I am happy to see my thoughts were fallacious. During this wonderful journey, countless people supported my efforts. I would like to express my heartful gratitude to all of them.

This journey could not have come this far and achieved all these accomplishments without the support of a wonderful supervisor. I direct my appreciation and deepest gratitude to my supervisor, Prof. Arne Nysveen for his support, mentorship, and encouragement, provided with a perfect blend of insight and humor throughout the Ph.D. project. And I am grateful for his trust in letting me pursue research relatively independently. He exudes an image of the consummate professional, one that I can only hope to one day emulate.

I am extremely thankful to my co-supervisor, Prof. Robert Nilssen, for his advice and delightful guidance. His experience in innovation and providing guidance and support during my innovation project were invaluable.

I also express my gratitude to Prof. Bilal Akin, at the University of Texas at Dallas, Prof. Jose A. Antonino Daviu, at the University of Valencia, Prof. Sang Bin Lee, at the Korea University, and Prof. Konstantinos N. Gyftakis, at University of Edinburgh, for their collaboration and insightful discussions that resulted in a couple of publications.

Alongside my Ph.D. research work, I spent almost a year on my innovation project. I admit that it was arduous work to deal with patent attorneys and to try to sell the license to companies. Although it was tiresome, the effort was worthwhile. I thank my innovation project manager, Oddbjørn Rødsten, at the Technology Transfer Office, Knut J. Egelie, IPR expert at the Technology Transfer Office, Jonas Bergmann-Paulsen, technology manager at HydroCen, and Ida Fuchs, technology manager at the department of electric power engineering for their support.

During my Ph.D. journey, I had a chance to become a co-supervisor of several talented master's students, including Ingrid Linnea Groth, Johan Henrik Holm Ebbing, Gaute Lyng Rødal, Tarjei Nesbø Skreien, Ole Sørheim, Gaute Hagen Hallingstad, and Markus Fredrik Johansen. All of your great work is much appreciated.

My Special thanks go to my colleagues at the Department of Electric Power Engineering at NTNU, who have been of great support. I am also grateful to the

Summary

The Ph.D. research work presented in this thesis deals with the health monitoring of synchronous generators utilized in hydropower plants. Although various methods are available for fault detection in synchronous generators, the applicability of the available tools in the real world encounters numerous difficulties. A novel health monitoring system that can address the challenges in the field is proposed, consisting of a tailor-made sensor, signal processors, pattern recognition algorithm, and artificial intelligence. The proposed health monitoring system utilizes a stray magnetic field that can be measured on the stator backside of hydro generators. The proposed non-invasive health monitoring system is able to detect the fault type, estimate the severity, and find the location of the fault in the hydro generator. Moreover, the proposed health monitoring system has a high sensitivity that can detect a fault with low severity. In addition, the proposed pattern recognition algorithm is able to detect the fault without any need for prior knowledge about the reference generator.

Finite element modeling of five synchronous generators is performed to investigate the existence of the stray magnetic field on the stator back side. In addition, the impact of topology, power rating, and design specification on the amplitude and pattern of the stray magnetic field are investigated. Although the amplitude of the stray magnetic field can be changed, the hidden pattern in the calculated signal for the faulty operation of the generators is identical. Several faults are investigated, including inter-turn short circuit fault in the rotor field winding, static eccentricity, dynamic eccentricity, mixed eccentricity, and broken damper bar faults. The impact of a fault on the stray magnetic field is also investigated using finite element modeling.

Pattern recognition is the key part of this Ph.D. work. Several signal processing tools are used to extract the hidden patterns in the stray magnetic field signal. Fast Fourier transform, short-time Fourier transform, discrete wavelet transform, and continuous wavelet transform are used for feature extraction. Three unique patterns for the inter-turn short circuit fault are introduced that can detect even 1 shorted turn in the rotor field winding. A comprehensive algorithm is also proposed to detect eccentricity faults (static, dynamic, and mixed). The proposed algorithm is able to detect the location of the static eccentricity fault. Finally, the application of wavelet entropy on a stray magnetic field based on a broken damper bar fault is proposed that can detect the broken damper bar during both transient and steady-state operations of the generators.

Reducing human error and reducing the cost of educating technicians to evaluate the patterns of the health monitoring system is achieved using an artificial intelligence system. Various classifiers are trained and their performance is assessed based on several meticulous evaluation functions. Among the proposed classifiers,

a stacking classifier with logistic regression as a meta-classifier is selected due to its high performance and low computational complexity. The proposed method is tested using hand-out data and shows that the method can detect a fault with 92.74% precision.

Extensive experimental tests are conducted on a tailor-made 100 kVA synchronous generator to verify the theoretical hypothesis. Various types of fault, including the inter-turn short circuit fault, static eccentricity fault, misalignment, and broken damper bar fault, with different severity can be applied to the setup. The tests are performed in both the no-load and on-load operations while the generator is connected to the local load and power grid. A custom-made sensor is designed to capture the stray magnetic field on the stator backside. Finally, two field tests are conducted in two hydro power plants in Norway to validate the proposed health monitoring system in reality.

Contents

1 Introduction

1.1 Introduction

In Norway, approximately 98 percent of electricity production comes from renewable energy resources, with hydropower plants playing a crucial role. The potential energy of the water flow in rivers and waterfalls became a source of electricity production in the late 1800s, and from then until today, hydropower plants have been the basis for Norwegian development of the industry and the welfare of Norwegian society. Close to 90 percent of the electricity in Norway is produced in hydropower plants [1]. In the last decade, the share of wind power in the power market has increased rapidly; however, wind energy still accounts for only a small portion of Norwegian power production.

Salient pole synchronous generators are the most prevalent type of generators used in hydropower plants [2] and are therefore ubiquitous throughout Norwegian hydropower plants. Although large synchronous generators have a rigid structure and have a reliable operation for several decades in hydropower plants, the number of failed generators has markedly increased during the past years [3]. In addition, the situation for the run-off river-type power plants is critical if a fault results in an unplanned stoppage of the generator, especially during the high production season. This is because the capacity of the weir is only sufficient to store the water flow for less than 24 hours, whereas the maintenance of the generator can take a few weeks. These issues indicate that an unplanned outage of the generator can incur not only a considerable expenditure to restore the power plant but also a remarkable cost to society.

The rate of failure has increased in the past years as generators have operated as intermittent power sources. The load variation and frequent starts and stops accelerate aging of the insulation and impose forces on the shaft and bearings. Therefore, undetected incipient defects in generators can give rise to a large fault that is tripped from the power grid unexpectedly by the power relays. A combination of periodic inspection and online condition monitoring can avoid abrupt outages and extend the expected lifetime of the generators.

Economic analysis in [4] shows up to a 60% cost reduction in the case of reactive maintenance, although the transition from reactive maintenance to predictive maintenance can increase the cost reduction markedly. According to [5], approximately USD 2 billion is spent on maintenance of electric machines. However, 70% of that is used for electric machines that do not have a condition monitoring

system, indicating that maintenance cost reductions will have immense benefit to the industry. Although a great demand exists for a practical condition monitoring system, the state-of-the-art online fault diagnosis in synchronous generators is still lacking in this respect.

The aim of this introduction section is to point out the main motivation behind the conducted Ph.D. research work. A crucial goal of the work was to address industry concerns by developing an intelligent health monitoring system. The developed algorithm had to be able to detect various electrical and mechanical faults. Early stage detection and avoiding further development of the fault were also prerequisites, since the maintenance team can plan ahead to stop the generator in the low-demand period of production while planning to purchase spare parts. In this work, several algorithms are proposed to detect electrical and mechanical faults during the transient and steady-state operation of the generator. The numerical models are developed to evaluate and interpret the impact of faults on the operation of the generator. The algorithm analyzes the measured signal utilizing advanced signal processing methods. Finally, theoretical findings are justified both in the laboratory setup and field test in two hydropower plants.

1.2 Objectives and Scope of the Work

The main objective of the Ph.D. project is to provide an affordable, non-invasive, and sensitive system for health monitoring of synchronous generators in hydropower plants. The work is focused on magnetic signals, since those signals are the most informative among the available signals from a fault detection point of view. The project is funded by Hydrocen, which is a Centre for Environment-friendly Energy Research. Therefore, the scope of the Ph.D. work is only limited to hydropower plants, whereas the application area of the developed method is generally applicable to wind power, electric aviation, ships, electric installations in the oil and gas platforms, and electric cars.

Both electrical faults and mechanical faults are investigated in this research study. Specifically, inter-turn short circuit (ITSC) faults in the rotor field winding are investigated as electric faults in this research study. Static eccentricity (SE), dynamic eccentricity (DE), mixed eccentricity (ME), and broken damper bar (BDB) faults are also considered among various mechanical faults.

This research work is focused on the analysis of the impact of various faults on electromagnetic signals, such as the stator voltage and current, rotor field winding voltage and current, vibration, air gap magnetic field, and stray magnetic field. Among these signals, the stray magnetic field is selected since it can provide an informative signal that is sensitive to faults. Therefore, the thesis is concentrated on investigation of the impact of electrical and mechanical faults

on the stray magnetic field in salient pole synchronous generators. The numerical tools are used to model several synchronous generators. Although the stray magnetic field has a three-dimensional nature, only two-dimensional finite element modeling (FEM) is performed due to the high computational complexity of three-dimensional FEM. In addition, sensors in a two-dimensional FEM can capture a combination of radial and axial magnetic fields to provide an informative signal. Several synchronous generators are modeled in FEM to evaluate the impact of the power rating and specification of the generators on the captured stray magnetic field.

The main objective of this Ph.D. thesis is to provide an inexpensive health monitoring solution based on the application of a stray magnetic field. Therefore, a custom-made passive sensor is developed to measure the signal on the stator backside. The available solutions have used spectrum analysis using fast Fourier transform (FFT). However , the power rating and specification of the generator can influence the pre-defined threshold levels for fault detection. In addition, some faults, such as static eccentricity, do not change the frequency spectrum. Therefore, various signal processing tools are applied to the measured signal to extract a unique fingerprint for each specific fault. An analytical assessment based on the wave and permeance method is also conducted to formulate which harmonics are influenced by each fault, and this is then used for pattern recognition using the frequency spectrum. Although the signal processing tools are not developed by the author, the pre-processing, parameter selection, and optimization of the signal processors are conducted in this thesis.

An automated health monitoring system is needed if the sensor system is to be installed in thousands of generators and motors. Therefore, analyzing the data requires input from several experts, but this impedes the timely scheduling of the maintenance due to the limitations in human resources. At the same time, the cost of hiring experts and educating them impedes the utilization of affordable health monitoring systems for the small power plant owner. Therefore, utilizing an automated health monitoring system based on the application of machine learning tools is also investigated in this thesis. The performed research is limited to identification of the healthy state or faulty state. The application of a convolutional neural network for the fault type and severity estimation is not within the scope of this Ph.D. work.

1.3   Background

The importance of synchronous generators in electricity production is undeniable. Although synchronous generators are robust and long-lasting equipment in the power system, several factors, such as aging, intermittent operation, improper manufacturing, and environmental factors, can result in their failure. Faults
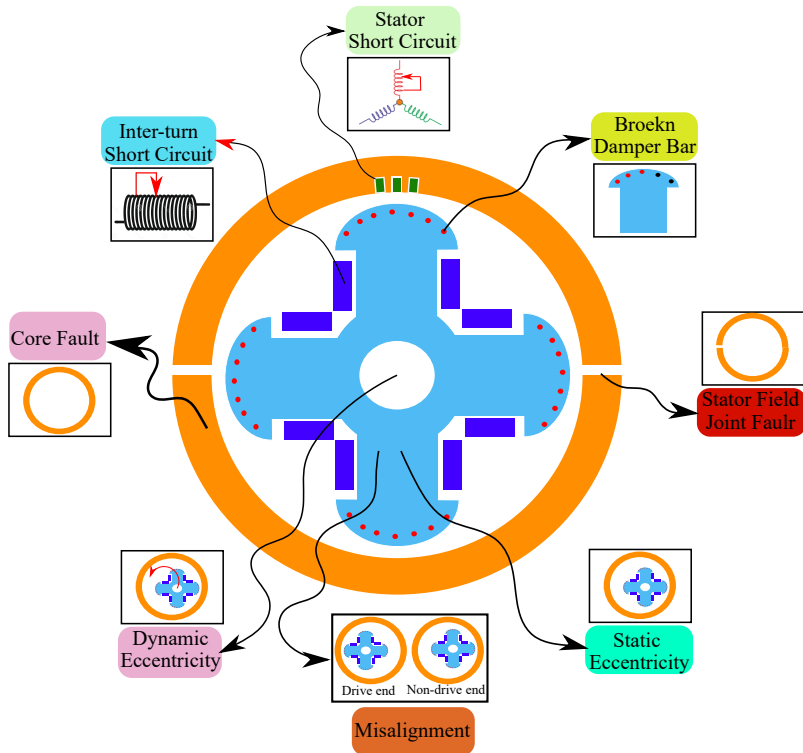
Figure 1.1: The various types of electrical and mechanical faults in large salient pole synchronous generators.

in large salient pole synchronous generators can be divided into two categories: electrical faults and mechanical faults. Short circuit and open circuit faults in the stator winding and ITSC faults in the rotor field winding are classified as short circuit faults [6]. Eccentricity faults, such as SE, DE, and ME, misalignment, BDB, broken end rings, stator inter-laminar fault, and stator joint field fault are categorized as the mechanical faults in large salient pole synchronous generators [6]. Fig. 1.1 shows the various types of electrical and mechanical faults in the salient pole synchronous generator.

Researchers have been working on fault detection in synchronous generators for a long time. The procedure of fault detection includes three steps: signal selection, signal processor selection for pattern recognition, and artificial intelligence. Several methods and commercialized technologies are available for fault detection of synchronous generators based on a combination of various signals and signal processing tools. However, a comprehensive survey of the state-of-the-art tools indicates that the available methods shown in Fig. 1.2 have several limitations [6]:

Figure 1.2: The procedure for fault detection includes proper signal selection, pattern recognition using advanced signal proce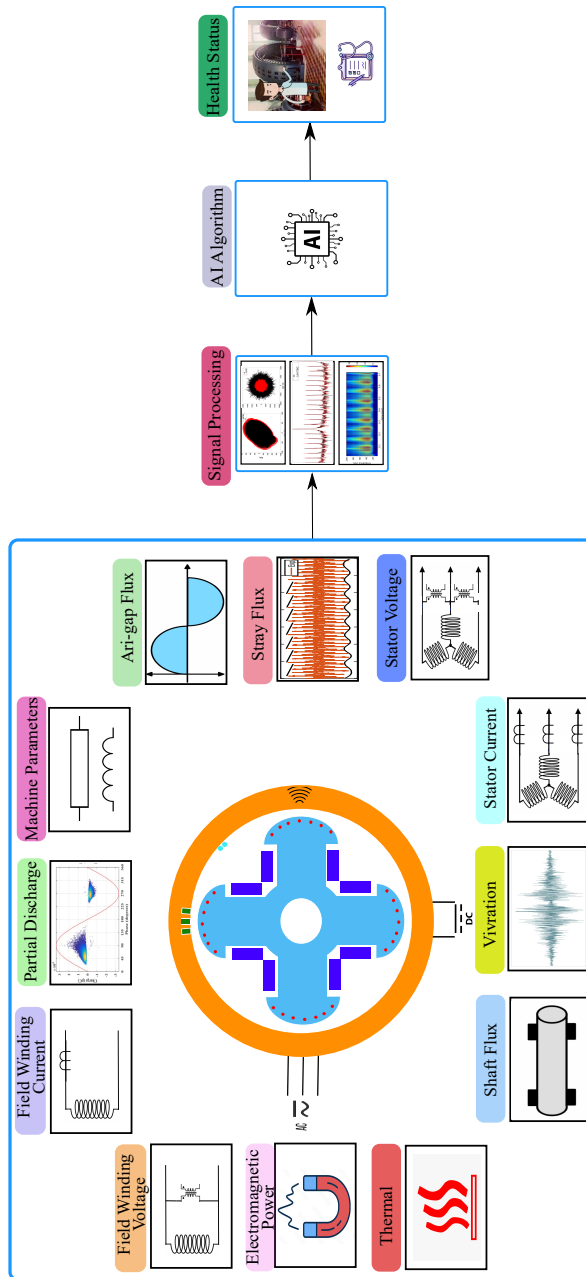ssing methods, and an intelligent algorithm to recognize the fault pattern and determine the health status of the salient pole synchronous generator.

1.3.1 Invasive

Different signals, including air gap magnetic field [7–17], current [18–24], voltage [25, 26], vibration [27–32], and shaft voltage [33–37], are used for the ITSC fault detection in synchronous generators. SE, DE, and BDB fault detection utilizes the same signals, including air gap magnetic field [26, 38–42], current [39, 43–48], voltage [49–54], and shaft voltage [33–35, 55–60]. Among these signals, the air gap magnetic field is the only informative signal that shows high sensitivity to all fault types. However, it has an invasive nature that impedes its application in hydropower plants and industries. Two types of sensors, namely a search coil around a stator tooth and Hall-effect sensors, are predominantly used to capture the air gap magnetic field. The search coil is more robust than the Hall-effect sensors, but the rotor must be removed to allow access to the stator teeth. Although the attachment of Hall-effect sensors to the stator tooth is straightforward, these sensors are fragile and improper adjustment of the current source of the sensor can give an incorrect magnitude of the signal.

1.3.2 Low-sensitivity

To overcome the invasive nature of the air-gap magnetic field sensors, researchers have proposed utilizing voltage, current, vibration, and shaft voltage. The required sensors, such as current transformers (CT), potential transformers (PT), and accelerometers, are simple to install. The current and voltage on the generator terminals do not require measurement, indicating that remote health monitoring can be implemented. Although CTs, PTs, and accelerometers are non-invasive, the early-stage detection of a fault is not possible using these signals. The studies by [28, 42, 49] show that having at least a minimum eccentricity fault of 50% degrees can give rise to the appearance of some fault-related harmonics in the voltage, current, and vibration frequency spectra. Nevertheless, low-degree faults, such as one ITSC fault in the rotor field winding, an eccentricity fault below 10%, and one broken damper bar fault, can be detected using an air gap magnetic field.

In addition, the current, voltage, and vibration are not suitable signals for detecting some faults, such as SE and BDB. The SE fault does not influence the voltage, current, or vibration since the SE fault only distorts the magnitude of the magnetic field in the air gap, not the frequency content. BDB has a very low impact on the magnetic field variation in the air gap, and its impact on these signals is not noticeable.

1.3.3 Analysis Methods

Vibration is the most dominant commercialized tool used for fault detection of hydro-generators. The measured vibration is compared with the pre-defined threshold level available in the IEC standard to identify the health status of the generator [5]. Trend analysis is also used if the measured vibration and its report are stored. However, both trend analysis and threshold level can give general information regarding the generator operating condition. In addition, an increased vibration level can be due to several factors, such as improper coupling of the shaft and improper installation of the generator on the bed. Therefore, the use of vibration is not a reliable or informative method.

Harmonic analysis is also a popular method for the analysis of measured signals, but using harmonic analysis has two difficulties:

1. Harmonics such as 7th, 11th, 13th, 17th, 19th, 21nd, and 23rd are frequently used for fault detection. First, based on the generator design, these harmonics exist in the frequency spectrum of a healthy generator. Therefore, a fault may increase or decrease the amplitude of the harmonics, so the fault occurrence cannot be diagnosed due to the existence of the harmonics. In addition, the same harmonics exist in the power grid; therefore, distinguishing the root cause of the harmonics becomes more complicated.

2. Several research studies have proposed the use of a threshold level in the frequency spectrum of the signals to determine a fault occurrence [6]. For example, [61,62] proved that the power rating and configuration of the generator can influence the threshold level. Therefore, the use of a generalized threshold level is not reliable.

1.3.4 Priori Knowledge of a Healthy Generator

Several signal processing tools, such as time-domain signal processors, frequency domain signal processors, and time-frequency signal processors, can be applied to different signals to detect faulty generators [6]. However, the proposed methods are based on a comparison of the faulty case with the healthy one, indicating that a priori knowledge of a healthy generator is required. Although the method based on comparing faulty results with healthy ones appears promising, it is only valid for experimental tests conducted in laboratories. Asking the simple question "Is it really possible to have baseline data for a synchronous generator that has been operating in a power plant for a couple of decades?" easily invalidates the proposed methods.

1.3.5 Fault Type Detection

In addition to the early warning of the fault occurrence, knowledge of fault type can significantly help a maintenance team to reduce the downtime of the generator overhaul. Three detection methods, namely trend analysis, threshold level, and harmonic analysis, are unable to provide any information regarding the type of fault that occurred in the generator, since any fault increases the magnitude of the harmonics and increases the amplitude of the vibration level.

1.3.6 Human Error

An inaccurate decision is highly possible if the outcome of complicated patterns and algorithms is analyzed by a human being. Therefore, automated health monitoring based on the use of artificial intelligence is considered as a solution [13]. Several methods have been proposed, based on different configurations of machine learning tools. The results show accuracy as high as 100% in many cases. However, the lack of sufficient data to train the algorithm and the utilization of the same data for testing gives rise to the high accuracy obtained using these proposed fault detection methods.

1.4 Research Objectives

The previous section provides insights into fundamental aspects of the development of a health monitoring system that overcomes the limitations that impede the proper monitoring of generators that are likely to fail in the near future. Moreover, a cost-effective health monitoring system is not only suitable for large power plants owned by large states, it is also an appealing solution for the owners of unregulated power plants that cannot afford costly and complicated health monitoring systems. The number of these unregulated power plants is approximately 400 units in Norway.

The conducted research activities in this thesis are rooted in the three research objectives (ROs):

RO1 To develop a cost-effective and sensitive sensor that provides an informative signal as an air gap magnetic field while avoiding the need to halt the generator to mount a sensor inside the air gap.

RO2 To use the unique patterns to identify the fault type without any need for baseline data of a healthy generator.

RO3 To minimize human error, automate the process, and increase the accuracy of the health monitoring decision-making using machine learning tools.

1.5 Scientific Contributions

During the Ph.D. project, a health monitoring system is developed that can overcome the majority of the indicated limitations. Five types of faults are studied: the ITSC fault in the rotor field winding, SE fault, DE fault, ME fault, and BDB fault. Among several signals, the stray magnetic field is selected due to the high sensitivity, simple installation, and low cost of the sensor. Several unique patterns are extracted, based on the application of signal processing tools to the measured stray magnetic fields. Among the numerous signal processing tools, FFT, short-time Fourier transform (STFT), continuous wavelet transform (CWT), and discrete wavelet transform (DWT) are used because of their low computational complexity and their simplicity of the implementation. The effect of electromagnetic noise on the measured signal and the introduced patterns is also studied in this Ph.D. study, since noise is prevalent in the industrial environment. The application of several machine learning algorithms to facilitate the automated health monitoring system is also investigated in this work.

The following contributions can be derived from the conducted research study during the Ph.D. period:

C1 Four finite element models of salient pole synchronous generators are simulated to investigate the pattern and magnitude of the stray magnetic field measured on the stator backside in a healthy and faulty operation. The modeled generators are a 100 kVA 14-pole, 22 MVA 8-pole, 42 MVA 16-pole, and 105 MVA 16-pole.

C2 A custom-made passive sensor is designed to capture the stray magnetic field on the stator backside of a 100 kVA synchronous generator. The sensor is used for both experimental tests at the NTNU laboratory and field tests in two hydropower plants.

C3 Two sets of unique patterns, based on a frequency domain signal processor and time-frequency domain-based signal processors, are proposed. The introduced patterns using FFT are suitable for ITSC and DE fault detection. Two patterns are also introduced for the ITSC fault detection using STFT and CWT. CWT is also used to introduce a pattern for SE, DE, and ME fault detection. Finally, a method based on wavelet entropy is proposed for BDB fault detection.

C4 The proposed patterns for faulty cases do not require a pattern for the healthy generator, indicating that the baseline data of the generator are

not required. Therefore, methods can be used in real situations for fault detection of hydro generators that have been operating for several decades in power plants.

C5 Extensive experimental tests are carried out on a custom-made 100 kVA 14-pole synchronous generator that resembles the typical configuration of a generator in Norwegian power plants. The proposed methods are validated using this setup.

C6 The sensor is designed to have a high signal-to-noise ratio. The cost of materials for its fabrication are kept as low as possible.

C7 Various configurations of machine learning classifiers are examined, with the ultimate choice of an ensemble stacking classifier trained on 2500 samples that showed an accuracy and precision above 90%.

The methods and discussions in this thesis are based on the results presented in 9 journal papers. Fig. 1.3 presents a sketch of the connections between the nine papers in this Ph.D. study. Section I (Review Paper) explores the state of the art and discusses the research gaps. Section two includes the methodologies and implemented approaches for electrical faults, such as ITSC, and for mechanical faults, such as SE, DE, ME, and BDB, and covers six papers. Section three explores the noise impact on the signal processors and how noise can mask the patterns. Section four explores the approaches for an automated health monitoring system. The main contribution of each journal paper is summarized as follows:
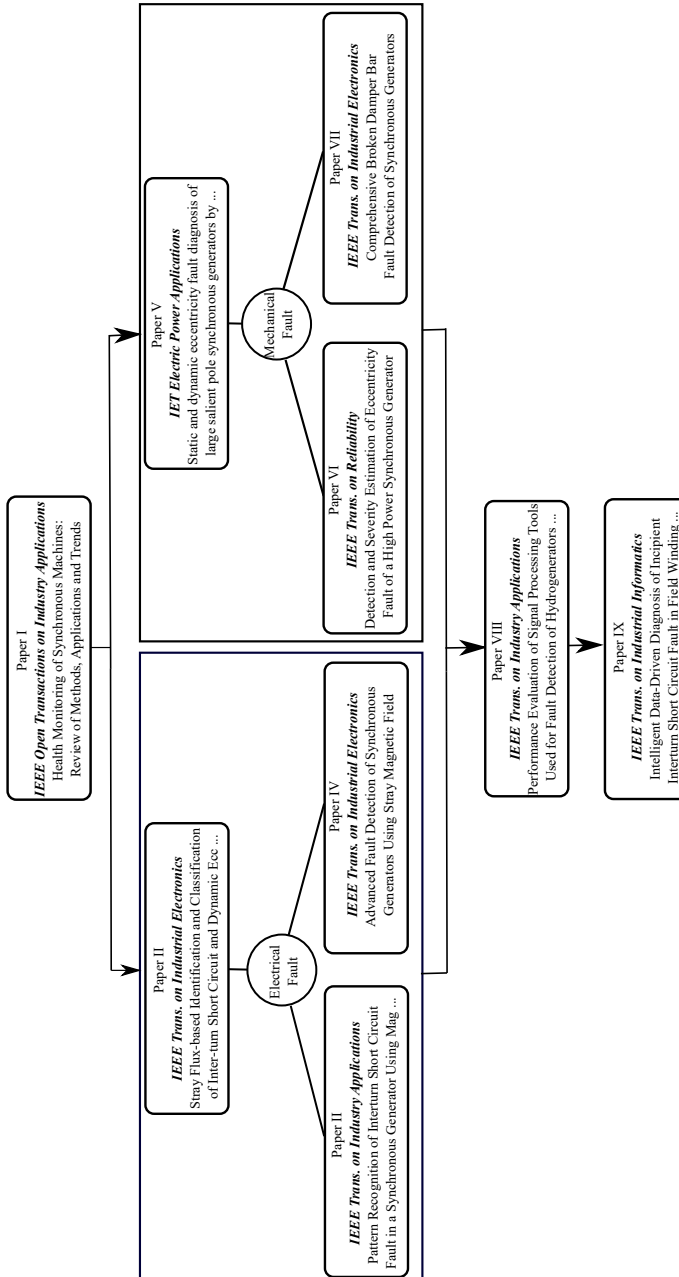
Figure 1.3: A sketch of the connection between the nine papers generated in this Ph.D. study.

1. H. Ehya, A. Nysveen, B. Akin, and J. A. Antonino Daviu, "Health Monitoring of Synchronous Machines: Review of Methods, Applications and Trends," in IEEE Open Journal of Industry Applications, Under Review.

   This paper provides a comprehensive review of the state of the art. The root cause and failure mechanism of electrical faults, such as short circuit fault in the stator, and the ITSC fault are explained. The solutions available for short circuit fault detection are then explained. The fault detection methods for short circuit faults are discussed and their limitations are explained in detail. In section three of the paper, mechanical faults, including eccentricity, broken damper bars, and stator core-related faults, are extensively investigated. The root cause of each mechanical fault and its corresponding solutions are discussed. The fault detection methods for both electrical and mechanical faults are categorized based on the type of signal used in the monitoring system. The signals that are predominantly used include the air-gap magnetic field, voltage, current, shaft voltage, and stray magnetic field. The last part of the paper discusses the research gaps and some proposals to overcome the challenges A noteworthy point to mention is that the papers that are reviewed can be implemented in the industry and provide insight into the operating condition of a generator.

2. H. Ehya, A. Nysveen and J. A. Antonino-Daviu, "Stray Flux-based Identification and Classification of Inter-turn Short Circuit and Dynamic Eccentricity Faults in Synchronous Generators," in IEEE Transactions on Industrial Electronics, Under Review.

   In this article, two distinct patterns are proposed for diagnosing ITSC and DE faults by applying FFT to the stray magnetic field. An analytical method using the wave and permeance method is proposed to detect the sub-harmonics that are influenced by having a short circuit fault and an eccentricity fault. Two distinct patterns are then proposed for each fault type. The proposed patterns eliminate the need for knowledge of the frequency spectrum of a healthy generator. Furthermore, extensive analyses are also performed to realize how the existence of two simultaneous faults can influence the frequency patterns. The developed detection method is examined on a 100 kVA synchronous generator in the laboratory and on a 22 MVA generator in a power plant. The obtained results validate the theoretical proposals.

3. H. Ehya and A. Nysveen, "Pattern Recognition of Interturn Short Circuit Fault in a Synchronous Generator Using Magnetic Flux," in IEEE Transactions on Industry Applications, vol. 57, no. 4, pp. 3573-3581, July-Aug. 2021.

   This paper describes a new approach for inter-turn short circuit fault detection based on the application of short-time Fourier transform to the stray magnetic field in a synchronous generator. A detailed FEM modeling of a 100 kVA synchronous generator is described that considers the eddy effect

in the damper bars, non-linearity of the material, saliency of the poles, and winding distribution. A detailed specification of the designed sensor to pick the stray magnetic field is also described. The amplitude of the frequency spectrum of the stray magnetic field is shown to increase in the presence of one inter-turn short circuit fault. However, the magnitude of the same harmonics is increased by having a DE fault. Therefore, short-time Fourier transform is proposed to identify the fault type and even the number of faulty poles. Extensive experimental tests are performed for various degrees of short circuit fault in the rotor pole during no-load and on-load operation of the generator. The severity of the fault is also estimated using an image processing tool.

4. H. Ehya, A. Nysveen and J. A. Antonino-Daviu, "Advanced Fault Detection of Synchronous Generators Using Stray Magnetic Field," in IEEE Transactions on Industrial Electronics, vol. 69, no. 11, pp. 11675-11685, Nov. 2022.

   This paper proposes a new algorithm for ITSC fault detection in the rotor field winding of synchronous generators. Two generators are considered in this study: a 100 kVA 14-pole and a 22 MVA 8 pole. FEM is performed for both case studies, and the expected pattern and magnitude of the stray magnetic field are investigated. Since the primary analysis indicated the existence of an inherent DE fault in the 100 kVA laboratory setup, the DE impact on the stray magnetic field is also studied. FFT is applied to stray magnetic fields and analysis proved that the power rating and configuration of the generator can influence the harmonics. In addition, both ITSC fault and DE fault give rise to the same harmonics in the FFT spectrum that make fault type detection impossible. Therefore, unique patterns based on the application of continuous wavelet transform are proposed for ITSC and DE fault detection. The pattern does not require any baseline data from the healthy generator. The proposed method is validated both in the laboratory and in the power plant.

5. Ehya, H., Nysveen, A., Nilssen, R. and Liu, Y. (2021), Static and dynamic eccentricity fault diagnosis of large salient pole synchronous generators by means of external magnetic field. IET Electr. Power Appl, 15: 890-902.

   This article describes a comprehensive theoretical study on the impact of static and dynamic eccentricity on the stray magnetic field. In addition, the paper illustrates how a stray magnetic field is related to the air gap magnetic field. The impact of an eccentricity fault on the self and mutual inductance are also characterized. A numerical model of a 22 MVA synchronous generator is used to evaluate the proposed detection method. In this paper, a detection method is introduced based on the application of two stray magnetic field sensors installed opposite each other on the stator backside. The detection method assumes that the differential induced voltage in the sensors must be almost zero in the case of a healthy generator.

The static eccentricity and dynamic eccentricity faults are characterized using wavelet entropy. The effect of the load variation and eccentricity fault severity on the wavelet entropy is also discussed. Finally, some considerations regarding the sensor displacement and its impact on the proposed method are discussed.

6. H. Ehya, A. Nysveen, B. Akin, and J. A. Antonino-Daviu, "Detection and Severity Estimation of Eccentricity Fault of a High Power Synchronous Generator," in IEEE Transactions on Reliability, Major Revision.

Although a DE fault can significantly change the frequency content of the magnetic field, the SE fault only changes the magnitude of the magnetic field inside the stator core and in the vicinity of the stator core, indicating that the detection of SE is arduous. This paper describes the impact of both dynamic and static eccentricity faults on the induced voltage in the sensors installed on the stator backside. Three generators with distinct power ratings and configurations are used to demonstrate that the threshold levels in the frequency spectrums defined in IEC and IEEE standards are invalid. Therefore, a method is proposed based on the application of continuous wavelet transform. Unique patterns are proposed that can easily detect the fault type and its severity. The method is highly sensitive and can be used for the early-stage detection of eccentricity fault. Extensive tests have been performed in the laboratory on the 100 kVA generator, in addition to two field tests in a power plant. The method is able to detect eccentricity faults in the noisy environment of the power plant while the generator remains connected to the grid.

7. H. Ehya and A. Nysveen, "Comprehensive Broken Damper Bar Fault Detection of Synchronous Generators," in IEEE Transactions on Industrial Electronics, vol. 69, no. 4, pp. 4215-4224, April 2022.

This paper delves into BDB fault detection, which is one of the problematic fault types for diagnosis. A finite element model coupled to the electrical circuit is proposed to model the damper bar circuit in detail. Since the damper bars are active during the transient operation of the generator, the detection method proposes an analysis of the stray magnetic field during ramp-up and ramp-down. However, the findings indicate that a broken damper bar fault can also be detected during the steady-state operation of the generator in the case of a fractional winding layout. The detection method is based on the analysis of wavelet entropy. The impact of the BDB location on the proposed index is also analyzed. The findings indicate that the detection of a BDB located at the rotor pole corner is straightforward, whereas the detection of a BDB located in the middle of the rotor pole is almost impossible.

8. H. Ehya, A. Nysveen and T. N. Skreien, "Performance Evaluation of Signal Processing Tools Used for Fault Detection of Hydrogenerators Operating

in Noisy Environments," in IEEE Transactions on Industry Applications, vol. 57, no. 4, pp. 3654-3665, July-Aug. 2021.

Signal processing is the core part of fault detection of electric machines. Noise is unavoidable in power plants and industrial settings and it can interfere with data acquisition. A measured noisy signal can mask the fault pattern in signal processing. This paper describes the types of noise possibly encountered in the industrial environment and their root causes. The most prevalent type of noise is identified as white Gaussian noise. Five types of signal processing tools are studied: fast Fourier Transform, short-time Fourier transform, continuous wavelet transform, discrete wavelet transform, and time-series data mining. The measured stray magnetic field during healthy and under short circuit fault is first examined using the previously mentioned signal processors. Additive white Gaussian noise is then added to the signal to determine which level of the signal-to-noise ratio can be a safe margin for fault detection.

9. H. Ehya, T. N. Skreien and A. Nysveen, "Intelligent Data-Driven Diagnosis of Incipient Interturn Short Circuit Fault in Field Winding of Salient Pole Synchronous Generators," in IEEE Transactions on Industrial Informatics, vol. 18, no. 5, pp. 3286-3294, May 2022.

This paper examines various machine learning algorithms to automate the fault detection procedure. The air gap magnetic field is measured during no-load and under various load conditions for training and testing of the classifiers. The data are pre-processed to have sufficient data sets for the training. In addition, signal processing tools are used to pinpoint the exact changes in the signal due to the fault. Feature extraction tools used include FFT, energies of the discrete wavelet, and time-series feature extraction based on the scalable hypothesis (TSFRESH). Among several classifiers, ensemble classifiers demonstrate a promising result, as the algorithm can detect a short circuit fault with precision above 90%. The results presented in this paper are based on 'hand-out' data rather than the training result, thereby indicating the reliability of the method.

1.6   List of Publications and Patent

The papers listed below are the backbone of the research study carried out during the Ph.D. work. The publication list is divided into two parts: the first part presents the journal papers and the second part lists the conference papers. The first publication list consists of 9 journal papers, two published and one under review in *IEEE Transactions on Industrial Electronics*, one published in *IEEE Transactions on Industrial Informatics*, two published in *IEEE Transactions on Industry Application*, one under review in *IEEE Transactions on Reliability*, one published in *IET Electric Power Applications*, and one under review in *IEEE*

Open Transaction on Industry Applications. In the remainder of the thesis, the journal papers will be referred to as Paper I to Paper IX. In this document, only journal papers will be discussed, and explanations of the conference paper will not be covered. Moreover, a patent was filed in October 2019 as an umbrella patent that covers the established methods and algorithms for fault detection of synchronous machines. The patent status is in the national phase and is filed in the US, EU, UK, Canada, China, Australia, Singapore, Japan, and South Korea. The content of the patent will not be discussed in this thesis.

Journal Papers:

1. [Paper I] H. Ehya, A. Nysveen, J. A. Antonino Daviu, and Bilal Akin, "Health Monitoring of Synchronous Machines: Review of Methods, Applications and Trends," in IEEE Open Journal of Industry Applications, Under Review.

2. [Paper II] H. Ehya, A. Nysveen and J. A. Antonino-Daviu, "Advanced Fault Detection of Synchronous Generators Using Stray Magnetic Field," in IEEE Transactions on Industrial Electronics, vol. 69, no. 11, pp. 11675-11685, Nov. 2022.
   DOI: 10.1109/TIE.2021.3118363.

3. [Paper III] H. Ehya and A. Nysveen, "Pattern Recognition of Interturn Short Circuit Fault in a Synchronous Generator Using Magnetic Flux," in IEEE Transactions on Industry Applications, vol. 57, no. 4, pp. 3573-3581, July-Aug. 2021.
   DOI: 10.1109/TIA.2021.3072881.

4. [Paper IV] H. Ehya, A. Nysveen and J. A. Antonino-Daviu, "Stray Flux-based Identification and Classification of Inter-turn Short Circuit and Dynamic Eccentricity Faults in Synchronous Generators," in IEEE Transactions on Industrial Electronics, Under Review.

5. [Paper V] Ehya, H., Nysveen, A., Nilssen, R. and Liu, Y. (2021), Static and dynamic eccentricity fault diagnosis of large salient pole synchronous generators by means of external magnetic field. IET Electr. Power Appl, 15: 890-902.
   DOI: 10.1049/elp2.12068

6. [Paper VI] H. Ehya, A. Nysveen, B. Akin, and J. A. Antonino-Daviu, "Detection and Severity Estimation of Eccentricity Fault of a High Power Synchronous Generator," in IEEE Transactions on Reliability, Major Revision.

7. [Paper VII] H. Ehya and A. Nysveen, "Comprehensive Broken Damper Bar Fault Detection of Synchronous Generators," in IEEE Transactions on Industrial Electronics, vol. 69, no. 4, pp. 4215-4224, April 2022.
   DOI: 10.1109/TIE.2021.3071678.

8. [Paper VIII] H. Ehya, A. Nysveen and T. N. Skreien, "Performance Evaluation of Signal Processing Tools Used for Fault Detection of Hydrogenerators Operating in Noisy Environments," in IEEE Transactions on Industry Applications, vol. 57, no. 4, pp. 3654-3665, July-Aug. 2021.
DOI: 10.1109/TIA.2021.3078136.

9. [Paper IX] H. Ehya, T. N. Skreien and A. Nysveen, "Intelligent Data-Driven Diagnosis of Incipient Interturn Short Circuit Fault in Field Winding of Salient Pole Synchronous Generators," in IEEE Transactions on Industrial Informatics, vol. 18, no. 5, pp. 3286-3294, May 2022.
DOI: 10.1109/TII.2021.3054674.

Patent:

1. H. Ehya, and A. Nysveen, "Fault Detection in Synchronous Machines," UK. Patent Office, WO2021/074248, October 2019.

Conference Papers:

1. H. Ehya, A. Nysveen and J. A. Antonino-Daviu, "Static, Dynamic and Mixed Eccentricity Faults Detection of Synchronous Generators based on Advanced Pattern Recognition Algorithm," 2021 IEEE 13th International Symposium on Diagnostics for Electrical Machines, Power Electronics and Drives (SDEMPED), 2021, pp. 173-179.
DOI: 10.1109/SDEMPED51010.2021.9605488.

2. H. Ehya, A. Nysveen, J. A. Antonino-Daviu and B. Akin, "Inter-turn Short Circuit Fault Identification of Salient Pole Synchronous Generators by Descriptive Paradigm," 2021 IEEE Energy Conversion Congress and Exposition (ECCE), 2021, pp. 4246-4253.
DOI: 10.1109/ECCE47101.2021.9595993.

3. H. Ehya, T. N. Skreien, A. Nysveen and R. Nilssen, "The Noise Effects on Signal Processors Used for Fault Detection Purpose," 2020 23rd International Conference on Electrical Machines and Systems (ICEMS), 2020, pp. 183-188.
DOI:10.23919/ICEMS50442.2020.9290831.

4. H. Ehya, G. Lyng Rødal, A. Nysveen and R. Nilssen, "Condition Monitoring of Wound Field Synchronous Generator under Inter-turn Short Circuit Fault utilizing Vibration Signal," 2020 23rd International Conference on Electrical Machines and Systems (ICEMS), 2020, pp. 177-182.
DOI:10.23919/ICEMS50442.2020.9291088.

5. H. Ehya, A. Nysveen and R. Nilssen, "Pattern Recognition of Inter-Turn Short Circuit Fault in Wound Field Synchronous Generator via Stray Flux Monitoring," 2020 International Conference on Electrical Machines (ICEM), 2020, pp. 2631-2636.
   DOI:10.1109/ICEM49940.2020.9270986.

6. H. Ehya, A. Nysveen, I. L. Groth and B. A. Mork, "Detailed Magnetic Field Monitoring of Short Circuit Defects of Excitation Winding in Hydrogenerator," 2020 International Conference on Electrical Machines (ICEM), 2020, pp. 2603-2609.
   DOI: 10.1109/ICEM49940.2020.9270942.

7. H. Ehya, A. Nysveen and R. Nilssen, "A Practical Approach for Static Eccentricity Fault Diagnosis of Hydro-Generators," 2020 International Conference on Electrical Machines (ICEM), 2020, pp. 2569-2574.
   DOI:10.1109/ICEM49940.2020.9270675.

8. H. Ehya, A. Nysveen, R. Nilssen and U. Lundin, "Time Domain Signature Analysis of Synchronous Generator under Broken Damper Bar Fault," IECON 2019 - 45th Annual Conference of the IEEE Industrial Electronics Society, 2019, pp. 1423-1428.
   DOI:10.1109/IECON.2019.8927529.

1.7   Outline of the Thesis

This Ph.D. thesis consists of two parts. The first part includes three chapters: an introduction, methodologies and contributions, and a conclusion. The first part of the thesis is kept brief, providing the key concept, research gaps, developed methods, and a summary of the conducted research and the major findings. A detailed explanation of the simulation, experimental and field test results, signal processing, machine learning tools, and detailed analysis of results are all presented in the appended papers. The second part of the thesis includes the nine appended journal papers and one patent. The first part of the thesis is outlined as follows.

1. Chapter 1 includes an introduction to the importance of a health monitoring system for hydropower plants. The objectives and the scope of the work are clarified. The project background and a state-of-the-art review are included, followed by enumeration of the research gaps in the field. Finally, the main contribution of the Ph.D. study, with its scientific contributions, is listed.

2. Chapter 2 gives a brief introduction to various faults in synchronous generators and the root causes of the faults. Finite element modeling of the

generators, faults, and sensors are briefly explained. The experimental setup and the field tests performed in two power plants are illustrated. Different signal processing tools are succinctly introduced. In the contribution sections, the developed methods based on the pattern recognition methods for each fault type are discussed.

3. Chapter 3 provides a summary of the Ph.D. work and suggestions for future research activities.

2 Methodologies and Contributions

2.1 Faults in Synchronous Generators

The impact of faults on the performance of the synchronous generator depends on the type of fault and the operational environment. Recognizing the origin of the fault can markedly accelerate the determination of the health status of the electric machine and help the maintenance team in their planning. Fault detection must be performed at the early stage of the fault, since faults begin from an initial defect and progress to become severe faults.

Several faults can occur in synchronous generators and are categorized, based on their location, as stator faults and rotor faults. The research conducted in this Ph.D. study is limited to rotor faults. The faults known to occur in the rotor of salient pole synchronous generators are:

1. Inter-turn and turn-to-ground short circuit fault

2. Eccentricity fault

3. Misalignment

4. Broken damper bar and broken end ring

In the following subsections, the definition, root cause, and impact of each fault on the performance of salient pole synchronous generators are briefly described.

2.1.1 Rotor Short Circuit Fault

Two separate winding circuits—the rotor field winding and the damper winding—are present in the rotor of a synchronous generator, as shown in Fig. 2.1. The rotor field winding has tens of turns concentrated around each rotor pole. A short circuit fault in the rotor field winding can be divided into two categories:

1. Inter-turns short circuit fault
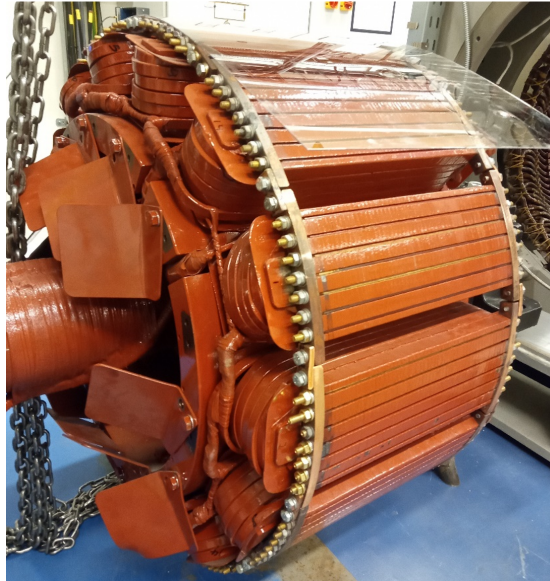
2. Turn to ground fault

Figure 2.1: Rotor circuits of a 100 kVA synchronous generator that consists of a field winding circuit and rotor damper bar circuit.

Unlike a short circuit fault in the stator winding, that is mostly due to a high voltage difference between the turns, which degrades the insulation system, the voltage difference between two adjacent turns in the rotor winding is low. Aging, the operating conditions, and environmental factors are the main causes of ITSC faults in the rotor field winding. A generator can operate with a short circuit fault in the rotor winding for a long time. However, the vibration level can be increased, which results in a reduction in the maximum output power by a vibration protection relay to avoid tripping the generator from the power grid.

The local temperature rise due to a short circuit leads to acceleration of insulation degradation. Therefore, the number of shorted turns increase over time. If the short circuit happens close to the groundwall insulation, the possibility of having a turn to ground fault increases, and the generator is tripped by the ground fault protection relay.

An asymmetric magnetic field in the air gap is the main consequence of a short circuit fault in the rotor field winding. The asymmetric magnetic field creates a circulating current in small synchronous generators that closes their path to the ground through the rotor shaft and bearings. Increases in the circulating current in the rotor shaft can cause significant destruction of the bearings. In large synchronous generators, the bearing is isolated to avoid circulating current in the bearing. However, the induced voltage in the shaft and bearing can reach

up to 200 V.

2.1.2   Eccentricity Fault

In principle, the length of the minimum air gap in a salient pole synchronous generator must be kept constant. However, obtaining a uniform air gap is almost impossible. Even in brand new synchronous generators, depending on the technology of the manufacturing, a slight and permissible eccentricity exists, called the 'inherent eccentricity' fault. Several factors give rise to eccentricity faults in synchronous generators [6]:

1. Incorrect location of the stator and rotor to one another

2. Incorrect location of the bearings

3. Displaced or bent shaft

4. Abrasion of bearings

5. Internal elliptical cross-section of the stator core

6. Misaligned connection of the synchronous generator shaft

The type of eccentricity fault depends on the position of the rotor rotational axes. Three eccentricity types exist:

1. Static eccentricity (SE)

2. Dynamic eccentricity (DE)

3. Mixed eccentricity (ME)

Note: From the fault detection point of view, a uniform air gap exists if the distance between the middle of the rotor pole and stator tooth is constant. However, generally speaking, the air gap length is not uniform in the salient pole synchronous generator due to the rotor pole saliency and the gap between the rotor poles.

Synchronous generators have three longitudinal axes: the rotor symmetrical axis, the stator symmetrical axis, and the rotor rotational axis. In an ideal healthy generator, all centers coincide with each other. In the case of an SE fault, the minimum air gap length varies only with the position. As shown in Fig. 2.2, the center of the rotor is shifted toward the stator core while it rotates around its center axis. The possibility of having an SE fault is low due to the high precision
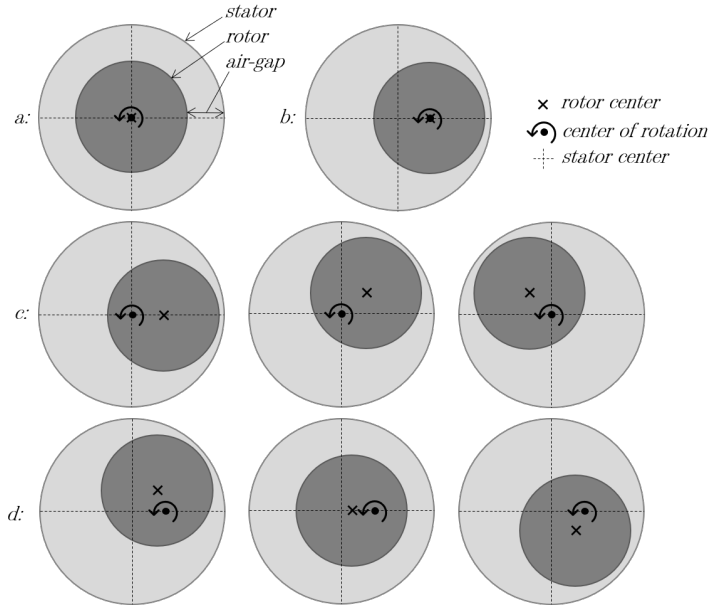
Figure 2.2: Definition of a healthy and an eccentric generator based on the location of the rotor with respect to the stator. a) healthy, b) SE fault, c) DE fault, and d) ME fault. (The rotor is drawn as a non-salient pole machine for the sake of simplicity.)

in the manufacturing process. However, the SE fault is one of the prevalent faults in the hydro generators located inside the mountains, where rockmass instability gives rise to the SE fault.

In the case of a DE fault, the rotor rotational axis revolves around the stator center axis while the rotor center point is displaced. The minimum air gap length varies with both time and position when DE fault happens as shown in Fig. 2.2.

The coexistence of both SE and DE faults in the synchronous generator is so-called mixed eccentricity. In the case of the ME fault, as shown in Fig. 2.2, the rotor is close to the stator on one side due to the SE fault, while the rotor whirling location varies with time and location owing to the DE fault.

Three types of eccentricity faults bring about the unbalanced magnetic field in the air gap. Unbalanced magnetic pull and vibration are the main consequence of an eccentricity fault. In the case of the SE fault, the generator operates while the rotor becomes closer to the stator than what has been designed, resulting in local saturation and a consequent local temperature rise. The increased temperature, in the long term, can accelerate thermal aging of the insulation system.

In addition, the increased vibration level puts more tension on the generator end winding, which is prone to high insulation stress. The unbalanced magnetic field also creates a circulating current in the rotor shaft and bearing, and this current deteriorates the bearing. A defected bearing clearly increases the eccentricity fault degree, and if precautionary actions are not taken, the rotor may touch the stator.

2.1.3 Misalignment fault

Misalignment is a sub-category of eccentricity fault wherein the air gap length varies along the axial axis of the synchronous generator. In the case of SE, DE, and ME faults, the air gap length along the axial axis of the machine is assumed to be symmetric. Similar to eccentricity faults, three types of misalignment faults are recognized: static misalignment, dynamic misalignment, and mixed misalignment.

Assuming a horizontally mounted synchronous generator operating under static misalignment, both the drive-end and non-drive-end of the machine are located opposite each other. In the case of a static misalignment fault, the location of both ends is fixed and does not vary with time. The dynamic misalignment fault gives rise to a variation in the rotor in both the radial and axial directions of the synchronous generator. The simultaneous existence of both static and dynamic misalignment in the machine leads to a mixed misalignment fault.

A misalignment fault is the most destructive fault type and can destroy the stator and rotor even with a low-severity fault. Therefore, during the inspection period, both ends of the generator must be evaluated to avoid a false negative fault. The root cause and consequence of a misalignment fault on the performance and parameters of the synchronous generator are similar to those of an eccentricity fault.

2.1.4 Broken damper bar fault

The damper winding is the second circuit in the rotor of the salient pole synchronous generator. Damper bars are embedded in the rotor pole shoe and are short-circuited on both sides by the end rings. Fig. 2.1 shows damper bars and end rings. The role of damper bars is evident in the case of salient pole synchronous motor as the motor start is similar to that of the induction motor as it is aided by the damper winding and the DC voltage applied to the rotor field winding when the rotational speed becomes close to the synchronous speed. However, in synchronous generators, the damper bars are used to suppress the transient dynamics in the rotor caused by an external fault in the power system
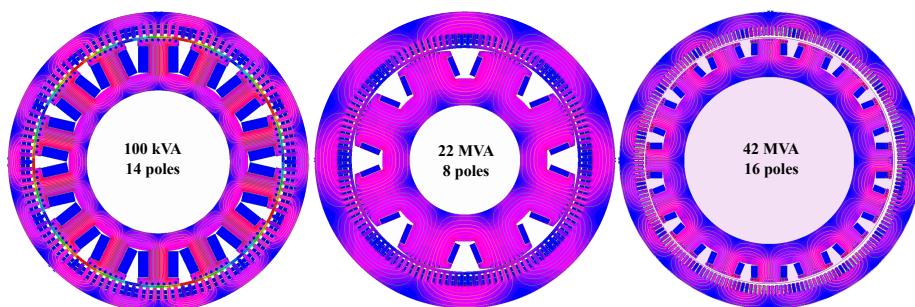
Figure 2.3: Finite element models of three salient pole synchronous generators.

and the sudden load variation. In addition, the damper bars act as a shield to protect the rotor field winding during transients in the stator winding caused by the power network perturbation.

Frequent starts and stops of the synchronous machines that operate in pump-storage power plants, and inadequate connections in the joints between the damper bars and end rings result in the broken damper bar fault. Since the damper bars are active during transient operation of the synchronous machines, the detection of broken damper bars is difficult due to the limited time window.

2.2 Finite Element Modeling

Electrical machine modeling is the first step in the fault detection procedure. Analytical methods, such as modified winding function and magnetic equivalent circuits, are widely used for fault detection of induction motors due to their simplicity. However, finite element modeling is preferred due to its high accuracy, since geometry, saturation, eddy effect, and material properties can be considered. The FEM is still computationally expensive for fault detection of electric machines as at least several mechanical revolutions of the machine are required and the entire geometry must be considered due to the lack of symmetry caused by the fault.

In this Ph.D. study, five salient pole synchronous generators are modeled in FEM: 100 kVA 14-pole, 22 MVA 8-pole, 42 MVA 16-pole, 105 MVA 14-pole, and 400 MVA 60-pole. The FEM of three generators is shown in Fig. 2.3. Since the procedure of the modeling is the same in four synchronous generators, a 100 kVA synchronous generator with 14 salient poles is explained in more detail.
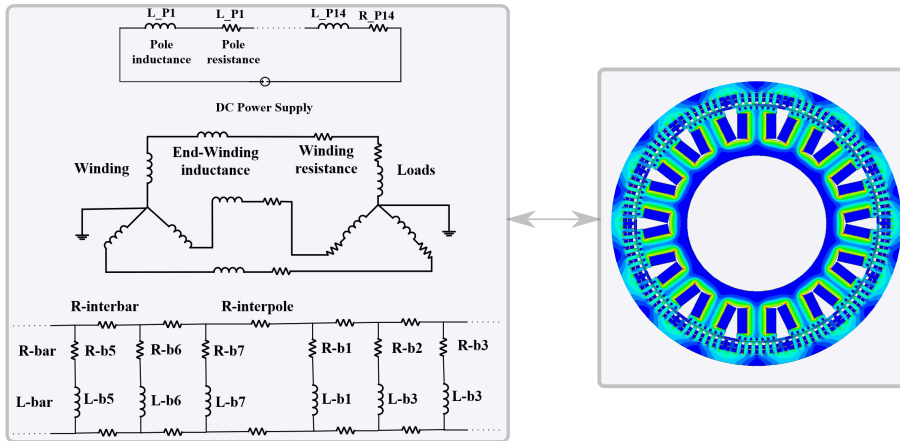
Figure 2.4: Coupled circuits of the stator winding and load, rotor field winding, and damper circuit with FE simulation of a 100 kVA synchronous generators.

2.2.1 Modeling of a 100 kVA Synchronous Generator

The FEM of a synchronous generator provides an in-depth understanding of how faults can influence the various signals, such as voltage, current, vibration, and magnetic fields. Fig. 2.4 shows the FEM model of a 100 kVA salient pole synchronous generator linked to the electrical circuit. The non-linearity of the stator and rotor cores are taken into account, since saturation can influence sub-harmonics in the magnetic field [63]. The eddy effect is only considered in the damper bars.

The detailed geometry of the FEM is considered as the slots in the stator and rotor influence the magnetic field distribution in the air gap. In addition, the saliency of the rotor poles is considered. The generator under study is a 14-pole/114-slot machine with fractional winding. The precise distribution of the windings in the stator slots is crucial, especially for broken damper bar fault detection. The fractional winding creates sub-harmonics that, in turn, result in a current flow in the damper bars even during steady-state operation of the generator.

Each rotor pole includes seven damper bars that are distributed in the rotor pole shoe. The dampers are short-circuited by end rings on both sides. The short circuited damper cages in each rotor pole are connected to neighboring poles by the interpole connection rings. An external circuit that is modeled in Ansys Electronics [64] consists of three circuits:
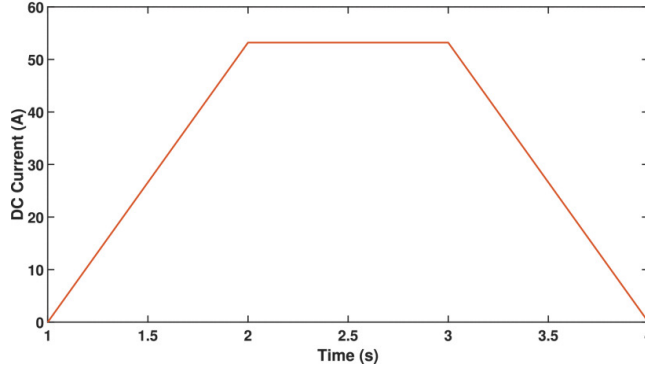
1. rotor field winding

Figure 2.5: Waveform of the current applied to the rotor field winding of 100 kVA synchronous generator.

2. stator winding and load circuit

3. rotor damper winding and end ring circuit

In FEM, the DC current applied to the rotor magnetization winding has a constant value based on the load point. However, a trapezoidal shape waveform is applied to the rotor field winding for the BDB fault detection. Fig. 2.5 shows the DC current applied to the rotor field winding of a 100 kVA generator. The applied current contains two transient periods during which the current is increased from zero to nominal no-load current (53.2 A) during the ramp-up period and it is decreased to zero during the ramp-down period. The period between these two operation modes is a steady-state mode during which a constant 53. 2 A is fed to the rotor field winding. The damper bars are active during both ramp-up and ramp-down periods. However, if the generator has a fractional winding, a current is present in the damper winding even during steady-state operation.

2.2.2   Data acquisition of magnetic field

Air gap magnetic field

The magnetic field can be stored for any time step at any arbitrary point using commercial software; however, the computation time significantly can be increased. Therefore, it is recommended to measure the air gap magnetic field at the desired point where the magnetic field sensor must be installed. A point in the air gap close to the stator tooth is selected to measure the magnetic field in the air gap. This point resembles the Hall-effect sensor. A search coil mounted around the stator tooth can also be used for the air gap magnetic field measure-
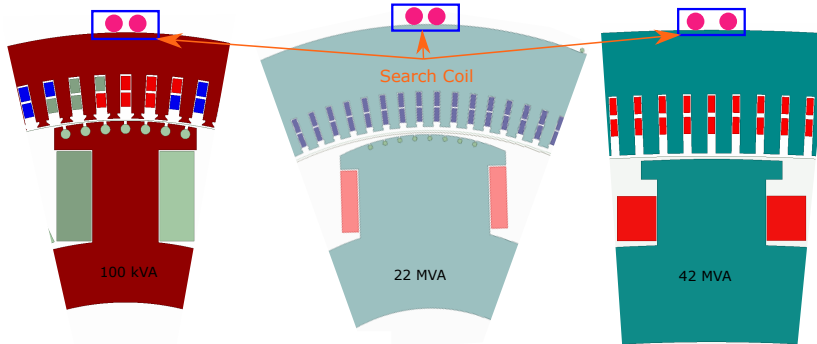
Figure 2.6: Location of search coil on the backside of three generators to measure the stray magnetic field.

ment. In this case, two circles with the desired number of turns must be mounted on two sides of a stator tooth.

Stray Magnetic Field

The stray magnetic field, which is a so-called mirror of the air gap magnetic field, can also be measured on the stator backside of the synchronous generator. A large hydro generator does not have the metallic housing common to induction motors since the wall of the generator pit acts as a generator housing. Therefore, direct access to the generator backside is possible for mounting the sensors. For this reason, the generator housing (metallic frame) is not modeled in the FEM. The amplitude of the stray magnetic field on the stator backside is in the order of micro Tesla and the stray magnetic field vanishes if the sensor is mounted at a distance of more than ten centimeters. Therefore, a high signal-to-noise ratio can be achieved by deploying a proper search coil mounted close to the stator core. Two types of stray magnetic fields, namely radial and axial stray magnetic fields, can occur. Calculating pure axial magnetic fields requires 3D FEM. In-depth analysis and experimental results obtained during this Ph.D. study indicated that the signal is informative when the sensor can capture both the radial and axial stray magnetic fields. This combination of radial and axial stray magnetic fields can be measured when the search coils are modeled as shown in Fig. 2.6.

2.2.3   Fault Modeling

Three types of fault, namely ITSC fault, eccentricity fault (SE, DE, and ME), and BDB fault, are investigated. The following sections explain how the faults

are modeled in the FEM of the synchronous generator.

ITSC fault

In the case of an ITSC fault in the field winding, the magnetomotive force of the relevant pole is reduced, resulting in a weaker magnetic field. An inter-turn fault in the field winding can be simulated by reducing the total number of conductors in the excitation coil while keeping the current constant. In this case, the specified excitation currents based on the load situation must be applied to the field winding.

Eccentricity Fault

The minimum air gap length is not uniform when a synchronous generator operates under eccentricity fault. An SE fault in FEM can be simply implemented by moving the stator core and stator winding along the x- or y-axis. The degree of eccentricity fault can be calculated as follows:

$$EccentricityDegree = \frac{d}{g} \times 100 \tag{2.1}$$

where g is the radial air gap length in the healthy generator and d is the stator displacement in the any direction.

The DE fault can be modeled in FEM by moving the rotor core, field windings, damper bars, and shaft in a preferred direction. The degree of the DE fault can be determined using 2.1, where d is the rotor displacement. The ME can be implemented by a combination of both SE and DE faults, where both stator and rotor must be displaced.

BDB Fault

A complete FEM of a salient pole synchronous generator is required while the machine operates under a BDB fault, since BDB creates an asymmetric magnetic field in the air gap. Fig. 2.4 shows the external circuit of the synchronous generator with 14 salient poles and 7 damper bars in each rotor pole shoe. The detailed resistance and inductance of the damper bars and inter-connections must be included. The resistance of the healthy damper bar is in the order of $\mu\Omega$. In the case of a broken damper bar fault, the damper bar resistivity must be increased up to kilo-ohms to limit the current that passes through the damper. Therefore, a low current passes through the damper bar, even during a broken damper bar
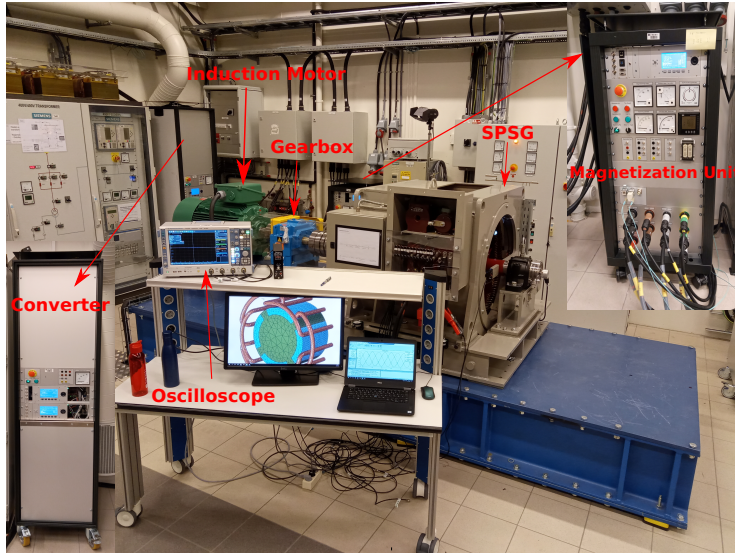
Figure 2.7: Experimental setup of a 100 kVA salient pole synchronous generator.

fault.

2.3 Experimental Setup

Although analytical and numerical modeling can give in-depth insight into the fault impact on the signals of the synchronous generator, an experimental setup is required to verify the obtained results. In this Ph.D. research, extensive tests have been performed on a 100 kVA synchronous generator with 14 salient poles which resembles a typical Norwegian hydro generator.

2.3.1 Laboratory setup

The main test rig consists of a 100 kVA 400 V synchronous generator, as shown in Fig. 2.7. The generator has 14 salient poles, which is the second most common number of poles in Norwegian hydropower plants. Synchronous generators with 16 poles are the most dominant ones. Table. 2.1 shows the key parameters and nameplate data of the generator. The stator winding has the possibility to be arranged in series or parallel connections. The entire experiment has been performed while the windings were in series connection. A 90 kW induction motor drives the generator shaft at speed of 1485 rpm. The induction motor is

Table 2.1: Specification of 100 kVA, 50 Hz, Synchronous Generator

Quantity	*Values*	*Quantity*	*Values*
No. of slots	114	No. of damper bars/pole	7
Winding connection	Wye	Number of poles	14
No. of stator turns	8	No. of rotor turns / pole	35
Nominal speed	428 rpm	Power factor	0.90
Nominal voltage	400 V	Nominal current	144.3 A
Nominal exc. current	103 A	No-load exc. current	53.2 A
Nominal exc. voltage	20 V	No-load exc. Voltage	10.5 V

controlled by a programmable converter that provides control of the active power while the generator is connected to the power grid.

An oversized 20 kW magnetizing unit is used to feed a required a DC current to the rotor field winding. The magnetization unit can be used to provide no-load to full-load current for the rotor field winding in two modes of local load and grid connection. The magnetizing unit has the capability to perform the following steps when the generator feeds the power grid:

1. The magnitude of the induced line voltage in the stator terminal must be equal to the grid voltage.

2. The frequency of the generator and the grid must be equal.

3. The phase sequence of both the generator and the grid must equal.

4. The phase angle must be equal.

The nominal speed of a 14-pole synchronous generator is 428 rpm, while the prime over has a nominal speed of 1485 rpm. Therefore, a gearbox unit with a gear ratio of three to one is used to reduce the rotational speed.

2.3.2   Fault Implementation

A custom-made 100 kVA synchronous generator has the feasibility of emulating three fault types: the ITSC fault in the rotor field winding, the static eccentricity fault, and the broken damper bar fault. The following sections describe how the faults are emulated.
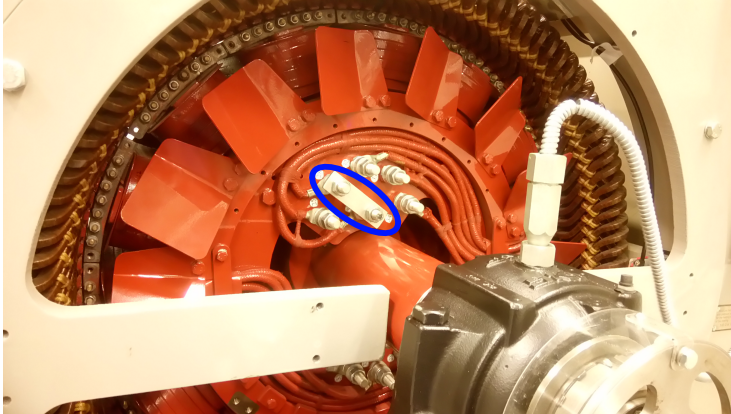
Figure 2.8: Location of the shorted turns tap on the rotor.

ITSC fault

The ITSC fault can be applied to two poles of a 100 kVA synchronous generator with 14 salient poles. Each rotor pole contains 35 turns, and several turns can be removed. Although a short circuit fault in the rotor field winding causes asymmetry in the air gap magnetic field, having a short circuit fault in two opposite poles tries to alleviate the non-uniform magnetic field. Thus, this custom-made synchronous generator has the possibility of analyzing this situation.

Different taps connected to the rotor field winding are connected to the bolts on the rotor. Removal of 1, 2, 3, 7, or 10 turns is possible. A copper plate is used to emulate the ITSC fault. The copper plate connects the common bolt to any of the bolts, which represent the number of turns desired to be removed. Fig. 2.8 shows the rotor of the 100 kVA synchronous generator in which 7 turns are removed.

Static eccentricity

The housing of the custom-made 100 kVA generator can be moved along the horizontal axis to emulate the static eccentricity fault. Two bolts on both sides of the generator are used to move the stator frame smoothly. To measure the eccentricity fault severity, four measuring clocks are installed on both sides of the generator housing (two on each side). The clocks are set to zero on both sides, and moving the generator changes the clocks and shows the eccentricity fault severity. Fig. 2.9 shows the location of the bolts and measuring clocks.
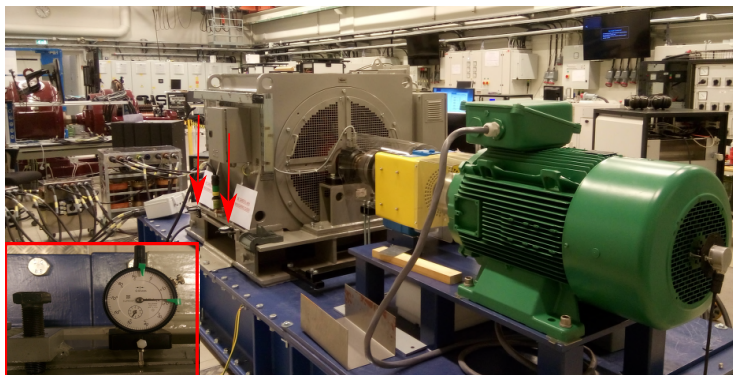
Figure 2.9: Two bolts are mounted on each side of the synchronous generator to move the stator frame in order to emulate the SE fault, and measuring clocks are installed on each side to measure the SE fault.
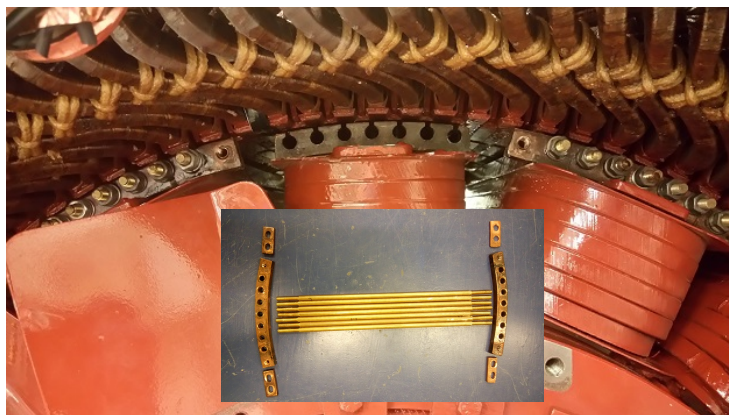

Figure 2.10: Removed damper bars, end rings and the interpole connection segments from one rotor pole

Broken damper bar fault

Both a broken damper bar fault and broken end ring can be applied to the 100 kVA synchronous generator. Removable damper bars are embedded in the slots in the rotor pole shoes. Each rotor pole contains seven damper bars that are short-circuited on both sides using end rings. Fig. 2.10 shows the removed damper bars, end ring, and interpole connections.

2.3.3 Sensors

The signal is the most important ingredient in the fault detection of electric machines. The measurement approaches in fault detection of electric machines are divided into two categories:

1. Invasive: In this approach, a sensor must be installed inside the electric machines, so this demands remarkable modification and preparation. For instance, to measure the air gap magnetic field, the air gap must be accessible, which means that the machine must be stopped and dismantled.

2. Non-invasive: In this method, signals can be measured without any modification to the machine, and the use of an existing sensor is possible. Current, voltage, vibration, and stray magnetic fields are examples of non-invasive methods.

Note: In this Ph.D. study, different fault detection methods are proposed based on various signals such as voltage, current, vibration, shaft voltage, air-gap magnetic field, and stray magnetic field. Detailed simulation and experimental results analysis indicated that the voltage, current, vibration, and shaft voltage have low sensitivity. In addition, the cost of the used sensors is high while the provided data has poor content. Therefore, a developed health monitoring system is proposed based on the air-gap magnetic field and stray magnetic field. The results related to air gap magnetic field and stray magnetic are considered for further discussion.

Hall-effect sensor

The most informative signal that can reveal the health status of the electric machine is the air gap magnetic field, although it is an invasive method. Both search coils and Hall-effect sensors can be used for the measurement of the magnetic field in the air gap. However, the Hall-effect sensor is used in this Ph.D. study. Since the air gap length in the 100 kVA generator is 1.75 mm, the size of the Hall-effect sensor becomes the first selection criteria. AST244 is selected, with a size of (3.0×5.0×0.8) mm. The sensor is able to measure magnetic fields varying from a few µT to more than 10 T. It also has low noise and low pick-up EMC characteristics, as well as a low-temperature coefficient, which makes it a good choice for operating inside a generator. The sensor must be supplied by a constant DC power supply. Hall-effect sensors are sensitive to the amplitude of the constant current that feeds into their circuit, indicating that the variation in the amplitude of the supply current may result in the incorrect amplitude of the measured magnetic field. In addition, Hall-effect sensors are sensitive to electromagnetic noise; therefore, the wires must be shielded.
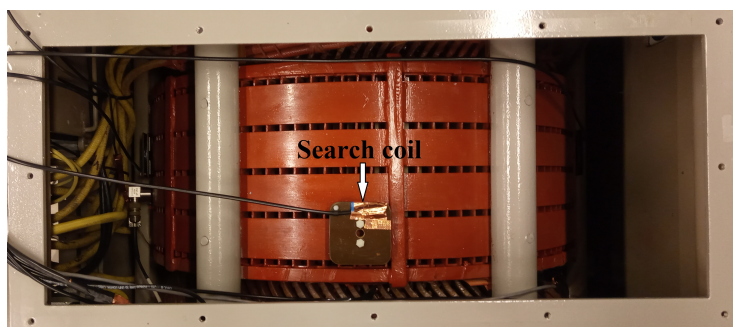
Figure 2.11: Custom-made search coil mounted on the stator backside of a 100 kVA synchronous generator

Stray magnetic field sensor

The stray magnetic field is the so-called "mirror" of the air gap magnetic field, which indicates that it can be a suitable and non-invasive substitute for the air gap magnetic field (Detailed discussion is provided in Section 2.6). Various sensors are available to measure the stray magnetic field on the stator backside of electric machines; these include flux-gates, Hall-effect sensors, and search coils. Search coils are preferred since they are passive sensors and can be custom designed.

A search coil consists of a plastic reel and thousands of turns of copper wire. The designed search coil used in this study is (100×100×10) mm. It contains 3000 turns of copper wire with a diameter of 0.12 mm. The resistivity and the inductance of the search coil at the terminal are 912 Ω and 714 mH, respectively. The output of the sensor is connected to the coaxial cable to avoid any disturbance or noise coming from the operational environment. A BNC port is utilized to connect the sensor output to an oscilloscope. Fig. 2.11 shows a search coil mounted on the backside of a 100 kVA synchronous generator.

2.3.4   Data Acquisition

Data acquisition plays a key role in the health monitoring of electric machines. Although the quality of the measured data depends on the quality of the sensors and the operating environment, the sampling rate at which the data must be recorded is also crucial, since some fault-related harmonics can simply vanish in this process. An advanced oscilloscope (ROHDE & SCHWARZ RTO2044) is used with a sampling frequency of 10 kHz. This oscilloscope has a high sampling rate with high sensitivity to noise. The length of the data is limited to 40 seconds in order to provide sufficient data for machine learning purposes. Fig. 2.7 shows

the utilized oscilloscope for the data acquisition.

2.4   Field Tests

Two field tests are performed in two power plants in Norway. The vibration level of a power plant located in mid-Norway was high and limited the maximum power production. The power plant has a single unit with a 22 MVA 8-pole synchronous generator. The generator has a metallic frame with several hatches that provide access to the stator backsides. Therefore, only a stray magnetic field sensor that was previously used in the laboratory setup is mounted on the stator backside. Measuring the air magnetic field is impossible since the rotor must be removed in order to gain access to the air gap. Four stray magnetic field sensors are mounted on the stator backside and data is recorded at a sampling frequency of 10 kHz. The test was performed during no-load and partial load (17 MW) when the generator is connected to the power grid.

The second field test is performed in a hydropower plant that has four units. One unit is suspected to be operating under a faulty condition since a maintenance service company reported an abnormally increased vibration level. The 42 MVA generator has 16 poles and cannot reach its maximum loading due to an increase in vibration level. Three types of sensors are mounted: four Hall-effects sensors in the air gap, four start magnetic field sensors, and four accelerometers. The data were recorded at the sampling frequency of 10 kHz for 40 seconds. Since the hydropower plant has four units, the noise captured by the start magnetic field is also recorded.

2.5   Signal Processing

Hidden fault-related patterns in the signals can be revealed using signal processing tools. Signal processing is the act of applying mathematical tools to raw data to obtain deep insight into the data components. Various signal processing tools are developed based on needs in certain fields and have been adapted for use in other fields, such as health monitoring of electric machines. Signal processing tools used in fault detection of electric machines are divided into three categories:

1. Time-domain, such as time series feature extraction based on scalable hypothesis tests (TSFRESH) and time-series data mining (TSDM)

2. Frequency-domain, such as fast Fourier transform (FFT)

3. Time-frequency domain, such as short-time Fourier transform (STFT), discrete wavelet transform (DWT), and continuous wavelet transform (CWT)

Several signal processing tools have been used during the Ph.D. study; however, the above-mentioned signal processing tools will be briefly explained since the results in the published journal papers are based on them.

2.5.1 TSFRESH

Feature extraction from a time series is a complicated and time-consuming process since several algorithms must be considered. The Python package of TSFRESH combines 63 time-series characterization algorithms and can extract 794 features. The method also provides a feature selection tool that eliminates the less relevant features to reduce the computational complexity of the method. Some of the features are absolute energy, first maximum and minimum, kurtosis, FFT coefficients, variance, CWT coefficient, and DWT energies [65].

2.5.2 Fast Fourier transform

The FFT is a mathematical transform that decomposes a function, which could be a signal or a function of time, into its constituent frequencies, indicating that the signal can be demonstrated based on its constituent frequency components. FFT is a suitable signal processing tool for stationary signals, suggesting that signals containing transient periods cannot be treated well. The loss of time information of the processed signal by FFT is the main disadvantage of this approach [66]. Therefore, FFT is not an appropriate approach for processing non-stationary signals if the temporal location of the frequencies is required. Furthermore, the computational complexity of FFT is $O(n.log(n))$, where n is the number of data samples [67]. The quality of the frequency spectrum of FFT depends on several factors, such as the sampling frequency, length of data, and the windowing function. In this study, the signals are sampled at a frequency of 10 kHz, with a data length of 40 seconds and a Hanning window [7].

2.5.3 Short time Fourier transform

The lack of temporal resolution of the FFT is compensated by introducing STFT. STFT is widely used when a time and frequency demonstration of the signal is required. STFT can analyze the non-stationary and transient period in the signal, which makes it suitable for health monitoring applications. The STFT applies the FFT to a section of the signal using a window function. The window function is then swiped across the entire data set to find the magnitude for given frequencies and time instants [66].
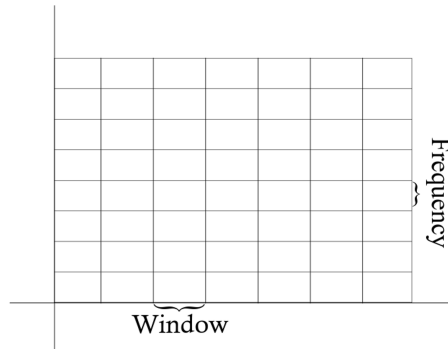
38

Figure 2.12: Resolution grid of a STFT of a signal.

The result of the STFT is demonstrated in a spectrogram, which is an image with time as the horizontal axis and frequency as the vertical axis, and the intensity of the spectral data is designated by color. The optimal result can be achieved by adjusting the type of window function, the length of the window, and the length of the data set. The computational complexity of the STFT in comparison to the FFT is notable since the computational complexity of the STFT is $O(n.mlog(m))$, where n is the window length, indicating that the FFT must be performed n times in order to achieve the STFT spectrogram.

The grid resolution of STFT is uniform across the entire time and frequency values, as shown in Fig. 2.12. According to the uncertainty principle, which states that one cannot know with a high degree of certainty both a property and its integration in the time interval at the same instant [66], obtaining a high resolution in both frequency and time is not achievable. Therefore, the best window length must be selected based on the desired frequency that needs to be tracked.

2.5.4 Continuous wavelet transform

CWT is a signal processing tool that decomposes a signal into a set of primary waveforms. Analyzing the wavelet coefficient of the waveforms can provide valuable insight into the hidden pattern in the signal. CWT is introduced to resolve the low time-frequency resolution of STFT caused by the uniform grid resolution. The wavelet transform divides a time-frequency space from coarse to fine sizes, while the STFT divides a time-frequency space into equal sizes. A grid resolution of CWT is shown in Fig. 2.13.

Unlike STFT, which uses FFT as a window function that is dilated over the entire signal to perform FFT, the signal is convoluted to wavelet function in the
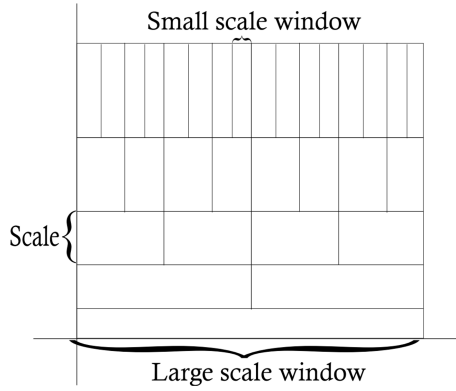
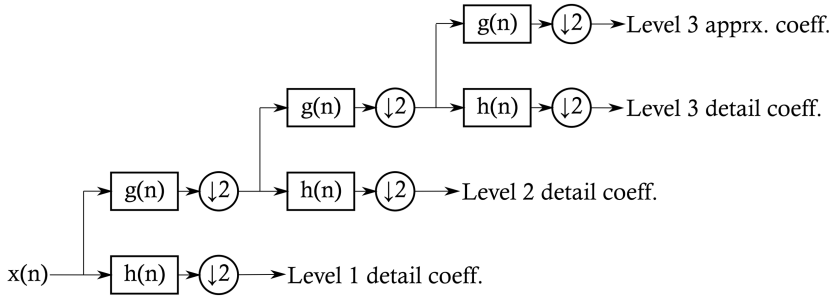Figure 2.13: Resolution grid of a CWT of a signal.

Figure 2.14: A filter bank of a three-level DWT including filter banks and down-sampling

wavelet transform [68], indicating that the wavelet behaves such as the windowing function. The frequencies of interest can be traced with the help of wavelet scaling factors that can stretch or compress the wavelet.

The type of mother wavelet must be selected based on the signal type and the frequency of interest, indicating that no clear rule of thumb exists for selection of the mother wavelet. It must be selected by trial and error. The computational complexity of the CWT is $(O(n))$ per scale, where n is the length of data [69].

2.5.5 Discrete wavelet transform

The theory behind DWT is similar to CWT. The signal is convoluted to the selected mother wavelet that can extract a hidden pattern from the faulty signals. The DWT implementation using a filter bank is the most prevalent approach.

Each level of the filter bank consists of high-pass and low-pass filters, while the output is downsampled by a factor of 2 at each level. The output of the high pass filter that is downsampled is called the detail coefficient (h(n)), whereas the output of the low pass filter that is downsampled is the so-called approximate coefficient (g(n)). The approximate coefficient is fed to the next cascade filter bank, while the detail coefficient is saved. The number of DWT levels determines the number of decompositions. Fig. 2.14 shows a three-level filter bank.

The computational complexity of the DWT is $O(n)$ per scale, where n is the length of the data. However, the required storage for DWT is less than CWT, which makes it a suitable signal processing tool for real-time implementation. Although the method is called the "discrete" wavelet transform, both CWT and DWT are implemented discretely in the field of signal processing. However, the difference is that CWT is defined continuously and performs an infinite number of swipes on an infinitesimal length, whereas DWT, as the discrete algorithm, shifts the length of the wavelet.
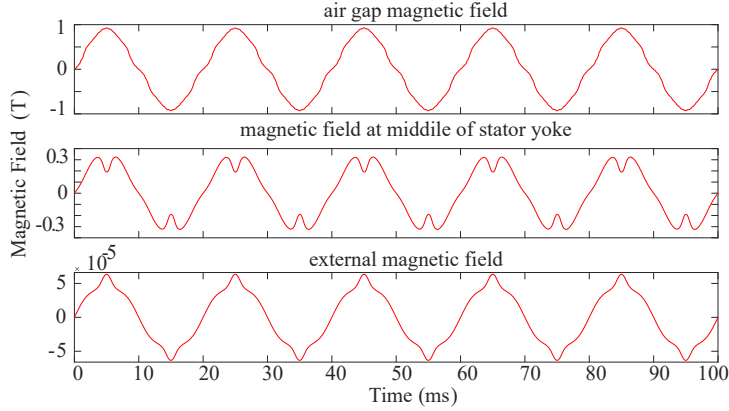
Figure 2.15: The radial magnetic field in 22 MVA synchronous generator, the air gap magnetic field (top), the magnetic field at middle of stator yoke (middle), and stray magnetic field (bottom) - Simulation results.

2.6   Fault Detection Methods

The magnetic field in electric machines is the most informative signal and is similar to blood in the human vessel. Analysis of the magnetic field can reveal information regarding the performance and health status of the electric machine. The magnetic field in an ideal electric machine is confined inside the stator core, whereas a weak magnetic field exists on the stator backside. Fig. 2.15 shows the radial magnetic field at three points in a 22 MVA synchronous generator. The magnetic field is measured in the air gap, at the middle of the stator yoke, and on the stator backside. The magnitude of the magnetic field is reduced when moving away from the air gap toward the stator's backside. The amplitude of the stray magnetic field becomes negligible (in the order of micro Tesla) compared with the magnetic field in the air gap. However, the pattern and periodicity are approximately identical. Consequently, the stray magnetic field 'mirrors' the magnetic field in the air gap. The detection methods proposed in this Ph.D. thesis are based on the application of the stray magnetic field. Three types of faults, namely the ITSC fault, eccentricity fault, and broken damper bar fault, are examined and several unique approaches are proposed that deploy advanced signal processing methods.

The impact of the power rating and topology of the salient pole synchronous generators on the measured stray magnetic field sensor installed on the stator backside is investigated using FEM. The five generators are: a 100 kVA 14-pole, a 22 MVA 8-pole, a 42 MVA 16-pole, a 105 MVA 14-pole, and a 400 MVA 60-pole. The induced sensor voltage of five generators operating in healthy conditions is
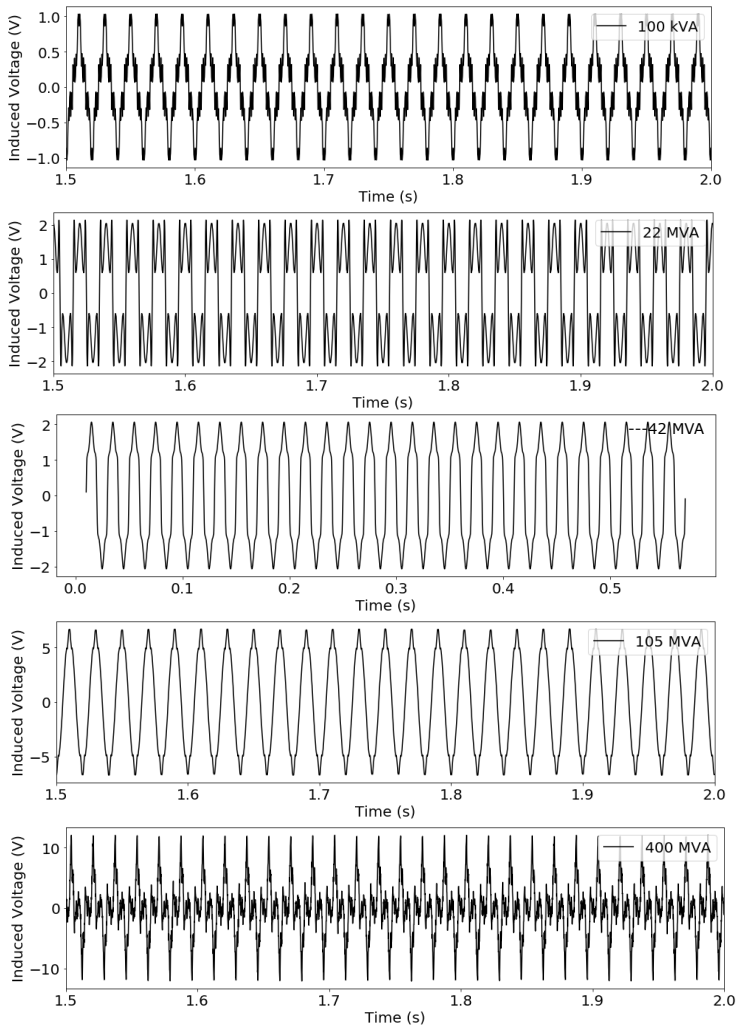
Figure 2.16: Induced sensor voltage in a healthy operation of the 100 kVA 14-pole, 22 MVA 8-pole, 42 MVA 16-pole, 105 MVA 14-pole, and 400 MVA 60-pole.

shown in Fig. 2.16. The 100-kVA, 14-pole synchronous generator has an outer diameter and stack length of 0.78 m and 0.24 m, and the 400-MVA, 60-pole synchronous generator has an outer diameter and stack length of 11.27 m and 1.62 m; these two are the smallest and largest modeled generators among the five models. The results illustrate that the thickness of the stator core, the number of poles, the power rating, and the topology of the generator do not eradicate the stray magnetic field on the stator backside.
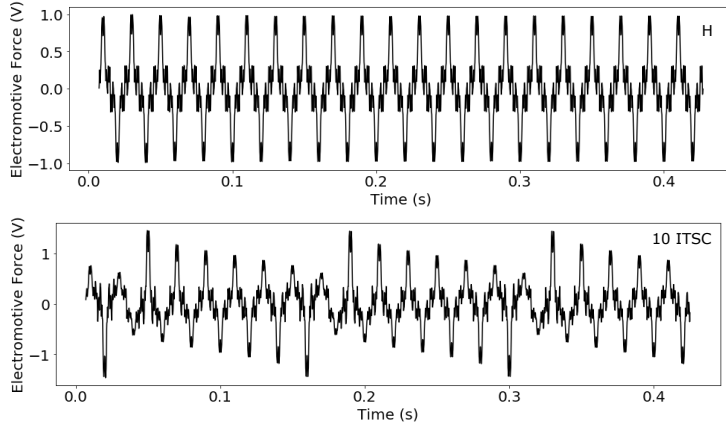
Figure 2.17: Induced sensor voltage in a 100 kVA 14-pole synchronous generator operating in a healthy case (top) and under a 10 ITSC fault (bottom) in the rotor field winding.

2.6.1 ITSC fault detection

Although an ITSC fault in the rotor field winding is not a destructive fault and the generator can operate for a long time under faulty conditions, the generator cannot operate up to the full load condition due to the increased vibration level. Three methods are proposed based on utilizing FFT, STFT, and CWT.

FFT analysis

The magnetic field in the air gap consists of the stator magnetic field and rotor magnetic field. When an ITSC fault happens in the rotor field winding, the magnetomotive force of the defected rotor pole is reduced since the flowing current is assumed to be constant whereas the number of healthy turns in the rotor pole is reduced. The reduction in the magnetomotive force results in an unbalanced magnetic field in the air gap and, consequently, stray magnetic field on the stator backside. Fig. 2.17 shows the induced voltage in the search coil mounted on the stator back side of a 100 kVA generator. Compared with the healthy case, both the amplitude and the pattern of the induced sensor voltage are changed by having the ITSC fault in the rotor field winding. The variation in the pattern of the induced sensor voltage is due to the fault-related harmonics, which can be characterized as follows:
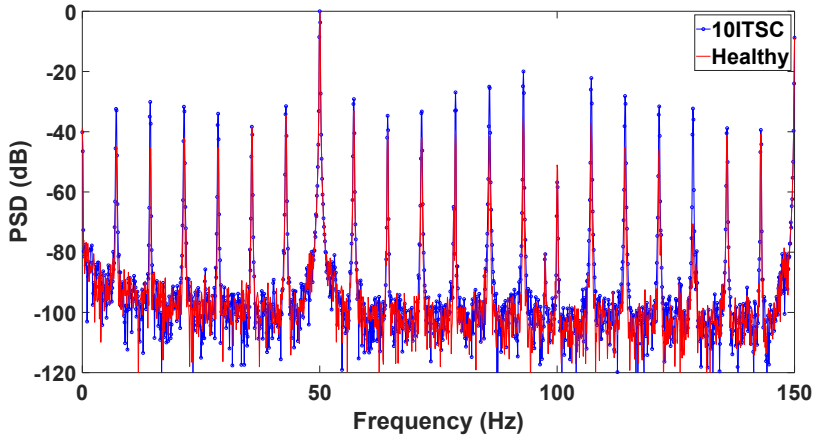
Figure 2.18: Frequency spectrum of induced sensor voltage of a 100 kVA 14-pole synchronous generator operating in a healthy case and under a 10 ITSC fault.

Table 2.2: Selected harmonic components in Hz to number of ITSC in no-load operation of a 100 kVA synchronous generator in Decibel

[Hz]	*Healthy*	*1 ITSC*	*2 ITSC*	*3 ITSC*	*7 ITSC*	*10 ITSC*
7.1	-44.9	-43.6	-41.9	-40.3	-34.8	-32.4
14.3	-45.4	-43.9	-41.8	-39.7	-33.1	-30.1
85.7	-41.5	-39.4	-36.8	-34.5	-27.9	-25.0
92.9	-34.8	-33.1	-31.2	-29.9	-22.9	-19.9
107.2	-37.2	-35.1	-33.2	-31.4	-25.0	-22.1
114.3	-45.1	-42.8	-39.9	-37.5	-31.0	-28.1

$$f_{sc} = (2\kappa \pm \frac{\nu}{p})f_s \qquad (2.2)$$

where f_s is the operating frequency of the generator, p is the number of pole pairs, and κ and ν are any integers. Although the introduced index is based on an analysis of the air gap magnetic field, it can be used for the fault-related harmonic analysis in the stray magnetic field since the stray magnetic field is the mirror of the air gap magnetic field, as explained in section 2.5.5.

Fig. 2.18 shows the frequency spectrum of the induced sensor voltage of a 100 kVA generator operating in a healthy case and under a 10 ITSC fault. The amplitude of the fault-related harmonics, which are spaced with the mechanical frequency of the generator, is markedly increased. Table. 2.2 shows the amplitude of the harmonics that are extremely sensitive to the ITSC fault.
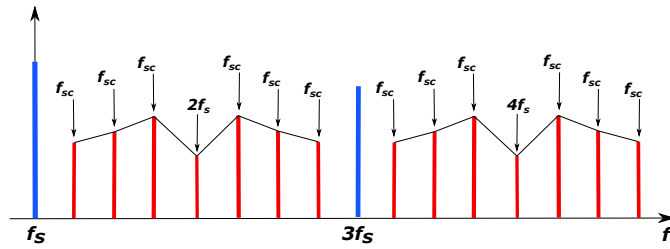
Figure 2.19: Introduced pattern for ITSC fault detection based on the frequency spectrum of induced sensor voltage in a salient pole synchronous generators.
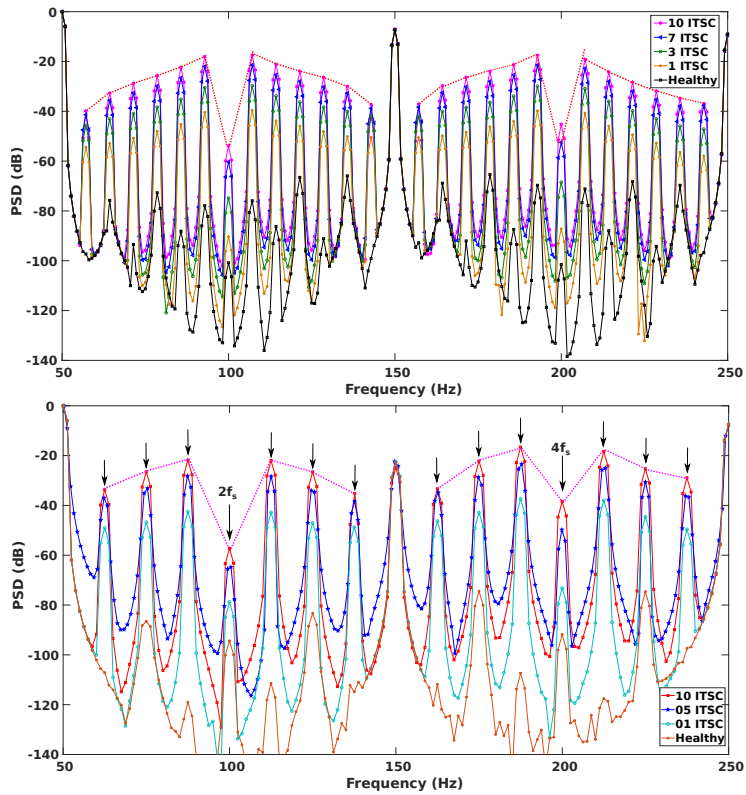

Figure 2.20: Frequency spectrum of a 100 kVA (top) and a 22 MVA (bottom) synchronous generators operating in no-load case under various degree of ITSC faults.

Although the frequency spectrum indicates the ITSC fault occurrence, the frequency spectrum of a healthy generator or a pre-defined threshold value is re-
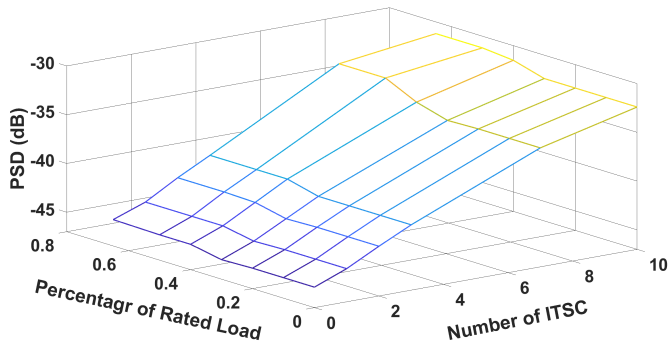
Figure 2.21: Magnitude variation of the sub-harmonic component versus load variation and various numbers of ITSC faults

quired. However, due to the lack of proper documentation of the commissioning data of a synchronous generator, providing healthy generator data is almost impossible. In addition, the threshold value can change based on the power rating and the configuration of the generator. Detailed investigation of the frequency spectrum of the induced sensor voltage in healthy and faulty conditions illustrates that the frequency spectrum of the induced sensor voltage follows a unique pattern under ITSC fault, whereas the frequency spectrum of the healthy machine shows a chaotic distribution of the harmonics. Fig. 2.19 shows the introduced pattern for the ITSC fault detection in salient pole synchronous generators. As shown in Fig. 2.19, the magnitude of the fault-related harmonics between the f_s and $2f_s$ is increased and the magnitude of the ones located between the $2f_s$ and $3f_s$ is decreased. The same pattern is repeated between $3f_s$ and $5f_s$. The pattern is identical for the salient pole synchronous generators, regardless of their power rating and topologies. Fig. 2.20 shows the frequency spectrum of two synchronous generators with power ratings of 100 kVA and 22 MVA.

The load has a remarkable influence on the fault-related harmonics of the current and voltage. However, analysis indicates that the loading condition of the synchronous generator does not change the amplitude of the fault-related harmonics, as shown in Fig. 2.21. According to Fig. 2.21, the amplitude of the fault signature increases with an increasing number of shorted turns in the rotor field winding, whereas increasing the generator's load does not change the amplitude of the fault-related signature. Thus, a short circuit fault detection using the proposed signature and pattern does not require knowledge of the load condition of the generator.
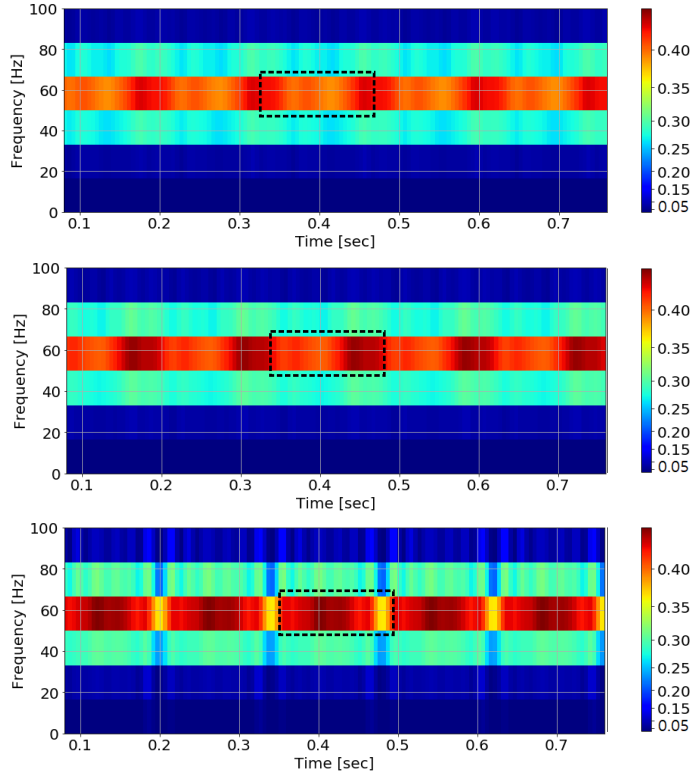
Figure 2.22: Time-frequency plots of induced sensor voltage of a 100 kVA synchronous generator operating in a healthy case (top), and under 1 ITSC fault (middle) and a 10 ITSC fault (bottom).

STFT analysis

A new pattern is proposed using STFT to compensate for the lack of baseline data of a healthy generator during commissioning. Fig. 2.22 shows the time-frequency plot of the induced sensor voltage of a 100 kVA 14-pole synchronous generator operating in a healthy case and under 1 and 10 ITSC faults. A black dotted window is used to show the fault periodicity in the time-frequency plot. The length of the window is equal to one mechanical revolution of the generator; for a generator with 14 poles, this is 140 ms. The parameters of the STFT are selected to have three frequency bands between 35 Hz and 85 Hz that show high sensitivity to the fault. The time-frequency of a healthy generator exhibits a uniform pattern distribution in the mentioned frequency bands, while a negligible repetitive variation can be observed due to the inherent eccentricity fault. The intensity and the pattern of the time-frequency plot are changed by having only
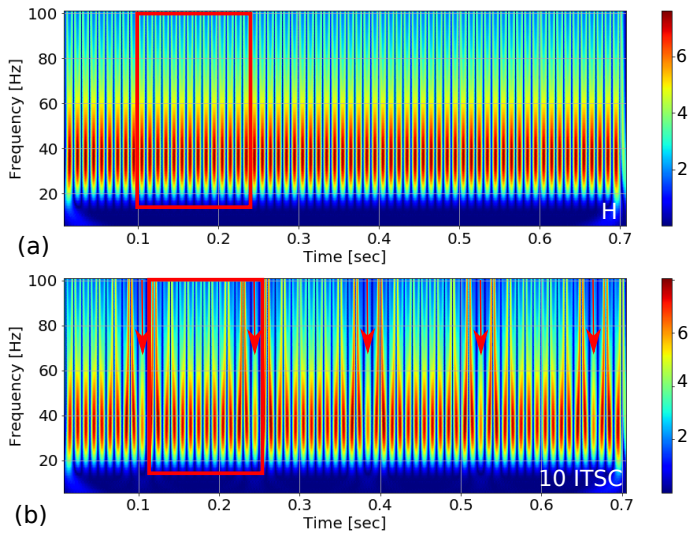
48

Figure 2.23: Time-frequency plots of induced sensor voltage of a 100 kVA synchronous generator operating in a healthy case, and under a 10 ITSC fault.

one ITSC fault. Increasing the fault severity to ten shorted turns yields a significant variation in the time-frequency plot. The length of the yellow band is equal to 10 ms, which is equal to one rotor pole in a generator with 14 poles. The load impact on the time-frequency plot of the induced sensor voltage shows that the intensity and pattern of the plots do not change, and the results are similar to those for the no-load operation of the generator, provided that the fault severity increase directly influences the intensity of the time-frequency plot.

CWT analysis

The third developed method for ITSC fault detection is based on the application of CWT to the induced voltage in the stray magnetic field sensor mounted on the stator backside. Fig. 2.23 shows the time-frequency plot of the induced sensor of a 100 kVA 14-pole synchronous generator. Each stalk in the time-frequency plot represents one rotor pole, and each red window contains the rotor poles that represent one mechanical revolution of the generator. In the healthy operation of the synchronous generator, the size and intensity of the stalks are constant, and the time-frequency plot has a uniform pattern. When 10 turns of a rotor pole are short-circuited, the length and intensity of one of the stalks are markedly reduced, which represents the faulty rotor pole. The pattern of the faulty stalk is repetitive, indicating that the faulty pole is passed over the search coil installed on the stator back side.
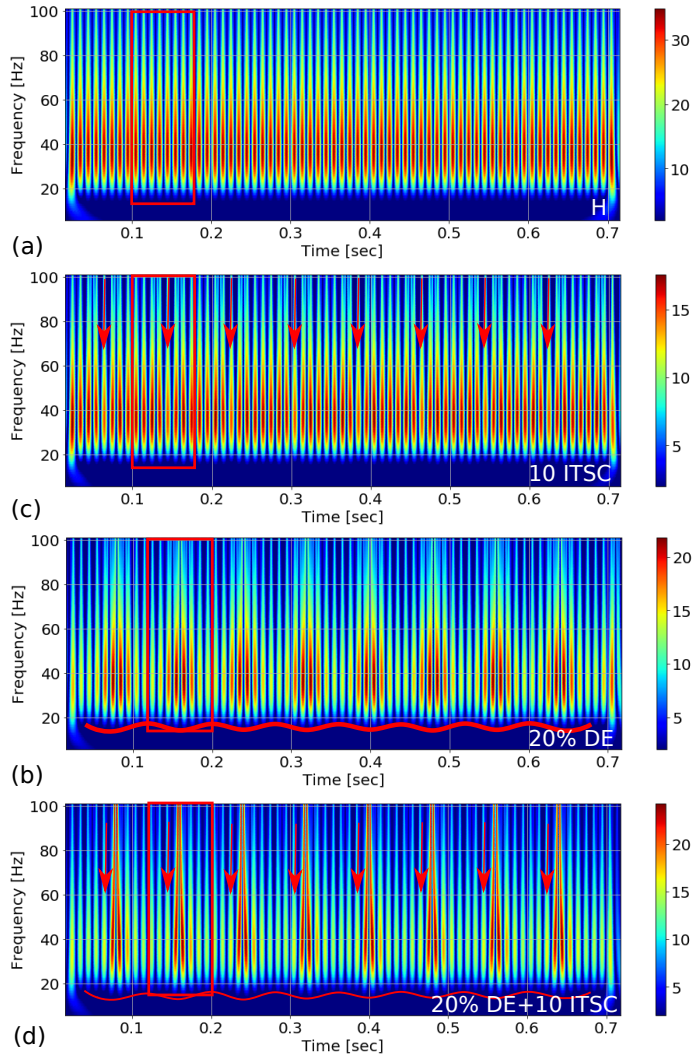
Figure 2.24: Time–frequency plots of the induced sensor voltage of a 22-MVA synchronous generator operating in a no-load condition in a healthy case, under a 10-ITSC fault, under a 20% DE fault, and under mixed fault of 20% DE and 10-ITSC faults.

The pattern introduced by deploying CWT to an induced sensor voltage is identical for salient pole synchronous generators regardless of their power rating and topology. Fig. 2.24 presents a time-frequency plot of a 22 MVA 8-pole synchronous generator in a healthy case and under 10 shorted turns out of 58 turns in one of the rotor poles. The pattern is similar to Fig 2.23, thereby proving the

aforementioned claim.

One of the main concerns of health monitoring of electric machines is fault type detection. Therefore, the DE fault is also applied to the 22 MVA synchronous generator to understand the impact of the DE fault on the time-frequency plot using CWT. As shown in Fig. 2.24, a DE fault creates a distinctive pattern that differs significantly from the ITSC fault pattern, indicating that the fault type can be simply diagnosed using the proposed method. In addition, the introduced method is able to detect the co-existence of two critical faults, such as the ITSC fault and the DE fault. Fig.2.24 shows the time-frequency plot for a case of 10 shorted turns in the rotor winding while the generator operates under 20% DE fault. Compared with a DE fault that has a symmetrical pattern, the short circuit fault distorts the DE pattern, reducing the length and the intensity of the faulty stalk and indicating that the method is able to provide unique patterns for each type of fault, in addition to alerting to the co-existence of two faults.

The load impact on the proposed method is also studied. The time-frequency pattern of the induced sensor voltage for a full load operation of the generator is also similar to its no-load operation. However, the pattern of the ITSC fault in the grid-tided operation of the generator becomes more evident, since the amplitude of current that passes through the rotor winding is increased.
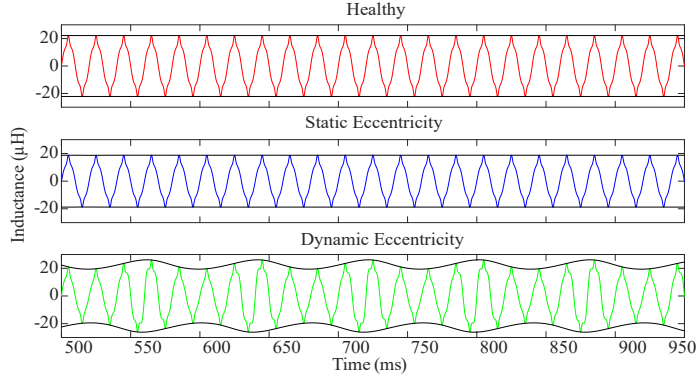
Figure 2.25: Mutual inductance between the rotor field winding and the search coil mounted on the backside of a 22 MVA generator operating in a healthy, 20% SE fault, 20% DE fault.

2.6.2 Eccentricity Fault Detection

The eccentricity fault distorts the symmetry of the magnetic field. The analysis of mutual inductance between rotor winding and the search coil mounted on the stator backside indicates that an eccentricity fault markedly affects both the amplitude and the patterns of the mutual inductance. Fig. 2.25 shows the mutual inductance between the rotor field winding and the search coil for a healthy case, 20% SE fault, and 20% DE fault in a 22 MVA synchronous generator. A comparison between the healthy case and the SE fault demonstrates that only the amplitude of the mutual inductance is changed, whereas the pattern is identical. The amplitude reduction due to the SE fault reflects an increase in the reluctance of the path for the linkage flux. Therefore, the mutual inductance between the rotor and search coil is reduced. By contrast, a DE fault not only changes the amplitude of the mutual inductance but it also alters the pattern and the mutual inductance starts to swing. The same analogy is valid for the mutual inductance of three phases and the search coil mounted on the stator backside. In conclusion, the amplitude of the induced voltage in the search coil due to SE fault should be increased or decreased while the frequency content must be unchanged. On the contrary, both the amplitude and frequency contents of the induced voltage in the search coil must be changed under a DE fault. Sensitivity analysis shows that the induced voltage in the search coil located on the stator backside has a high capability to detect an eccentricity fault at low degrees, such as 5% SE and 5% DE fault. Fig. 2.26 shows the induced voltage sensor voltage in a 42 MVA synchronous generator under various degrees of SE and DE faults. Four methods are proposed for eccentricity fault detection in this thesis, as described in the following sections.
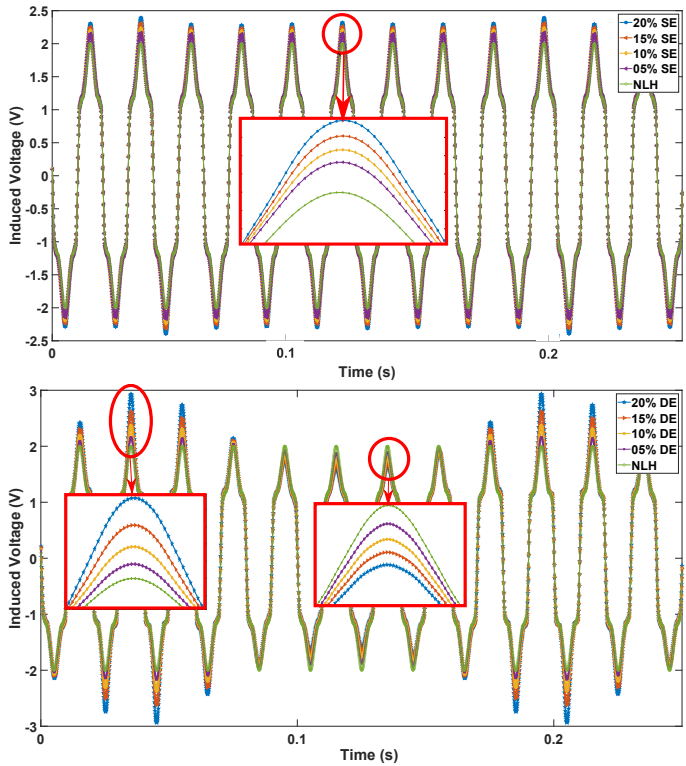
Figure 2.26: Induced sensor voltage of a 42 MVA synchronous generator operating in a no-load condition in a healthy state and under various degrees of SE fault (top) and DE fault (bottom row).

Time-domain analysis

The SE fault only influences the amplitude of the magnetic field, whereas the frequency contents of the induced sensor voltage are constant, indicating that mounting several sensors on the stator backside can simply provide in-depth insight regarding the occurrence of the SE fault. In the case of vertically mounted hydro generators, at least four sensors are needed for the detection of an SE fault and its direction. For the detection of misalignment, at least eight sensors must be installed at the drive end and non-drive end of the generator. Both experimental tests on a 100 kVA generator and a field test on a 42 MVA generator proved the proposed method. Fig. 2.27 shows the induced sensor voltage in four sensors mounted on the backside of a 42 MVA generator. The induced sensor voltage in sensors (S-1) and (S-3) and in sensors (S-2) and (S-4) are compared together, since they are mounted on opposite sides of each other. The amplitudes of the
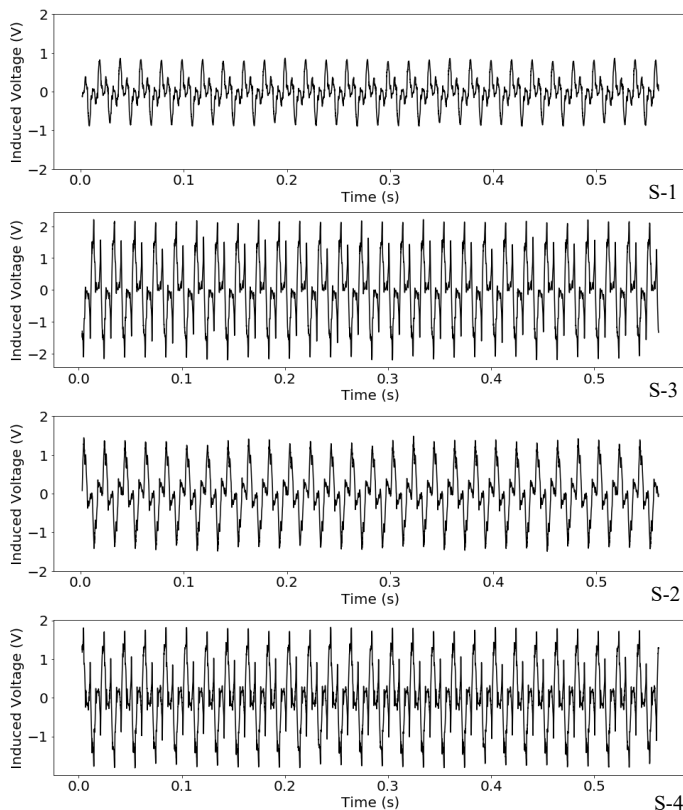
Figure 2.27: Induced sensor voltage in two pairs of sensors mounted to the stator backside of a 42 MVA synchronous generator operating under a SE fault. Four sensors are mounted on the stator backside with 90 mechanical degrees of distance where sensor pairs (S-1 and S-3) and (S-2 and S-4) are opposite each other.

induced sensor voltages in S-1 and S-3 are 1 V and 2.1 V, indicating that the generator suffers from an SE fault. Although the amplitudes of S-2 and S-4 are not exactly the same, the difference is not significant. The direction of the SE vector is toward the S-1 and S-3.

The impact of DE fault in the time domain signal is also evident. As shown in Fig. 2.26, the upper and lower envelope of the induced sensor voltage is changed under the DE fault. The envelope variation is an indication of the frequency component variation. Although the impact of each fault causes a unique pattern in the stray magnetic field, a low-severity fault is difficult to recognize by visual inspection, indicating that a signal processing tool is needed.

FFT analysis

The feasibility of the real-time implementation of FFT makes it still a valid approach for the health monitoring of electric machines. FFT is applied to the induced sensor voltage of a 22 MVA 8-pole generator operating in a healthy case and under the various degrees of SE and DE faults, as shown in Fig. 2.28. The amplitude of the frequency components under an SE fault hardly varies, and even imposing a 20% SE fault barely changes the amplitude of the frequency spectrum compared with the healthy case. Although under the SE fault the frequency sideband components around the main frequency and its odd multiple are increased, the amplitude of the sideband harmonics for the healthy case is similar to the faulty ones, since the ideal generator is simulated in FEM and manufacturing asymmetry, which increases the amplitude of the aforementioned harmonics, is ignored. The amplitude of the frequency components is markedly changed by having a 5% DE fault. Increasing the severity of the DE faulty up to 20%, as shown in Fig. 2.28, results in amplification of the frequency components, which can be determined using $(1 \pm (\frac{k}{p}))f_s$, where k is an integer, f_s is the stator terminal frequency, and p is the number of pole pairs.

A unique pattern for DE fault detection using FFT is proposed in this Ph.D. study as shown in Fig. 2.29. The FFT spectrum of a healthy generator has a chaotic frequency spectrum pattern, whereas applying a 5% DE fault imposes a distinctive pattern. The amplitude of the sub-harmonics can be determined using $(1 \pm (\frac{k}{p}))f_s$. The amplitude of the fault-related harmonics is increased by increasing the fault severity from 5% to 10%, 15%, and 20%. Fig. 2.29 shows an introduced pattern for DE fault detection that does not require a priori knowledge of a healthy generator. The amplitude of the fault-related harmonics between f_s and $2f_s$ are decreased, while the harmonics between $2f_s$ and $3f_s$ are increased. The same pattern is repeated between $3f_s$ and $5f_s$. The introduced pattern is observed for several synchronous generators with different topologies and power ratings, indicating the robustness of the introduced method.

Wavelet entropy

Providing the baseline data of a healthy generator or having a pre-defined threshold for fault detection purposes based on frequency spectrum analysis is almost impossible. Therefore, a method based on differential electromotive force is defined. In this method, at least two search coils must be mounted opposite each other on the stator backside. The differential induced electromotive force is assumed to be almost zero if the generator operates in a healthy condition. Thus, a non-zero differential electromotive force indicates that the generator is operating under faulty conditions. This assumption is valid since the construction tolerance of large synchronous generators is tight and an imbalance due to the machining
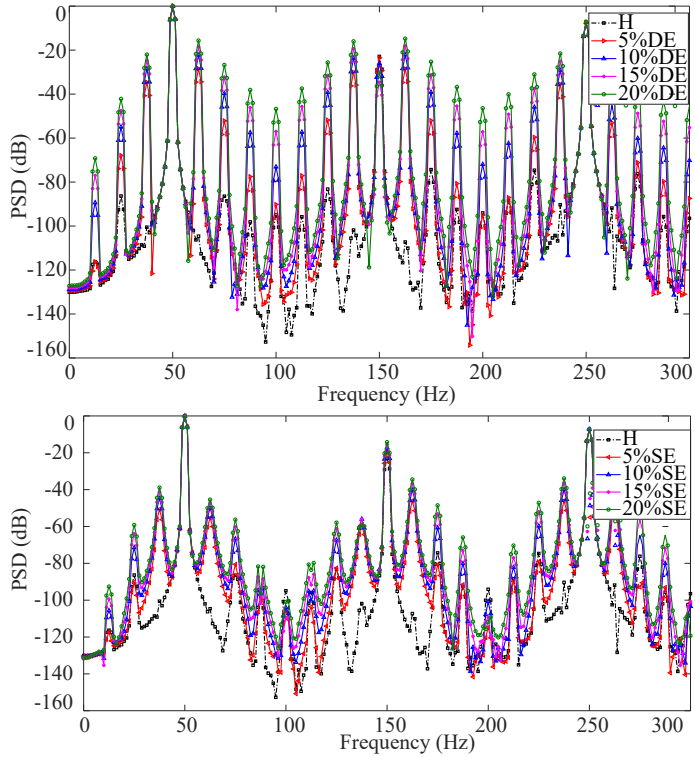
Figure 2.28: Frequency spectrum of induced sensor voltage of a 22 MVA generator operation in a no-load case for various degrees of DE fault and SE fault.

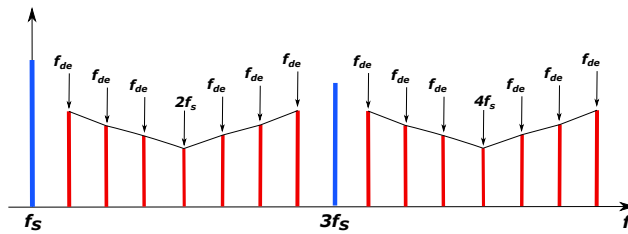Figure 2.29: Introduced pattern based on the frequency spectrum of induced sensor voltage for detection of DE fault detection in salient pole synchronous generators

of the stator and rotor cores is impossible. The detection of the fault type is proposed by deploying wavelet entropy to the differential electromotive force.

DWT with Daubechies-8 as a mother wavelet is applied to the differential electro-
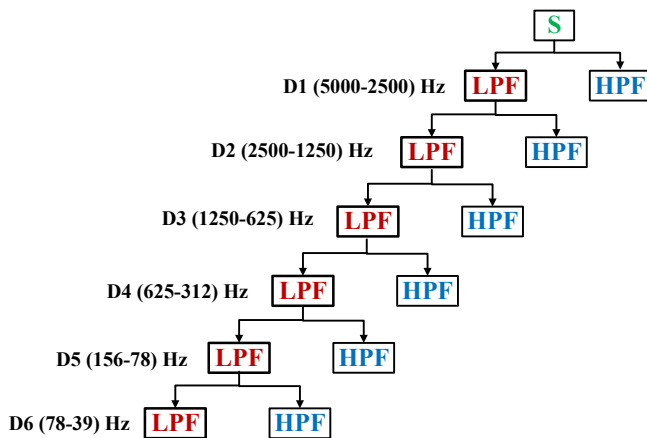
Figure 2.30: 8-level DWT with corresponding frequency bands based on the sampling frequency of 10 kHz.

motive force, which is sampled as a frequency of 10 kHz. The mother wavelet of Daubechies-8 is selected due to its promising performance in the fault detection of electric machines [70] Fig. 2.30 shows the corresponding frequency bands for the eight sub-bands. Fig. 2.31 shows the application of the DWT to the differential electromotive force of a 22 MVA synchronous generator operating in a healthy case and under 20% SE, and 20% DE faults. The amplitude of the electromotive force for a healthy, 20% SE fault, and 20% DE fault are 10 mV, 1 V, and 2 V, respectively. A comparison between the healthy case and SE fault for the entire sub-band indicates that the frequency contents are similar in both cases, while the amplitudes differ. On the contrary, both the frequency and the amplitudes of the sub-bands are distinctive compared with the healthy case in the case of DE fault. The load has a noticeable impact on the wavelet sub-bands, whereas the amplitude of the sub-bands is suppressed due to the stator-contributed magnetic field that tries to reduce the irregularity in the air gap magnetic field. However, the pattern and amplitude are distinguishable, even under the on-load operation of the synchronous generator.

Application of the wavelet entropy to the differential electromotive force can provide an in-depth insight into the health status of the synchronous generator. The value of the entropy shows the degree of disorder in the signal. If the entropy equates to zero shows a perfect order, while 1 indicates a disorder. However, there is no upper limit for the entropy. Shannon entropy, which shows a probability distribution of the signal, is used as follows:

$$Entropy_{sh}(n) = -\Sigma_{i=1}^{j} P_i log P_i \tag{2.3}$$
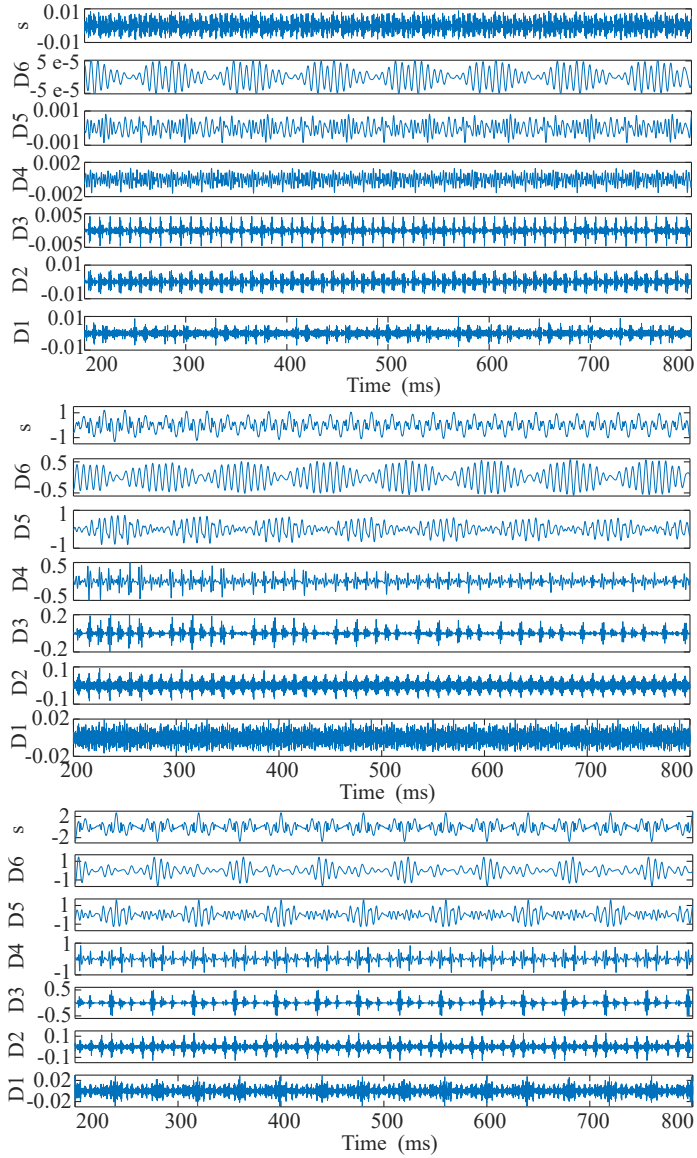
$$P_i = \frac{E_j}{E} \tag{2.4}$$

Figure 2.31: DWT of induced differential electromotive force in a 22 MVA synchronous generator operating in the no-load case in healthy (top), 20% SE fault (middle), and 20% DE fault (bottom).

where P_i is a relatively normalized value of each wavelet sub-band energy (E_j) to the total energy of the signal (E). Fig. 2.32 shows the proposed index value
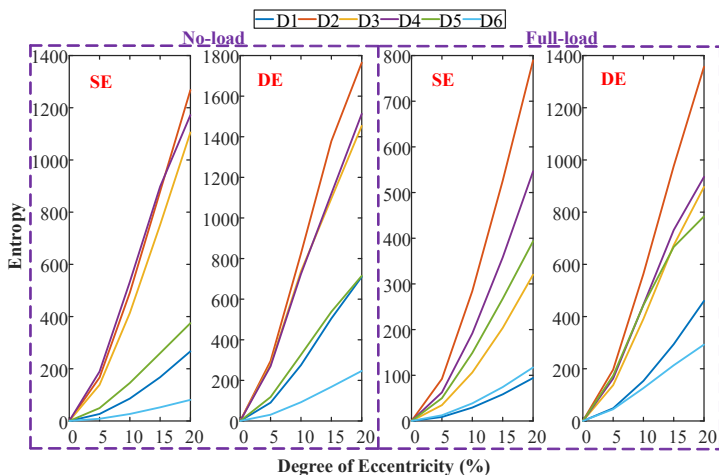
Figure 2.32: The wavelet entropy of sub-bands (D1 to D6) for different degrees of SE and DE faults in no-load and full-load cases of a 22 MVA synchronous generator.

for the wavelet sub-bands of D_1 to $D-6$ for the different degrees of SE and DE faults. The wavelet entropy is zero for a healthy case, but increasing the fault severity increases the wavelet entropy value. Among the sub-bands, D_2, $D3$, and D_4 have a higher sensitivity to fault progress under both SE and DE faults. This index does not require a threshold value, since any value above zero is the fault indication.

The proposed fault detection method is valid for both the no-load and on-load operating conditions of the synchronous generators. Compared with the no-load case, the amplitude of the wavelet entropy is decreased to the same degree as the fault in the on-load operation. The reduction is due to the contributed magnetic field from the stator winding, which tries to reduce the magnetic field asymmetry caused by the eccentricity fault. Although the amplitude of the index during on-load operation is reduced, the method can only detect a faulty operating synchronous generator.

CWT-based approach

A unique eccentricity fault detection approach based on the application of CWT proposed in this Ph.D. study addresses the limitations of the previously developed methods. The limitations are:

1. Although the time domain analysis of the induced sensor voltage can reveal
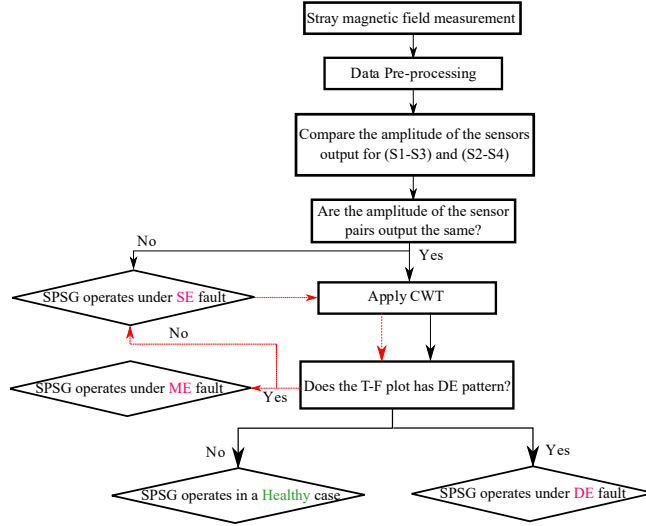
Figure 2.33: Eccentricity fault detection algorithm in a salient pole synchronous generator.

the health status of the synchronous generator, the co-existence of multiple faults creates difficulties in diagnosis, indicating that a signal processing method is required.

2. Although the proposed pattern for the DE fault detection eliminates the need for baseline data of a healthy generator and predefined threshold for the FFT analysis, the fault cannot be detected using frequency spectrum analysis.

3. The detection method based on wavelet entropy is applicable for eccentricity fault detection; however, a short circuit fault can also change the value of the wavelet entropy of the differential electromotive force.

In conclusion, a new algorithm, shown in Fig. 2.33, is proposed to detect the SE, DE, and ME faults in synchronous generators. At least four sensors are required to detect the SE fault. If the amplitude of the sensor pairs located opposite each other is equal, the data of one sensor is fed to the signal processing section, which applies CWT. If the introduced pattern is determined in the time-frequency plot, the generator operates under the DE fault; otherwise, the generator operates in a healthy condition. In the case where the amplitude of at least one pair of sensors is unequal, the generator has at least an SE fault. The analyzed signal must be checked for DE fault diagnosis. If the signal shows the DE pattern in the time-frequency plot, the generator has an ME fault; otherwise, it operates under the SE fault.
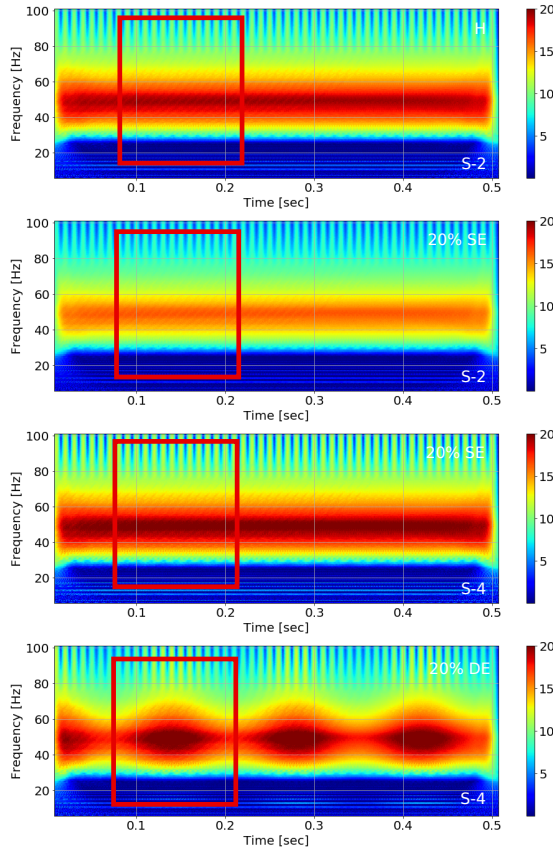
Figure 2.34: Time–frequency plot of an induced sensor voltage in a 100 kVA synchronous generator operating in a no-load condition, in a healthy case (first row), and under 20% SE fault (second and third row for sensors S-2 and S-4) and 20% DE fault.

Fig. 2.34 shows the time-frequency plot of the induced sensor voltage of two search coils (S-4) and (S-2) mounted opposite each other on the stator backside of a 100 kVA synchronous generator. The mother wavelet and parameters of the CWT are selected and adjusted to partition the frequency bands between 0 and 40 Hz, 40 Hz and 60 Hz, and 60 Hz and 100 Hz. These frequency bands are desired, since the most variation in the frequency components of the faulty frequency spectrum is located near the fundamental frequency of the synchronous generator. A red window is defined that shows one mechanical revolution of the generator, which is 140 ms for the 100 kVA 14-pole synchronous generator under study.

The time-frequency plot of a healthy case contains a uniform pattern with a constant intensity along each frequency. The impact of a 20% SE fault gives rise to intensity variation of the time-frequency plot, while the pattern is similar to the healthy case, thereby confirming that the frequency content of the induced sensor voltage is unchanged due to the SE fault. The intensity of the time-frequency plot in S-2 is reduced, while it is increased in S-4, since the air gap length is large on the S-2 side and smaller on the S-4 side. The last row of Fig. 2.34 shows the impact of DE fault on the time-frequency plot. The DE fault modifies both the pattern and the intensity of the time-frequency plot. Both the upper and lower envelopes of the time-frequency plot contains a sine wave variation, which is similar to the time domain signal of the stray magnetic field.

The method is successfully applied to three synchronous generators with different power ratings and topologies: 100 kVA 14-pole, 22 MVA 8-pole, and 42 MVA 16-pole. In the field test of a 42 MVA generator, the analysis indicates that the generator operates under an SE fault with high severity, whereas the parallel windings in the stator winding reduce the SE fault intensity when the generator is connected to the power grid. The time-frequency plot of a 22 MVA generator also reveals that the generator suffers from the DE fault.
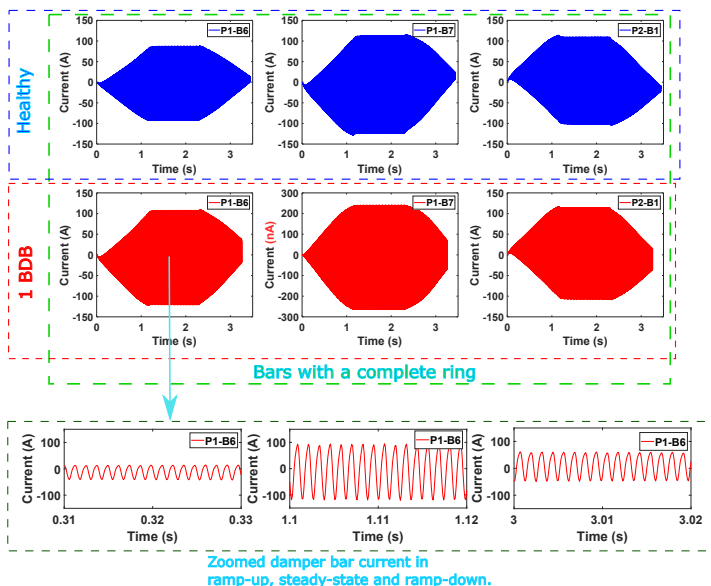
Figure 2.35: Induced current in the rotor bars due to the trapezoidal shape of the field current in a healthy generator during no-load operation (blue waveform) and with one BDB fault (Pole #1, bar #7 (P1-B7)) (red waveform).

2.6.3 Broken Damper Bar Fault Detection

Although the BDB fault does not happen frequently in synchronous machines, it is a fast progressing fault that can damage the stator core and winding if the damper bar protrudes from the rotor pole shoe. Damper bars are active during transient operation of the synchronous machine; however, there is an exception if the stator has a fractional winding. The DC current, as shown in Fig. 2.5, is applied to the 100 kVA generator, which rotates under synchronous speed. Fig. 2.35 shows the current in the damper bars in a healthy case and under one BDB fault. According to Fig. 2.35, a high current passes through the damper bars during both transient and steady-state operation of the synchronous generator. For this reason, the detection of the BDB fault in the synchronous generator in three modes of ramp-up, steady-state, and ramp-down using stray magnetic field monitoring is proposed in this Ph.D. study.

In theory, the air gap magnetic field of the rotor consists of a magnetic field of the rotor field winding and a magnetic field of the damper winding. Therefore, the BDB fault causes irregularities in the magnetic field of the air gap and consequently the stray magnetic field. Fig. 2.36 presents the induced sensor voltage on a search coil installed on the stator backside of a 100 kVA generator. The
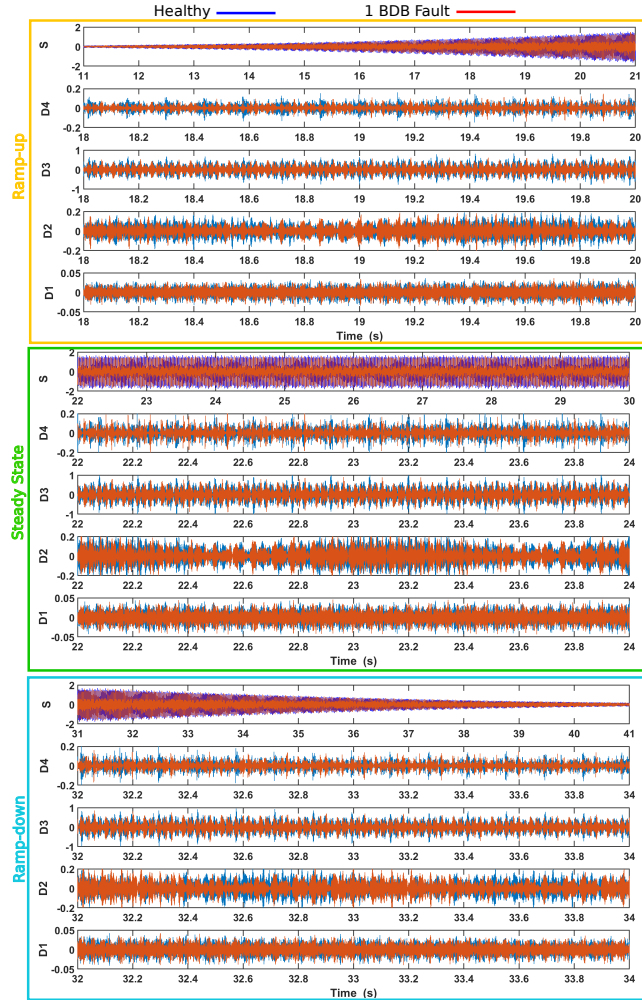
Figure 2.36: DWT of induced sensor voltage of a 100 kVA synchronous generator in healthy case (blue waveform) and with one BDB fault (red waveform) in three cases: RU (top section), SS (middle section), and RD (lower section).

waveform is divided into three sections: ramp-up, steady-state, and ramp-down. The blue waveform shows the induced sensor voltage during the healthy operation of the generator, while the red waveform shows the generator having one BDB fault in one of the rotor poles.

Although an evident difference is obvious when comparing the healthy and faulty induced sensor voltage, the DWT is selected to analyze the transient behavior of the induced sensor voltage. The Daubechies-8 is used as a mother wavelet, and

sub-bands D1 to D4 exhibit high sensitivity to the BDB fault. Shannon entropy is applied to these sub-bands to quantify the degree of disorder caused by the BDB fault. The magnitudes of the Shannon wavelet entropy for sub-bands D4 and D3 under one BDB are increased from 405 to 482 and 6610 to 7166, respectively, during the ramp-up period. The amplitude of the wavelet entropy during the ramp-down period is also increased for the D4 and D3 sub-bands, from 382 to 607 and from 6397 to 8355, respectively. The magnitudes of the D4 and D3 sub-bands during steady-state operation are increased from 959 to 1181 and from 10 403 to 11 473, respectively.

A criterion function is introduced to generalize the proposed BDB fault detection algorithm as follows:

$$CriterionFunction = \frac{|WEH_{Di} - WEF_{Di}|}{WEH_{Di}} \times 100 \qquad (2.5)$$

where WEH_{Di}, and WEF_{Di} are the wavelet entropy of the corresponding wavelet sub-band in the healthy and faulty cases, respectively. Analysis of the results for the criterion function of the selected wavelet sub-bands indicated that sub-band D-4 has higher sensitivity to a BDB fault in all three operational modes. The damper bar location has a considerable impact on the criterion function value, since the damper bars are distributed along the rotor pole curvature. The highest current passes through the damper bars located at the edge of the rotor pole while the smallest current passes through the damper bar located in the middle of the rotor pole. Therefore, the breakage of the middle damper bar has a trivial influence on the criterion function value.

The damper bars are designed to carry the current that the stator is designed for. The current of the BDB passes through the adjacent damper bar. The increased current results in a local temperature rise and, in the long term, gives rise to damper fracture, indicating that the breakage of one damper bar ultimately causes breakage of several damper bars. Analysis of the criterion function shows that multiple breakages increase the value of the criterion function. The least variation in the value of the criterion function occurs for a BDB in the middle damper bars and their adjacent dampers. In the case of breakage of the entire damper bars of one pole, the value of the criterion function is markedly increased.

2.7 Noise Impact

The technical term 'signal' in the field of signal processing refers to the 'demand' data that are measured. However, the measured data are prone to noise interference during data acquisition, storage, and conversion. The noise is unavoidable in the industrial environment, indicating that the measured data always have undesired data that may disturb the signal contents. The quality of the signal is measured based on the signal-to-noise ratio (SNR), and several factors, such as the sensor, data acquisition system, and working environment, influence the SNR.

The noise type can be determined based on its frequency characteristics. The measured data might have noise, and that noise may contain high-frequency components or may spread over a wide frequency range. Th noise can be of various types, including white Gaussian noise, Pink noise, Brownian noise, Blue noise, and Violet noise. The electromagnetic noise source interferes with the measured data for the fault detection of electric machines consisting of the noise generated from the electric machines, converters, and transformers.

The analysis of the measured noise using the stray magnetic field sensor mounted on the stator backside of a 42 MVA generator shows the existence of white Gaussian noise. The data were measured while the generator was halted; however, three units were operating during the data acquisition process. The analysis shows that the amplitude and the power density of the noise are identical throughout the frequency span, which indicates the behavior of the white Gaussian noise.

The noise impact can be suppressed by increasing the SNR. The amplitude of the magnetic field on the stator backside is low; therefore, increasing the number of turns can increase the SNR. In addition, coaxial cable and copper foil are used to shield the data during data acquisition. However, the experimental tests and field tests confirmed the existence of the noise. Thus, the impact of the noise on signal processing tools utilized for the purpose of fault detection in this Ph.D. thesis was evaluated . White additive white Gaussian noise is added to the measured air-gap magnetic field of a 100 kVA synchronous generator operating in a healthy case and under 10 ITSC fault. The following sections show the impact of noise on the signal processing tools FFT, STFT, CWT, and DWT, and TSDM.

2.7.1 Noise Effect on FFT

The noise impact on the data analyzed with FFT was examined by adding white Gaussian noise to the measured air gap magnetic field. Fig. 2.37 shows the FFT spectrum of an air gap magnetic field for a 100 kVA generator with 7 pole pairs operating in a healthy case and under 10 shorted turns in one of the rotor
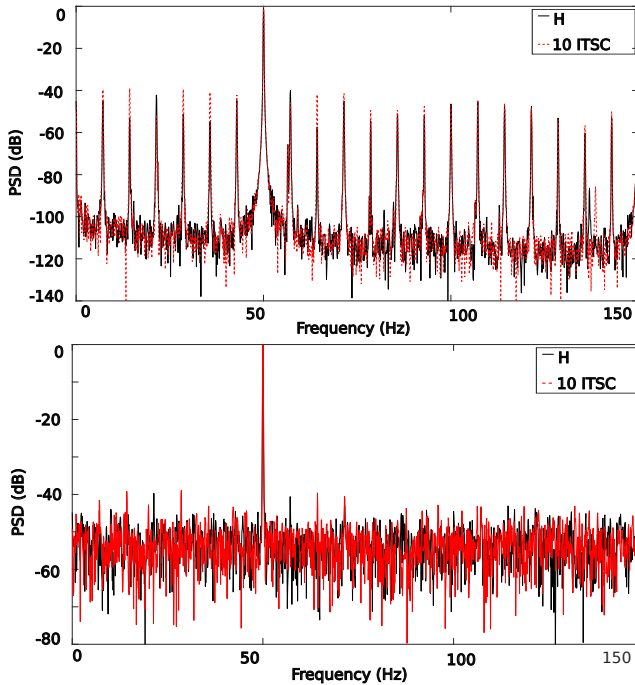
Figure 2.37: Frequency spectrum of an air-gap magnetic field in a healthy state and under a 10 ITSC fault, without noise interference (top), and with 20-dB SNR (bottom).

poles. Compared with the frequency spectrum of a healthy synchronous generator, having 10 shorted turns in one of the rotor poles increases the amplitude of the frequency spectrum. The analysis shows that moving from a no-noise data to data with a 20 dB SNR does not change the amplitude of the fault signatures, whereas the noise level is increased markedly when the SNR equals 30 dB. Although the fault signatures can be detected, the noise level above these value can totally mask the fault signatures.

2.7.2 Noise Effect on STFT

STFT is applied to the air gap magnetic field of a healthy and faulty generator. The impact of 40 dB and 20 dB white Gaussian noise is shown in Fig. 2.38. The patterns are still identical for a SNR equal to 40 dB. However, decreasing the SNR causes chaotic patterns in the time-frequency plot of the STFT. Detailed analysis of a 20 dB SNR using image processing indicates that the white Gaussian noise can modify the healthy pattern in a way that makes it looks like a faulty

Figure 2.38: Time-frequency plot of an air-gap magnetic field using STFT in a healthy state and under a 10 ITSC fault, without noise interference (top), and with 20-dB SNR (bottom).

Figure 2.39: Time-frequency plot of an air-gap magnetic field using CWT in a healthy state and under a 10 ITSC fault, without noise interference (top), and with 20-dB SNR (bottom).

pattern. Consequently, a low SNR may lead to a false positive fault if the signal is processed using STFT. Even though the window length of STFT can be increased to alleviate the noise impact on the time-frequency plot, this yields a reduction in temporal resolution, thereby limiting the usefulness of STFT.

2.7.3   Noise Effect on CWT

CWT shows a promising outcome among the presented results for health monitoring of hydro-generators. The impact of noise on CWT performance is shown in Fig. 2.39 for a healthy case and under 10 ITSC fault. The time-frequency plots of the air gap magnetic field up to 40 dB SNR still show healthy and faulty pat-
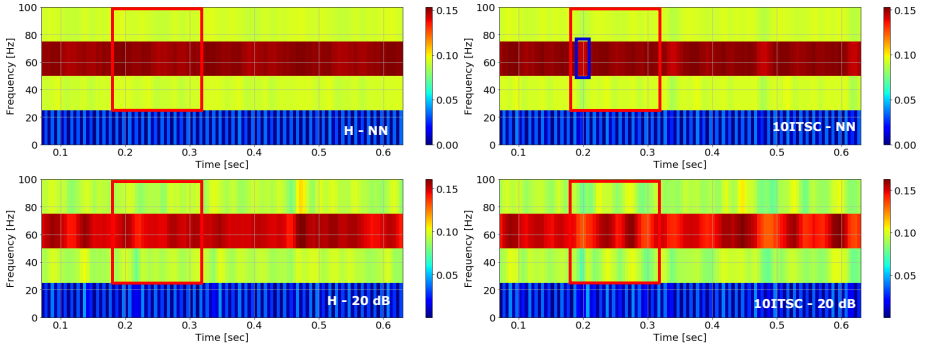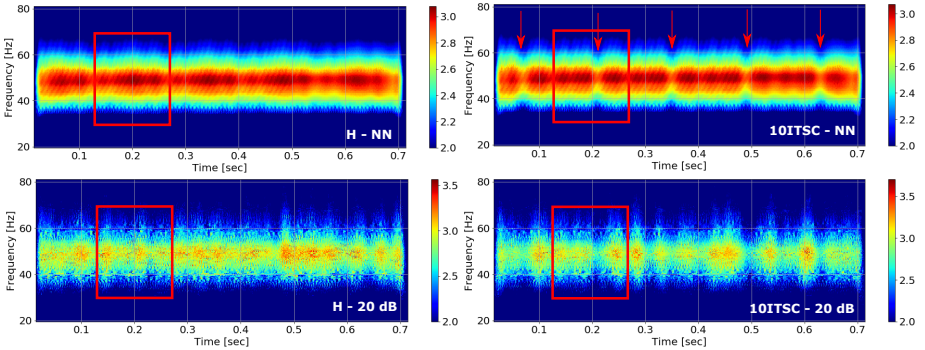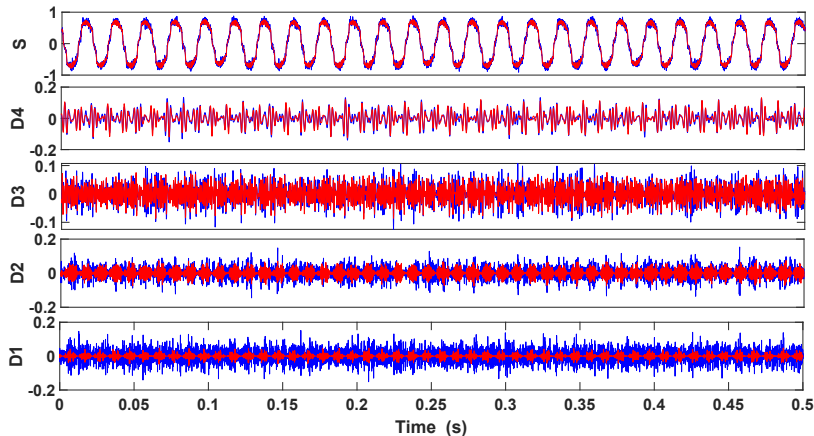
Figure 2.40: Time-frequency plot of an air-gap magnetic field using DWT in a healthy state without noise interference (red), and with 20-dB SNR (blue).

Table 2.3: Energy of various DWT sub-bands applied to air-gap magnetic field in a healthy and under ITSC fault.

	D6	*D5*	*D4*	*D3*	*D2*	*D1*
Healthy - No-Noise	0.83	0.94	0.97	1.0	1.06	1.35
Faulty - No-Noise	0.81	0.88	0.83	0.79	0.72	0.65
Healthy - 20 dB	0.81	0.88	0.83	0.79	0.72	0.65

terns with high accuracy. However, increasing the noise level to 20 dB SNR has a discernible impact on the CWT plot. The time-frequency plot becomes completely distorted if a high level of noise interferes with the measured data. Here, the selection of an appropriate mother wavelet is the only solution to suppress the noise effect on the measured data.

2.7.4   Noise Effect on DWT

Unlike CWT, where the noise impact is discernible on the time-frequency plot, identifying the impact of additive white Gaussian noise on the performance of the DWT is not straightforward. Hence, quantitative measurements, such as the energy of each sub-band, are needed to evaluate the noise impact. Fig. 2.40 shows the DWT sub-bands of air gap magnetic field of a healthy generator with/without additive white Gaussian noise. The energy of each sub-band is calculated as follows:

$$E = \int_{-\infty}^{+\infty} |D_n|^2 dt \qquad (2.6)$$

69

where D_n is the magnitude of each wavelet sub-band. Daubechies-8 is used as a mother wavelet, and the energy of eight sub-bands for a healthy no-noise, healthy 20 dB SNR, and faulty no-noise are shown in Table. 2.3. The analysis shows that having a 20 dB SNR can result in a false positive fault alarm if the index is defined in sub-bands between D1 and D6. Thus, using DWT if the operational environment is noisy and can provide a false indication of the fault.

2.8   Automated Fault Detection Algorithm

The aim of using algorithms based on artificial intelligence in the health monitoring of electric machines is to automate the fault detection process and eliminate the possible human error. An automated health monitoring system can be implemented in three ways:

1. Detection of the electric machine's healthy or faulty operation mode.

2. (1) + Fault type detection

3. (1) + (2) + Location identification and severity estimation of the fault

Note: *In this Ph.D. thesis, the result of first approach (detection of the electric machine's healthy or faulty operation mode) is only discussed since the results are published in [Paper IX].*

The accuracy of the automated health monitoring system depends on various factors, such as:

1. The type of signal and the number of signals

2. The number of training data sets

3. The developed algorithm

Note: *In this Ph.D. thesis, the results obtained based on air gap magnetic field are only discussed, since the results of the published paper [Paper IX] are only based on the mentioned signal. However, during the Ph.D. study, an algorithm based on sensor fusion that utilized stray magnetic field, vibration, voltage, and current, was implemented. The results showed that the application of sensor fusion outperformed the single signal approach. Moreover, the proposed algorithm in [Paper IX] is applied to stray magnetic field and the result indicates that the trained algorithm for the dataset based on stray magnetic field outperforms the air gap magnetic field.*

Fig. 2.41 shows the implementation procedure of the machine learning approach developed in this Ph.D. study. The algorithm consists of five steps: data acquisition, data pre-processing, feature extraction, feature selection, and machine learning. Several experiments on a 100 kVA 14-pole synchronous generator are performed in the healthy case and under various degrees of ITSC fault. The air gap magnetic field is measured and recorded at a frequency of 50 kHz. In total, 48 experiments are performed (eight healthy cases and 40 faulty cases) under various loading conditions and with different fault severity. Adequate data sets are
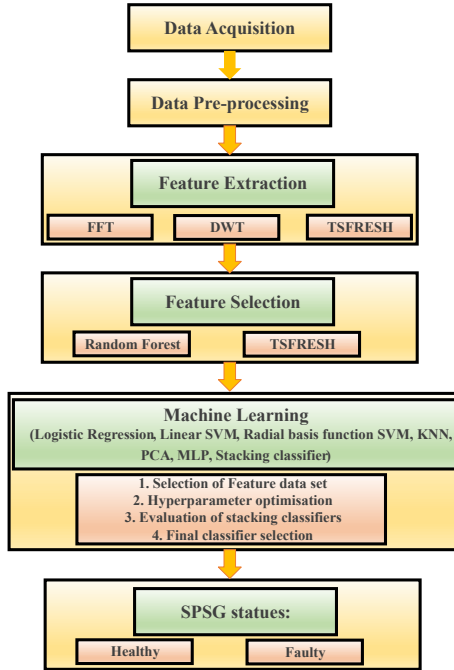
Figure 2.41: Procedure of intelligent health monitoring of synchronous generators

provided by defining a reduced sample series (RSS) consisting of one mechanical revolution of the generator. Therefore, the number of data sets is approximately equal to 2500.

Three feature extraction tools are used: FFT, DWT, and Time Series FeatuRe Extraction based on Scalable Hypothesis tests (TSFRESH). The frequency spectrum of the air gap magnetic field shows that an ITSC fault increases the amplitude of the harmonics at the interval of the mechanical frequency of the generator. Therefore, FFT is applied to each RSS, and the frequency components are selected for training. DWT with a Haar mother wavelet with 12-level decomposition is selected for the feature extraction due to its simple implementation. Instantaneous, Teager, hierarchical, and relative wavelet energies are computed for each decomposition level as a separate feature. Lastly, TSFRESH is applied to each RSS and several time-domain features using 63 time series characteristic methods are extracted. The total number of extracted features is 417. The entire set of extracted features cannot provide informative data, indicating that the most informative data must be selected. Two feature selection methods, namely random forest and TSFRESH, are used. The feature selection method based on random forest provides 81 of the 417 features, while TSFRESH provides 301 of the 417. Both data sets are used for the training the different proposed
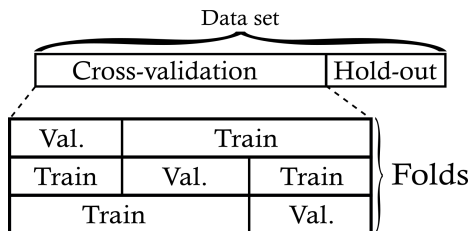
72

Figure 2.42: Threefold cross-validation of the data set. Each fold includes a training and validation set.

Table 2.4: The results from the stacking classifier comparison.

Meta-classifier	Accuracy	Sensitivity	Precision	F1-score
Logistic Regression	0.7840	0.8701	0.8260	0.8432
Multi-layer Perceptron	0.7479	0.8057	0.8276	0.8107
Gradient boosting forest	0.7663	0.8268	0.8304	0.8255
Random Forest	0.7704	0.8216	0.8388	0.8265

algorithms; however, the feature data set based on TSFRESH outperforms the random forest.

The data set is divided into three parts: training, testing, and hand-out data set. Only 20% of the data is kept as the hand-out data set. The data set is not entirely uniform, indicating that the non-uniform splitting of the train/test sets may affect the result of the machine learning algorithm. Thus, cross-validation with k-folds is used to avoid misclassification of the data set. When using k-fold cross-validation, the performance of the model is the average performance of the model over each fold. Fig. 2.42 shows the threefold cross-validation.

Eleven models are used: logistic regression w/w.o PCA, KNN w/w.o PCA, SVM (radial basis function) w/w.o PCA, SVM (linear) w/w.o PCA, XGBOOST, multi-layer Perceptron, and stack. The analysis shows that every classifier combined with PCA has a drop in performance. Consequently, the PCA is not considered in further study. The classifiers are optimized by conducting a grid search on hyperparameters. Several tools are available for evaluating the performance of the classifiers. Four tools are used: accuracy, sensitivity, precision, and F1-score (these evaluators are explained in Paper [IX]). The F1-score for five classifiers on a five-fold data set is shown in Table. 2.4.

Although the F1-score of every single classifier shows promising results, ensemble learners are preferred since they combine several weak learners that may have poor performance to create a more powerful classifier. A few approaches can accomplish this, mainly by bagging, boosting, and stacking. A stacking classi-

Table 2.5: The results of the best of the single and stacking classifiers on the hold-out data samples.

Classifier	Accuracy	Sensitivity	Precision	F1-score
Logistic Regression	0.7569	0.6961	0.9435	0.8011
Logistic Reg. stack	0.8448	0.8456	0.9274	0.8846

fier consists of two levels of classifiers, the base classifiers and meta classifiers. The stacking classifier outperforms the base classifier since the meta-classifier is trained based on the output of the base classifier. Four stacking classifiers are created with different meta classifiers: logistic regression, MLP, gradient boosting forest, and a random forest classifier. The F1-score of the stacking classifier is higher when the logistic regression is selected as its meta classifier. Therefore, the model with the logistic regression as a meta-classifier is chosen. The developed model with improved performance based on optimized hyperparameters is examined with hold-out data, as shown in Table. 2.5. The same hold-out data set is used to examine the single classifier of logistic regression. According to Table. 2.5, the F1-score of the stacking classifier with logistic regression as a meta classifier is 8% higher than that of a single classifier. The logistic regression stacking classifier has an accuracy of 0.8448, a sensitivity of 0.8456, and a precision of 0.9274. This indicates that the classifier correctly classified 84.48% of all the samples in the hold-out dataset and that 84.56% of the faulty samples present were correctly classified as such. Of the samples that were classified as faulty, 92.74% were correctly classified.

3   Conclusion

This thesis proposed several approaches to address the limitations of the previously developed health monitoring methods for hydropower generators. The thesis provides practical solutions to meet the research objectives and has made contributions toward functional health monitoring algorithms. The main findings and potential future works are discussed in the following sections.

3.1   Concluding remarks

In this thesis, health monitoring of hydro generators based on the application of a non-invasive sensor is proposed. A tailor-made sensor that can pick up the stray magnetic field on the stator backside is proposed. The induced sensor voltage of the signal is able to provide informative data, while its installation can be conducted even during synchronous generator operation. Although the stray magnetic field on the stator backside is minuscule, the precise signal is captured due to the direct access to the stator backside and the proper design of the custom-made sensor.

Detection of a fault at the early stage can provide adequate time for the maintenance team to plan for the stoppage of the generator at a reasonable time. The stray magnetic field has a high sensitivity to the low degree of faults. The analysis of the signals indicates that the amplitude and the pattern of the signal are changed even by having one shorted turn in the rotor field winding or having a 5% eccentricity fault; while detection of the fault at the mentioned level for non-invasive methods based on voltage, current, and the vibration is almost impossible.

The previously developed methods need a priori knowledge of the healthy generator, which is almost impossible to acquire due to the lack of documentation during the commissioning of the hydro generator. That problem is solved by introducing several detection algorithms that extract a unique feature for each fault type using signal processing methods, such as FFT, STFT, CWT, and DWT. The spectrum analysis of the stray magnetic field for a healthy generator demonstrates a chaotic amplitude variation of the harmonics, while the frequency spectrum shows a unique pattern for each type of the inter-turn short circuit fault and DE fault. In addition, a unique pattern for short circuit fault detection is also introduced using STFT, whereby the faulty pole can be detected simply and without any need for healthy generator data. A distinctive method based on de-

ploying CWT to the stray magnetic field for the short circuit fault is introduced, and the method is able to provide a unique pattern for both short circuit and eccentricity fault.

Detection of an SE fault is almost impossible based on the available commercialized and state-of-the-art approaches. The method developed in this thesis can diagnose an SE fault with low severity based on time-domain data analysis. In addition, the direction of the fault can be detected if four sensors are mounted at a distance of 90 mechanical degrees on the stator backside. Two unique patterns are also proposed for the detection of a DE fault based on the application of FFT and CWT. The proposed methods do not require prior knowledge of the generator.

In this thesis, a method for the detection of a broken damper bar (BDB) during steady state and transient operation of the synchronous generator is proposed. The method is based on the analysis of the stray magnetic field measured on the stator backside. The DWT is used to locate the sub-bands that have the highest sensitivity to the occurrence of the BDB fault. The method can detect the BDB fault during ramp-up and ramp-down, since a high current passes through the damper bars during the transient. However, the damper bars are active even during the steady state operation of the generator if the generator has a fractional winding. The proposed index based on wavelet entropy can simply show the variation in the frequency component caused by the BDB fault.

The introduced patterns make fault type detection easier, thereby resulting in significant time savings for the maintenance team. The proposed methods are also checked regarding the noise impact on their performance. Noise is suppressed by designing a sensor that has a high signal-to-noise ratio. In addition, additive white Gaussian noise, which is the dominant type of noise in the industrial environment, is also added to the measured signal that is analyzed by the signal processor. The analysis shows that a safe margin of up to 40 dB SNR exists that signal processors can use to detect the fault precisely.

An intelligent detection algorithm is also proposed in this thesis that can detect the inter-turn short circuit fault with a high F-score. Although the number of experiments is limited, the data are pre-processed to achieve 2500 data sets. Three feature extraction tools, including FFT, DWT, and TSFRESH, provided a total of 417 features. The computational complexity of the method is diminished by reducing the number of irrelevant features using feature selection tools. Eleven single classifiers, in addition to four ensemble stacking classifiers, are examined to achieve high accuracy and precision. Finally, a method based on ensemble learners that uses four base classifiers in addition to the meta classifier is selected due to the high F-score. The logistic regression as a meta classifier shows a promising result among various classifiers. However, the proposed algorithm is only able to detect the presence or absence of an inter-turn short circuit fault in

the generator.

Fig. 3.1 summarizes the abilities and limitations of available commercialized solutions. Several factors have been compared, such as the ability to detect the fault and identify its type, sensitivity, noise impact, invasive or non-invasive sensor, level of difficulty in the implementation, and cost of sensor assuming the same data acquisition system is used. Among the available approaches, a method based on the stray magnetic field has a high superiority and can make the developed methods favorable for health monitoring problems encountered in the industrial setting.

3.2 Recommendations for future work

This research study investigates rotor-related faults, such as inter-turn short circuit faults, eccentricity, and broken damper bar faults. The superiority of the developed health monitoring algorithms based on the stray magnetic field using advanced signal processing methods is demonstrated. The same approach can be used to detect a short circuit fault in the stator winding of synchronous generators with multi-turn windings. The method must provide a distinctive pattern that is able to detect the turn-to-turn fault at an early stage before the short circuit fault burns out the entire stator winding.

Research studies to detect the stator core-related faults are currently limited, and the available methods are based on offline inspection. A method based on the application of a stray magnetic field is suggested here to allow the detection of stator core-related faults while the generator is operating. In large hydro generators, the stator core consists of two or three segments. The imposed force during operation, rockmass force, and aging deteriorates the joints of the segments. Therefore, the stator becomes oval in the long run and the stator core segments in the joint are eroded, resulting in a core short circuit. A method based on the application of a stray magnetic field can be proposed to detect the stator joint fault.

A comprehensive intelligent algorithm based on ensemble learners that utilize the sensor fusion application can be proposed to increase the F-score above 95%. In addition, deep neural networks based on the application of convolutional neural networks need to be proposed to automate fault type detection. The development of severity estimation is also needed to provide insight regarding the operational condition of the generator and when the generator must be stopped for inspection and maintenance.

Signal	Fault Detection							Fault Type Detection	Location of Fault	Invasive or Non-invasive	Sensitivity to Fault Severity	Noise Impact on Signal	Difficulty of Implementation	Additional Equipment
	SSC	ITSC	SE	DE	BDB	MA	SC							
Partial Discharge	✓	✗	✗	✗	✗	✗	✗	SSC	✗	Invasive	High	High	Difficult	PD Senors, Data Acquisition
Thermal	✓	✓	✗	✗	✗	✗	✓	SSC, ITSC, SC	✓	Non-invasive	Low	Low	Easy	No
Vibration	✓	✓	✓	✓	✗	✓	✗	✗	✗	Non-invasive	Low	High	Easy	Power Source
Voltage	✓	✓	✗	✓	✗	✓	✗	✗	✗	Non-invasive	Low	Low	Easy	No
Current	✓	✓	✗	✓	✗	✓	✗	✗	✗	Non-invasive	Low	Low	Easy	No
Shaft Voltage/Current	✓	✓	✓	✓	✓	✓	✗	All Faults expect SC	✓	Invasive	Low	High	Difficult	Brsuh & Holder
Air-gap Magnetic Field	✓	✓	✓	✓	✓	✓	✗	All Faults expect SC	✓	Invasive	High	High	Difficult	Power Source
Stray Magnetic Field	✓	✓	✓	✓	✓	✓	?	All Faults expect SC	✓	Non-invasive	High	Low	Easy	No

Figure 3.1: Comparison of the available commercialized and the state-of-the-art methods with the developed method in this Ph.D. thesis

Bibliography

[1] "08308: Produksjon av elektrisk kraft (GWh), etter statistikkvariabel, region og år." [Online]. Available: https://www.ssb.no/statbank/table/08308/tableViewLayout1/

[2] D. P. Kothari and I. J. Nagrath, *Electric Machines*. Tata McGraw-Hill Education, 2004, google-Books-ID: axGw7r3SOEMC.

[3] R. electrical machines committee, "Survey of hydrogenerator failures," *Technical Brochures*, vol. WG A1.10, pp. 1–22, 2009.

[4] Electric Power Reasearch Institute, "Main generator on line monitoring and diagnostics," EPRI, Tech. Rep., 1996.

[5] P. Tavner, L. Ran, J. Penman, and H. Sedding, *Condition monitoring of rotating electrical machines*. IET, 2008, vol. 56.

[6] H. Ehya, A. Nysveen, J. Antonino-Daviu, and B. Akin, "Health monitoring of synchronous generators: Review of methods, applications and trends," *IEEE Open Access*, 2022.

[7] H. Ehya, A. Nysveen, I. Groth, and B. A. Mork, "Detailed magnetic field monitoring of short circuit defects of excitation winding in hydro-generator," in *2020 International Conference on Electrical Machines (ICEM)*, vol. 1. IEEE, 2020, pp. 2603–2609.

[8] Y. Park, S. B. Lee, J. Yun, M. Sasic, and G. C. Stone, "Air gap flux-based detection and classification of damper bar and field winding faults in salient pole synchronous motors," *IEEE Transactions on Industry Applications*, vol. 56, no. 4, pp. 3506–3515, 2020.

[9] D. Albright, "Interturn short-circuit detector for turbine-generator rotor windings," *IEEE transactions on power apparatus and systems*, no. 2, pp. 478–483, 1971.

[10] M. Sasic, G. C. Stone, J. Stein, and C. Stinson, "Detecting turn shorts in rotor windings: A new test using magnetic flux monitoring," *IEEE Industry Applications Magazine*, vol. 19, no. 2, pp. 63–69, 2012.

[11] M. Sasic, S. Campbell, and B. Lloyd, "Flux monitoring improvement," *IEEE industry applications magazine*, vol. 17, no. 5, pp. 66–69, 2011.

[12] G. C. Stone, M. Sasic, J. Stein, and C. Stinson, "Using magnetic flux monitoring to detect synchronous machine rotor winding shorts," in *Conference Record of 2012 Annual IEEE Pulp and Paper Industry Technical Conference (PPIC)*. IEEE, 2012, pp. 1–7.

[13] H. Ehya, T. Skreien, and A. Nysveen, "Intelligent data-driven diagnosis of incipient inter-turn short circuit fault in field winding of salient pole synchronous generators," *IEEE Transactions on Industrial Informatics*, 2021.

[14] O. Kokoko, A. Merkhouf, A. Tounzi, M. Essalhi, E. Guillot, B. Kedjar, and K. Al Haddad, "Detection of short circuits in the rotor field winding in large hydro generator," in *2018 XIII International Conference on Electrical Machines (ICEM)*. IEEE, 2018, pp. 1815–1820.

[15] S. Afrandideh, M. E. Milasi, F. Haghjoo, and S. M. Cruz, "Turn to turn fault detection, discrimination, and faulty region identification in the stator and rotor windings of synchronous machines based on the rotational magnetic field distortion," *IEEE Transactions on Energy Conversion*, vol. 35, no. 1, pp. 292–301, 2019.

[16] S. Afrandideh, F. Haghjoo, S. Cruz, and M. E. Milasi, "Detection of turn-to-turn faults in the stator and rotor of synchronous machines during startup," *IEEE Transactions on Industrial Electronics*, vol. 68, no. 8, pp. 7485–7495, 2020.

[17] J. Yun, S. Park, C. Yang, Y. Park, S. B. Lee, M. Šašić, and G. C. Stone, "Comprehensive monitoring of field winding short circuits for salient pole synchronous motors," *IEEE Transactions on Energy Conversion*, vol. 34, no. 3, pp. 1686–1694, 2019.

[18] J. Penman and H. Jiang, "The detection of stator and rotor winding short circuits in synchronous generators by analysing excitation current harmonics," 1996.

[19] J. Sottile, F. C. Trutt, and A. W. Leedy, "Condition monitoring of brushless three-phase synchronous generators with stator winding or rotor circuit deterioration," *IEEE Transactions on Industry Applications*, vol. 42, no. 5, pp. 1209–1215, 2006.

[20] W. Shuting, L. Heming, L. Yonggang, and W. Yi, "The diagnosis method of generator rotor winding inter-turn short circuit fault based on excitation current harmonics," in *The Fifth International Conference on Power Electronics and Drive Systems, 2003. PEDS 2003.*, vol. 2. IEEE, 2003, pp. 1669–1673.

[21] Z. Zhou, Y. Wang, W. Guo, B. Li, and J. Mao, "Fault identification of turbine generator rotor system based on spectrum monitor and analysis," in *2011 Asia-Pacific Power and Energy Engineering Conference*. IEEE, 2011, pp. 1–5.

[22] L. Hao, Y. Sun, A. Qiu, and X. Wang, "Steady-state calculation and on-line monitoring of interturn short circuit of field windings in synchronous machines," *IEEE Transactions on Energy Conversion*, vol. 27, no. 1, pp. 128–138, 2011.

[23] W. Shuting, L. Yonggang, L. Heming, and T. Guiji, "The analysis of generator excitation current harmonics on stator and rotor winding fault," in *2006 IEEE International Symposium on Industrial Electronics*, vol. 3. IEEE, 2006, pp. 2089–2093.

[24] T. D. Batzel, D. C. Swanson, and J. F. Defenbaugh, "Predictive diagnostics for the main field winding and rotating rectifier assembly in the brushless synchronous generator," in *4th IEEE International Symposium on Diagnostics for Electric Machines, Power Electronics and Drives, 2003. SDEMPED 2003.* IEEE, 2003, pp. 349–354.

[25] M. Valavi, K. G. Jørstad, and A. Nysveen, "Electromagnetic analysis and electrical signature-based detection of rotor inter-turn faults in salient-pole synchronous machine," *IEEE Transactions on Magnetics*, vol. 54, no. 9, pp. 1–9, 2018.

[26] I. Sadeghi, H. Ehya, and J. Faiz, "Analytic method for eccentricity fault diagnosis in salient-pole synchronous generators," in *2017 International Conference on Optimization of Electrical and Electronic Equipment (OPTIM) & 2017 Intl Aegean Conference on Electrical Machines and Power Electronics (ACEMP).* IEEE, 2017, pp. 261–267.

[27] H. Ehya, G. L. Rødal, A. Nysveen, and R. Nilssen, "Condition monitoring of wound field synchronous generator under inter-turn short circuit fault utilizing vibration signal," in *2020 23rd International Conference on Electrical Machines and Systems (ICEMS).* IEEE, 2020, pp. 177–182.

[28] M. Cuevas, R. Romary, J.-P. Lecointe, and T. Jacq, "Non-invasive detection of rotor short-circuit fault in synchronous machines by analysis of stray magnetic field and frame vibrations," *IEEE Transactions on Magnetics*, vol. 52, no. 7, pp. 1–4, 2016.

[29] M. Cuevas, R. Romary, J.-P. Lecointe, F. Morganti, and T. Jacq, "Noninvasive detection of winding short-circuit faults in salient pole synchronous machine with squirrel-cage damper," *IEEE Transactions on Industry Applications*, vol. 54, no. 6, pp. 5988–5997, 2018.

[30] Y.-L. He, Y. Wang, H.-C. Jiang, P. Gao, X.-H. Yuan, D. Gerada, and X.-Y. Liu, "A novel universal model considering sage for mfd-based faulty property analysis under risc in synchronous generators," *IEEE Transactions on Industrial Electronics*, vol. 69, no. 7, pp. 7415–7427, 2021.

[31] M. Rahnama, A. Vahedi, A. M. Alikhani, and A. Montazeri, "Machine-learning approach for fault detection in brushless synchronous generator using vibration signals," *IET Science, Measurement & Technology*, vol. 13, no. 6, pp. 852–861, 2019.

[32] X.-H. Yuan, Y.-L. He, M.-Y. Liu, H. Wang, S.-T. Wan, and G. Vakil, "Impact of the field winding interturn short-circuit position on rotor vibration properties in synchronous generators," *Mathematical Problems in Engineering*, vol. 2021, 2021.

[33] J. S. Hsu and J. Stein, "Shaft signals of salient-pole synchronous machines for eccentricity and shorted-field-coil detections," *IEEE transactions on energy conversion*, vol. 9, no. 3, pp. 572–578, 1994.

[34] W. Yucai, L. Yonggang, and L. Heming, "Diagnosis of turbine generator typical faults by shaft voltage," in *2012 IEEE Industry Applications Society Annual Meeting*. IEEE, 2012, pp. 1–6.

[35] W. Yucai, M. Qianqian, and C. Bochong, "Fault diagnosis of rotor winding inter-turn short circuit for sensorless synchronous generator through screw," *IET Electric Power Applications*, vol. 11, no. 8, pp. 1475–1482, 2017.

[36] J.-E. Torlay, C. Corenwinder, A. Audoli, J. Herigault, and A. Foggia, "Analysis of shaft voltages in large synchronous generators," in *IEEE International Electric Machines and Drives Conference. IEMDC'99. Proceedings (Cat. No. 99EX272)*. IEEE, 1999, pp. 607–609.

[37] G. Stone, B. Lloyd, and M. Sasic, "Monitoring of shaft voltages and grounding currents in rotating machines," in *2014 17th International Conference on Electrical Machines and Systems (ICEMS)*. IEEE, 2014, pp. 3361–3364.

[38] H. Ehya, A. Nysveen, and R. Nilssen, "A practical approach for static eccentricity fault diagnosis of hydro-generators," in *2020 International Conference on Electrical Machines (ICEM)*, vol. 1. IEEE, 2020, pp. 2569–2574.

[39] M. Babaei, J. Faiz, B. M. Ebrahimi, S. Amini, and J. Nazarzadeh, "A detailed analytical model of a salient-pole synchronous generator under dynamic eccentricity fault," *IEEE Transactions on Magnetics*, vol. 47, no. 4, pp. 764–771, 2011.

[40] M. F. Shaikh, H. Kim, S. B. Lee, and C. Lim, "Online airgap flux based diagnosis of rotor eccentricity and field winding turn insulation faults in synchronous generators," *IEEE Transactions on Energy Conversion*, 2021.

[41] N. A. Al-Nuaim and H. Toliyat, "A novel method for modeling dynamic airgap eccentricity in synchronous machines based on modified winding function theory," *IEEE Transactions on energy conversion*, vol. 13, no. 2, pp. 156–162, 1998.

[42] H. A. Toliyat and N. A. Al-Nuaim, "Simulation and detection of dynamic air-gap eccentricity in salient-pole synchronous machines," *IEEE transactions on industry applications*, vol. 35, no. 1, pp. 86–93, 1999.

[43] J. Faiz, M. Babaei, J. Nazarzadeh, B. Ebrahimi, and S. A. Velashani, "Time-stepping finite-element analysis of dynamic eccentricity fault in a three-phase salient pole synchronous generator," *Progress in Electromagnetics Research B*, vol. 20, pp. 263–284, 2010.

[44] I. Tabatabaei, J. Faiz, H. Lesani, and M. Nabavi-Razavi, "Modeling and simulation of a salient-pole synchronous generator with dynamic eccentricity using modified winding function theory," *IEEE Transactions on Magnetics*, vol. 40, no. 3, pp. 1550–1555, 2004.

[45] B. M. Ebrahimi, M. Etemadrezaei, and J. Faiz, "Dynamic eccentricity fault diagnosis in round rotor synchronous motors," *Energy Conversion and Management*, vol. 52, no. 5, pp. 2092–2097, 2011.

[46] M. Kiani, W. Lee, R. Kenarangui, and B. Fahimi, "Detection of rotor faults in synchronous generators," in *2007 IEEE International Symposium on Diagnostics for Electric Machines, Power Electronics and Drives*. IEEE, 2007, pp. 266–271.

[47] C. Bruzzese, "Diagnosis of eccentric rotor in synchronous machines by analysis of split-phase currents—part i: Theoretical analysis," *IEEE Transactions on Industrial Electronics*, vol. 61, no. 8, pp. 4193–4205, 2013.

[48] ——, "Diagnosis of eccentric rotor in synchronous machines by analysis of split-phase currents—part ii: Experimental analysis," *IEEE Transactions on Industrial Electronics*, vol. 61, no. 8, pp. 4206–4216, 2013.

[49] C. Bruzzese and G. Joksimovic, "Harmonic signatures of static eccentricities in the stator voltages and in the rotor current of no-load salient-pole synchronous generators," *IEEE Transactions on Industrial Electronics*, vol. 58, no. 5, pp. 1606–1624, 2010.

[50] G. Joksimovic, C. Bruzzese, and E. Santini, "Static eccentricity detection in synchronous generators by field current and stator voltage signature analysis-part i: Theory," in *The XIX International Conference on Electrical Machines-ICEM 2010*. IEEE, 2010, pp. 1–6.

[51] C. Bruzzese, G. Joksimovic, and E. Santini, "Static eccentricity detection in synchronous generators by field current and stator voltage signature analysis-part ii: Measurements," in *The XIX International Conference on Electrical Machines-ICEM 2010*. IEEE, 2010, pp. 1–5.

[52] R. Perers, U. Lundin, and M. Leijon, "Saturation effects on unbalanced magnetic pull in a hydroelectric generator with an eccentric rotor," *IEEE Transactions on Magnetics*, vol. 43, no. 10, pp. 3884–3890, 2007.

[53] M. Wallin, M. Ranlof, and U. Lundin, "Reduction of unbalanced magnetic pull in synchronous machines due to parallel circuits," *IEEE transactions on magnetics*, vol. 47, no. 12, pp. 4827–4833, 2011.

[54] H. Ehya, A. Nysveen, R. Nilssen, and U. Lundin, "Time domain signature analysis of synchronous generator under broken damper bar fault," in *IECON 2019-45th Annual Conference of the IEEE Industrial Electronics Society*, vol. 1. IEEE, 2019, pp. 1423–1428.

[55] T. Plazenet, T. Boileau, C. Caironi, and B. Nahid-Mobarakeh, "A comprehensive study on shaft voltages and bearing currents in rotating machines," *IEEE Transactions on Industry Applications*, vol. 54, no. 4, pp. 3749–3759, 2018.

[56] K. Darques, A. Tounzi, Y. Le Menach, K. Beddek, and M. Biet-Evrard, "An approach to model shaft voltage of wound rotor synchronous machines," in *2016 IEEE Conference on Electromagnetic Field Computation (CEFC)*. IEEE, 2016, pp. 1–1.

[57] P. I. Nippes, "Early warning of developing problems in rotating machinery as provided by monitoring shaft voltages and grounding currents," *IEEE Transactions on energy conversion*, vol. 19, no. 2, pp. 340–345, 2004.

[58] M. J. Costello, "Shaft voltages and rotating machinery," *IEEE Transactions on Industry Applications*, vol. 29, no. 2, pp. 419–426, 1993.

[59] G. D'Antona, P. Pennacchi, C. Pensieri, and C. Rolla, "Turboalternator shaft voltage measurements," in *2012 IEEE International Workshop on Applied Measurements for Power Systems (AMPS) Proceedings*. IEEE, 2012, pp. 1–4.

[60] W. Doorsamy, W. A. Cronje, and A. S. Meyer, "Multiple fault diagnosis on a synchronous 2 pole generator using shaft and flux probe signals," in *2013 IEEE International Conference on Industrial Technology (ICIT)*. IEEE, 2013, pp. 362–367.

[61] H. Ehya, A. Nysveen, B. Akin, and J. Antonino-Daviu, "Detection and severity estimation of eccentricity fault of a high power synchronous generator," *IEEE Transactions on Reliability*, 2022.

[62] H. Ehya, A. Nysveen, and J. A. Antonino-DAVIU, "Advanced fault detection of synchronous generators using stray magnetic field," *IEEE Transactions on Industrial Electronics*, 2021.

[63] J. Faiz, B. M. Ebrahimi, and H. A. Toliyat, "Effect of magnetic saturation on static and mixed eccentricity fault diagnosis in induction motor," *IEEE Transactions on magnetics*, vol. 45, no. 8, pp. 3137–3144, 2009.

[64] ANSYS®, "Academic Research Electronics Desktop," Release R2.4.

[65] M. Christ, N. Braun, J. Neuffer, and A. W. Kempa-Liehr, "Time series feature extraction on basis of scalable hypothesis tests (tsfresh–a python package)," *Neurocomputing*, vol. 307, pp. 72–77, 2018.

[66] R. Priemer, *Introductory signal processing*. World Scientific, 1991, vol. 6.

[67] G. D. Bergland, "A guided tour of the fast fourier transform," *IEEE spectrum*, vol. 6, no. 7, pp. 41–52, 1969.

[68] C. Torrence and G. P. Compo, "A practical guide to wavelet analysis," *Bulletin of the American Meteorological society*, vol. 79, no. 1, pp. 61–78, 1998.

[69] K. Ho, "Fast cwt computation at integer scales by the generalized mra structure," *IEEE transactions on signal processing*, vol. 46, no. 2, pp. 501–506, 1998.

[70] H. A. Toliyat, S. Nandi, S. Choi, and H. Meshgin-Kelk, *Electric machines: modeling, condition monitoring, and fault diagnosis*. CRC press, 2012.

Journal Publications

Paper I

H. Ehya, A. Nysveen, J. A. Antonino Daviu, and Bilal Akin, "Health Monitoring of Synchronous Machines: Review of Methods, Applications and Trends," in IEEE Open Transaction on Industry Applications, Under Review.

This paper is not yet published and therefore not included.

Paper II

This paper is not yet published and therefore not included.

Paper III

Pattern Recognition of Interturn Short Circuit Fault in a Synchronous Generator Using Magnetic Flux

Hossein Ehya ⓘ, *Student Member, IEEE*, and Arne Nysveen ⓘ, *Senior Member, IEEE*

Abstract—**This article provides a novel approach for discriminating the interturn short circuit (ITSC) fault in a salient pole synchronous generator (SPSG) based on the use of noninvasive sensors. A stray magnetic field is used as a signal that can provide valuable data regarding the health condition of the SPSG. Generally, the captured signal under an ITSC fault is examined using a classical signal processing tool based on fast Fourier transforms (FFTs). The amplitude of the side-bands to the frequency spectrum is increased by ITSC, eccentricity, and broken damper-bar faults. Therefore, determining the type of fault is not possible by analyzing the FFT side-bands. A unique feature is introduced using a short-time Fourier transform to identify the ITSC in its early stage. The proposed feature can locate and recognize the ITSC fault with high accuracy in either the no-load or the full-load operation of the SPSG. This novel methodology is verified by applying an ITSC fault to a 100 kVA custom-made SPSG.**

Index Terms—**Condition monitoring, fault detection, feature extraction, finite element modeling, pattern recognition, spectrum analysis, stray magnetic field, synchronous generator.**

I. INTRODUCTION

INTERTURN short circuits (ITSCs) of rotor field windings are a critical and serious failure among various kinds of faults in a rotor pole of salient pole synchronous generators (SPSGs) and can affect the operation of the machine. Although the SPSGs found in power plants often operate well for decades, ITSC faults can shorten their effective life span. The increased temperature due to an ITSC fault does not allow the power producers to overload the SPSG temporarily, since dynamic derating of a faulty machine might rapidly progress into a severe fault. Therefore, a need exists for accurate and low-cost condition monitoring systems to avoid unplanned stoppages of the SPSGs.

An ITSC fault can occur due to electrical or mechanical problems in the rotor field winding insulation. ITSC failure can give rise to local hot spots and vibrations that, in turn, can accelerate the degradation of insulation [1]. Numerous approaches have been proposed to detect the fault in the SPSG, but most rely on harmonic analysis of the stator phase voltage [2], air-gap magnetic field [3], [4], phase currents [5], [6], and vibrations in the frame [7]. However, these methods have some drawbacks, including the following.

1) Although the air-gap magnetic field provides detailed data for detecting an ITSC, it is an invasive approach and difficult to implement in SPSGs that are already under operation. Hall-effect sensors or search coils installed on the stator tooth are also fragile and the possibility of sensor failure during operation is quite high.
2) The harmonic contents of the phase voltage, current, and vibration demonstrate some changes in the fast Fourier transform (FFT) spectrum "only" in a case of severe ITSC fault.

These problems have recently been tackled using the stray magnetic field to detect the ITSC fault [7]–[9]. This is a noninvasive method that uses sensors that can easily be installed on the machine frame or on the back side of the stator yoke. The leakage flux creates a weak magnetic field outside the machine and this field can be captured utilizing search coils, hall effect sensors, optical fibers [10], and radio frequency sensors [11]. However, the search coil is preferred over the other sensors since it is inexpensive and robust and works well in a power plant or industrial environment. The amplitude of the induced electro-motive force (EMF) in the search coil is proportional to the rate of leakage flux variation and the number of turns. The distance between the search coil and the machine's frame also significantly influences the amplitude of the induced EMF.

Numerous signal processing tools are proposed for processing faulty electric machine signals. The majority of these tools are categorized into one of three groups—namely, time domain, frequency domain, and time-frequency domain. In [12] and [13], the time-series data mining method was used to detect a broken damper bar fault, where the radius of the created gyration was introduced as a fault signature. This signature shows substantial changes under a faulty condition, but it also shows the same changes for any type of fault, so identification of the fault type is not possible. In addition, an extracted feature based on the time series data mining method is sensitive to noise, since the working principle of this method is based on the temporal variation of a variable.

FFT is the most prevalent frequency domain signal processing tool and is widely used in fault diagnosis of electrical machines.

In [6] and[14], FFT was used to analyze the phase voltage and current of an SPSG under eccentricity and an ITSC fault. The amplitude of the low-frequency side-bands was used to detect both faults. Although the air-gap magnetic field is a noninvasive method, it was also used to diagnose the eccentricity and ITSC fault in [6] and [15]. The amplitude of the frequency spectrum of the air-gap magnetic field under both faults shows the same variation. FFT was also applied to a stray magnetic field to demonstrate how the amplitude of the frequency spectrum changes under faulty conditions. Ultimately, since any type of fault changes the frequency contents of the signals, identification of the type of fault is not possible based on FFT analysis.

Fault diagnosis of electric machines often uses various time-frequency domain signal processing tools, such as continuous and discrete wavelet families, multiple signal classification (MUSIC), and short-time Fourier transforms (STFTs). The use of time-frequency domain signal processors results in numerous challenges in the search for a specific pattern for a faulty machine, such as finding proper windowing function, mother wavelet, and color maps, in addition to adjusting window length and data length. Discrete and continuous wavelet transforms have been used to diagnose broken damper bars in induction motors in [16]–[19]. A specific pattern due to a broken damper bar in an induction motor has appeared, and the intensity of the pattern changed with the increasing severity of the fault. The stray magnetic field was analyzed by MUSIC to detect the rotor-related fault in induction motors, and the same pattern, introduced based by continuous wavelet transform, appeared in the MUSIC plots [20]. STFT has been widely applied to faulty induction motor signals to detect rotor related faults [21]–[23]. The broken damper bar and rotor field winding fault were also investigated by applying STFT to an air-gap magnetic field in a SPSG [24]–[26]. Although the patterns that emerged were a good indication of fault occurrence, estimation of the precise severity of the fault is lacking in the available literature.

The present work is a detailed study of the application of the stray flux for diagnosis of an ITSC fault in the rotor field winding of an SPSG. Although the feasibility of using stray flux to detect ITSC was studied in [27], the main target of the present article is to introduce a unique pattern based on time-frequency domain signal processing tools, like STFT, to detect ITSC in an SPSG. The severity estimation is carried out by applying image processing to the STFT plots. Section II presents the comprehensive finite element analysis using search coils. The occurrence of the fault is shown to change the variation of the induced EMF in the sensor. Spectrum analysis is used to characterize the induced subharmonics in EMF under ITSC fault in Section III. In Section IV, the experimental setup used to verify the accuracy of the theoretical findings is explained in detail. In Section V, a new pattern for ITSC fault diagnosis, based on STFT and following severity estimation based on image processing, is discussed in detail. The competency of STFT over FFT to discriminate between eccentricity and ITSC fault is studied in Section VI. Section VII then shows that the load variation does not have any effect on the feature in question.
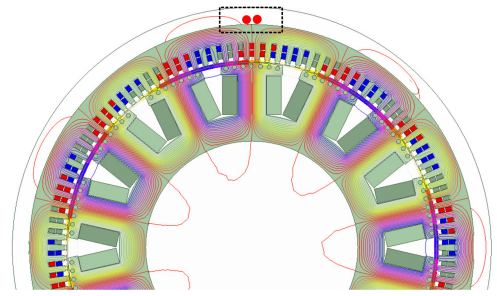

Fig. 1. Geometric configuration of the modeled salient pole synchronous generator using 2-D FEM. The locations of the search coils are demonstrated in red circles.

TABLE I
100 kVA, Cos ϕ 0.9400 V, 428 R/MIN, 14 POLES, SALIENT POLE SYNCHRONOUS GENERATOR

Quantity	Values	Quantity	Values
No. of slots	114	No. of damper bars/pole	7
Winding connection	Wye	Number of poles	14
No. of stator turns	8	No. of rotor turns / pole	35
Nominal speed	428 rpm	Power factor	0.90
Nominal voltage	400 V	Nominal current	144.3 A
Nominal exc. current	103 A	No-load exc. current	53.2 A

II. FINITE ELEMENT MODELING AND ANALYSIS

The 2-D geometry specification of the simulated SPSG is displayed in Fig. 1. The detailed geometrical characteristics of the stator and rotor slots, the nonlinearity of the stator lamination sheets, the spatial distribution of the stator winding, and the saliency of the rotor poles are considered, since the accuracy of the fault features depends on the precision of the finite element model (FEM) [28]. The stator winding layout also has considerable impacts on fault detection, since the winding distribution affects the harmonic components of the magnetic field. In this modeling, the stator has a two-layer fractional winding, so the corresponding spatial distribution is also considered. A constant direct current, according to the generator's loading, is fed into the rotor field windings.

The generator is modeled and analyzed using ANSYS Maxwell [29]. The specification of the proposed three-phase SPSG is summarized in Table I. A 2-D-model is employed, where the 3-D-effects on the stator and rotor windings are included using external circuits in the FEM model. The simulation is made in the time domain until a steady state is reached in the simulation. Rotation is included in the simulation. The nonlinearity of the steel in both the rotor and stator is included, but the eddy-current effects are disregarded, except in the damper bars.

The location of the sensor determines whether the measured signal is the axial flux, radial flux, or both. The location of the sensor should therefore be chosen based on which stray flux is desired to be investigated [30]. The radial stray flux of the machine is captured by mounting a search coil that contains 3000 stranded turns onto the backside of the stator yoke. The
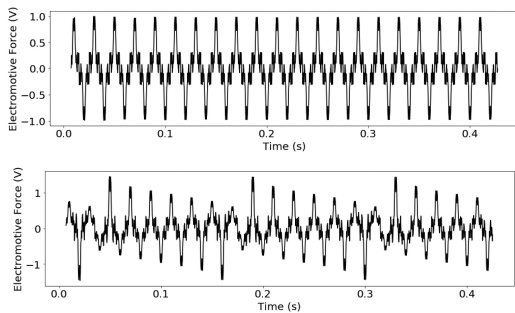
Fig. 2. Induced electromotive force in the sensor due to stray flux variation in the healthy (top) and 10 ITSC fault (bottom) operation: Simulation result.

stray magnetic field outside the machine is in the order of μT; therefore, in order to increase the signal-to-noise ratio, the number of turns in the search coil must be high. The ITSC fault in the rotor field winding was simulated by reducing the total number of conductors, based on the fault severity in the field winding of the desired pole, while applying the specified excitation currents at a no-load or a nominal-load condition.

Fig. 2 shows the magnitude of the induced EMF due to the variation of the stray magnetic flux on the back side of the stator core in the SPSG for a healthy no-load operation and for a 10 ITSC fault in a no-load operation. As shown in Fig. 2, the ITSC fault incurs a variation in the amplitude of the induced EMF. When a short circuit fault occurs, the effective number of field windings decreases, which results in a reduction in the net magneto-motive force in the air-gap. An unbalanced distribution of the magneto-motive force leads into an asymmetric magnetic field in the air-gap and, as a consequence, a distorted stray magnetic field outside the SPSG. The harmonic contents of the stray magnetic field are similar to those of the air-gap magnetic field, since both are influenced by changes in the air-gap magnetomotive force. The intensity of the amplitude variation of EMF in search coil depends on the severity of the ITSC fault.

III. Laboratory Test

A. Experimental Setup

The SPSG performance under an ITSC fault was investigated using the following experimental setup, as shown in Fig. 3.

1) A custom made 100 kVA, 400 V synchronous generator with 14 salient poles, constructed to resemble a Norwegian hydropower generator and with the detailed specifications given in Table I, is utilized. The generator windings are star-connected, and the neutral point is grounded.

2) A 90 kW induction motor with four poles and a rated speed of 1482 r/min was used as a prime mover of the synchronous machine.

3) The prime mover is connected to the synchronous machine using a gearbox with a transfer rate of 10/3.

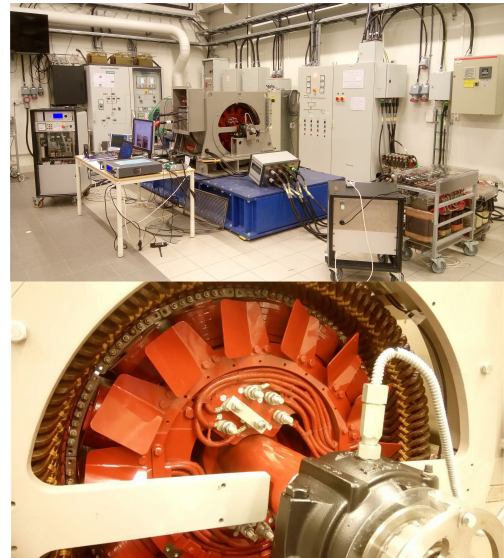4) The rotor field winding is supplied by a 20 kW dc power source (LAB-HP/E2020).

Fig. 3. Experimental setup of 100 kVA custom-made SPSG for the purpose of fault detection (top), the rotor of the generator, and the taps of the field winding to apply ITSC fault.

5) A programmable converter is used to feed the induction motor based on its parameters. A rectifier connected to the grid is used to supply the converter.

6) A high-resolution 16-b oscilloscope (Tektronix MSO 3014) with a sampling frequency of 10 kHz is used for data acquisition.

7) Passive loads are used to run the SPSG in the loaded operation to avoid grid harmonics interference on the measured data. The water-cooled resistor bank consists of two parallel sets of resistors, whereas the total resistance can be controlled and adjusted in steps by contactors and relays from the control panel. The per-phase resistance can be varied from a maximum of 160 Ω to a minimum of about 2.78 Ω. At the maximum load setting, the dissipated power of the resistors amounted to about 57 kW.

8) Two three-phase inductors, with each of their phases linked in series, are connected to the SPSG by a three-phase transformer to increase the inductance value by the transformer turn ratio. The transformer has a star-to-delta connection. The approximate value of the inductance in each phase, based on the turn ratio of the transformer, is equal to 22 mH.

9) A healthy rotor pole of the SPSG contains 35 turns. A copper plate is used to shunt the desired number of turns in a faulty pole, as depicted in Fig. 3. Table II shows the number of possible shorted turns and its percentage with respect to one pole and the total number of turns in the rotor field windings.

10) A rigid search coil is designed to capture the induced EMF on the back side of the stator yoke, as shown in

TABLE II
NUMBER AND PERCENTAGE OF SHORTED TURNS IN THE FAULTY POLE OF THE
SALIENT POLE SYNCHRONOUS GENERATOR

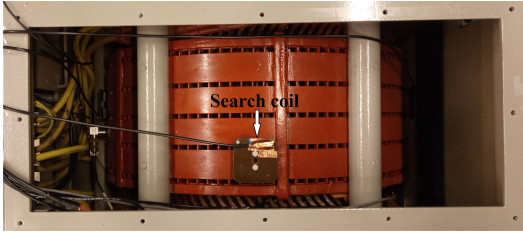| Number of Turns	Total % per Pole	Total % per Total Poles
1 turn	2.86%	0.204%
2 turns	5.71%	0.408%
3 turns	8.57%	0.612%
7 turns	20%	1.428%
10 turns	28.57%	2.045%

Fig. 4.   Location of the sensor installed on the back side of stator yoke to measure electromotive force.
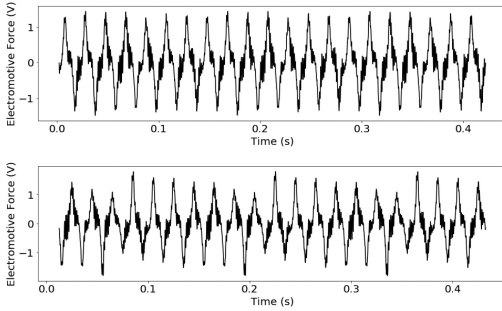

Fig. 5.   Induced electromotive force in the sensor due to stray flux variation in the healthy (top) and 10 ITSC fault (bottom): Experimental result.

Fig. 4. The dimensions of the sensor are $(100 \times 100 \times 10)$ mm. The sensor has 3000 turns of copper wire with a diameter of 0.12 mm. The resistivity and inductance of the search coil at its terminal is 912 Ω and 714 mH. The sensor was installed on a stator yoke to capture the radial flux. The laboratory working environment is vulnerable to noise from converters, so a coaxial cable is used for data transmission in order to reject the noise. There exist no need to redesign a new sensor to capture the stray magnetic field for a machine with a different topology and higher power rating. A series of tests performed in several hydro generators with different power ratings and specifications proved the mentioned claim.

B. Experimental Measurement

The measured EMF induced in the search coil attached to the back side of the stator yoke is shown in Fig. 5. A comparison between healthy cases in both simulation and experimental results demonstrates the presence of a slight variation in the experimental peak magnitude due to the inherent eccentricity
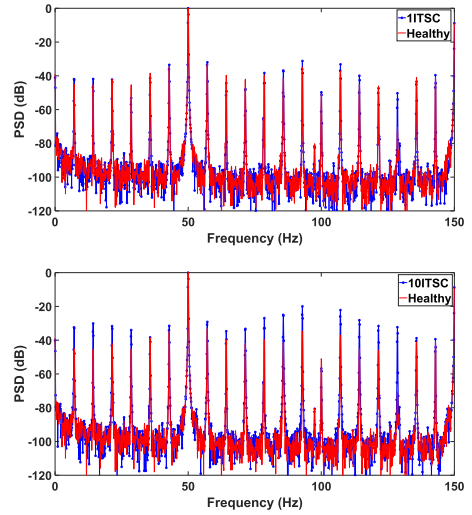

Fig. 6.   Spectrum density of the induced EMF in the sensor in no-load for healthy and a 2 ITSC fault (top), and healthy and 10 ITSC fault (bottom): Experimental results.

fault. In addition, the radial cooling duct and end winding effects are neglected in the FEM results in a slight difference in the waveform shape. However, the amplitude and waveform pattern of the measured EMF in both the healthy and faulty cases agree well with the simulation results.

IV. SPECTRUM ANALYSIS

Fig. 6 depicts the power spectrum density (PSD) of the healthy and faulty synchronous generator with 1 and 10 ITSC faults. A comparison between the healthy and 1 ITSC faults illustrates that the presence of the fault increases the amplitude of the side-band components around the main frequency, according to the following:

$$f_{\text{sideband}} = \left(\frac{p \pm k}{p} \right) f_s \qquad (1)$$

where p is the number of pole pairs, f_s is the main frequency, and k is an integer. These side-bands components are equal to a mechanical frequency that, for a 14 pole synchronous generator with a frequency of 50 Hz, is equal to 7.1, 14.2, 21.3 Hz, etc. As shown in Fig. 6, the amplitude of all the side-bands does not increase significantly, especially for a low degree of fault severity. However, a regular pattern is evident, in which all frequency components around the fundamental frequency and its multiplier (i.e., 50, 100, and 150 Hz) undergo a significant increase when a fault occurs. The frequencies are 85.7, 92.9107.2, and 114.3 Hz. According to Fig. 6, the amplitudes of these frequencies are −41.5, 34.8, −37.2, and −45.1 dB, respectively. The occurrence of one ITSC fault in one of the rotor field windings, which is equal to 2.86% of one rotor pole winding and 0.2% of the whole rotor field winding, increases the magnitudes of these frequencies to −39.4, −33.1, −35.1,

TABLE III
VARIATION OF EXTRACTED SIDE-BANDS COMPONENTS IN HZ TO NUMBER OF
ITSC IN NO-LOAD IN DECIBEL

[Hz]	Healthy	1 ITSC	2 ITSC	3 ITSC	7 ITSC	10 ITSC
7.1	-44.9	-43.6	-41.9	-40.3	-34.8	-32.4
14.3	-45.4	-43.9	-41.8	-39.7	-33.1	-30.1
85.7	-41.5	-39.4	-36.8	-34.5	-27.9	-25.0
92.9	-34.8	-33.1	-31.2	-29.9	-22.9	-19.9
107.2	-37.2	-35.1	-33.2	-31.4	-25.0	-22.1
114.3	-45.1	-42.8	-39.9	-37.5	-31.0	-28.1

TABLE IV
VARIATION OF EXTRACTED SIDE-BANDS COMPONENTS IN HZ TO NUMBER OF
ITSC IN FULL LOAD IN DECIBEL

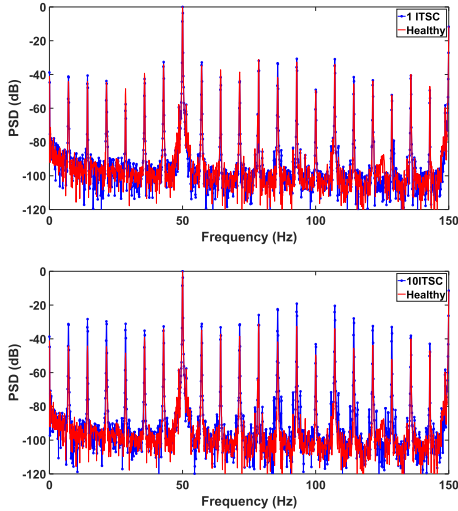| [Hz]	Healthy	1 ITSC	2 ITSC	3 ITSC	7 ITSC	10 ITSC
7.1	-44.3	-43.1	-41.2	-39.5	-32.5	-31.2
14.3	-44.2	-42.8	-40.6	-38.5	-31.5	-28.3
85.7	-41.7	-36.8	-33.4	-31.1	-24.7	-22.4
92.9	-32.6	-32.1	-30.7	-28.9	-23.2	-19.2
107.2	-33.9	-32.6	-30.9	-29.2	-24.4	-20.4
114.3	-45.5	-43.7	-41.5	-39.3	-32.1	-27.9

Fig. 7. Spectrum density of the induced EMF in the sensor in full-load for healthy and a 2 ITSC fault (top), and healthy and 10 ITSC fault (bottom): Experimental results.

and −42.8 dB, respectively. According to Fig. 6, the side-band amplitudes with 10 ITSCs at frequencies of 85.7, 92.9107.2, and 114.3 Hz increases from −41.7, −32.6, −33.9, and −45.5 dB to −22.4, −19.2, −20.4, and −27.9 dB, respectively. Therefore, a comparison between the healthy and faulty cases shows considerable changes occurring in the amplitude of the proposed index. The variation in the extracted feature for the severity of the ITSC fault in the no-load condition are shown in Table III.

Fig. 7 demonstrates the frequency spectrum of the stray flux of the healthy and faulty synchronous generator at full load. As seen with the no-load condition, the harmonic components of the frequency spectrum in full load indicates the same degree of sensitivity to the occurrence and progression of the fault. For instance the proposed side-bands for one ITSC at frequencies of 85.7, 92.9107.2, and 114.3 Hz increase from −41.7, −32.6, −33.9, and −45.5 dB to −36.8, −32.1, −32.6, and −43.7 dB, respectively. A significant increment also occurs in the amplitude of these frequencies to −22.4, −19.2, −20.4, and −27.9 dB, respectively, when the severity of the fault is increased to 10 ITSC. This response shows that the load cannot fluctuate or mask the proposed side-bands. The variation in the extracted feature for the severity of the ITSC fault in the no-load condition are shown in Table IV.

V. TIME-FREQUENCY ANALYSIS

The STFT was introduced to compensate for the lack of temporal resolution for FFT. STFT performs FFT on a smaller portion of the signal and collects its frequency information using a windowing function. The windowing function then swipes across the entire signal to obtain information regarding the magnitude of the signal in that specific time and frequency [24], [31]. The obtained information is plotted in a time-frequency plane. STFT compared with other time-frequency domain signal processing tools such as wavelet transform, or Hilbert Huang transforms has a low computational complexity which provides an online implementation for fault detection. Moreover, achieving an informative pattern for fault detection purpose using STFT requires few parameter adjustments while a mother wavelet selection in the wavelet transform or avoiding mode mixing in Hilbert Huang transforms require time and an expert in the field. The mathematical representation of the STFT is as follows:

$$STFT(f,t) = \frac{1}{2\pi} \int_{-\infty}^{\infty} x(t)h(t-\tau)e^{-i2\pi f\tau}d\tau \quad (2)$$

where $x(t)$, f, and t represent the signal, frequency, and time, respectively. The shape of the windowing function $h(t)$ and the length of the analyzed portion must be adjusted according to the signal characteristics and the desired optimal result. The frequency resolution of the STFT increases with increasing window length, while the time resolution is inversely proportional to the length of the time window. Based on the uncertainty principle, a high resolution in both time and frequency cannot be obtained [31]. The results obtained with SFTF are depicted in a spectrogram: an image with frequency along its vertical axis, time along its horizontal axis, and spectral intensity indicated by color.

The resolution in the spectrogram is uniform across the entire time and frequencies, indicating that it is a rectangular time-frequency resolution. Uniform frequency resolution is constructive if the frequencies of interest are markedly separated at the high frequencies and barely separated at the low frequencies. This constraint is formulated based on the uncertainty principle, as follows:

$$\Delta f \Delta t \geq \frac{1}{4\pi} \quad (3)$$

The end effect is mitigated by using a proper window function. A suite of windowing functions, such as Slepian, Gaussian, Blackman, Hamming, Dirichlet, Blackman-Harris, Bartlett-Hann, Hann, Bartlett, and Bohman, exist for this purpose.
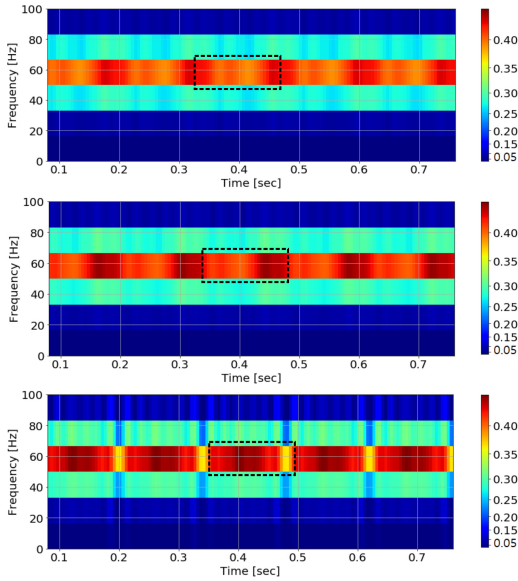
Fig. 8. Spectrogram of the induced EMF in the search coil for healthy, 1 ITSC, and a 10 ITSC fault in no-load operation of the SPSG: Experimental results.
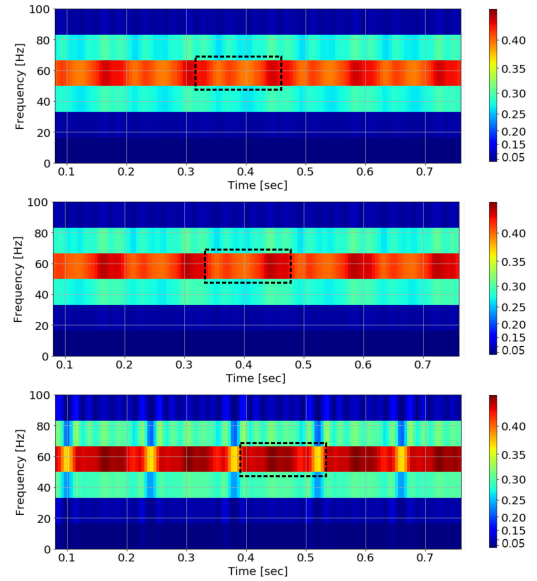

Fig. 9. Spectrogram of the induced EMF in the search coil for healthy, 1 ITSC, and a 10 ITSC fault in full load operation of the SPSG: Experimental results.

The EMF during steady-state operation of the SPSG in a no-load and under the full-load condition for different degrees of fault is stored for analysis by STFT, which is used to track the fault evolution. Since the machine has 14 poles, each mechanical revolution takes 140 ms, indicating that each pole requires 140 ms to pass through the installed search coil on the back side of the stator yoke. In a healthy condition, only fundamental harmonics, in addition to the stator and rotor slot harmonics and subharmonics due to the stator winding layout, must appear in the spectrogram. A faulty case is expected to have regular patterns due to a fault in the spectrogram.

Figs. 8 and 9 represent the STFT applied to the captured EMF signal, which is due to the radial stray magnetic field in a no-load and full-load operation of the SPSG. This method provides a clear time-frequency visualization of the EMF signal. Fig. 8 shows the spectrogram in a no-load operation in a healthy and under 1 ITSC and 10 ITSC faults. Since the ITSC fault components are embedded in the low frequencies, the window length, type of window, and window overlaps are set in a way that shows the focused low-frequency bands. Three bands (two cyan and one red) cover the three frequency bands between 35 and 50 Hz, between 50 and 65 Hz, and between 65 and 85 Hz.

The dashed window in the STFT map shows one mechanical revolution of the SPSG. One mechanical revolution starts from a red color with low intensity and extends to a slightly higher intensity by the end of the dashed window. Contrary to the obtained result by the FFT spectrum during one ITSC fault, a clear pattern exists in the spectrogram of one ITSC obtained by STFT. The color of the dashed window for one mechanical revolution is significantly changed by introducing 1 ITSC. The reason is that an ITSC fault induces subharmonics with a frequency introduced in (1), since the fault frequency

of interest lies in the low-frequency range and the STFT has a remarkable potential in the low-frequency content demonstration. Increasing the severity of the fault to 10 ITSC, as shown in Fig. 8, significantly changes the time-frequency pattern and the yellow color appears in the frequency band between 50 and 65 Hz. A fault pattern due to a severe ITSC fault also appears in the frequency bands between 35 and 50 Hz and between 65 and 85 Hz. The width of the new pattern in all three frequency bands is 10 ms, which indicates one faulty rotor pole winding. Fig. 9 represents an STFT plot of an SPSG operated in full-load condition. The same pattern seen in the no-load operation is obtained during full-load operation, indicating that loading does not have an impact on the ITSC fault pattern.

The applied STFT to the obtained EMF from the sensor installed on the back side of the stator core in the FEM is shown in Fig. 10 for a no-load operation of the SPSG. The spectrogram of the EMF in Fig. 10 compared with Fig. 8 indicates that the FEM has a high accuracy for faulty machine modeling since the spectrogram plots are approximately the same. However, the intensity of the frequency band between 50 and 65 Hz in the experimental spectrogram is slightly different which is due to the inherent dynamic eccentricity fault in the 100 kVA SPSG in the laboratory set-up. By having one ITSC fault, the intensity of the frequency band for a faulty pole is decreased, and increasing the fault severity result in a significant reduction of the intensity in a frequency band between 50 and 65 Hz.

Although STFT shows a clear pattern in a case of an ITSC fault and it can detect one ITSC fault, a method is required to quantify the severity of the fault. Image processing software is used to analyze the STFT spectrogram. A colorful image is changed into an 8-b grayscale image to process the image. Only a frequency band between 50 and 70 Hz is considered for image processing,
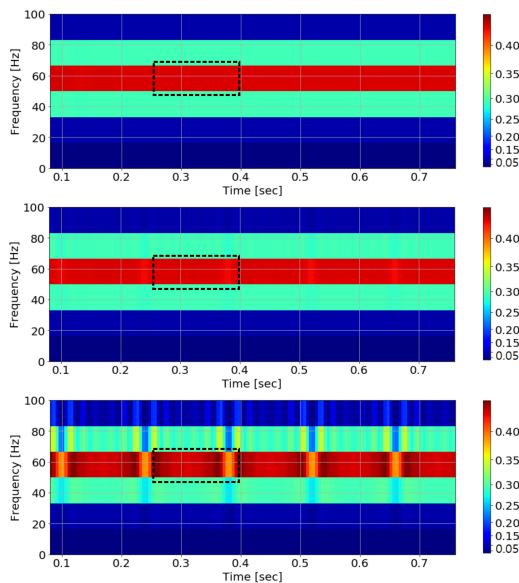
Fig. 10. Spectrogram of the induced EMF in the search coil for healthy, 1 ITSC, and a 10 ITSC fault in no-load operation of the SPSG: Simulation results.

Fig. 12. Amplitude variation of the side-band component versus load variation and various numbers of ITSC faults: Experimental results.

intensity of the targeted frequency band for 1 ITSC fault varies between 26% and 48%. The intensity of the frequency band for 1 ITSC fault, when compared to a healthy case, increases by 8%, which is a significant change for detecting a fault in its early stage. The intensity for 2 and 3 ITSC faults, in comparison to healthy case, is increased by 11% and 17%, respectively. The intensity pattern for 7 and 10 ITSC faults differs from that of a low severity fault since there is a dip in the plot. The intensity under 7 and 10 ITSC faults, in comparison to a healthy case, is increased by 29% and 33%, respectively. The same pattern is observed in a case of a partially loaded operation, which proves that the loading conditions do not change the fault signature.

VI. LOAD EFFECTS ON THE PROPOSED FEATURE

Investigation of the influence of the load on any proposed fault requires indices. Accurate fault detection depends on the relationship between the suggested feature, load variation, and fault severity. In [32], the amplitude of the harmonic side-bands in induction motors, in the presence of eccentricity fault, was shown to increase under the load condition. The amplitude of the harmonic components of the faulty induction motor with a broken rotor bar fault also decreases with increasing load levels [33]. Consequently, any comparisons of healthy and faulty machines must be scrutinized using the same loads.

Fig. 12 depicts the variation of the proposed features for different levels of ITSC severity versus the load variation. According to Fig. 12, the amplitude of these criteria increases with an increasing number of shorted turns in the rotor field winding, and this increase is reasonably constant from the no-load to the full-load condition. In other words, use of the proposed method based on utilizing the stray flux is robust against the load variation. Therefore, a short circuit fault detection based on the proposed feature does not need to specify the generator load.

The same behavior seen with FFT is expected for STFT analysis, since the harmonic contents are the same. The application of STFT to an EMF signal from the no-load to full-load operation demonstrates that the intensity of the frequency band between 50 and 70 Hz does not change with a changing load percentage, while its intensity increases by increasing the fault severity.

VII. FAULT TYPE DETECTION

No method exists for determining which type of fault happened in the machine, since FFT only exhibits the frequency
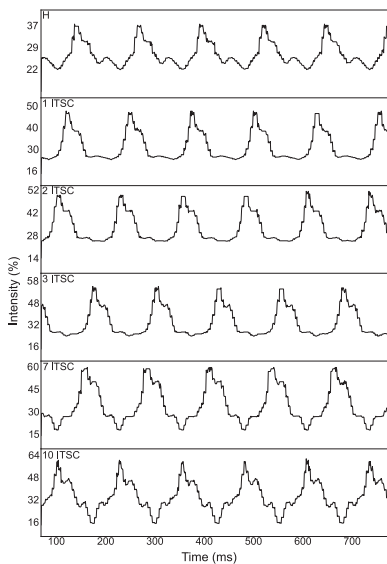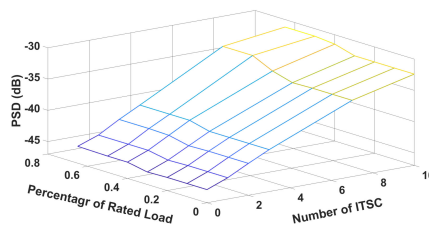

Fig. 11. Intensity of the spectrogram in healthy and 1, 2, 3, 7, and 10 ITSC faults for frequency band between 50 and 70 Hz: Experimental results.

and a pixel line along the time axis is chosen, since the intensity of the color map along the frequency axis is constant. Fig. 11 shows the processed images of healthy and faulty SPSGs. The first row represents the healthy SPSG, and the intensity of the band varies between 23% and 37%. The intensity pattern of the entire images is similar for either healthy SPSGs or those with 1, 2, 3, 7, and 10 ITSC faults, especially for 1, 2, and 3 ITSCs. The
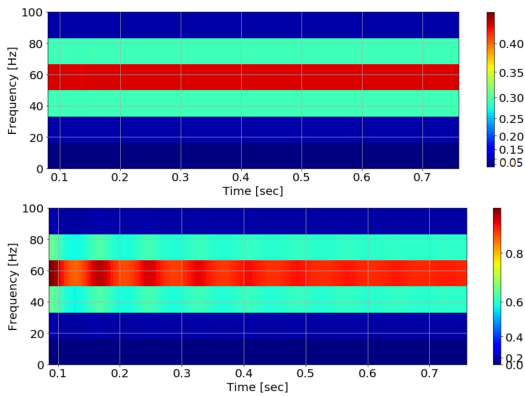
Fig. 13.   Spectrogram of the induced EMF in a search coil installed on the back side of a stator yoke for a healthy (top), and under 20% static eccentricity: Simulation results.
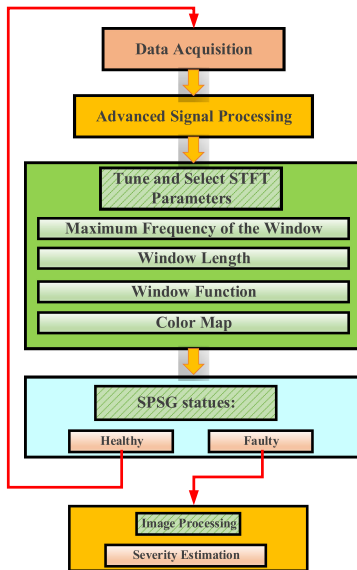

Fig. 14.   Flowchart of the proposed method for ITSC fault detection of SPSG.

contents of the signal. Conversely, the STFT representation of the EMF signal under an eccentricity fault is totally different from that under an ITSC fault, since the magnetic field does not pulsate in a case of a static eccentricity fault like it does for an ITSC fault, indicating that only the intensity of the frequency bands change while the pattern is the same as healthy case. The intensity of the frequency band for the measured EMF on each side of the SPSG that is prone to static eccentricity fault is different. The intensity of the frequency band where the rotor is close to the stator is higher while the intensity of the frequency band for a point with a larger air-gap is decreased. Fig. 13 shows the STFT representation of the EMF signal in a healthy and under 20% static eccentricity fault.

VIII. CONCLUSION

The stray magnetic field is used to detect an ITSC fault in the rotor field winding of the SPSG. Finite element modeling is used to simulate a 100 kVA SPSG under a short-circuit fault. The location, distance, and the number of turns are the main criteria for capturing the induced EMF in the installed search coil on the back side of the stator yoke. The severity of the fault and its impacts on the stray magnetic field has been studied and the induced EMF is shown to have a high degree of sensitivity to the fault severity and could even detect a one-turn short circuit fault.

The traditional signal processing tool is used to analyze the harmonic components of the signal. The side-band harmonics near the main frequency and its multipliers also increase significantly for severe ITSC faults while its sensitivity to detect early-stage faults is low. STFT has a superior ability for determining the low-frequency components, which results in a precise determination of the ITSC fault in its early stage, even with only one ITSF fault. It also shows a different pattern in the case of an ITSC fault since a severe fault changes the intensity of the STFT map. An image processing tool is used to quantify the severity of the fault. The load effect on the extracted feature is also studied, and the load variation is also confirmed to have no effect on the signature in the FFT spectrum and the STFT spectrogram since the low-frequency subharmonics are the same. The procedure of the proposed method in this article is shown in Fig. 14. The superiority of the method over the previously proposed methods are the following.

1) The method is based on stray magnetic field analysis that enables measurement even during the operation of the SPSG.
2) The method is noninvasive, and it is possible to install the sensor and measure the stray magnetic field even during the SPSG operation.
3) Image processing of the STFT spectrogram provides a quantitative tool to measure the intensity of the fault.
4) The method can detect one ITSC fault that shows the high sensitivity of the method.
5) Fault type recognition is an advantage of the method since static eccentricity does not modify the pattern in the spectrogram while occurring a ITSC make a new pattern compared with a healthy case.
6) The proposed method is independent of the SPSG typologies since it only requires the number of poles to determine the widths of the window for one mechanical revolution in the STFT plot. Indicating that the power rating, and specification of the machine cannot change the result of the method.

REFERENCES

[1] I. Sadeghi, H. Ehya, J. Faiz, and A. A. S. Akmal, "Online condition monitoring of large synchronous generator under short circuit fault-a review," in *Proc. IEEE Int. Conf. Ind. Technol.*, 2018, pp. 1843–1848.
[2] S. E. Dallas, A. N. Safacas, and J. C. Kappatou, "Interturn stator faults analysis of a 200-MVA hydrogenerator during transient operation using FEM," *IEEE Trans. Energy Convers.*, vol. 26, no. 4, pp. 1151–1160, Dec 2011.

[3] G. C. Stone, M. Sasic, J. Stein, and C. Stinson, "Using magnetic flux monitoring to detect synchronous machine rotor winding shorts," in *Proc. Rec. Conf. Papers Ind. Appl. Soc. 58th Annu. IEEE Petroleum Chem. Ind. Conf.*, Sep. 2011, pp. 1–7.

[4] Y. Park, S. B. Lee, J. Yun, M. Sasic, and G. C. Stone, "Air gap flux-based detection and classification of damper bar and field winding faults in salient pole synchronous motors," *IEEE Trans. Ind. Appl.*, vol. 56, no. 4, pp. 3506–3515, Jul./Aug. 2020.

[5] P. Neti, A. B. Dehkordi, and A. M. Gole, "A new robust method to detect rotor faults in salient-pole synchronous machines using structural asymmetries," in *Proc. IEEE Ind. Appl. Soc. Annu. Meeting*, Oct. 2008, pp. 1–8.

[6] M. Valavi, K. G. Jørstad, and A. Nysveen, "Electromagnetic analysis and electrical signature-based detection of rotor inter-turn faults in salient-pole synchronous machine," *IEEE Trans. Magn.*, vol. 54, no. 9, pp. 1–9, Sep. 2018.

[7] M. Cuevas, R. Romary, J. Lecointe, and T. Jacq, "Non-invasive detection of rotor short-circuit fault in synchronous machines by analysis of stray magnetic field and frame vibrations," *IEEE Trans. Magn.*, vol. 52, no. 7, pp. 1–4, Jul. 2016.

[8] M. Faizan Shaikh, J. Park, and S. B. Lee, "A non-intrusive leakage flux based method for detecting rotor faults in the starting transient of salient pole synchronous motors," in *IEEE Trans. Energy Convers.*, to be published, doi: 10.1109/TEC.2020.3021207.

[9] M. Cuevas, R. Romary, J. Lecointe, F. Morganti, and T. Jacq, "Noninvasive detection of winding short-circuit faults in salient pole synchronous machine with squirrel-cage damper," *IEEE Trans. Ind. Appl.*, vol. 54, no. 6, pp. 5988–5997, Aug. 2018.

[10] J. M. Corres, J. Bravo, F. J. Arregui, and I. R. Matias, "Unbalance and harmonics detection in induction motors using an optical fiber sensor," *IEEE Sensors J.*, vol. 6, no. 3, pp. 605–612, Jun. 2006.

[11] J. G. Mueller and T. G. Pratt, "A radio frequency polarimetric sensor for rotating machine analysis," *IEEE Sensors J.*, vol. 13, no. 12, pp. 4866–4873, Dec. 2013.

[12] R. J. Povinelli, J. F. Bangura, N. A. O. Demerdash, and R. H. Brown, "Diagnostics of bar and end-ring connector breakage faults in polyphase induction motors through a novel dual track of time-series data mining and time-stepping coupled fe-state space modeling," *IEEE Trans. Energy Convers.*, vol. 17, no. 1, pp. 39–46, Aug. 2002.

[13] H. Ehya, A. Nysveen, R. Nilssen, and U. Lundin, "Time domain signature analysis of synchronous generator under broken damper bar fault," in *Proc. 45th Annual Conf. IEEE Ind. Electron. Soc.*, 2019, pp. 1423–1428.

[14] I. Sadeghi, H. Ehya, and J. Faiz, "Analytic method for eccentricity fault diagnosis in salient-pole synchronous generators," in *Proc. Int. Conf. Optim. Elect. Electron. Equip. Int. Aegean Conf. Elect. Mach. Power Electron.*, May 2017, pp. 261–267.

[15] H. Ehya, A. Nysveen, I. L. Groth, and B. A. Mork, "Detailed magnetic field monitoring of short circuit defects of excitation winding in hydro-generator," in *Proc. 24th Int. Conf. Elect. Mach.*, 2020, pp. 1–6.

[16] J. Pons-Llinares, J. A. Antonino-Daviu, M. Riera-Guasp, M. Pineda-Sanchez, and V. Climente-Alarcon, "Induction motor diagnosis based on a transient current analytic wavelet transform via frequency B-splines," *IEEE Trans. Ind. Electron.*, vol. 58, no. 5, pp. 1530–1544, May 2011.

[17] G. Georgoulas et al., "The use of a multilabel classification framework for the detection of broken bars and mixed eccentricity faults based on the start-up transient," *IEEE Trans. Ind. Inform.*, vol. 13, no. 2, pp. 625–634, Apr. 2017.

[18] J. Pons-Llinares, J. A. Antonino-Daviu, M. Riera-Guasp, S. Bin Lee, T. Kang, and C. Yang, "Advanced induction motor rotor fault diagnosis via continuous and discrete time-frequency tools," *IEEE Trans. Ind. Electron.*, vol. 62, no. 3, pp. 1791–1802, Mar. 2015.

[19] J. A. Antonino-Daviu, J. Pons-Llinares, and S. B. Lee, "Advanced rotor fault diagnosis for medium-voltage induction motors via continuous transforms," *IEEE Trans. Ind. Appl.*, vol. 52, no. 5, pp. 4503–4509, Sep./Oct. 2016.

[20] I. Zamudio-Ramirez et al., "Automatic diagnosis of electromechanical faults in induction motors based on the transient analysis of the stray flux via music methods," *IEEE Trans. Ind. Appl.*, vol. 56, no. 4, pp. 3604–3613, Jul./Aug. 2020.

[21] P. A. Panagiotou, I. Arvanitakis, N. Lophitis, J. A. Antonino-Daviu, and K. N. Gyftakis, "On the broken rotor bar diagnosis using time-frequency analysis: 'is one spectral representation enough for the characterisation of monitored signals?," *IET Elect. Power Appl.*, vol. 13, no. 7, pp. 932–942, Feb. 2019.

[22] P. A. Panagiotou, I. Arvanitakis, N. Lophitis, J. A. Antonino-Daviu, and K. N. Gyftakis, "A new approach for broken rotor bar detection in induction motors using frequency extraction in stray flux signals," *IEEE Trans. Ind. Appl.*, vol. 55, no. 4, pp. 3501–3511, Mar. 2019.

[23] I. Zamudio-Ramirez, J. A. Antonino-Daviu, R. A. Osornio-Rios, R. deJ. Romero-Troncoso, and H. Razik, "Detection of winding asymmetries in wound-rotor induction motors via transient analysis of the external magnetic field," *IEEE Trans. Ind. Electron.*, vol. 67, no. 6, pp. 5050–5059, Jun. 2020.

[24] J. Yun et al., "Comprehensive monitoring of field winding short circuits for salient pole synchronous motors," *IEEE Trans. Energy Convers.*, vol. 34, no. 3, pp. 1686–1694, Sep. 2019.

[25] J. Yun et al., "Airgap search coil-based detection of damper bar failures in salient pole synchronous motors," *IEEE Trans. Ind. Appl.*, vol. 55, no. 4, pp. 3640–3648, Jul. 2019.

[26] J. Yun, S. B. Lee, M. Šašić, and G. C. Stone, "Reliable flux-based detection of field winding failures for salient pole synchronous generators," *IEEE Trans. Energy Convers.*, vol. 34, no. 3, pp. 1715–1718, Sep. 2019.

[27] H. Ehya, A. Nysveen, and R. Nilssen, "Pattern recognition of inter-turn short circuit fault in wound field synchronous generator via stray flux monitoring," in *Proc. Int. Conf. Elect. Mach.*, 2020, pp. 2631–2636.

[28] B. M. Ebrahimi, M. J. Roshtkhari, J. Faiz, and S. V. Khatami, "Advanced eccentricity fault recognition in permanent magnet synchronous motors using stator current signature analysis," *IEEE Trans. Ind. Electron.*, vol. 61, no. 4, pp. 2041–2052, Apr. 2014.

[29] A. Maxwell, *Release 2019 R3*. 7, ANSYS, Inc., ANSYSR©, "Academic Research Electronics Desktop," Release R2.4, 2020.

[30] A. Ceban, R. Pusca, and R. Romary, "Study of rotor faults in induction motors using external magnetic field analysis," *IEEE Trans. Ind. Electron.*, vol. 59, no. 5, pp. 2082–2093, May 2012.

[31] R. Priemer, *Introductory Signal Processing*. Singapore: World Scientific, 1991.

[32] J. Faiz, B. M. Ebrahimi, B. Akin, and H. A. Toliyat, "Comprehensive eccentricity fault diagnosis in induction motors using finite element method," *IEEE Trans. Magn.*, vol. 45, no. 3, pp. 1764–1767, Mar. 2009.

[33] A. M. Da Silva, R. J. Povinelli, and N. A. Demerdash, "Induction machine broken bar and stator short-circuit fault diagnostics based on three-phase stator current envelopes," *IEEE Trans. Ind. Electron.*, vol. 55, no. 3, pp. 1310–1318, Mar. 2008.

Hossein Ehya (Student Member, IEEE) received the M.Sc. degree in electrical engineering from the Department of Electrical and Computer Engineering, University of Tehran, Tehran, Iran, in 2013. He is currently working toward the Ph.D. degree in electrical engineering with the Norwegian University of Science and Technology (NTNU), Trondheim, Norway.

From 2013 to 2018, he worked as an Electrical Machine Design Engineer with electrical machine companies. His research interests include the design and condition monitoring of electrical machines, signal processing, pattern recognition, and machine learning.

In 2020, he was awarded with the ICEM Jorma Luomi Award in Gothenburg, Sweden.

Arne Nysveen (Senior Member, IEEE) received the Dr. Ing. degree (Ph.D.) in electric power engineering and the M.Sc. degree in electric power engineering from the Norwegian Institute of Technology (now NTNU), Trondheim, Norway, in 1994 and 1988, respectively.

From 1995 to 2002, he was a Senior Scientist with ABB Corporate Research, Oslo, Norway. Since 2002, he has been a Professor with the Norwegian University of Science and Technology (NTNU), Trondheim, Norway. He is currently a Manager for the research with Turbine and Generator Technologies, Norwegian Research Center for Hydropower Technology (HydroCen), Trondheim, Norway. His current research interests include design, modeling, and monitoring of hydroelectric generators.

Paper IV

Advanced Fault Detection of Synchronous Generators Using Stray Magnetic Field

Hossein Ehya [ID] , *Student Member, IEEE*, Arne Nysveen [ID] , *Senior Member, IEEE*, and Jose A. Antonino-Daviu [ID] , *Senior Member, IEEE*

Abstract—**Many methods used for precise fault detection in salient pole synchronous generators (SPSGs) often require *a priori* knowledge of the healthy case, but this requirement impedes application of the methods since an accurate analysis of different machine quantity waveforms is not usually carried out during commissioning. The inspection and maintenance processes in SPSGs are also costly and time consuming; therefore, reliable methods that can detect and discriminate between different faults without comparison with the healthy condition are highly desirable. This article proposes a precise method for detection and discrimination between different fault types in the SPSG. The method does not require healthy machine data and is applied to diagnose both interturn short circuits (ITSCs) in the field winding and dynamic eccentricities (DEs). The proposed nonintrusive detection algorithm is based on advanced signal analysis of stray magnetic field data and can be applied during SPSG operation. The method is highly precise for monitoring the condition of the rotor field winding and yields a unique pattern for diagnosing possible ITSC faults. Moreover, a distinctive pattern for the DE fault enables the discrimination between both considered failures, even if they are present at the same time. The proposed method is validated through finite-element modeling and experimentally on 100-kVA and 22-MVA SPSGs to demonstrate its applicability in real power plants.**

Index Terms—**Condition monitoring, continuous wavelet transforms (CWTs), fault detection, hydro power plant, interturn short circuit (ITSC), reliability, synchronous generator.**

I. INTRODUCTION

LARGE synchronous generators can be built with a salient pole concentrated excitation rotor or with a nonsalient pole distributed excitation rotor (cylindrical rotor) [1]. The former is typically used in low-speed generators or hydro generators,

while the latter is employed in high-speed turbo alternators. Cylindrical rotors in turbo alternators are usually based on solid iron rotors for better mechanical rigidity and heat transmission [1]. In lower speed synchronous generators, such as hydro generators, the rotor pole shoes are made by laminations to reduce rotor losses. In these low-speed machines, the rotor pole shoes incorporate slots that house copper bars that are short-circuited by end rings to form the damper cage.

The salient pole synchronous generators (SPSGs) in hydroelectric plants must operate in a sufficiently healthy condition due to the severe consequences of an eventual forced outage, not only for the plant itself, but also for the electric system. Therefore, these machines are usually subjected to maintenance protocols that are much more exhaustive than those used in industrial synchronous motors. In this regard, specific condition monitoring systems, such as vibroacoustic sensors, internal search probes, thermal probes (PT100), or partial discharge monitoring systems (e.g., stator slot couplers), are usually employed to guarantee accurate knowledge of the SPSG condition.

Despite the application of special maintenance protocols to synchronous machines, different types of failures have been reported in the literature for this type of machine. For example, broken damper bars have been reported both in salient pole synchronous machines and nonsalient pole synchronous machines [2]–[6]. The number of reported broken damper bar failures in the synchronous motor compared with the synchronous generator is higher; however, faults due to broken dampers may have serious implications concerning the starting of synchronous machines [7]. Other faults, such as eccentricities [8], [9], shaft current discharges [10], and field winding [11] and stator turn faults [12], have also been reported in hydro generators. The negative effects of most of these failures can eventually lead to forced synchronous generator outages; therefore, an intensive effort has been devoted to the development of intelligent techniques that are able to detect these faults when they are in their early stages of development [11]–[13].

In this context, the analysis of flux data has been a recurrent alternative for the diagnosis of most of these faults. The basic idea relies on evaluating the signatures that the anomaly leaves, either on the waveform of the air-gap flux or on its frequency content. In this regard, air-gap flux analysis has been proposed to detect field winding failures [14], [15], damper faults [5], [16], eccentricities [17], or even stator turn faults. In spite of its good results, the air-gap flux has some important constraints related to the intrusive nature of the necessary sensors or to the reduced

flexibility caused by the exclusive dependence on sensors that have already been installed during the manufacturing process. These sensors can be difficult to replace or modify in case of failure or when measurements in alternative locations are required.

Due to these constraints, an emerging trend in recent years is to rely on the analysis of stray flux data. Today, stray flux data can be acquired in a noninvasive way using the currently available sensors with advanced features [18]. Several studies have confirmed the validity of the technique for diagnosing faults in induction motors and even in permanent magnet machines [19]. In addition, new techniques based on the advanced analysis of stray flux data under transient conditions have been confirmed to provide important advantages when compared with the analysis of stationary flux signals [20]–[22].

Some recent work has suggested the analysis of stray flux data for the detection certain faults in SPSGs, such as field winding faults [23], [24], damper faults [24], [25], eccentricities [9], or even stator faults [27]. This work has verified the potential of this technique for reliable detection of these faults and for their discrimination from other faults or nonfault-related phenomena. Despite this, further research work is still required in this area to develop alternative methods that are effective in real SPSG operating in power plants.

In this context, this work proposes a precise stray flux-based method to diagnose interturn short circuit (ITSC) faults and parallel dynamic eccentricities (DEs) in an SPSG. The application of the proposed methods yields characteristic signatures that are specific to each type of failure, thereby enabling their respective detection and discrimination. The effectiveness of the method is proven both with simulated data and with laboratory and field test data obtained in 100-kVA and 22-MVA SPSGs operating in a hydropower plant. Application of the approach enabled the avoidance of an eventual catastrophic failure, thanks to the early detection of the faults. This article first presents the laboratory and field tests, in which the fault effects on the captured stray flux signals are observed. This is followed by the justification of these observations, both by simulations with finite-element models and by advanced time–frequency analyses of the experimental data.

II. LABORATORY AND FIELD TEST

A. Laboratory Setup

Numerous tests were performed in the laboratory on a 100-kVA SPSG. The objective was to obtain the corresponding stray flux signals and to observe their corresponding waveforms that could be indicative of certain faults. These waveforms are processed later, and the observed phenomena are properly described and justified via time–frequency analyses. A detailed description of the experimental setup, as shown in Fig. 1, is as follows.

1) A 100-kVA 400-V custom-made synchronous generator with 14 salient poles is used to investigate the ITSC fault in the rotor field winding.
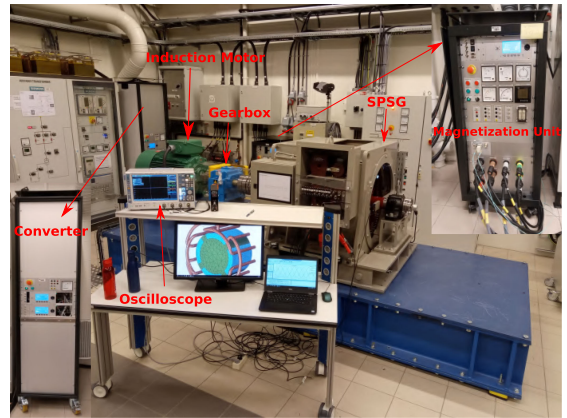2) A 100-kVA induction motor with four poles is used as a prime mover of the SPSG.

Fig. 1.　Experimental setup of a 100-kVA SPSG.

3) The SPSG and the induction motor are connected using a gearbox with a gear ratio of 4:1.
4) A 100-kVA converter is used to drive the induction motor and to provide the SPSG with the required active power at constant speed.
5) A static rotor magnetization unit is used to control the current in the rotor field winding. Controlling the power field excitation is possible both in a local mode, while the generator is connected to the passive loads or when it is integrated into the power grid.
6) A stray magnetic field is recorded by a homemade sensor that consists of an air-core coil with 3000 turns of thin copper wire (0.12 mm^2). The sensor can be attached both on the stator backside to pick up the radial stray flux and in front of the stator end winding to pick up the axial stray flux. The sensor picks up both axial and radial stray flux if it is tangentially attached to the stator backside, as shown in Fig. 2. The size of the sensor is optimized to cover an adequate area of the stator backside ($100 \times 100 \times 10$ mm).
7) A high-resolution 16-bit oscilloscope (Rohde Schwarz RTO2000) is used to sample the stray magnetic field using a sampling frequency of 10 kHz.
8) The ITSC fault on one of the rotor pole windings is created by removing the desired number of turns. Removal of one, two, three, seven, or ten turns from one of the rotor poles is possible using a copper plate, as shown in Fig. 2.

B. Laboratory Measurement

The procedure for experimental measurement is as follows: a copper plate is mounted between the common point of the rotor pole winding and the desired tap of the rotor pole winding to remove the specific turns in the standstill. The SPSG is then accelerated until it reaches the synchronous speed. The dc current is then applied to the field winding based on the loading condition.

Fig. 2. Location of the shorted turns tap on the rotor (top) and the location of the stray magnetic field sensor installed on the stator backside of an SPSG.
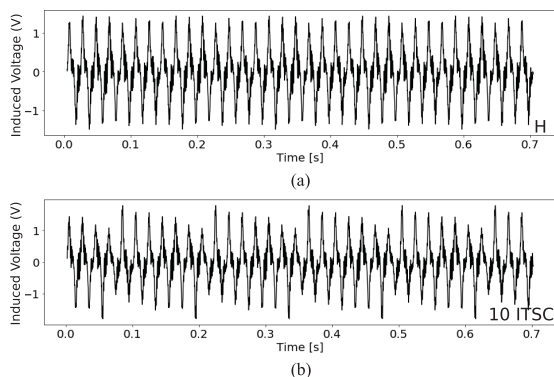

Fig. 3. Induced voltage due to a stray magnetic field in the sensor attached on the stator backside of a 100-kVA SPSG during no-load operation (a) in a healthy case and (b) under a 10-ITSC fault—Laboratory measurements.

Fig. 3 shows the waveforms of the induced voltage in the sensor attached on the stator backside of the 100-kVA SPSG for the healthy and the ITSC fault condition. A clear variation exists in the amplitude of the induced voltage under a 10-ITSC fault compared with the healthy case. Each mechanical revolution consists of seven periods that are in concordance with the number of pole pairs in the laboratory machine. The pattern arises because the ITSC fault in the rotor field winding is periodic as long as the rotor passes over the installed sensor on the stator backside. The reduction in the amplitude of the induced voltage under the ITSC fault is due to the reduced number of turns in the faulty rotor field winding that contribute to the magnetomotive force in the air gap.
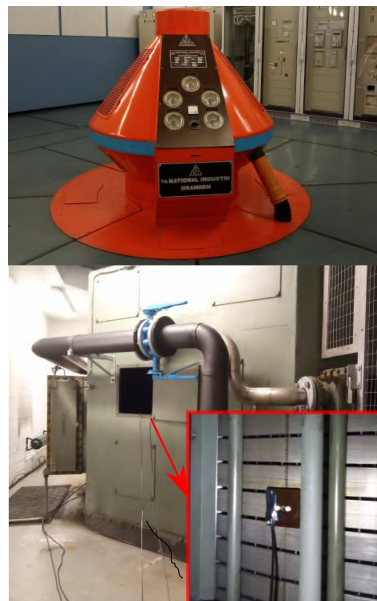

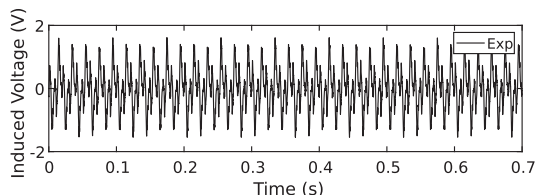Fig. 4. Single unit hydropower plant with an operating 22-MVA SPSG.

Fig. 5. Induced voltage in the installed sensor on the stator backside of a 22-MVA SPSG during no-load operation—Field test measurement.

C. Field Test Measurement

Fig. 4 shows a 22-MVA synchronous generator with eight salient poles operating in a Norwegian hydropower plant. Several inspections had revealed a clear elevation in the measured amplitude of the vibration according to the power plant report. Therefore, measurement of the stray magnetic field was proposed to determine the origin of this symptom. The SPSG was completely covered by an iron housing, but several hatches enabled access to the stator yoke backside. Fig. 4 shows the installed sensor on the stator yoke through one of the hatches. At least four sensors are required to detect a static eccentricity fault in a vertically mounted SPSG, while one sensor is adequate for ITSC fault and DE fault diagnosis. However, since the type of fault in the SPSG is unknown, four sensors were installed at a distance of 90 mechanical degrees.

Fig. 5 shows the induced voltage in one of the installed sensors on the stator backside of a 22-MVA SPSG. A clear sign of amplitude variation is evident in the induced voltage. The amplitude reduction of the induced voltage shows an obvious pattern that is

similar to the pattern in the100-kVA SPSG, whereas a significant difference is detected in the lower envelope of the signal, since the envelope of the signal does not follow the pattern expected for an ITSC fault. The lower envelope of the induced voltage, in this case, is similar to a sine wave. This indicates that, in addition to the ITSC fault, another source is generating the fault in the 22-MVA SPSG. The amplitudes of the signals captured by the four sensors installed with a mechanical distance of 90° are checked to inspect the possibility of a static eccentricity fault. The amplitude of one pair of sensors installed in front of each other must differ in a way that ensures that the amplitude of the induced voltage in one of the sensors is high and that of the other sensor is low for a static eccentricity fault to occur [9]. However, the amplitudes of the induced voltages in this pair of sensors are similar, which indicates the absence of a static eccentricity fault in the 22-MVA SPSG.

III. ELECTROMAGNETIC ANALYSIS

The aim of this section is to evaluate the impact of different faults on the stray magnetic field distribution of the SPSG. Two SPSGs with power ratings of 100 kVA and 22 MVA are modeled by considering two types of faults: ITSC and DE. The pattern of the voltage signal induced in the sensor by the stray magnetic field is analyzed to determine the impact of both failures under consideration. The occurrence of both ITSC and DE faults results in the magnetic field variation in the air gap. The magnetomotive force of the faulty rotor pole compared with the healthy poles decreased due to the reduced number of turns. The reduced magnetomotive force affects the symmetry of the air-gap magnetic field and consequently its amplitude. The DE fault also disturbs the air-gap magnetic field symmetry distribution in the air gap. Therefore, in the case of both faults, the reluctance of the path between the air gap and the search coil starts to change. The reluctance variation results in the leakage flux variation and consequently the induced voltage variation in the sensor due to the faults.

Both the detailed specification of the SPSG geometry and the nonlinearity of the material are considered in finite-element modeling (FEM), since both have a marked impact on the stray flux distribution. The eddy effect in damper bars is also considered since a synchronous machine with a fractional winding layout has a circulating current in the damper bars even during steady-state operation [4]. A 2-D FEM model of the SPSGs is adequate since the rotor or damper bars are not skewed. The complete geometry is required for FEM, since both machines have a fractional slot winding layout; therefore, both ITSC and DE result in an asymmetric distribution of the magnetic field. The simulation is performed using the ANSYS ELECTRONICS software package [28].

A. FEM Study of a 100-kVA SPSG

A 100-kVA, 400-V, star-connected SPSG with 14 poles (each pole including seven damper bars) and with 114 stator slots is modeled in FEM, as shown in Fig. 6. The detailed specifications of the 100-kVA SPSG are shown in Table I. The rotor field winding of each pole has 35 turns. The analysis is performed
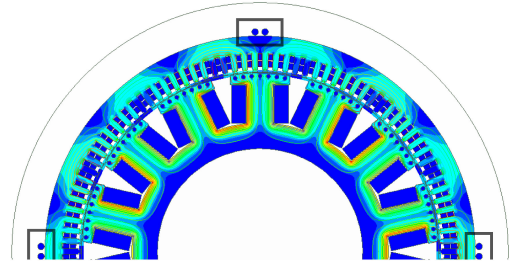

Fig. 6.   Finite-element model of a 100-kVA SPSG and the location of the stray magnetic field sensor installed on the backside of the stator yoke.

TABLE I
100-kVA, 50-Hz, SYNCHRONOUS GENERATOR TOPOLOGY
SPECIFICATION AND NAMEPLATE DATA

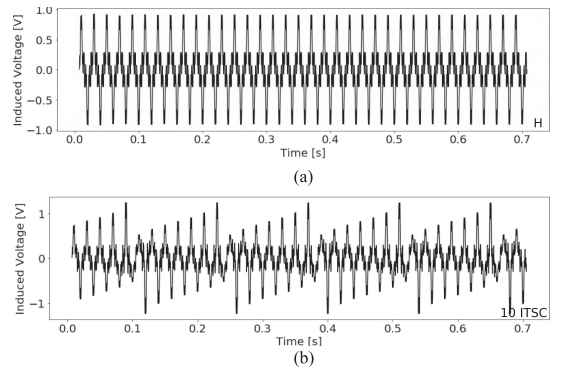| *Quantity*	*Values*	*Quantity*	*Values*
Stator outer diameter	780 mm	Number of poles	14
Stator inner diameter	649 mm	Nominal exc. current	103 A
Length of stack	208 mm	Power factor	0.90
No. of damper bars/pole	7	Terminal current	144.3 A
No. of rotor turns / pole	35	Terminal voltage	400 V
No. of stator turns	8	No. of slots	114
Nominal speed	428 rpm	Winding connection	Wye

Fig. 7.   Induced voltage in the sensor installed on the stator backside of a 100-kVA SPSG operating in a no-load condition (a) in a healthy case and (b) under a 10-ITSC fault—Simulation results.

for five different severities of an ITSC fault in the rotor field winding: ten shorted turns (28.57%), seven shorted turns (20%), three shorted turns (8.5%), two shorted turns (5.7%), and one shorted turn (2.85%). The corresponding number of turns in each rotor pole is eliminated in order to model the ITSC fault with FEM. Therefore, the effective magnetomotive force decreases, which results in a nonuniform air gap magnetic field.

Fig. 7 shows the calculated induced voltage in the sensor installed on the stator backside of the simulated SPSG in the FEM for both a healthy case and for a 10-ITSC fault. A symmetrical pattern is evident in the healthy operation of the machine, whereas the pattern is distorted by the 10-ITSC fault (see the bottom row of Fig. 7). The amplitude of the induced voltage is decreased when the faulty rotor pole passes over the sensor
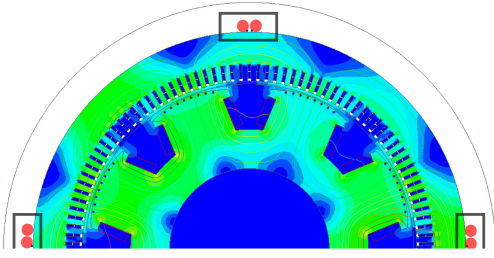
Fig. 8. Finite-element model of the 22-MVA SPSG and the location of the installed stray magnetic field sensor.

TABLE II
22-MVA, 50-Hz, SYNCHRONOUS GENERATOR TOPOLOGY SPECIFICATION AND NAMEPLATE DATA

Quantity	Values	Quantity	Values
Stator outer diameter	2640 mm	Number of poles	8
Stator inner diameter	2040 mm	Nominal exc. current	440 A
Length of stack	1220 mm	Power factor	0.90
No. of damper bars/pole	8	Terminal current	1650 A
No. of rotor turns / pole	58	Terminal voltage	7700 V
No. of stator turns	1	No. of slots	126
Nominal speed	750 rpm	Winding connection	Wye

installed on the stator backside. A comparison between the experimental measurements, shown in Fig. 3, and the simulation results, depicted in Fig. 7, proves that the ITSC fault causes a reduction in the effective magnetomotive force and, consequently, a decrease in the stray magnetic field in the vicinity of the stator yoke. The shape, periodicity, and pattern are the same for both the experimental results and the FEM results; however, the direction of the peak amplitude reduction differs due to the polarity of the installed sensor.

B. FEM Study a 22-MVA SPSG

The FEM model of the 22-MVA SPSG is illustrated in Fig. 8. Table II shows the detailed specifications of the machine. The generator has eight poles, and each pole contains eight damper bars. The required magnetomotive force to generate 7.7 kV on the stator terminals is provided by 53 turns in each rotor field winding. The stator windings are connected in series, and unlike a generator with a parallel winding layout, they do not yield a circulating current to compensate for the asymmetric magnetic field caused by a short circuit fault or eccentricity fault. Two pairs of sensors are installed exactly in front of each other, and the amplitude of the induced voltage in all the sensors was the same, indicating that the SPSG does not have a static eccentricity fault. Consequently, only the DE and ITSC faults are simulated in FEM.

A comparison between the simulation result and the measurement in the power plant shows the accuracy of the FEM model; only a small difference is apparent in the shape of the signal, and this difference is due to ignoring the 3-D effect and the radial air duct effect, as well as the SPSG housing. The impact of a 20% DE fault on the induced voltage in the sensor is shown Fig. 9. A periodic fluctuation occurs in both the upper and lower
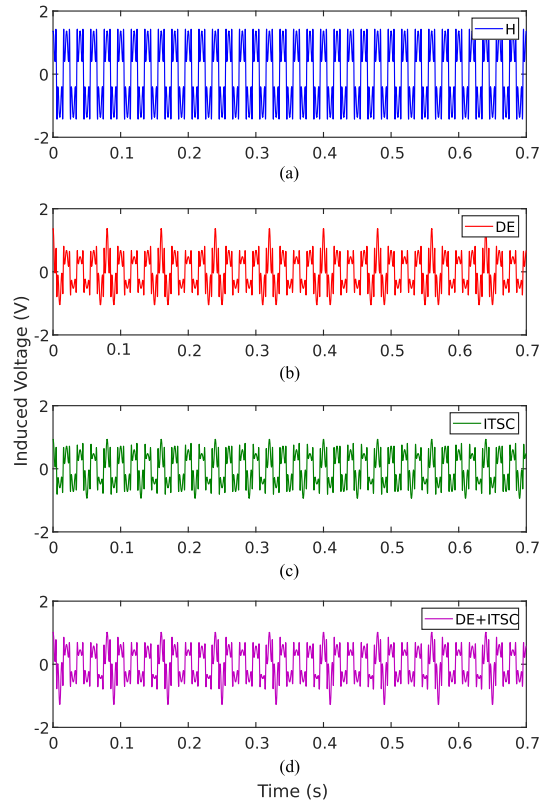

Fig. 9. Measured induced voltage in a sensor installed on the stator backside of a 22-MVA SPSG operating in a no-load condition (a) in a healthy case, (b) under a 20% DE fault, (c) under a 10-ITSC fault, and (d) under a combination of both DE and ITSC faults—Simulation results.

envelopes of the signal due to the DE fault. Conversely, the effect of the ITSC fault on the induced voltage of the sensor also results in a reduction in the peak amplitude, as indicated in green in the plot shown in Fig. 9. However, a comparison between the measured voltage in Fig. 5 and the FEM results under only an ITSC or DE fault indicates that both ITSC and DE faults exist simultaneously in the 22-MVA SPSG. The last plot of Fig. 9 shows the simultaneous occurrence of a 10-ITSC and a 20% DE fault. The obtained pattern for this mixed fault is a combination of the fault-related patterns of both the ITSC and DE faults, since the upper envelope is similar to the upper envelope of the ITSC fault and the lower envelope is similar to the DE fault.

IV. ADVANCED SIGNAL PROCESSING

Digital signal processing is a broad field that encompasses numerous mature techniques for treating a signal and extracting useful information based on the required needs. Several signal processing tools are available, and these can be classified,
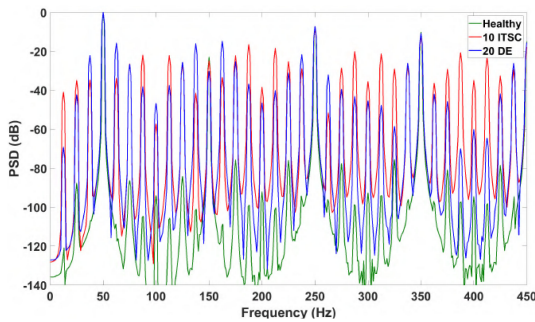
Fig. 10. Frequency spectrum of the sensor-induced voltage in a 22-MVA SPSG operating at no-load condition in a healthy case and under 10-ITSC and 20% DE faults—Simulation results.

Fig. 11. Time–frequency representation of the induced voltage in the a sensor installed in a 100-kVA SPSG operating in a no-load condition (a) in a healthy case and (b) under a 10-ITSC fault—Simulation results.

according to their application in fault detection of electrical machines, into three categories, including time-domain, frequency-domain, and time–frequency-domain tools. The application is based on the signal properties and the required format for data interpretation. Application of fast Fourier transforms to the induced sensor voltage in a healthy case and under ITSC and DE fault is presented in Fig. 10. Although the faulty frequency spectrum demonstrates the significant increase in the amplitude of both subharmonics and interharmonics, both faults intrigue the same fault harmonic components, indicating that fault type detection using frequency spectrum is impossible. This article proposes a time–frequency representation of the voltage induced in the sensors installed on the stator backside and uses the continuous wavelet transform (CWT) as a time–frequency tool. The Gaussian mother wavelet is selected based on the signal characteristics. The frequency band is assigned to 100 Hz, and the window length must be selected to have at least two mechanical revolutions in order to exhibit the periodicity of the fault signature.

CWT is a powerful tool for analyzing localized variations of power spectral density within a time data series. Wavelet transforms decompose the time data series into a time–frequency map that enables determination of both the dominant modes of variability and how the modes vary in time. Implementation of the CWT, compared with other tools like the discrete wavelet transform (DWT), is also straightforward since a mother wavelet is constructed simply by dilating and translating the signal. The frequency component of the signal is extracted using a convolution process, and the transform convolutes the signal with a wavelet instead of running the Fourier transform [29].

One of the main concerns of fault detection methods proposed in several published studies is their prerequisite for knowledge of the healthy condition of the SPSG. This requirement can be easily satisfied under laboratory conditions, where the fault is applied intentionally and the healthy data are accessible. However, this is not the case for machines in real power plants. Consequently, some methods proposed in the literature, although suitable in principle for SPSGs, are difficult to apply in the field. The method proposed in this article, based on CWT, extract
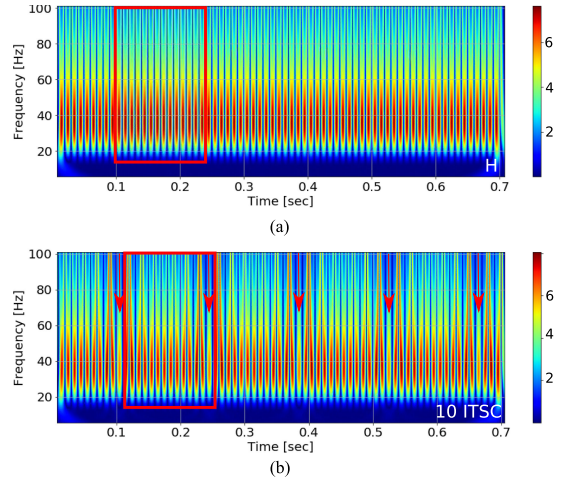
a clear pattern that reveals the SPSG health status without requiring any knowledge of the healthy operation data.

V. RESULTS AND DISCUSSIONS

Although the obtained time data series results have a clear pattern indicating the occurrence of the fault in both 100-kVA and 22-MVA SPSGs, an advanced signal processing tool, such as CWT, can be used to support the findings and identify the amplified frequency components. The following two sections include analyses of the voltage induced in the sensor in the healthy and faulty cases for simulations, laboratory experiments, and field tests.

A. Study Results of a 100-kVA SPSG

Fig. 11 shows the CWT results of the voltage induced in the sensor by a stray magnetic field for the healthy condition and for a 10-ITSC fault in the field winding, using simulated data obtained with FEM. The time–frequency analysis of the induced voltage yields numerous stalks, each corresponding to one rotor pole. The 100-kVA SPSG has 14 poles that yield 14 stalks for each mechanical revolution, as shown in Fig. 11. The frequency range of each stalk for a healthy case spans from 20 to 100 Hz. The presence of a 10-ITSC fault in one of the rotor field windings reduces the magnetomotive force produced by a faulty pole, thereby influencing the stray magnetic field on the stator yoke backside. The time–frequency plot of the induced voltage for the 10-ITSC fault reveals a significant reduction in the stalk length and intensity, indicating a faulty rotor pole winding (red arrows designate a faulty pole). The time–frequency plot contains five mechanical revolutions of the 100-kVA SPSG. Each time a faulty pole passes over the sensor, a faulty pole with a reduced stalk length appears in the time–frequency plot.
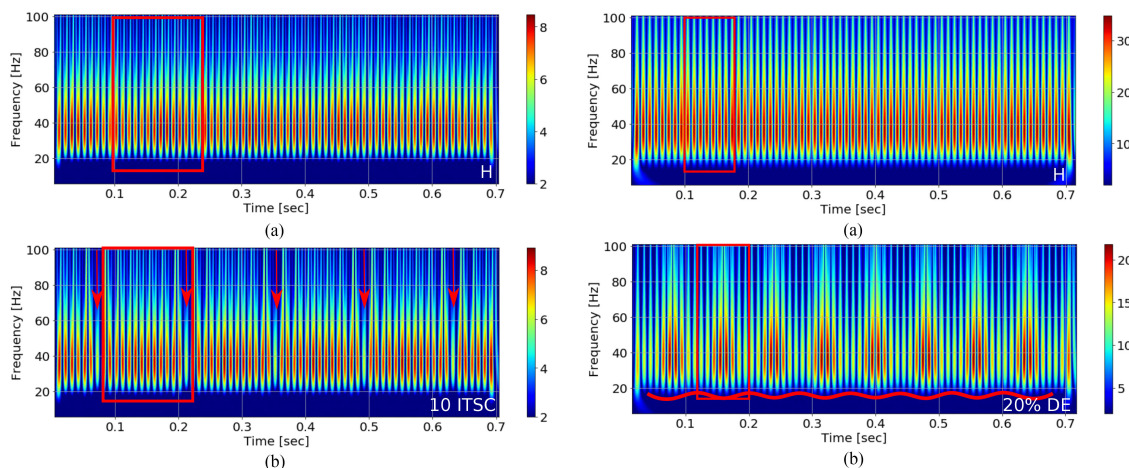
Fig. 12. Time–frequency representation of the induced voltage in the a sensor installed in a 100-kVA SPSG operating in a no-load condition (a) in a healthy case and (b) under a 10-ITSC fault—Laboratory measurements.

The application of the CWT to the experimental data of a 100-kVA SPSG is shown in Fig. 12 for a healthy case and a 10-ITSC fault. The time–frequency plot for the healthy case is similar to that of Fig. 11; each 140 ms indicates one mechanical revolution with 14 stalks, which is evidence of a healthy rotor pole winding. Although the results of analysis are similar for the experimental data corresponding to the faulty machine and for the simulation data, the stalk length is (negligibly) shorter for the experimental result than for the simulation result. Therefore, the stalk length of a faulty pole spans slightly above 20 Hz, making the identification of a faulty pole more noticeable in practice.

B. Study Results of a 22-MVA SPSG

The identified fault types in a 22-MVA SPSG according to the FEM results are both the ITSC and DE, as verified based on the time–frequency presentation of the induced voltage both in field measurement tests and FEM. Fig. 13 shows the application of the CWT to the voltage induced by the stray magnetic field for the healthy condition (first row), 10-ITSC fault (second row), 20% DE fault (third row), and mixed fault of 10-ITSC and 20% DE faults. The 22-MVA SPSG has eight poles, shown in the red window in Fig. 13; the stalk frequencies are set between 20 and 100 Hz to have high resolution in the time–frequency plot. The highest stalk intensity concentrated in the 25–60-Hz range with a red hue. The 20% DE fault causes a time–frequency pattern modification. Three changes occur due to the DE fault in the time–frequency plot compared with the healthy case.

1) A fluctuating envelope appears at the bottom of the time–frequency plot, similar to the time data series shown in Fig. 9.
2) The healthy case shows a uniform distribution in the time–frequency plot, whereas the 20% DE fault shows
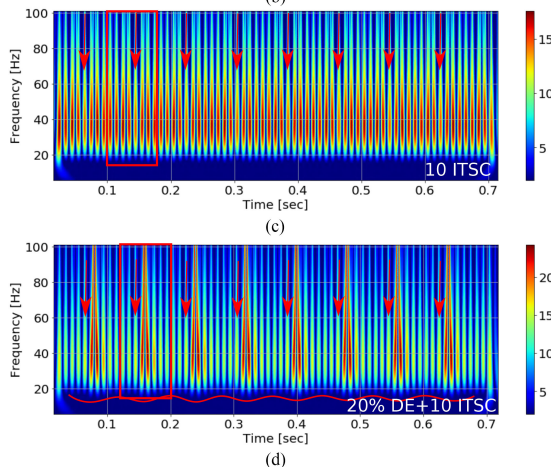

Fig. 13. Simulation result of the time–frequency representation of the induced voltage in the installed sensor on a 22-MVA SPSG operating in a no-load condition (a) in a healthy case, (b) under a 20% DE fault, (c) under a 10-ITSC fault, and (d) under mixed fault of 20% DE and 10-ITSC fault—Simulation results.

a distorted distribution, with each window shape resembling a fire flame.
3) The intensity of the stalks in the healthy case is the same for each mechanical revolution, as is the frequency range, whereas the 20% DE fault modifies the intensity pattern, with the highest intensity located in the middle of the window and a reduction in the stalk intensity at the edges.

A 10-ITSC fault reduces the stalk intensity of faulty pole in the time–frequency plot. The starting frequency point of each faulty stalk is slightly higher than 25 Hz, unlike a healthy stalk. Fig. 13 shows the time–frequency plot of an induced voltage in the sensor for a 22-MVA SPSG operating under simultaneous ITSC and DE faults. The expected pattern for ITSC and DE faults must appear in the time–frequency plot. Therefore, the fire flame shape pattern with a sine shape envelope at the bottom
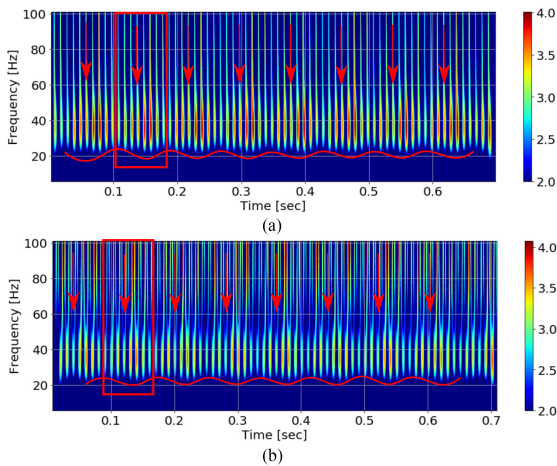
Fig. 14. Time–frequency representation of the induced voltage in a sensor installed in a 22-MVA SPSG (a) in a no-load operation and (b) under a loaded operation of 17 MW—Field test results.

of the plot appears, which indicates the occurrence of the DE fault. A comparison between the lengths of the stalks in the time–frequency plot of a DE fault indicates that there is a symmetry in the lengths of the stalks with respect to the window center. The existence of the ITSC fault while the machine has DE fault results in the length reduction in one of the stalks, which can be detected by comparing the length of opposite stalk.

Fig. 14 shows the time–frequency presentation of the measured voltage induced in an installed sensor in a 22-MVA SPSG in a hydropower plant operating under no load (top row) and under a 17-MW load (bottom row). The patterns suggest a combination of both ITSC and DE faults and are interpreted as follows.

1) A DE fault is indicated by the fluctuating envelope at the bottom, the flame shape of each mechanical revolution, and the concentrated high intensity of the stalks at the center of the window in the time–frequency plot.
2) The frequency ranges of one of the stalks are initiated slightly higher than for a healthy winding stalk. The stalk intensity that shows the ITSC fault in a rotor winding is low compared to the rest of the neighboring stalks.

C. Load Impact

The SPSG in hydropower plants always operates under different loading conditions, indicating that the load impact on the proposed method must be investigated. The main difference between no-load and loading conditions is the contribution of the stator magnetic field due to the current in the stator windings. The stator magnetic field has two impacts on the stray magnetic field. The magnitude of the stray magnetic field is slightly increased compared with the no-load case. The stray magnetic field in the loading condition has a phase shift compared with the no-load case. However, the frequency contents of the stray magnetic field do not change due to loading conditions. Therefore, the

introduced pattern due to the loading condition of SPSG must stay unchanged, while its intensity due to increment in the amplitude of the stray magnetic field must be changed.

The ITSC and DE fault pattern in the time–frequency plot is more noticeable in a loaded SPSG than in a no-load SPSG, as shown in Fig. 14. The reason is that the amplitude of the current in the rotor field winding increases by increasing the load in the SPSG; therefore, the impact of reduced contributing magnetomotive force from the faulty pole in the air-gap magnetic field and correspondingly in the stray magnetic field becomes more tangible. Consequently, the intensity of the faulty stalk due to an ITSC fault is markedly reduced under the 17-MW load. Conversely, the electromotive force of the faulty pole is decreased compared with the healthy poles; therefore, increasing the current reduces the magnetomotive force due to the ITSC fault. The power plant operator also stated that the amplitude of the vibration increased during loading conditions, possibly due to the ITSC fault. The DE pattern in the time–frequency plot under the loading condition does not change because the winding layout is not parallel; parallel windings would compensate for the nonuniform magnetic field caused by the fault.

D. Generalization of the Method

The proposed method has a high sensitivity to detect the fault in an early stage. The lowest ITSC fault and DE fault that can be detected with a visual inspection of the time–frequency plot are shown in Fig. 15. The ITSC fault is applied to a 22-MVA SPSG by removing five turns out of 58 turns in one of the rotor field windings. The length and the intensity of the faulty stalk in the time–frequency map are decreased, as shown in Fig. 15. The DE fault with 5% and 10% severity is also applied to the 22-MVA SPSG and the same pattern for a severe fault such as 20% DE fault is observed for the low severity fault. The introduced pattern is able to detect the coexistence of ITSC and DE faults in an early stage, as shown in Fig. 15. The fire flame pattern due to the DE fault in the symmetrical at the middle of the window while having ITSC fault changes the symmetry due to the reduced length and intensity of the faulty stalk.

The proposed method in this article only requires the number of poles in the SPSG, and the machine configuration does not have any impact on the introduced pattern. Fig. 16 shows the time–frequency map of a sensor-induced voltage in a 42-MVA synchronous generator with 16 salient poles in the rotor. The red window Fig. 15 shows one mechanical revolution of the 42-MVA SPSG that includes 16 stalks, which represent 16 poles. The introduced pattern for the DE fault is observed in Fig. 16, where 10% DE fault is applied to the SPSG. Conclusively, the SPSG topology does not have any influence on the introduced pattern based on the application of CWT to the induced voltage in the sensor installed on the stator backside.

The method provided in this article has several advantages and some limitations compared with the previously developed methods as follows.

1) ITSC and DE fault detection based on the application of FFT on the stray magnetic field in an SPSG is proposed in [9] and [30]. The method compares the frequency
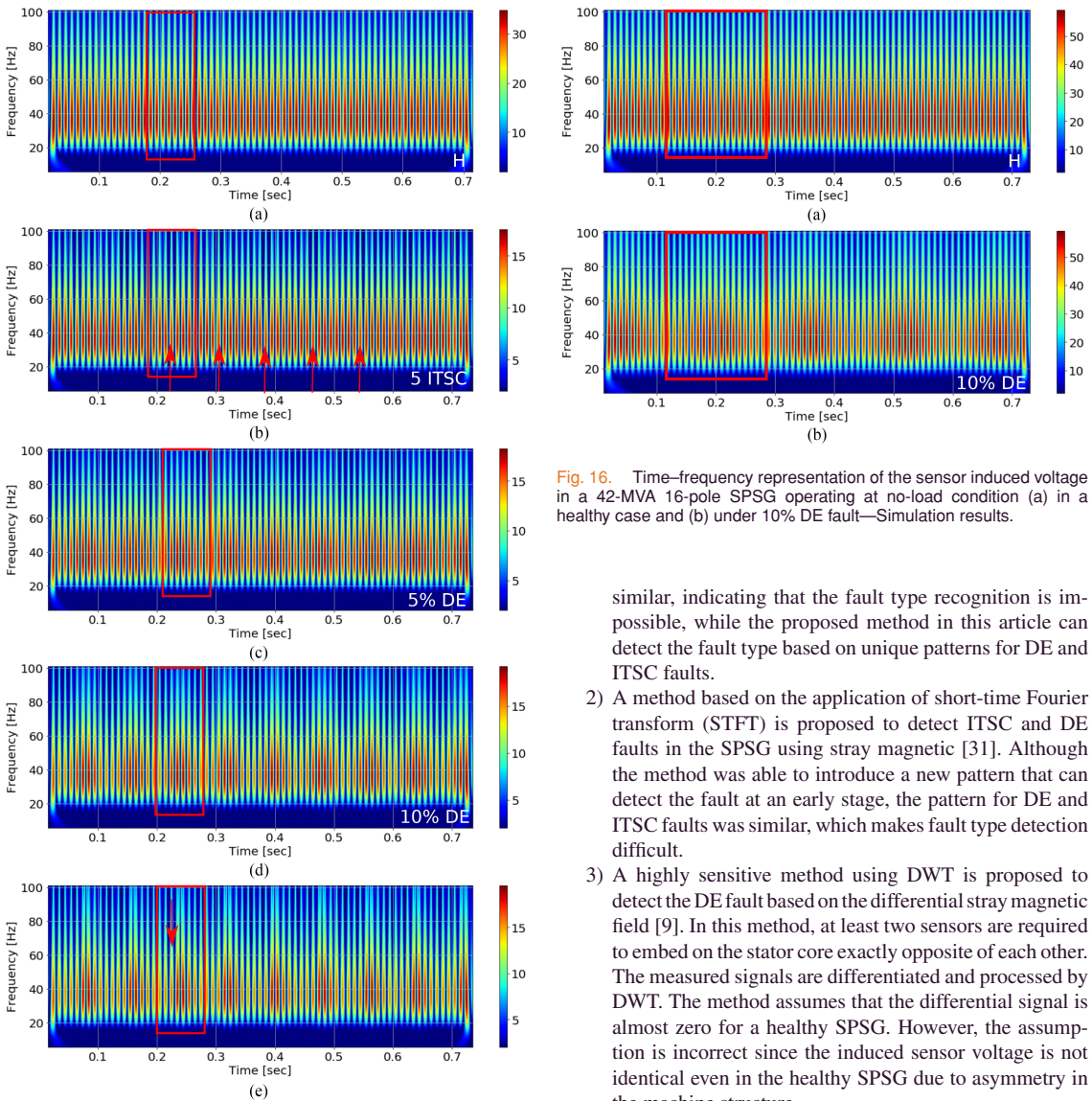
Fig. 15. Time–frequency representation of the sensor induced voltage in a 22-MVA SPSG operating at no-load condition (a) in a healthy case, (b) under a 5-ITSC fault, (c) under 5% DE fault, (d) under 10% DE fault, and (e) under mixed fault of 10% DE and 5-ITSC faults—Simulation results.
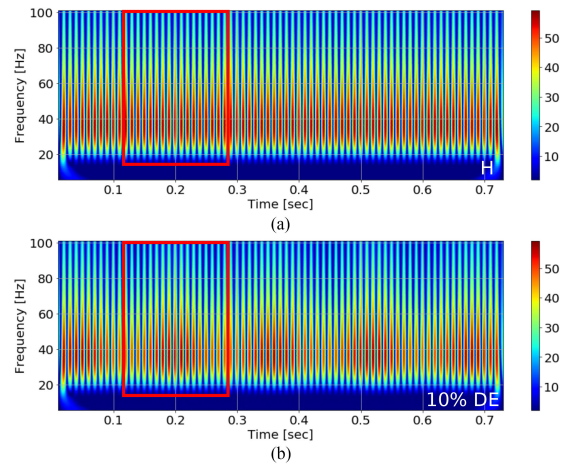

Fig. 16. Time–frequency representation of the sensor induced voltage in a 42-MVA 16-pole SPSG operating at no-load condition (a) in a healthy case and (b) under 10% DE fault—Simulation results.

spectrum of the faulty SPSG with a healthy SPSG in order to determine the health status of the machine. Although the method is able to detect the fault at an early stage since the frequency contents of a faulty machine are increased compared with a healthy machine, the frequency spectrum is unable to determine the fault type. The intrigued frequency components due to ITSC and DE faults are similar, indicating that the fault type recognition is impossible, while the proposed method in this article can detect the fault type based on unique patterns for DE and ITSC faults.

2) A method based on the application of short-time Fourier transform (STFT) is proposed to detect ITSC and DE faults in the SPSG using stray magnetic [31]. Although the method was able to introduce a new pattern that can detect the fault at an early stage, the pattern for DE and ITSC faults was similar, which makes fault type detection difficult.

3) A highly sensitive method using DWT is proposed to detect the DE fault based on the differential stray magnetic field [9]. In this method, at least two sensors are required to embed on the stator core exactly opposite of each other. The measured signals are differentiated and processed by DWT. The method assumes that the differential signal is almost zero for a healthy SPSG. However, the assumption is incorrect since the induced sensor voltage is not identical even in the healthy SPSG due to asymmetry in the machine structure.

4) The proposed methods based on the frequency spectrum are highly sensitive to the noise, while the methods based on time–frequency methods such as STFT and CWT are highly robust to the noise in the datasets [32].

Although the proposed method in this article has several merits that make it practical especially in the field, there exist some constraints as follows.

1) A high-resolution signal can be achieved if the sensor is mounted on the stator core. The SPSG frame can significantly attenuate the stray magnetic field.

2) The sensor design must be optimized based on the stray magnetic field type, the strength of the stray magnetic field, and the sensor location.

3) The sensor must be shielded and a coaxial cable must be used to transfer the data in order to reject the noise impact.

4) The data acquisition system with at least 16-bit resolution is required for fault detection based on the stray magnetic field.

5) Although the proposed method can be easily utilized by the end user since the pattern for each fault type is unique, the application of a deep neural network in pattern recognition can facilitate automate fault detection.

VI. CONCLUSION

This article presented a unique methodology for the detection of both ITSC and DE faults in an SPSG by applying CWT to the induced voltage in a flux sensor installed on the stator yoke backside. When compared with previously proposed methods for the detection of ITSC and DE faults, the detection algorithm in this article has the following advantages.

1) No *a priori* knowledge of the healthy operation of the SPSG is required because the time–frequency plot provides an informative and reliable pattern for fault detection.

2) The method can identify and discriminate fault types with high accuracy based on the obtained time–frequency patterns. The occurrence of the ITSC fault in one rotor field winding causes a reduction of the stalk length, whereas a DE fault yields an envelope at the bottom of the time–frequency plot, and each mechanical revolution of the machine resembles a fire flame.

3) The nonintrusive nature of the method, based on stray magnetic field monitoring that induces a voltage in installed sensors on the stator backside, allows assessment even during machine operation. Unlike previously proposed methods, it does not require machine stoppage or access to its internal parts.

4) The proposed method is applicable to different types of SPSGs. The only required information is the number of poles.

The FEM provides insight into the changes in time–frequency patterns due to ITSC and DE faults in 100-kVA and 22-MVA SPSGs when CWT is applied. The experimental results for a small-scale 100-kVA SPSG verified the feasibility of the methodology to detect an ITSC fault. The proposed method is able to detect and discriminate coexisting ITSC and DE faults in a 22-MVA SPSG operating in one of the Norwegian hydropower plants under a no-load or a loaded condition, supporting the feasibility of this method in real power plants.

REFERENCES

[1] I. Boldea, *Synchronous Generators*. Boca Raton, FL, USA: CRC Press, 2015.

[2] J. Bacher, "Detection of broken damper bars of a turbo generator by the field winding," *Renewable Energy Power Qual. J.*, vol. 1, no. 2, pp. 199–203, 2004.

[3] G. Ebi, "Ageing generator rotor: Refurbishment or removal from service?," *Power Eng. Int.*, vol. 17, pp. 118–123, 2009.

[4] H. Ehya and A. Nysveen, "Comprehensive broken damper bar fault detection of synchronous generators," *IEEE Trans. Ind. Electron.*, to be published, doi: 10.1109/TIE.2021.3071678.

[5] H. Karmaker, "Broken damper bar detection studies using flux probe measurements and time-stepping finite element analysis for salient-pole synchronous machines," in *Proc. 4th IEEE Int. Symp. Diagnostics Electr. Mach., Power Electron. Drives*, 2003, pp. 193–197.

[6] A. Schwery, "Large hydro generators experience and references," in *Proc. CIGRE Session*, Paris, France, 2008.

[7] J. Antonino-Daviu *et al.*, "Electrical monitoring of damper bar condition in salient-pole synchronous motors without motor disassembly," *IEEE Trans. Ind. Appl.*, vol. 56, no. 2, pp. 1423–1431, Mar./Apr. 2020.

[8] Q. Sun, C. Ma, S. Xiao, L. Niu, J. Pu, and Y. Wu, "Analysis of influence of uneven air gap of hydrogenerator on magnetic field strength and rotor magnetic pole stress change," in *Proc. IEEE Int. Conf. Energy Internet*, 2020, pp. 147–151.

[9] R. N. H. Ehya, A. Nysveen, and Y. Liu, "Static and dynamic eccentricity fault diagnosis of large salient pole synchronous generators by means of external magnetic field," *IET Electr. Power Appl.*, vol. 15, pp. 890–902, 2021, doi: 10.1049/elp2.12068.vv

[10] O. Blancke, A. Merkhouf, N. Amyot, J. Pedneault-Desroches, C. Hudon, and K. Haddad, "Strategic fault diagnosis approach for hydrogenerator shaft current discharges," in *Proc. IEEE 22nd Int. Conf. Elect. Mach.*, 2016, pp. 2346–2351.

[11] A. Mugarra, C. Platero, J. Martínez, and U. Albizuri-Txurrka, "Large salient pole synchronous machines field windings diagnosis by frequency response," in *Proc. IEEE 13th Int. Conf. Elect. Mach.*, 2018, pp. 1875–1880.

[12] W. Hong and M. Arshad, "Experience with hydro-generator turn-to-turn insulation fault, investigation, and recommendation for new stator winding design and protection," in *Proc. IEEE Elect. Insul. Conf.*, 2018, pp. 459–464.

[13] H. Ehya, T. Skreien, and A. Nysveen, "Intelligent data-driven diagnosis of incipient inter-turn short circuit fault in field winding of synchronous generators," *IEEE Trans. Ind. Informat.*, to be published, doi: 10.1109/TII.2021.3054674.

[14] J. Yun, S. B. Lee, M. Šašić, and G. C. Stone, "Reliable flux-based detection of field winding failures for synchronous generators," *IEEE Trans. Energy Convers.*, vol. 34, no. 3, pp. 1715–1718, Sep. 2019.

[15] H. Ehya, A. Nysveen, I. Groth, and B. Mork, "Detailed magnetic field monitoring of short circuit defects of excitation winding in hydro-generator," in *Proc. IEEE Int. Conf. Elect. Mach.*, 2020, vol. 1, pp. 2603–2609.

[16] J. Yun *et al.*, "Airgap search coil-based detection of damper bar failures in salient pole synchronous motors," *IEEE Trans. Ind. Appl.*, vol. 55, no. 4, pp. 3640–3648, Jul./Aug. 2019.

[17] I. Sadeghi, H. Ehya, and J. Faiz, "Analytic method for eccentricity fault diagnosis in salient-pole synchronous generators," in *Proc. IEEE Int. Conf. Optim. Elect. Electron. Equip./Int. Aegean Conf. Elect. Mach. Power Electron.*, 2017, pp. 261–267.

[18] C. Jiang, S. Li, and T. G. Habetler, "A review of condition monitoring of induction motors based on stray flux," in *Proc. IEEE Energy Convers. Congr. Expo.*, 2017, pp. 5424–5430.

[19] G.-A. Capolino, R. Romary, H. Hénao, and R. Pusca, "State of the art on stray flux analysis in faulted electrical machines," in *Proc. IEEE Workshop Elect. Mach. Des., Control Diagnosis*, 2019, pp. 181–187.

[20] J. A. Ramirez-Nunez *et al.*, "Evaluation of the detectability of electromechanical faults in induction motors via transient analysis of the stray flux," *IEEE Trans. Ind. Appl.*, vol. 54, no. 5, pp. 4324–4332, Sep./Oct. 2018.

[21] I. Zamudio-Ramirez, J. A. Antonino-Daviu, R. A. Osornio-Rios, R. deJesus Romero-Troncoso, and H. Razik, "Detection of winding asymmetries in wound-rotor induction motors via transient analysis of the external magnetic field," *IEEE Trans. Ind. Electron.*, vol. 67, no. 6, pp. 5050–5059, Jun. 2020.

[22] P. A. Panagiotou, I. Arvanitakis, N. Lophitis, J. A. Daviu, and K. N. Gyftakis, "A new approach for broken rotor bar detection in induction motors using frequency extraction in stray flux signals," *IEEE Trans. Ind. Appl.*, vol. 55, no. 4, pp. 3501–3511, Jul./Aug. 2019.

[23] P. Tian, J. A. Antonino-Daviu, C. Platero, and L. D. Dunai, "Detection of field winding faults in synchronous motors via analysis of transient stray fluxes and currents," *IEEE Trans. Energy Convers.*, vol. 36, no. 3, pp. 2330–2338, Sep. 2021.

[24] M. F. Shaikh, J. Park, and S. B. Lee, "A non-intrusive leakage flux based method for detecting rotor faults in the starting transient of salient pole synchronous motors," *IEEE Trans. Energy Convers.*, vol. 36, no. 2, pp. 1262–1270, Jun. 2021.

[25] H. Castro-Coronado, J. Antonino-Daviu, A. Quijano-López, V. Fuster-Roig, and P. Llovera-Segovia, "Evaluation of the detectability of damper cage damages in synchronous motors through the advanced analysis of the stray flux," in *Proc. IEEE Energy Convers. Congr. Expo.*, 2020, pp. 2058–2063.

[26] B. Kedjar, A. Merkhouf, and K. Al-Haddad, "Large synchronous machines diagnosis based on air-gap and stray fluxes-an overview," in *Proc. Int. Conf. Elect. Mach.*, 2020, vol. 1, pp. 1384–1389.

[27] M. Cuevas, R. Romary, J.-P. Lecointe, F. Morganti, and T. Jacq, "Noninvasive detection of winding short-circuit faults in salient pole synchronous machine with squirrel-cage damper," *IEEE Trans. Ind. Appl.*, vol. 54, no. 6, pp. 5988–5997, Nov./Dec. 2018.

[28] ANSYS-Electronics, Release 2019 R3. 7, ANSYS, Inc., Canonsburg, PA, USA, 2019.

[29] C. Torrence and G. P. Compo, "A practical guide to wavelet analysis," *Bull. Amer. Meteorol. Soc.*, vol. 79, no. 1, pp. 61–78, 1998.

[30] H. Ehya, A. Nysveen, and R. Nilssen, "Pattern recognition of inter-turn short circuit fault in wound field synchronous generator via stray flux monitoring," in *Proc. Int. Conf. Elect. Mach.*, 2020, pp. 2631–2636, doi: 10.1109/ICEM49940.2020.9270986.

[31] H. Ehya and A. Nysveen, "Pattern recognition of inter-turn short circuit fault in a synchronous generator using magnetic flux," *IEEE Trans. Ind. Appl.*, vol. 57, no. 4, pp. 3573–3581, Jul./Aug. 2021, doi: 10.1109/TIA.2021.3072881.

[32] H. Ehya, A. Nysveen, and T. N. Skreien, "Performance evaluation of signal processing tools used for fault detection of hydro-generators operating in noisy environments," *IEEE Trans. Ind. Appl.*, vol. 57, no. 4, pp. 3654–3665, Jul./Aug. 2021, doi: 10.1109/TIA.2021.3078136.

Jose A. Antonino-Daviu (Senior Member, IEEE) received the M.Sc. and Ph.D. degrees in electrical engineering from the Universitat Politecnica de Valencia, Valencia, Spain, in 2000 and 2006, respectively.

He was with IBM, Endicott, NY, USA, and involved in several international projects. He is currently a Full Professor with the Department of Electrical Engineering, Universitat Politecnica de Valencia. He was an Invited Professor with the Helsinki University of Technology, Espoo, Finland, from 2005 to 2007; Michigan State University, East Lansing, MI, USA, in 2010; Korea University, Seoul, South Korea, in 2014; Universite Claude Bernard Lyon 1, Villeurbanne, France; and Coventry University, Coventry, U.K., in 2016. He is a coauthor of more than 200 papers published in technical journals and conference proceedings. He is also the coauthor of one international patent.

Dr. Antonino-Daviu is an Associate Editor for IEEE TRANSACTIONS ON INDUSTRIAL INFORMATICS, *IEEE Industrial Electronics Magazine*, and IEEE JOURNAL OF EMERGING AND SELECTED TOPICS IN INDUSTRIAL ELECTRONICS. He is the recipient of the IEEE Second Prize Paper Award of the Electric Machines Committee of the IEEE Industry Applications Society in 2013. He is also the Recipient of the Best Paper Award at IEEE Annual Conference International Council for Education Media in 2012, IEEE International Symposium on Diagnostics for Electric Machines, Power Electronics and Drives (SDEMPED) in 2011, IEEE SDEMPED 2019, and the "Highly Commended Recognition" of the IET Innovation Awards in 2014 and 2016. He was the General Co-Chair of SDEMPED 2013 and is a Member of the Steering Committee of IEEE SDEMPED. In 2016, he received the Medal of the Spanish Royal Academy of Engineering, Madrid, Spain, for his contributions in new techniques for predictive maintenance of electric motors. In 2018, he has been awarded with the prestigious "Nagamori Award" from the Nagamori Foundation, Kyoto, Japan. In 2019, he received the SDEMPED diagnostic achievement Award (Toulouse, France) for his contributions to electric motors advanced diagnosis.

Hossein Ehya (Student Member, IEEE) received the M.Sc. degree in electrical engineering from the Department of Electrical and Computer Engineering, University of Tehran, Tehran, Iran, in 2013. He is currently working toward the Ph.D. degree in electrical engineering with the Norwegian University of Science and Technology, Trondheim, Norway.

From 2013 to 2018, he was an Electrical Machine Design Engineer with Electrical Machine Companies. His research interests include design and condition monitoring of electrical machines, signal processing, pattern recognition, and machine learning.

Dr. Ehya was awarded with the ICEM Jorma Luomi Award in Gothenburg, Sweden, in 2020.

Arne Nysveen (Senior Member, IEEE) received the M.Sc. and Dr.Ing. (Ph.D.) degrees in electric power engineering from the Norwegian Institute of Technology (now Norwegian University of Science and Technology), Trondheim, Norway, in 1988 and 1994, respectively.

From 1995 to 2002, he was a Senior Scientist with ABB Corporate Research, Oslo, Norway. Since 2002, he has been a Professor with the Norwegian University of Science and Technology, where he is currently a Manager for the research on turbine and generator technologies with the Norwegian Research Center for Hydropower Technology. His current research interests include design, modeling, and monitoring of hydroelectric generators.

Paper V

ORIGINAL RESEARCH PAPER

Static and dynamic eccentricity fault diagnosis of large salient pole synchronous generators by means of external magnetic field

Hossein Ehya[1] | **Arne Nysveen**[1] | **Robert Nilssen**[1] | **Yujing Liu**[2]

[1]Department of Electric Power Engineering, Norwegian University of Science and Technology, Trondheim, Norway

[2]Division of Electric Power Engineering, Chalmers University of Technology, Göteborg, Sweden

Correspondence

H. Ehya, Department of Electric Power Engineering, Norwegian University of Science and Technology, Trondheim, Norway.
Email: hossein.ehya@ntnu.no

Abstract

Although synchronous generators are robust and long-lasting equipment of power plants, consistent electricity production depends on their health conditions. Static and dynamic eccentricity faults are among the prevalent faults that may have a costly effect. Although several methods have been proposed in the literature to detect static and dynamic eccentricity faults in salient pole synchronous generators (SPSGs), they are non-sensitive to a low degree of failure and require a predefined threshold to recognise the fault occurrence that may vary based on machine configuration. This article presents a detailed magnetic analysis of the SPSGs with static and dynamic eccentricity faults by focusing on the external magnetic field. The external magnetic field was measured using two search coils installed on the backside of the stator yoke. Also, advanced signal processing tools based on wavelet entropy were used to analyse the induced electromotive force (*emf*) in search coils to extract the fault index. The proposed index required no threshold to recognise the starting point of fault occurrence and was sensitive to a low degree of fault. It was also non-sensitive to load variation and noise that may induce a false alarm.

1 | INTRODUCTION

Periodic evaluation of critical components of large synchronous generators provides a reliable condition monitoring system that prevents severe unexpected failure in power plants [1]. The complex configuration of the salient pole synchronous generator (SPSG) requires an accurate condition monitoring system to avoid an unplanned stoppage of the power plant. The eccentricity fault is one of the common faults in SPSG where air-gap length varies. The main reasons for static eccentricity (SE) and dynamic eccentricity (DE) faults in hydropower generators are their vertical installation and imported forces to the body of the generator from the movement of the rock/cement, especially for power plants located inside mountains. More than 97% of electricity production in Norway is generated by hydropower plants, which are primarily located inside the mountains. Therefore, precise fault detection is required to reduce economic loss either for the producers or consumers.

The eccentricity fault creates subharmonics in the voltage and current of the machine that feeds into the grid and vibration on the machine's frame. The ultimate consequence of

severe eccentricity is that the rotor rubs the stator core and winding [2]. Therefore, early-stage detection of machine fault can avoid costly damages to the machine and economic loss. Detecting eccentricity fault is mostly based on methodologies relying on analysing stator current [3–5]. In that approach, the Fourier transform is applied to the phase current, and the harmonic components of the phase current are assigned as an index to detect eccentricity fault. In contrast, the sensitivity of this approach is quite low, and it requires a high degree of eccentricity to show slight changes. Besides, the proposed index is sensitive to load harmonics, which with certain harmonic loads could induce a false alarm. The split-phase current is used to detect the SE and DE faults in SPSG [6, 7]. The split-phase signature analysis is based on measuring the current in parallel branches of the windings. The current passing through the parallel branches is due to the distorted air-gap magnetic field. Although this approach can distinguish severe DE and SE faults, it applies only to a synchronous machine with parallel branches. SE and DE faults produce $2f_s$ and kf_s/p components in the rotor current of SPSG, where f_s and p are stator electric frequency and number of pole pairs, respectively [8]. Although the mentioned feature can detect 50% SE and

50% DE faults, the unbalanced load, short circuit and the broken damper bar faults also have the same effects on the rotor current [9, 10]. Fault detection based on parameter identification was also proposed in [11, 12] for induction motors. The same approach based on the machine parameter was applied to SPSG. It was shown in [13, 14] that self-inductance and mutual inductance of stator and rotor winding change under eccentricity fault. However, the variation rate is insignificant under a low degree of fault. Therefore, the introduced methods are not sensitive enough to detect the fault in its early stage. It has been shown that eccentricity can produce harmonic components of the no-load line to line or line to neutral voltage [8, 15, 16]. In [15], the subharmonics of the no-load voltage are used to predict the SE and DE faults. Although the harmonic components of a no-load voltage can detect the failure, they are sensitive to machine configuration since the amplitude of the nominated harmonics varies in different machines based on their geometrical configuration, winding layout and material properties. The type of winding connection significantly affects the harmonic content of no-load voltage. The sensitivity of the diagnostic approach is high in a machine with windings connected in series rather than in parallel [16]. Although the introduced index based on sub-harmonics of no-load voltage depends only on the number of machine poles [15], it also needs a threshold value to predict fault occurrence.

In [17–21], the air-gap magnetic field was used to diagnose the SE and DE faults in a synchronous generator. For the eccentricity fault, the air-gap magnetic field is distorted and contains subharmonics. Although the air-gap magnetic field is the most reliable source for fault detection regardless of fault type, it is an invasive approach. It is not a practical approach for a generator under operation because sensors need to be installed at a standstill and cope with the environment in the air gap. Furthermore, fixing a hall-effect sensor, search coil around the stator slot [18] or core in the axial direction through the radial ducts [19] is impractical for a synchronous generator with small air-gap length, which is used in the run-off river type power plants. The magnetic noise could also affect the performance of the induced voltage in the search coils (sensor) installed inside the machine.

The effectiveness of applying the external magnetic field to induction motors has been validated and explained in [22–27] for broken rotor bar, eccentricity, short circuit and bearing fault, respectively. Various types of advanced signal processing tools are used to extract the novel features that can recognise the type and severity of fault based on the external magnetic field captured on the induction motor frame. However, applying the external magnetic field to recognise the fault in SPSG is only limited to detecting interturn short circuit fault in the field winding in [28] and [29]. The acquired electromotive force (emf) is analysed using a fast Fourier transform, and it shows that the amplitude of the harmonic component of the signal is increased in the case of fault.

This article provides a detailed magnetic analysis of SPSGs under SE and DE faults using induced emf in search coils located on the backside of the stator yoke. The effect of the fault on the external magnetic field is studied, and how self-inductance and mutual inductance of the stator and rotor link with the search coil winding is shown. To improve the diagnostic technique, a new way to treat the emf is introduced by finding the difference in the induced emf in the sensors at opposite sides of the machine. In this way, the amplitude of the emf for a machine in a healthy case becomes almost zero. The trend of the emf is investigated using statistical tools such as mean, standard deviation (STD) and the energy of the signal in healthy and under SE and DE faults from no load to full load. To quantify the occurrence or evaluation of the fault, an advanced signal processing tool based on wavelet entropy is introduced.

2 | ELECTROMAGNETIC ANALYSIS

2.1 | Eccentricity fault

The eccentricity fault is divided into static, dynamic and mixed eccentricities [30]. For SE fault, the rotor symmetrical axis coincides with the rotor rotational axis, and it is displaced from the stator symmetrical axis. Although the air-gap distribution is not uniform, it is time invariant observed from the stator frame. For DE fault, the stator symmetrical axis and rotor rotational axis are identical, but the rotor symmetrical axis is displaced with respect to them. Here, the position of the minimum air gap depends on the rotor angular position. DE is time dependent, unlike SE, and the minimum air-gap length varies with time. The mixed eccentricity fault is the combination of SE and DE faults.

Severe eccentricity faults induce an unbalanced magnetic force called an unbalanced magnetic pull (UMP) that exerts mechanical stress on moving parts, such as the shaft and bearings. The prolonged operation of the machine under faulty conditions induces moving part breakage and eventually rubbing the rotor on the surface of the stator core. However, in a large synchronous machine with a damper circuit, parallel windings and saturation can significantly reduce the UMP effect. The damper circuit, regardless of the eccentricity direction, can lessen UMP, while winding layout and orientation of eccentricity concerning the winding configuration can either reduce or do not change the UMP amplitude [15, 31, 32].

2.2 | Finite element modelling

Precise and detailed modelling of the machine is the first step in the fault detection process. The detailed and real parameters of the machine considerably affect reliable fault detection. Figure 1(a) represents the finite element (FE) modelling of 22 MW SPSG. The detailed specification of the machine is provided in Table 1. Furthermore, the non-linearity of the stator and rotor core materials, the rotor shaft, the spatial distribution of the stator winding, the physical properties of the stator and rotor winding and damper bars and end rings are considered. To avoid additional computation complexity, the eddy effect is neglected, except for the damper winding, because a current
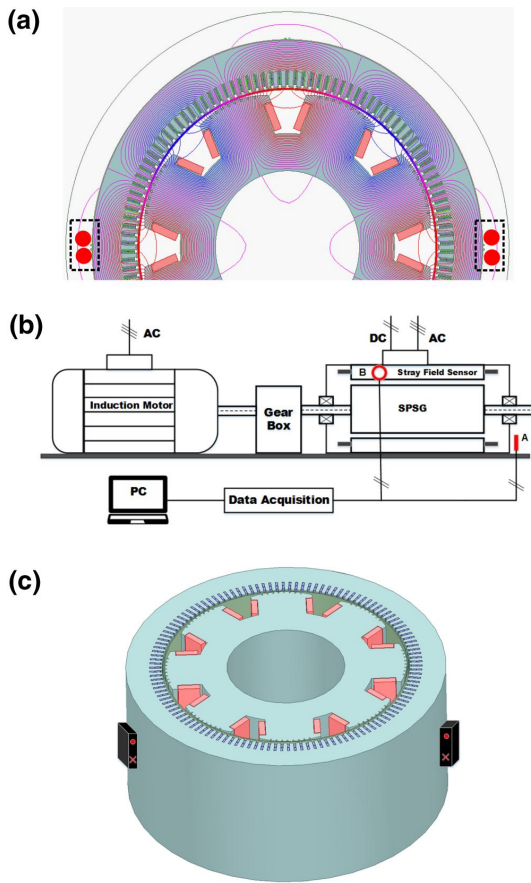
(a)

(b)

(c)

FIGURE 1 (a) The finite element modelling of the salient pole synchronous generator and the location of the installed sensors with red circle in two points, (b) location of sensors in axial direction (A) and radial direction on the backside of the stator yoke (B) of the synchronous generator, (c) location of two sensors in 3-D FEM, the red circle and cross sign show the direction of coils' current in the sensor. FEM, Fininte Element Model

TABLE 1 Specification of large salient pole synchronous generator

Quantity	Values
Rated power	22 MW
Rated speed	750 rpm
Number of poles	8
Stator terminal voltage	7700 V
Stator terminal current	1650 A
Excitation current (resistive load)	440 A
Stator outer diameter	2640 mm
Stator inner diameter	2040 mm
Minimum air gap length	22.5 mm
Length of stack	1220 mm
Number of turns per pole	58
Number of damper bars	8

asymmetries in the air-gap magnetic field distribution. The air-gap magnetic field is caused by the stator and rotor magneto-motive force, the stator and rotor slot permeance, and rotor pole saliency permeance. The eccentricity fault feeds additional subharmonics to the air-gap magnetic field. The magnetic field fluctuation depends on the type and severity of SE or DE fault. The distorted magnetic field distribution considerably affects machine parameters such as inductance, the magnetic field in the core and subsequently the external magnetic field.

The magnetic field of a machine under eccentricity fault trivially influences self-inductance and mutual inductance of the stator and the rotor winding. The amplitudes of self-inductance and mutual inductance between the stator and rotor of SPSG vary in the range of mH. Consequently, any perturbation due to a small degree of eccentricity fault up to 20% does not remarkably change their amplitudes. Therefore, all quantities such as the stator phase voltage and current that are correlated with the self-inductance and mutual inductance of SPSG are unreliable signals for SE or DE fault detection with a low degree of severity. It is, however, possible to use phase voltage or current if the fault severity is high [5].

There is always an external magnetic field outside the electric machine, whether in the radial or axial direction of the machine. The location of the sensor significantly affects the captured external magnetic field [34, 35]. There are two options to locate the sensor in the vicinity of the machine core, as shown in Figure 1(b). In position A, axial flux is measured by the sensor. In position B, the sensor may trap both radial and axial magnetic fields with the radial field as the dominant field in the captured signal. Regarding the sensor location, since the SE and DE faults have a radial nature with significant effects in the radial direction, the external field sensors are located on the backside of the stator yoke, as shown in Figure 1(c). Therefore, they are vulnerable to capture more radial signals, whether in a healthy or faulty situation.

The amplitude of the magnetic field is reduced when moving away from the air gap. Eventually, its amplitude

passes through the damper winding even in the steady state whether the generator operates in a healthy or faulty situation [9]. The external circuit with rotor field windings, stator winding and damper circuits is used. A DC voltage is applied to the field winding terminals. The magnetic field equations are combined with differential equations of the external circuits. The motion equation of the machine is finally combined with magnetic and external circuit equations in the FE model. In this paper, Ansys Maxwell 2-D package is used to model the SPSG [33].

2.3 | Magnetic field analysis

The magnetic field in electric machines contains all information about its detailed specification, which could be used to monitor the machine condition. The eccentricity fault causes

becomes negligible in order of μT at the outer radius of the backside of the stator yoke. Figure 2 depicts the air-gap magnetic field and the magnetic field at the middle and outer side of the stator yoke. Although the amplitude of the external magnetic field is remarkably smaller than the air-gap magnetic field, its shape and periodicity are similar. Moreover, the external magnetic field is the mirror of the air-gap magnetic field that includes harmonic components of both the stator and rotor magnetic fields.

The induced voltage in the installed sensor on the vicinity of the backside of the stator yoke is proportional to the sensor cross-section, the number of turns and external magnetic field. The number of turns and the cross-section of the copper wire in the sensor are 3000 turns and 0.12 mm². The dimension of sensor is 80 mm × 80 mm × 10 mm. The resistivity and inductance of the sensor in its terminal are 912 Ω and 714 mH. Figure 3 depicts the induced emf in the sensor caused by an external magnetic field. For SE fault, the emf shape does not change, whereas the amplitude of the signal based on its location changes slightly, in a way that the amplitude of induced emf increases for a sensor located on the side of the machine that the air-gap length is reduced and vice versa. Both the amplitude and emf shape in sensor dramatically change for DE fault.

The fluctuation of the induced emf in the sensors is due to varying mutual inductance between the stator and rotor windings with the coils of the sensors. Unlike stator and rotor self-inductance and mutual inductance, the eccentricity fault considerably affects self-inductance and mutual inductance of the sensor coils located on the backside of the stator yoke. Figure 4 depicts the mutual inductance between the rotor winding and the sensor in a healthy, 20% SE and 20% DE faults. Observably, there are no changes regarding the shape of mutual inductance for SE fault compared with the healthy case, while its amplitude is decreased. The reason is that the reluctance of the path for the linkage flux is increased and it reduces the mutual inductance between the rotor and sensor. For DE fault, as shown in Figure 4, the amplitude and shape of the mutual inductance change considerably since the DE fault varies in location, and time simultaneously changes the magnitude and shape of the mutual inductance. In addition to the oscillation, the mean value of the signal is also changed under DE fault.

The above argument is also valid by considering mutual inductance between the stator phase windings with a sensor coil. Figure 5 demonstrates the mutual inductance of stator phases A, B and C winding with sensor coil in the healthy, 20% SE and 20% DE faults, respectively. A comparison between the mutual inductance in the healthy case for all three phases reveals that the mutual inductance depends on the location and distribution of the winding with respect to the sensor coil. As seen, the amplitude of the mutual inductance between the phase winding and the sensor coil under SE fault decreases considerably more than the mutual inductance between the rotor and sensor coils because the path of the linkage flux is shorter in this case. Also, the air gap could not change and
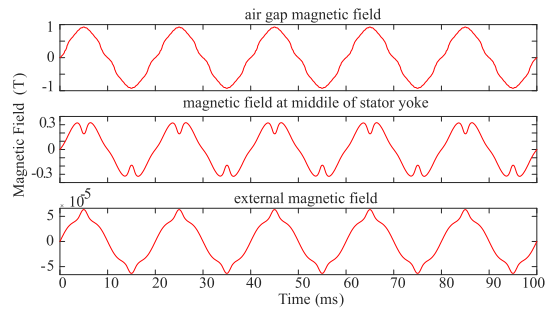

FIGURE 2 The radial magnetic field in the SPSG, air-gap magnetic field (top), magnetic field at the middle of the stator yoke (middle) and external magnetic field (bottom). SPSG, salient pole synchronous generator
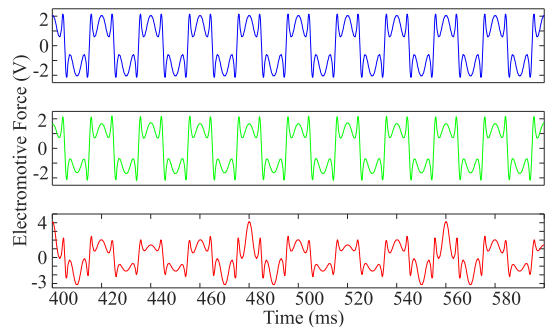

FIGURE 3 The induced electromotive force in the search coil in healthy, 20% SE and 20% DE faults. DE, dynamic eccentricity; SE, static eccentricity

reduce the flux. The oscillation of the mutual inductance between the phase winding and sensor coil is significant under DE fault, and a comparison between the envelope of the signals in Figure 5 reveals that DE fault makes additional subharmonics.

3 | SIGNAL PROCESSING

Fault detection based on unprocessed signal is a difficult task since the variation of the signal does not give meaningful information regarding the machine condition. Several signal processing tools are used to extract useful patterns inside the signals for fault detection that can be divided into three categories:

- Time domain [36, 37]
- Frequency domain [2–4, 13, 14]
- Time–frequency domain [22, 24, 34, 38]

In this section, statistical tools such as mean value, STD, energy, frequency domain and time–frequency domain
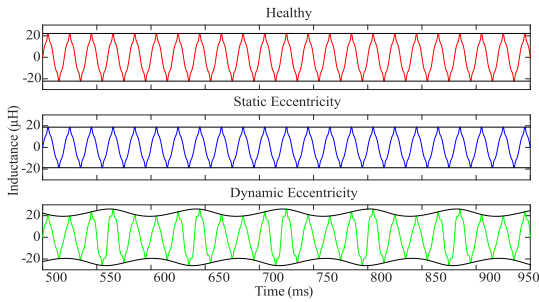
FIGURE 4 The mutual inductance between the rotor winding and search coil winding in a healthy, 20% SE and 20% DE cases in no-load generator. DE, dynamic eccentricity; SE, static eccentricity

processors based on fast Fourier transform and wavelet entropy are applied to *emf* to predict the machine health condition.

3.1 | Preprocessing—definition of differential electromotive force

Defining the threshold for processed data from the signal processing part is the most challenging part of the fault detection process. To overcome this challenge, two sensors are installed on two sides of the machine in a radial direction exactly opposite of each other. The acquired emf from each sensor in a healthy case must be the same. Therefore, the induced *emf* in both sensors is subtracted and the resultant differential electromotive force (*demf*) is almost zero for a healthy case and non-zero under SE and DE faults. The construction tolerance of the large SPSG in the hydropower plant is tight, and it is almost impossible to have an imbalance due to the machining of the stator or rotor core. However, in large SPSG with segmented stator core, the stator ovality is detectable by installing four sensors perpendicular to each other. Therefore, the assumption of considering *demf* equal to zero in large healthy SPSG is valid.

3.2 | STD and mean value of *demf*

The dispersion or variation of the data set is measured by the statistical term STD. According to its definition, the low value of STD indicates its tendency to the mean value of the data set, and the high value of STD suggests that the value is scattered over a wide range [39]. This definition could be used to analyse *demf* in a healthy or under SE and DE faults. The amplitude of *demf* in a healthy case is expected to be zero, which is not the case in reality due to tolerance in the manufacturing process. Therefore, the mean value and consequently the STD of *demf* may not be zero. Figure 6 demonstrates the variation of STD and the mean value of *demf* under SE and DE faults for no-load and full-load cases. As seen, either mean value or STD is
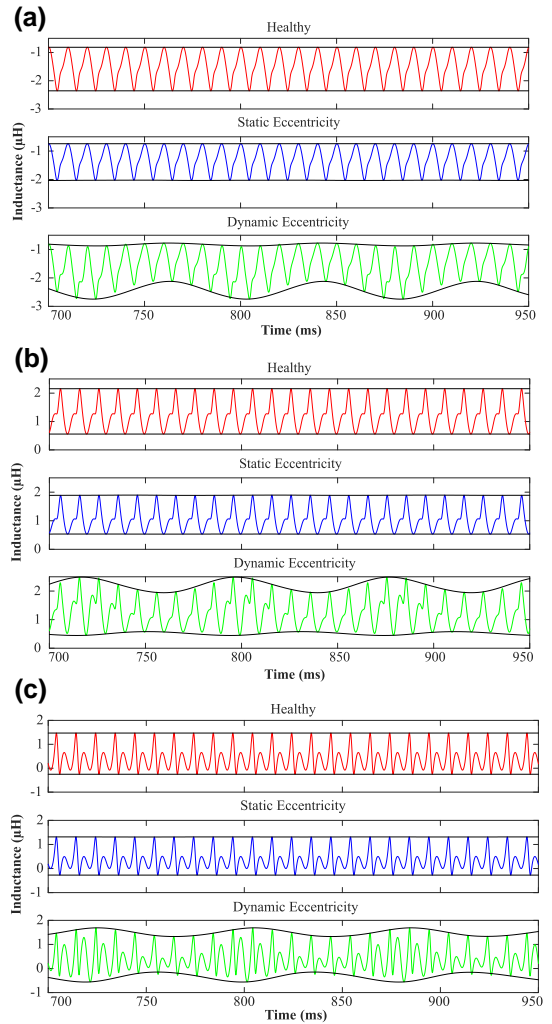

FIGURE 5 The mutual inductance between the stator phase winding and the search coil winding '1' in a healthy and under 20% SE and 20% DE cases in no-load generator. (a) phase A, (b) phase B and (c) phase C. DE, dynamic eccentricity; SE, static eccentricity

almost equal to zero in a healthy case, and its amplitude increases by increasing fault severity degree. The variation rate under DE fault is higher than that in SE fault since the fluctuation rate under DE fault is higher than that in SE fault. Therefore, the amplitude of STD under 20% DE tends to 1, which shows high degree of data dispersion, but it is 0 in healthy case. Besides, under SE fault, only the amplitude of the *demf* is altered, while under DE fault both the amplitude and some extra harmonics are also involved in *demf* waveform

According to Figure 6, it is possible to identify the severity of the fault based on STD and mean value of *demf* acquired by external field sensors. Besides, the value of the feature for the
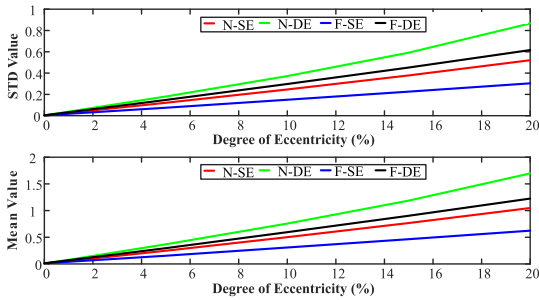
FIGURE 6 Variation of 'mean value' and 'standard deviation' (STD) versus the degree of SE and DE faults in no-load (N) and full-load (F) cases. DE, dynamic eccentricity; SE, static eccentricity

healthy case is almost zero and while increasing the fault severity, the amplitude of the STD and mean value significantly increase. In addition, the magnitude of the features in no-load case exceeds that of full-load case because the magnetic field created by parallel windings in the stator tries to balance the distorted air-gap magnetic field. The amplitude of the features in DE exceeds that of SE either in STD or mean value indicator because the waveform of the signal for DE is under considerable fluctuation. In contrast, the amplitude of the signal under SE fault depends on the location of the sensor which is increased or decreased. Alternatively, the emf of DE contains more harmonics. Indeed, the difference between the value of STD and mean value indicators for healthy and faulty conditions is significant, which demonstrates the effectiveness of the method.

3.3 | Energy of *demf*

The energy of a signal represents the strength of the signal since it gives the covered area under the curve of the power at any time interval [40]. Therefore, when the signal goes under any variation, it varies the energy as well. The energy of *demf* is derived as follows:

$$E = \int_{-\infty}^{+\infty} |demf(t)|^2 dt \qquad (1)$$

From Figure 3, the amplitudes of *demf* under SE and DE faults compared with the healthy case have increased, which induce energy level increment. According to Table 2, the energy of *demf* in the no-load case is increased from 1.5 in healthy situation to 81.5 and 66.6 under 5% SE and 5% DE faults, respectively. By increasing the severity of the fault, the amount of signal energy is also increased. Although under full-load condition, the amplitude of *demf* is increased, the loading decreases the sensitivity of the signal energy as the fault progresses. However, it has a high degree of sensitivity to the occurrence of the fault since under a low degree of a fault, the amplitude is increased significantly compared with the healthy case. Although the amplitude of the signal energy shows no

TABLE 2 The energy value of the *demf* under variation of static eccentricity (grey columns) and dynamic eccentricity faults in no-load and full-load cases

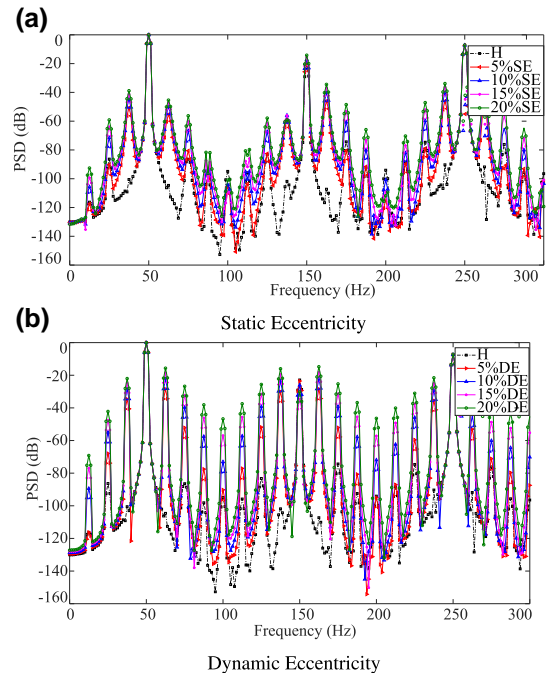| Load	H	5%	5%	10%	10%	15%	15%	20%	20%
No load	1.5	81.5	66.6	82.3	67.5	84.4	68.8	87.0	70.6
Full load	8.7	63.3	76.3	64.1	77.3	64.5	78.6	64.5	80.4

FIGURE 7 Comparison between spectrum density of electromotive force in healthy cases with various degrees of SE (a) and DE (b) faults in no load. DE, dynamic eccentricity; SE, static eccentricity

significant increment by increasing the fault severity, the sudden increase in the energy value by the fault occurrence is a fingerprint to demonstrate fault occurrence.

3.4 | Spectrum analysis

The fast Fourier transform is the most prevalent signal processing tool used in fault detection of electric machines. Its low computational complexity makes it a straightforward tool, especially for real-time assessment. Figure 7 demonstrates the spectrum density of emf under SE and DE faults. The amplitude of spectrum density either under SE or DE fault greatly increases compared with the healthy case. For instance, the amplitudes of frequency sidebands such as 25, 75 and 125 Hz are increased from 86.3, 86.4 and 82.5 dB in the healthy case to 90, 80.5 and 82.5 dB under 5% SE fault. The amplitudes of the mentioned

sidebands under 20% SE are increased to 59.1, 56.3 and 57.9 dB. A comparison between the healthy and 5% DE fault in Figure 7 (b) for frequency components of 25, 75 and 125 Hz shows that their magnitudes are increased to 68 52 and 51.8 dB. There is the same pattern of frequency component increment by increasing the fault severity.

A comparison between the magnitudes of sidebands of spectrum density for SE and DE faults exhibits that the variation of DE components is significantly higher than SE components. Although spectrum density of emf under SE and DE faults shows that the sideband components are increased due to the fault, the variation of each frequency component does not follow the same pattern by increasing the fault severity. For instance, some of the amplitudes of the faulty sidebands are the same as a healthy case or even less, which is misleading for faulty data interpretation. In addition, the machine specification and operating environment of SPSG considerably affect the amplitude of frequency components because white Gaussian noise can mask or change the sideband magnitudes. Moreover, the machine specification determines the amplitude of sidebands, indicating that a threshold level is required to determine fault occurrence, which is difficult to propose and it needs expert knowledge.

3.5 | Time–frequency analysis

The wavelet transform (WT) is a useful signal processing tool used in various fields like power systems [41] and electrical machines [38]. The time localisation of different frequency components of a signal is used in WT. The WTs, unlike traditional frequency-domain signal processing tools, do not use a fixed-width window. The wavelet analysing function adjusts its time widths according to the frequency component of a given signal, in which lower frequencies are in the broader window and higher frequencies in the narrower one. Alternatively, signals with oscillations and localised impulses could be treated using WT in a way that high-frequency and low-frequency components are decomposed in the short and long-time intervals, respectively. The signal is decomposed to its components by filtering the signal with high-pass (HPF) and low-pass filters (LPF). The output of the HPF is called details, while the output of the LPF is called approximations. The bandwidth of the two filters must be the same. After each step of decomposition, the sampling frequency of the signal is halved. The output of the LPF is decomposed recursively to produce the next sub-band of the wavelet. Equation 2 demonstrates the summation of all components of the *demf* signal into multiresolution decomposition as details and approximations:

$$demf(n) = \sum_{i=1}^{j} D_i(n) + A_j(n) \qquad (2)$$

where j is the number of decomposition level, $D(n)$ and $A(n)$ are details and approximations of wavelet.
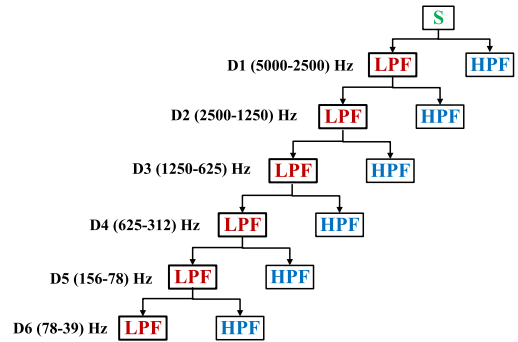

FIGURE 8 Discrete wavelet transform and the corresponding frequency bands based on the sampling frequency (10 kHz)

In this paper, Daubechies-8 ($n = 8$) is used as a mother wavelet. A higher order wavelet, similar to D-8, has a higher resolution that could improve the quality of fault detection in electrical machines. Figure 8 shows the procedure of signal decomposition using discrete WT, where S is the input signal, and LPF and HPF are low-pass and high-pass filters. Preliminarily, a given signal to WT is divided into two halves, which are the inputs of the LPF and HPF. The output of the first-level LPF is then separated into half the frequency bandwidth. This procedure is continued until the given signal is decomposed into the predefined value of that level. The sampling frequency in this paper is 10 kHz, and based on Nyquist's theorem, the highest frequency that the signal could contain would be 5 kHz. Consequently, the frequency bandwidth of the first sub-band of WT must be between 5 and 2.5 kHz.

Figure 9 shows the applied discrete wavelet model to the *demf* in H, 20% SE and 20% DE faults. By comparing the *demf* in all three cases, it shows that the amplitudes of *demf* under faulty situations are 100 and 200 times more significant than the healthy case for SE and DE faults, respectively. A comparison between the detailed signal of H and SE shows that the frequency contents of the detailed signal from D1 to D6 must be the same, and the only difference must be their amplitude. However, the comparison between H- and DE-detailed signals of *demf* (Figure 9(a) and (c)) shows that due to the nature of DE fault that rotation of the rotor and consequently magnetic field is a function of space and time, the shape and amplitude differ. Unlike some signals like air-gap magnetic field, torque, current or voltage, where only one of the wavelet sunbands shows remarkable deviation from the healthy case, the wavelet-detailed level of *demf* predominantly changes under SE and DE faults compared with H situation.

Figure 10 demonstrates WT of *demf* in H and under 20% SE and 20% DE faults for detailed sub-bands of D1 to D6. From Figure 10, SE and DE faults result in a variation of wavelet sub-band waveform. However, a comparison between no-load and full-load cases under SE fault reveals that loading condition reduces the fault effect on sub-band components. The mentioned reduction is evident in D6 sub-band. There is the same trend in the wavelet sub-band component under 20% DE fault in the full
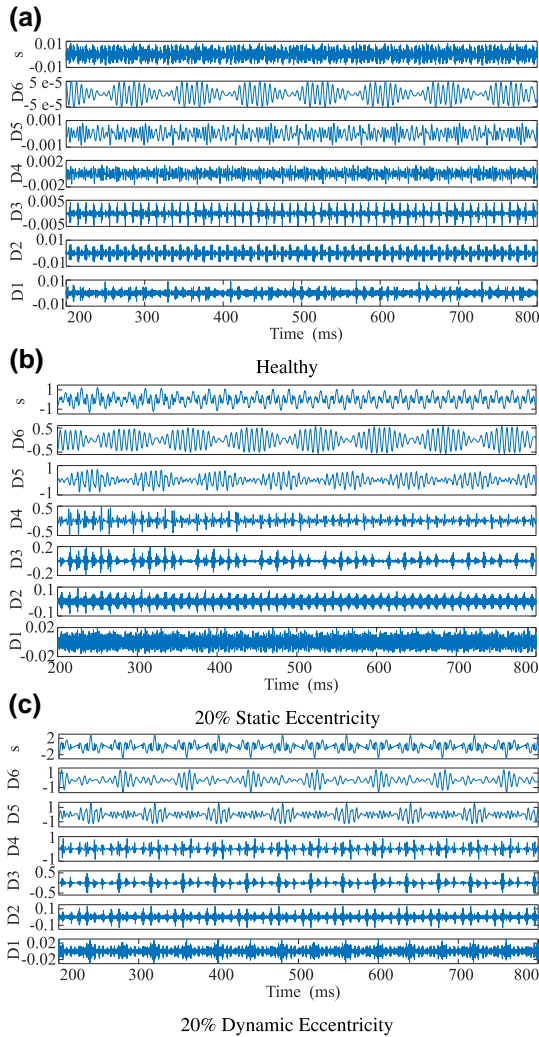
FIGURE 9 Discrete wavelet transform of induced differential electromotive force by means of the external magnetic field in the sensors in no load: (a) healthy, (b) 20% SE and (c) 20% DE faults. DE, dynamic eccentricity; SE, static eccentricity
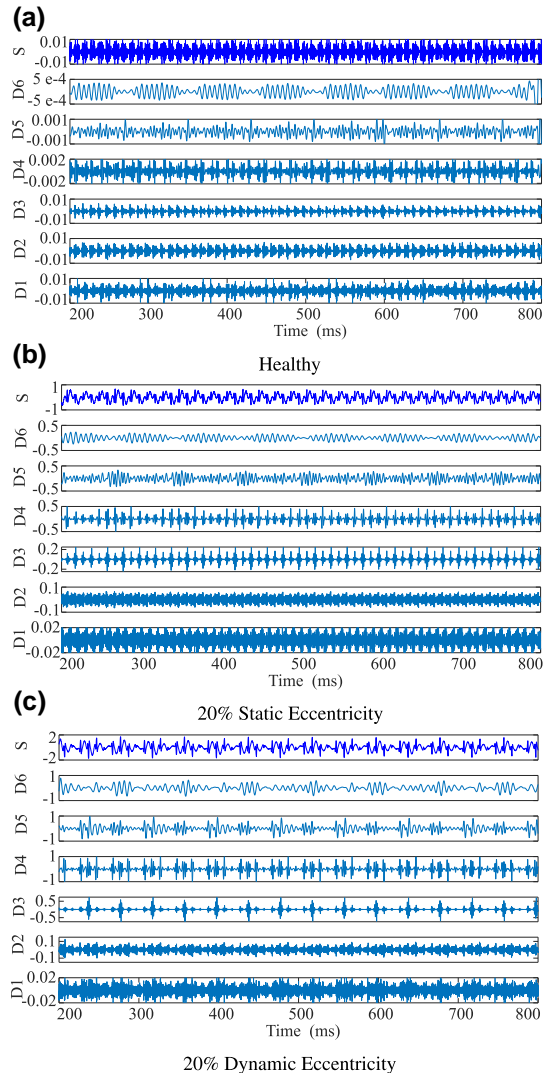

FIGURE 10 Discrete wavelet transform of induced differential electromotive force by means of an external magnetic field in the sensors in full load: (a) healthy, (b) 20% SE and (c) 20% DE faults. DE, dynamic eccentricity; SE, static eccentricity

load as in the no-load case. However, the loading condition under SE fault reduces wavelet sub-band amplitude. Generally, SE and DE faults predominantly affect *demf* either in no-load or full-load cases. Moreover, results prove that *demf* has adequate information about irregularities due to the fault in SPSG. However, an index must be introduced to quantify fault severity.

3.6 | Wavelet entropy

Combining WT with entropy can provide a novel tool to analyse the transient behaviour of the faulty signals that have a

non-stationary trend. The application of wavelet entropy in different fields like physiology [42], power systems [41] and condition monitoring of induction motors [43] shows that it could provide useful information. Therefore, wavelet entropy is unprecedentedly used to extract SPSG information under SE and DE faults. The wavelet entropy of the signal represents the degree of disorder in the wavelet sub-bands. The entropy is measured between 0 and 1, with 0 showing the perfect order, and 1 shows a high degree of disorder. However, the entropy value is not necessarily limited to an upper limit of 1, and it
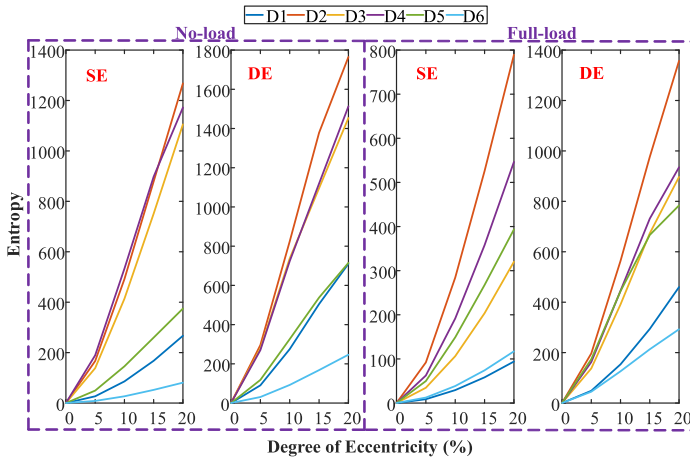
FIGURE 11 The entropy of wavelet sub-bands (D1 to D6) for different degrees of SE and DE faults in no-load and full-load cases. DE, dynamic eccentricity; SE, static eccentricity

could be more significant than that, which means a higher degree of disorder.

Shannon entropy provides a practical index for evaluating and analysing the probability distribution [44]. Shannon entropy that measures the uncertainty and disorder of wavelet sub-bands is defined as follows:

$$Entropy_{sb}(n) = -\sum_{i=1}^{j} P_i log P_i \qquad (3)$$

$$P_i = \frac{Ej}{E} \qquad (4)$$

where P_i is a relatively normalised value of each wavelet sub-band energy (E_j) to the total energy of the signal (E).

Figure 11 displays the rate of entropy changes under SE, and DE fault varies from healthy up to 20% eccentricity in no-load and full-load cases. From Figure 11, the entropy of wavelet sub-bands shows a high degree of sensitivity to occurrence and progression of fault. According to the entropy definition, the entropy value in the healthy case must be almost equal to zero, which reveals the less or none degree of disorder in wavelet sub-bands. By increasing the degree of SE or DE fault, the rate of signal disorder is increased inducing high entropy value. The entropy value for detailed signals $D7$ and $D8$ demonstrates minimal degree of changes compared with other detailed sub-bands. The magnitudes of entropy for $D7$ and $D8$ in no-load and full-load healthy cases are 0.34 and 0.22, which under 20% SE and 20% DE faults increase to 27.6 and 3.1, respectively. By comparing the entropy of different wavelet sub-bands, it is found that $D2$, $D3$ and $D4$ have a higher degree of sensitivity to fault progress, whether under SE or DE fault. In a full-load case, the rate of change for $D5$ is increased compared with $D3$, which is due to circulating third harmonic in a machine winding.

Although a specific value of the threshold for a fault indicator has been proposed for fault occurrence [38], the introduced index in this article requires no specific threshold. The method proposed in this paper requires no specific threshold to indicate the fault appearance since increasing the entropy value from zero (healthy case) to any value indicates fault. A high degree of index sensitivity to failure induces discrimination of fault in a low degree of severity even less than 10% eccentricity. For instance, by having 10% SE, the magnitude of wavelet entropy is increased from 0 to 85.9, which shows that the index can detect low severe fault with high precision.

3.7 | Load effects on proposed index

Figures 12 and 13 depict the variation of wavelet entropy under load variation from no load to full load under different degrees of SE and DE faults, respectively. Comparisons of the amplitude of entropy in no load and full load show that load reduces the entropy amplitude even by increasing the fault severity level. For no load, the most contributing magnetic field is produced by the rotor, and even a small degree of eccentricity causes a high degree of distortion in *demf*, whereas in loading condition, both the stator and rotor magnetic fields synergistically influence the air-gap magnetic field and consequently, the external magnetic field. Therefore, the machine, especially with a parallel winding layout, tries to balance the magnetic field in a faulty case. Hence, the degree of disorder in wavelet entropy of sub-bands under loading conditions must be reduced. In addition, the ratio of tangential to the radial magnetic field under loading conditions is increased, while the radial magnetic field is the dominant field captured by sensors in the no-load case. However, wavelet entropy of sub-band $D5$ is robust to load variation, while the variations of the other sub-bands ($D1$, $D2$, $D3$, $D4$ and $D6$) are in an acceptable range.

3.8 | Noise effects on proposed index

The term 'signal' in the field of fault diagnosis means only the desirable data that are measured [40]. However, the signal is
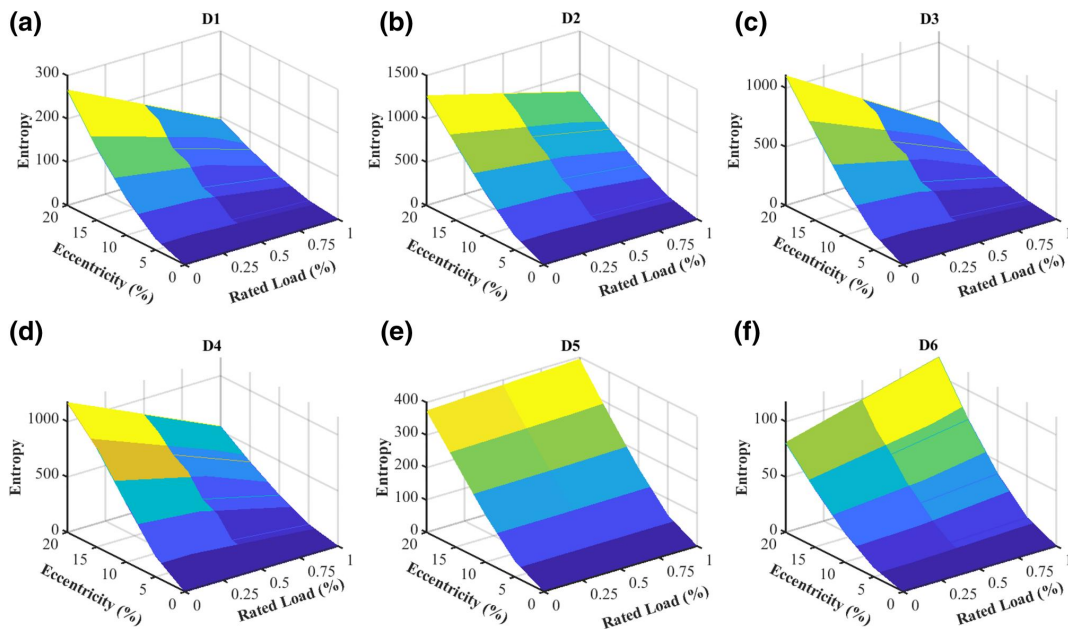
FIGURE 12 The load effect on wavelet entropy of sub-bands under SE fault: (a) D1, (b) D2, (c) D3, (d) D4, (e) D5 and (f) D6. SE, static eccentricity
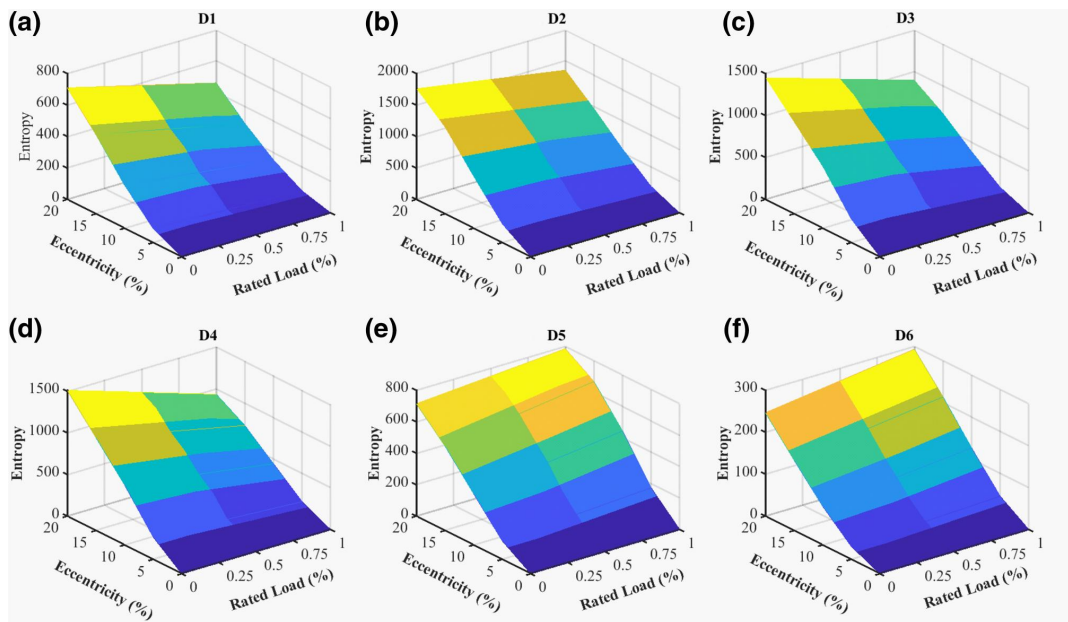
FIGURE 13 The load effect on wavelet entropy of sub-bands under DE fault: (a) D1, (b) D2, (c) D3, (d) D4, (e) D5 and (f) D6. DE, dynamic eccentricity

vulnerable to various noises during the process of data acquisition, storage and conversion. Different noises could specifically affect data, which can demonstrate its effect in signal processing. White Gaussian noise is one of the prevalent noises in the industry and power plant that could mask or even hide fault features for a high signal-to-noise ratio (SNR). The

TABLE 3 The noise effects on detailed signal of wavelet entropy in healthy (H), 10% and 20% static eccentricity and dynamic eccentricity (grey rows) faults

	D1			D2			D3			D4			D5			D6		
	H	10%	20%	H	10%	20%	H	10%	20%	H	10%	20%	H	10%	20%	H	10%	20%
No-N	0.001	85.9 / 275	267 / 710	0.001	491.6 / 824	1268 / 1765	0.007	414 / 737	1105 / 824	0.014	533 / 723	1172 / 1013	0.035	146 / 326	375 / 715	0.136	27 / 92	81 / 246
60 dB	0.001	86 / 275	267 / 710	0.002	492 / 824	1268 / 1765	0.01	414 / 737	1105 / 824	0.02	533 / 723	1172 / 1013	0.04	146 / 326	375 / 715	0.15	27 / 92	81 / 247
50 dB	0.007	85.8 / 275	267 / 710	0.1	492 / 825	1268 / 1765	0.03	414 / 737	1105 / 824	0.05	533 / 723	1172 / 1013	0.1	146 / 326	375 / 715	0.2	27.1 / 92.5	81 / 246
40 dB	0.03	85.4 / 275	268 / 710	0.09	491 / 824	1269 / 1765	0.12	413 / 737	1105 / 824	0.3	532 / 724	1172 / 1013	0.6	146 / 326	374 / 715	1.2	27.6 / 93	81.4 / 248
30 dB	0.36	86 / 273	2671 / 713	0.56	489 / 824	1269 / 1765	1.3	414 / 740	1109 / 822	2.5	536 / 723	1170 / 1016	4.3	147 / 329	376 / 715	8.4	33.8 / 97	85 / 251
20 dB	3.43	78 / 279	263 / 699	4.73	499 / 829	1266 / 1765	10.5	4174 / 741	1097 / 819.7	19.3	533 / 722	1171 / 1003	33.5	158 / 339	392 / 720	59.7	82.5 / 144	128 / 279

white noise effects on wavelet entropy features are presented in Table 3. The various rates of SNR from 60 dB as the lowest level up to 20 dB as the highest level are applied to *demf* signal in the healthy and under SE and DE faults. As shown in Table 3, by increasing SNR from 60 to 20 dB, the amplitude for the healthy case in $D1$ to $D6$ increases with the highest value in $D6$. However, the minimum amplitude of various wavelet entropy sub-bands is much higher than the maximum value of the healthy case under 20 db SNR. Although the proposed feature is robust to noise, the wavelet entropy of sub-band $D6$ among other sub-bands is vulnerable to serious variation in a noisy environment.

4 | APPLICATION, LIMITATION AND CONSIDERATION IN FIELD TEST

The application of this method for large SPSGs in hydropower plants is possible. It is possible to attach the sensor, as shown in Figure 1, to the backside of SPSG since hydropower generator has no steel housing like a turbo generator or induction machine. However, some circumstances may induce some differences between finite element model (FEM) and real-test results as discussed below:

- Lack of material data sheet in FE modelling may change the amplitude of *emf* and consequently, it induces variance in the measured data with simulation.
- The manufacturing tolerance is disregarded, which may also affect the simulation results.
- In large hydropower plants, the housing of SPSG is the wall in the generator pit that is usually made of concrete. The vertical and horizontal beams of frames are used to take up to the torsional force acting on the stator body. The distance between the horizontal and vertical beams exceeds 30 *cm*.
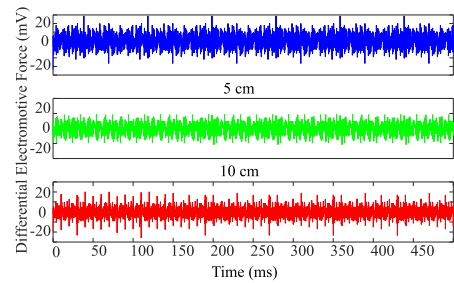

FIGURE 14 The effect of sensor installation location error on *demf*. Sensors are exactly in front of each (blue) with 5 cm (green) and 10 cm (red) installation errors

Notably, it could affect the signal since the material is iron. However, putting the sensor in the middle of the beams aids to avoid the effect of the frame. Therefore, for sensor attachment close to the frame, the modelling of the frame in FEM is mandatory.
- It is almost impossible to locate the sensors exactly in front of each other in a real-field test and there is a possibility of a few centimetre errors in the sensor installation. Therefore, one of the sensors in FE modelling is moved for 5 and 10 cm concerning the other sensor in the opposite direction. Results show that location error does not significantly affect the amplitude of *demf* as shown in Figure 14. The wavelet entropy is also applied to the signals and their amplitudes do not change substantially, and it increases 0.1 and 0.14 for 5 and 10 cm sensor relocation, respectively.
- The middle of SPSG yoke is the optimal position for the sensor installation in order to avoid the magnetic field effect on sensor due to end winding and high voltage bus bars.

- Since the working environment of SPSG in hydropower plants is vulnerable to magnetic noise, a shielded co-axial cable is required to reject the noise effect on the sensor.

5 | CONCLUSION

A new method is introduced to detect the SE and DE faults in SPSG. Different faults in induction machines induce significant variation in current, torque and speed waveform (characteristics). The mentioned signals in SPSG are robust to a low degree of fault; therefore, the only reliable source of fault detection is based on either the magnetic field in the air gap or external magnetic field. While the former is an invasive tool that is inappropriate for generators under operation, the latter is non-invasive, low cost, easy to design and fabricate, which makes the proposed method in this article noteworthy.

The proposed methods are based on the external magnetic field analysis. The mentioned external magnetic field is captured by installing two search coils on the backside of the stator yoke precisely opposite to each other. By having two signals from two sides of the machine, the net *demf* in a healthy case is almost zero, and by the occurrence of the fault, based on its type, the amplitude and shape of *demf* differ. Various approaches and signal processing tools are used to detect the appearance and evolution of the fault. The proposed method relies on the time–frequency analysis of *demf*, and discrete WT is used to identify the hidden pattern under SE or DE fault. Also, the following conclusions represent the summary of achievements in this paper.

1. The detailed and accurate modelling of SPSG in the FE model shows how the external magnetic field responds to SE and DE faults. The fault occurrence induces some subharmonics in the air-gap magnetic field in *emf*.
2. The investigation of self-inductance and mutual inductance between the rotor and stator with search coils shows that due to the low rate of inductance variation under faulty cases, the amplitudes of the stator and rotor self-inductance and mutual inductance show no significant changes, while the mutual inductance between search coil with rotor and stator windings show a high degree of variation.
3. The *demf* provides a sensitive signal with respect to fault since the amplitude of *demf* in the healthy case must be almost zero.
4. The variation of mean value and STD of *demf* proves that the fault alters the signal behaviour.
5. The occurrence of SE or DE fault significantly increases the energy of the signal that could be used as an early-stage fault indicator.
6. The studies of discrete wavelet sub-bands reveal that SE and DE faults greatly affect them. To quantify the fault severity, wavelet entropy is used. It shows that this approach can find SE and DE faults even in its early stage in SPSG. Furthermore, there is no need to specify the threshold value to detect the occurrence of failure, which is an additional advantage of this method.

ORCID

Hossein Ehya https://orcid.org/0000-0001-7264-2596

REFERENCES

1. Sadeghi, I., et al.: Online condition monitoring of large synchronous generator under short circuit fault—a review. In: 2018 IEEE international conference on industrial technology (ICIT), pp. 1843–1848. IEEE, Lyon (2018)
2. Nandi, S., Toliyat, H.A., Li, X.: Condition monitoring and fault diagnosis of electrical motors—a review. IEEE Trans. Energy Conversion. 20(4), 719–729 (2005)
3. Tabatabaei, I., et al.: Modeling and simulation of a salient-pole synchronous generator with dynamic eccentricity using modified winding function theory. IEEE Trans. Magn. 40(3), 1550–1555 (2004)
4. Babaei, M., et al.: A detailed analytical model of a salient-pole synchronous generator under dynamic eccentricity fault. IEEE Trans. Magn. 47(4), 764–771 (2011)
5. Al-Nuaim, N.A., Toliyat, H.: A novel method for modeling dynamic air-gap eccentricity in synchronous machines based on modified winding function theory. IEEE Trans. Energy Conv. 13(2), 156–162 (1998)
6. Bruzzese, C.: Diagnosis of eccentric rotor in synchronous machines by analysis of split-phase currents—part I: theoretical analysis. IEEE Trans. Ind. Electron. 61(8), 4193–4205 (2014)
7. Bruzzese, C.: Diagnosis of eccentric rotor in synchronous machines by analysis of split-phase currents—part II: experimental analysis. IEEE Trans. Ind. Electron. 61(8), 4206–4216 (2014)
8. Bruzzese, C., Joksimovic, G.: Harmonic signatures of static eccentricities in the stator voltages and in the rotor current of no-load salient-pole synchronous generators. IEEE Trans. Ind. Electron. 58(5), 1606–1624 (2011)
9. Ehya, H., et al.: Time domain signature analysis of synchronous generator under broken damper bar fault. In: IECON 2019 - 45th Annual Conference of the IEEE Industrial Electronics Society, vol. 1, pp. 1423–1428. Lisbon (2019)
10. Neti, P., Nandi, S.: Stator interturn fault detection of synchronous machines using field current and rotor search-coil voltage signature analysis. IEEE Trans. Ind. Appl. 45(3), 911–920 (2009)
11. Bellini, A., et al.: Advances in diagnostic techniques for induction machines. IEEE Trans. Ind. Electron. 55(12), 4109–4126 (2008)
12. Concari, C., Franceschini, G., Tassoni, C.: Toward practical quantification of induction drive mixed eccentricity. IEEE Trans. Ind. Appl. 47(3), 1232–1239 (2011)
13. Toliyat, H.A., Al-Nuaim, N.A.: Simulation and detection of dynamic air-gap eccentricity in salient-pole synchronous machines. IEEE Trans. Ind. Appl. 35(1), 86–93 (1999)
14. Ebrahimi, B.M., Etemadrezaei, M., Faiz, J.: Dynamic eccentricity fault diagnosis in round rotor synchronous motors. Energy Conversion Manage. 52(5), 2092–2097 (2011)
15. Sadeghi, I., Ehya, H., Faiz, J.: Analytic method for eccentricity fault diagnosis in salient-pole synchronous generators. In: 2017 International Conference on Optimization of Electrical and Electronic Equipment (OPTIM) & 2017 Intl Aegean Conference on Electrical Machines and Power Electronics (ACEMP), pp. 261–267. IEEE, Brasov (2017)
16. Kiani, M., et al.: Detection of rotor faults in synchronous generators. In: 2007 IEEE International Symposium on Diagnostics for Electric Machines, Power Electronics and Drives, pp. 266–271 Cracow (2007)
17. Iamamura, B.A.T., et al.: Study of static and dynamic eccentricities of a synchronous generator using 3-D FEM. IEEE Trans. Magn. 46(8), 3516–3519 (2010)
18. Iamamura, B.A.T., et al.: Study of synchronous generator static eccentricities — FEM results and measurements. In: 2012 XXth International Conference on Electrical Machines, pp. 1829–1835. Marseille (2012)
19. Simond, J., Xuan, M.T., Wetter, R.: An innovative inductive air-gap monitoring for large low speed hydro-generators. In: 2008 18th International Conference on Electrical Machines, pp. 1–5. Vilamoura (2008)
20. Perers, R., Lundin, U., Leijon, M.: Saturation effects on unbalanced magnetic pull in a hydroelectric generator with an eccentric rotor. IEEE Trans. Magn. 43(10), 3884–3890 (2007)

21. Biet, M.: Rotor faults diagnosis using feature selection and nearest neighbors rule: application to a turbogenerator. IEEE Trans. Ind. Electron. 60(9), 4063–4073 (2013)

22. Zamudio-Ramirez, I., et al.: Automatic diagnosis of electromechanical faults in induction motors based on the transient analysis of the stray flux via music methods. IEEE Trans. Ind. Appl. 56(4), 3604–3613 (2020).

23. Frosini, L., Harlişca, C., Szabó, L.: Induction machine bearing fault detection by means of statistical processing of the stray flux measurement. IEEE Trans. Ind. Electron. 62(3), 1846–1854 (2015)

24. Park, Y., et al.: Stray flux monitoring for reliable detection of rotor faults under the influence of rotor axial air ducts. IEEE Trans. Ind. Electron. 66(10), 7561–7570 (2019)

25. Jiang, C., Li, S., Habetler, T.G.: A review of condition monitoring of induction motors based on stray flux. In: 2017 IEEE energy conversion congress and exposition (ECCE), pp. 5424–5430. Cincinnati (2017)

26. Fireteanu, V.: Detection of the short-circuit faults in the stator winding of induction motors based on harmonics of the neighboring magnetic field. J. Phys. Conf. Ser. 450, 012021 (2013)

27. Fireteanu, V., Lombard, P., Constantin, A.I.: Detection of a short-circuit fault in the stator winding of induction motors through neighboring magnetic field harmonics. In: 2014 International Conference on Electrical Machines (ICEM), pp. 1555–1561. IEEE, Berlin (2014)

28. Cuevas, M., et al.: Noninvasive detection of winding short-circuit faults in salient pole synchronous machine with squirrel-cage damper. IEEE Trans. Ind. Appl. 54(6), 5988–5997 (2018)

29. Cuevas, M., et al.: Non-invasive detection of rotor short-circuit fault in synchronous machines by analysis of stray magnetic field and frame vibrations. IEEE Trans. Magn. 52(7), 1–4 (2016)

30. Faiz, J., Nejadi-Koti, H.: Eccentricity fault diagnosis indices for permanent magnet machines: state-of-the-art. IET Electr. Power Appl. 13(9), 1241–1254 (2019)

31. Wallin, M., Ranlof, M., Lundin, U.: Reduction of unbalanced magnetic pull in synchronous machines due to parallel circuits. IEEE Trans. Magn. 47(12), 4827–4833 (2011)

32. Wallin, M., Bladh, J., Lundin, U.: Damper winding influence on unbalanced magnetic pull in salient pole generators with rotor eccentricity. IEEE Trans. Magn. 49(9), 5158–5165 (2013)

33. Maxwell®, A.: ANSYS, Inc. Release (2019) R3.7

34. Ramirez-Nunez, J.A., et al.: Evaluation of the detectability of electromechanical faults in induction motors via transient analysis of the stray flux. IEEE Trans. Ind. Appl. 54(5), 4324–4332 (2018)

35. Ceban, A., Pusca, R., Romary, R.: Study of rotor faults in induction motors using external magnetic field analysis. IEEE Trans. Ind. Electron. 59(5), 2082–2093 (2011)

36. Povinelli, R.J., et al.: Diagnostics of bar and end-ring connector breakage faults in polyphase induction motors through a novel dual track of time-series data mining and time-stepping coupled Fe-state space modeling. IEEE Trans. Energy Conv. 17(1), 39–46 (2002)

37. Bangura, J.F., et al.: Diagnostics of eccentricities and bar/end-ring connector breakages in polyphase induction motors through a combination of time-series data mining and time-stepping coupled Fe-state-space techniques. IEEE Trans. Ind. Appl. 39(4), 1005–1013 (2003)

38. Zamudio-Ramirez, I., et al.: Detection of winding asymmetries in wound-rotor induction motors via transient analysis of the external magnetic field. IEEE Trans. Ind. Electron. 67(6), 5050–5059 (2020)

39. Bafroui, H.H., Ohadi, A.: Application of wavelet energy and Shannon entropy for feature extraction in gearbox fault detection under varying speed conditions. Neurocomputing. 133, 437–445 (2014) http://www.sciencedirect.com/science/article/pii/S0925231214000290

40. Oppenheim, A.V., Willsky, A.S., Nawab, S.H.: Signals Systems, 2nd ed. Prentice-Hall, Inc. New Jersey (1996)

41. Zheng-you, H., Xiaoqing, C., Ling, F: Wavelet entropy measure definition and its application for transmission line fault detection and identification; (part II: Fault detection in transmission line). In: 2006 International Conference on Power System Technology, pp. 1–5. Chongqing (2006)

42. Rosso, O.A., et al.: Wavelet entropy: a new tool for analysis of short duration brain electrical signals. J. Neurosci. Methods. 105(1), 65–75 (2001). http://www.sciencedirect.com/science/article/pii/S0165027000003563

43. Zamudio-Ramirez, I., et al.: Wavelet entropy to estimate the winding insulation healthiness in induction motors. In: IECON 2019 – 45th Annual Conference of the IEEE Industrial Electronics Society, vol. 1, pp. 3716–3722. Lisbon (2019)

44. Shannon, C.E.: A mathematical theory of communication. Bell Syst. Tech. J. 27(3), 379–423 (1948)

Paper VI

H. Ehya, A. Nysveen, B. Akin, and J. A. Antonino-Daviu, "Detection and Severity Estimation of Eccentricity Fault of a High Power Synchronous Generator," in IEEE Transactions on Reliability, Major Revision.

This paper is not yet published and therefore not included.

Paper VII

Comprehensive Broken Damper Bar Fault Detection of Synchronous Generators

Hossein Ehya ⓘ , *Student Member, IEEE*, and Arne Nysveen ⓘ , *Senior Member, IEEE*

***Abstract*—Reliable operation of synchronous generators in hydroelectric power plants is crucial for avoiding unplanned stoppages that can incur substantial costs. The damper winding of salient pole synchronous generators (SPSGs) contributes to machine operation only during transient periods; however, it is a critical component that preserves the dynamic stability and protects the rotor in case of a fault. Consequently, detection of a broken damper bar (BDB) fault is vital for safe operation. Current methods for the BDB detection depend on visual inspection or offline tests. However, most of the recently proposed approaches have used invasive sensors that can detect BDB faults only during transient operation. In this article, a novel method is proposed based on a noninvasive sensor with high sensitivity to BDB faults that can identify a BDB fault either during transient operation or in the steady-state (SS) period. The effectiveness of the proposed method is validated by finite-element modeling and by experimental results from a 100-kVA custom-made SPSG. The proposed method is confirmed to provide a reliable and sensitive diagnosis of BDB faults during transient or SS operation, even in noisy environments.**

***Index Terms*—Broken damper bar (BDB), condition monitoring, discrete wavelet transform, fault detection, salient pole synchronous generator (SPSG), stray magnetic field, wavelet entropy.**

I. Introduction

SALIENT pole synchronous generators (SPSGs) are the most commonly applied generator type in hydropower plants [1], and they are ubiquitous throughout the Norwegian power generation system. The generated hydroelectric power accounts for 95% of the total electricity production in Norway [2]; consequently, the proper operation and maintenance of hydroelectric generators are essential to meet the ever-increasing operational demands. Hydroelectric generators can suffer from incipient undetected faults that may result in catastrophic damage in the long term. The failure of an SPSG and the subsequent

steps required for restoration of power plant operations can create substantial expenses for the power producer.

The damper winding of the SPSG contributes to the operation of the machine both in transient and steady-state (SS) operation. It also improves the air-gap flux waveform. The transient periods of the synchronous generator includes the start-up period and the asynchronous operation due to power network transients. The damper winding protects the rotor field winding during a short-circuit fault on the stator side. The damper winding also affects the generator performance in the case of load, torque, and magnetization current variations [3]–[6]. Current continuously passes through the damper winding during both transient and SS operations. In transient operations, the synchronous generator operates in an asynchronous mode in which the magnetic field of the rotor and stator is not synchronized. This leads to the induction of voltages inside the damper cage and a consequent circulation of the current in the damper bars. Four factors cause these induced currents during SS operation of the machine: the air-gap magnetic field pulsation due to stator and rotor slotting effect [3], [7]; internal faults, like eccentricity and short circuits [8]; the stator load variation; and the space harmonics in the air-gap magnetic field due to the fractional slot winding layout [9].

Damper winding failure is not a prevalent type of fault in salient pole synchronous machines; however, this failure can significantly affect the performance of the machine. A broken damper bar (BDB) and a broken end ring fault in pumped storage generators, synchronous condensers, and salient pole synchronous motors are reported to cause starting failures, to reduce the efficiency of the performance, and ultimately to lead to machine depreciation [10]–[12]. Damper bar breakage can occur due to a deficient connection between the dampers and the end ring, to maloperation, to numerous starts and stops, and to thermo-mechanical stress due to uneven distribution of the current inside the rotor bars because of the saliency of the rotor pole [10]–[15]. A BDB creates higher currents, thereby, imposing greater mechanical and thermal tension on the remaining healthy damper bars.

The detection of a BDB fault in a synchronous machine has been mostly based on visual inspection [11]. In [16]–[18], offline test procedures have been proposed to detect BDB faults without machine disassembly. Although these proposed tests are effective and show superiority over visual inspection; however, they require stoppage of the machine, as well as the use of an extra controllable power source and access to the machine winding to conduct the tests. Moreover, the rotor must be rotated

manually, which is not possible for large-sized machines. In [19], an online method based on stator current harmonic analysis was introduced. However, the proposed method demonstrated a lack of sensitivity for BDB faults and also suggested that the harmonics for BDB detection were impacted by a static eccentricity fault. Previous work [10] confirmed that a BDB altered the air-gap magnetic field during the start-up period and could increase the start-up time of the machine, but other factors, like machine loading or improper coupling of the machine, can also increase the acceleration time. The air-gap magnetic field and stator current occurring during the acceleration time has been used to detect a BDB fault in [16]–[18]. However, although the air-gap magnetic field provides detailed information about the machine status, it is an invasive approach that requires dismantling of the machine and installing a Hall-effect sensor inside the air-gap on the stator teeth. Damper bar currents [20] and end ring currents [21] have also been used to detect a BDB fault during the SS operation of the machine. However, these methods are not practical in reality since they require expensive sensors and data transfer equipment from the rotor side to outside the machine, in addition to a damper winding modification. In [13], a synchronous generator was operated under a 25% unbalanced load to cause a negative sequence current to circulate inside the damper winding for detection of a BDB fault; however, the proposed method is again not practical for large synchronous generators. In [22], the induced voltage in the rotor field winding during acceleration time was utilized to detect a BDB fault; however, the use of a dc power source may affect the harmonic content and mask the fault harmonics.

A comprehensive study based on the state of the art and proposed methods in the industry demonstrates a need for a noninvasive and sensitive approach for discriminating a BDB fault. The novelty of this article is encompassed as follows.

1) *noninvasive* detection of a BDB fault based on the stray magnetic field;
2) BDB detection during *transient* or *SS* operation of the SPSG;
3) a novel criterion function to discriminate a BDB fault with high *sensitivity*.

The finite-element modeling (FEM) and experimental results of a 100-kVA custom-made SPSG under a controlled fault situation are provided to validate the proposed claims.

II. ELECTROMAGNETIC ANALYSIS

This section focuses on FEM of the synchronous generator. The motivation behind the use of FEM is to exhibit how the current inside the bars and end rings varies in a healthy generator and in one with a single BDB. Moreover, FEM is used to analyze the sensitivity of the stray magnetic field influenced by the generator configuration. FEM provides realistic results since it considers the nonlinearity of the applied material in the stator and rotor core. In addition, the eddy effect is taken into account.

The FEM obtains its geometrical specification and material characteristics from a custom-made 100-kVA, 400-V, 50-Hz synchronous generator with 14 salient poles. The synchronous generator under study is a 14-pole/114-slot machine with a
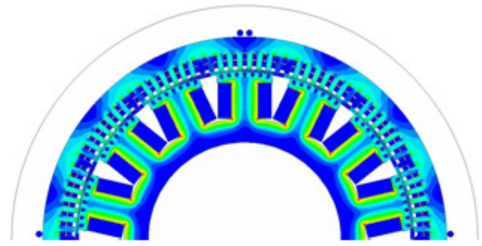

Fig. 1. FEM of an SPSG and the location of the installed sensor for radial flux measurement on the backside of the stator yoke.

TABLE I
100-kVA, 50-Hz, SYNCHRONOUS GENERATOR TOPOLOGY SPECIFICATION AND NAMEPLATE DATA

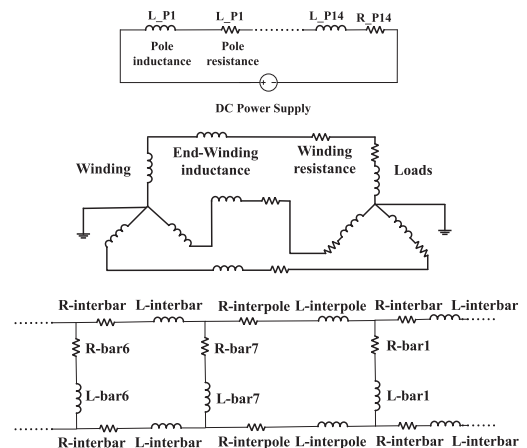| Quantity	Values	Quantity	Values
No. of slots	114	No. of damper bars/pole	7
Winding connection	Wye	Number of poles	14
No. of stator turns	8	No. of rotor turns / pole	35
Nominal speed	428 rpm	Power factor	0.90
Nominal voltage	400 V	Nominal current	144.3 A
Nominal exc. current	103 A	No-load exc. current	53.2 A

Fig. 2. External circuit of the salient pole synchronous generator linked into a finite element, including the rotor magnetization circuit, stator windings with connected loads, and damper bar circuit connections.

fractional slot winding. Each rotor pole consists of seven damper bars, which are distributed on the pole shoe. The dampers are short circuited on each side of the generator with two end rings. The connection between the rotor poles is made by the interpole connection rings. The two-dimensional FEM, as shown in Fig. 1, is utilized since the rotor is not skewed. The specification of the synchronous generator is presented in Table I. The ANSYS ELECTRONICS software is used to perform FEM [23]. The ANSYS external circuit, as shown in Fig. 2, is used to model the following [23]:

1) rotor field winding;
2) stator winding and load circuit;
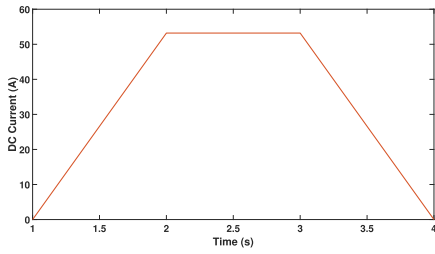3) rotor damper bars and end ring circuit.

Fig. 3. Waveform of the current applied to the rotor magnetization winding of 100-kVA SPSG during no-load operation.
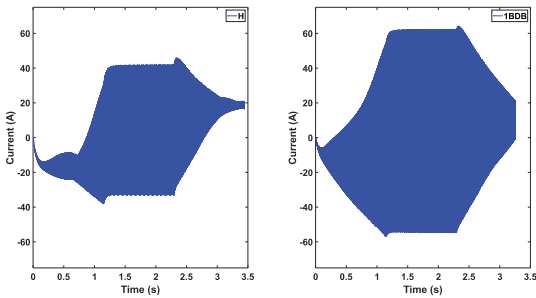

Fig. 4. Current in an interpole connection between two rotor poles based on an applied trapezoidal shape current at no-load at the rated speed. The left and right figures show healthy and faulty cases (one BDB), respectively.

In order to show how the current inside the damper bars and the end ring changes in a healthy case and under a BDB fault, a dc current source with a controllable waveform, as shown in Fig. 3, is utilized. The synchronous generator is under constant synchronous speed when the rotor field current is increased from zero to the nominal value, which is 53.2 A. The dc source waveform consists of three sections, in which the ramp-up (RU) and the ramp-down (RD) resemble the transient behavior of the machine, while a constant dc current is fed into the winding during the SS operation. In order to reduce the simulation time, each period is limited to eight mechanical revolutions of the machine. An accurate simulation is achieved by using a small time step (i.e., 10 μs).

An equivalent circuit of each damper bar and end ring consists of resistance and inductance. In the case of a BDB, the resistivity of the BDB is increased to reduce the amount of the current passing through the bar. This is obtained by considering a resistance in the order of megaohm for a faulty damper bar. Fig. 4 shows the current in the end ring in a healthy case and under a BDB fault (damper No. 7 in pole one is broken). The shape of the current amplitude inside the dampers and end rings is similar to the dc current imposed into the magnetization winding, which includes the transient and SS periods. The shape of the current amplitude inside the dampers differs since the location of the damper bars in the rotor shoe and their reluctance path also differ. Therefore, the shape of the current and the amplitude are different. The amplitude of the current in the bars located at the edge of the rotor pole shoe (in this generator, damper bar Nos.

Parameters	No. 1	No. 2	No. 3	No. 4
Rating power (MVA)	0.1	22	105	400
Frequency (Hz)	50	50	50	60
No. of poles	14	8	14	60
Stator outer Dia. (m)	0.78	2.64	4.54	11.27
Stator inner Dia. (m)	0.65	2.04	3.70	10.62
Stack length (m)	0.24	1.22	1.80	1.62

1 and 7) is higher than for the rest of the damper bars including damper bar Nos. 3, 4, 5, and 6. Since the reluctance of the path is higher for the bars located at the pole edge (damper bar Nos. 1 and 7), the more concentrated linkage flux is passed through the bar. The amplitude of the current decreases by reaching into the middle damper bar in the rotor pole shoe such as damper bar Nos. 3, 4, and 5 [22]. In the case of a BDB, the amplitude of the current in the faulty bar becomes almost zero, and the current of the adjacent bars, whether in the same pole or adjacent poles, is increased, as seen in Fig. 5 (blue and red waveforms). The amplitude of the maximum current in the adjacent faulty bar from the same pole ranges from 85 to 100 A, while the amplitude of the maximum current bar in the adjacent pole increases from 100 to 106 A. In Fig. 5, the green and pink waveforms represent the current in three damper bars where no interpole connection exists and the rotor poles are separated. In the case of one BDB fault, the BDB current does not flow in the interpole connection and it cannot affect the damper bar's current in the neighboring poles. Therefore, the damper bar current in the neighboring poles is unchanged, as shown in Fig. 5 (P2-B1 in green and pink waveforms).

In a large SPSG, the poles are connected to increase the subtransient reactance of the machine in the quadrature axis. A small subtransient reactance in the quadrature may lead to stability problems and cause vibrations. Therefore, the connection between the poles is indispensable. The end ring current changes in the case of a BDB. The amplitude of the current in the interpole connection between pole one and pole two is increased from an average of 32 A in a healthy case to 56 A in the case of one BDB in pole no. 1.

A. Impact of SPSG Configuration on the Stray Magnetic Field

Although the air-gap magnetic field provides accurate data for fault detection of the rotor failure, the stray magnetic field is the mirror of the air-gap magnetic field and can provide a fault-sensitive result. Four generators with different power ratings and topologies are modeled in FEM to investigate the impact of SPSG specification on the induced voltage in the installed sensor on the stator back side. Table II shows the specification of the generators used in FEM. The FEM of the SPSG No.1 is shown in Fig. 1, while the FEM of the SPSG No.2, No. 3, and No. 4 are depicted in Fig. 6. The 100-kVA, 14-poles SPSG has an outer diameter of 0.78 m and its stack length is 0.24 m, and a 400-MVA, 60-poles SPSG has an outer diameter of 11.27 m and its stack length is 1.62 m, are the smallest and largest modeled SPSG among the four models, respectively. Fig. 7 shows the
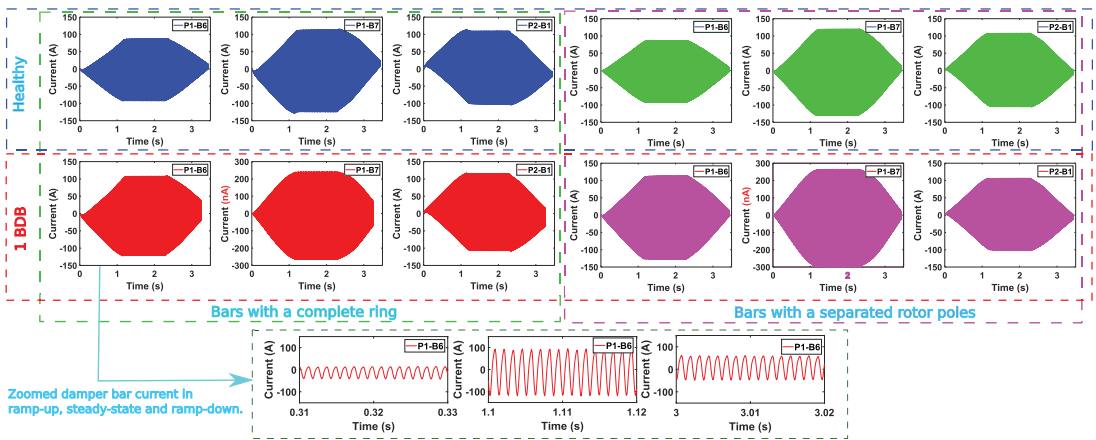
Fig. 5. Induced current in the rotor bars due to the trapezoidal shape of the field current in a healthy generator during no-load operation (blue and green waveforms) and with one BDB fault (Pole #1, bar #7 (P1-B7)) (red and pink waveforms). The first three columns are bars with a complete end ring, and the next three columns are for bars with separated rotor poles. The first three columns show the current in damper bar #6 in pole #1 (P1-B6), damper bar #7 in pole #1 (P1-B7), and damper bar #1 in pole #2 (P2-B1).
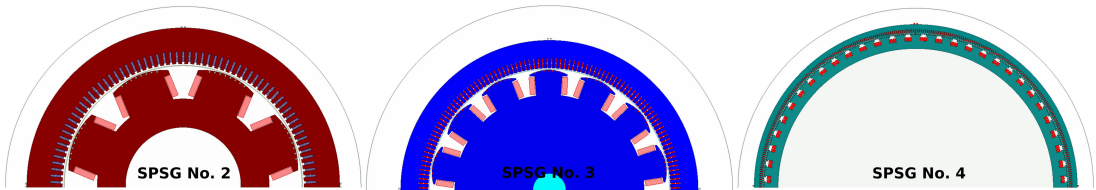

Fig. 6. FEM of three SPSGs with different power rating and topology.

existence of the stray magnetic field on the stator back-side of four modeled SPSGs regardless of their power rating, working frequency, number of pole pairs, the thickness and length of the stator yoke, and their topologies.

III. EXPERIMENTAL SETUP

The test rig shown in Fig. 10 was built to execute extensive experimental tests. The fault detection system consists of a 100-kVA, 400-V synchronous generator with 14 salient poles. The nameplate data and topology specification of the SPSG are presented in Table I. The SPSG was custom made to apply various kinds of faults, including BDB faults. The end ring and damper bars can be removed from each rotor pole. Fig. 9 shows a rotor pole, excluding the damper bars and end ring. A 90-kW, four-pole asynchronous motor drives the SPSG. The induction motor is supplied by a programmable frequency converter at the rated speed of 1482 r/min. The converter is connected to the power network. A 20-kW dc power supply (LAB-HP/E2020) is used to magnetize the rotor field windings. The connection between the SPSG and the motor is made by a gearbox.

The stray flux is captured with an in-house made sensor. The dimensions of the sensor are $(100 \times 100 \times 10)$ mm. The sensor has 3000 turns copper wire with a diameter of 0.12 mm. The resistivity and inductance of the search coil at its terminal is

912 Ω and 714 mH. The sensor is attached to the stator core and is capable of monitoring the combination of axial and radial flux. The designed sensor is cheap compared with Hall-effect sensors and it is robust to work in the industrial environment and power plants. A high-resolution 16-bit oscilloscope (Rohde Schwarz RTO2000) with a sampling frequency of 10 kHz is used for data acquisition.

The procedure of the experimental test was as follows: the damper bar was removed at standstill, then the SPSG, which was coupled to an induction motor, accelerated until it reached synchronous speed. A trapezoid shape dc current was fed into the magnetizing circuit, as depicted in Fig. 3. As shown in Fig. 3, the dc waveform included three stages. The RU and RD stages were used to resemble the transient behavior of the machine, while the constant dc current was for SS operation of the SPSG. The period of applied dc power source for each interval was 10 s. The test was carried out in no-load operation of the SPSG.

IV. SIGNAL PROCESSING

Different time-frequency processing methods have emerged and have been applied by developing signal processing technology. The time-frequency analysis has become crucial, especially for a signal with nonstationary characteristics. However, extracting a feature from a nonstationary signal is a difficult
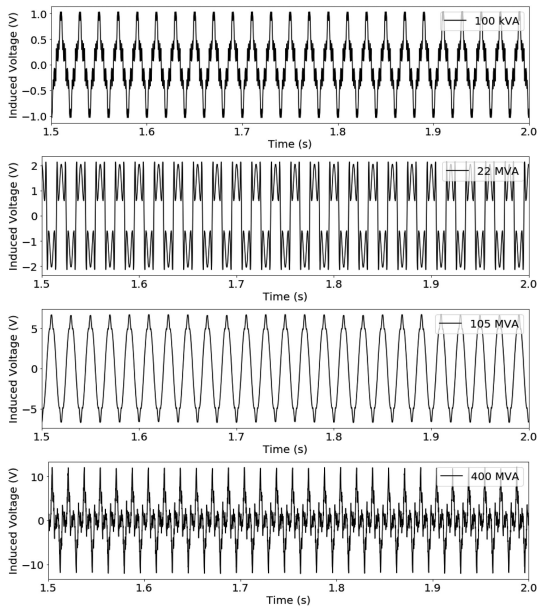
Fig. 7. Induced voltage in the sensor installed on the back side of the stator core due to the stray magnetic field in the no-load operation of four SPSGs with different power rating and specification.

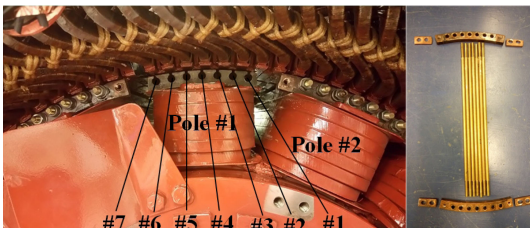Fig. 8. Experimental test rig of a 100-kVA synchronous generator with 14 salient poles.

Fig. 9. The pole with the removed rotor bars and end ring of the salient pole synchronous generator (left).The removed damper bars, end rings and the inter pole connection segments (right).

Fig. 10. Location of a noninvasive search coil sensor to capture the stray magnetic field installed on the back side of the stator yoke.

task. Therefore, a tool, referred to as information entropy, is required to investigate the information contained in a signal. A quantitative assessment of the signal is obtained by applying entropy to the processed data. Discrete wavelet transforms in a combination of Shannon entropy are utilized to introduce an index for the BDB fault diagnosis. The rudimentary concept behind the wavelet entropy is consideration of the wavelet subbands as a probability distribution and assessment of the degree of disorder in each subband based on the entropy concept. The next two sections provide a brief explanation of the discrete wavelet transform and Shannon entropy.

A. Discrete Wavelet Transform

The wavelet transforms of a discrete signal $S(k)$ contain the high-frequency and low-frequency components. The high-frequency and low-frequency components have their own coefficients at instant k and scale i, which are denoted as $d_i(k)$ and $a_i(k)$, respectively. The reconstruction of the signal frequency bands based on a discrete wavelet is shown as follows:

$$D_i(k) : [2^{-(i+1)} f_s, 2^{-i} f_s] \tag{1}$$

$$A_i(k) : [0, 2^{(i+1)} f_s] \tag{2}$$

where i is the maximum number of scales, and f_s is the sampling frequency of the signal. The sampling frequency of the signal and the number of subbands determine the frequency band of the levels. The reconstructed signal $S(k)$, based on its detail and approximate decomposition, is represented as follows:

$$S(k) = \Sigma_{i=1}^{i+1} D_i(k) \tag{3}$$

where A_i is substituted with $D_{i+1}(k)$. The common way to implement a discrete wavelet transform is based on a bank of high-frequency and low-frequency filters. The type of mother wavelet specifies the coefficients of the high-pass and low-pass filters. Among the various types of mother wavelets utilized for feature extraction of the faulty electric machines, the Daubechies family exhibits exceptional competency for fault detection purposes. Therefore, the Daubechies mother wavelet with eight subbands is used in this article.

B. Entropy

The states and probabilities of the event determine its uncertainty. The sample space, which includes all possible sets of the

state, is defined as follows:

$$S = s_1, s_2, s_3, \ldots, s_j \tag{4}$$

where the probability of each piece of information and its self-information are

$$P(s_i) = P_i \tag{5}$$

$$\Sigma P_i = 1 \tag{6}$$

$$I(s_i) = -\log P(s_i) = -\log P_i. \tag{7}$$

Although the self-information quantifies the whole information source, it is a random variable. Hence, it is not a suitable criterion. Consequently, to solve the random nature of the self-information, the mathematical expectation of the self-information is defined as the entropy of the information source, as follows:

$$E[I(S)] = E[\Sigma \log P_i] = -\Sigma P_i \log P_i. \tag{8}$$

The entropy gauges the uncertainty of events. In a case where whole events have the same probabilities, the uncertainty of the event, and consequently, its entropy attain maximum values. The value of the entropy is zero for any certain event.

Wavelet entropy was introduced in 1998 to process event-related potential [24]. Wavelet entropy has been used to analyze the nonstationary signal in various fields, like fault diagnosis of electric machines [25], power systems [26], and neuroscience [24]. In a case of a faulty situation, the information entropy will change, but it will not give detailed information about the frequency band that is distorted under the faulty situation. The wavelet transform, in combination with entropy, may discriminate the localized nonstationary frequencies due to the fault in each subband. The wavelet entropy is defined as follows:

$$WE = -\Sigma_j p_j \log p_j \tag{9}$$

where

$$p_j = \frac{E_{jk}}{E} \tag{10}$$

where E and E_j are the total signal energy and the energy of the each subband component, respectively, and are defined as follows:

$$E_{jk} = |D_j(k)|^2 \tag{11}$$

$$E_j = \Sigma_k E_{jk}. \tag{12}$$

V. RESULTS

The air-gap magnetic field of a synchronous generator in the no-load condition consists of a combination of the rotor magnetic field and the damper magnetic field. In the case of a loaded generator, the stator magnetic field also contributes to shaping the air-gap magnetic field. A BDB fault in an SPSG leads to an unbalanced distribution of the current in the damper winding, and consequently, an irregularity in the air-gap magnetic field. The stray magnetic field outside the machine mirrors the magnetic field inside the air-gap. Hence, the BDB fault in the SPSG changes the stray flux around the stator yoke. However,
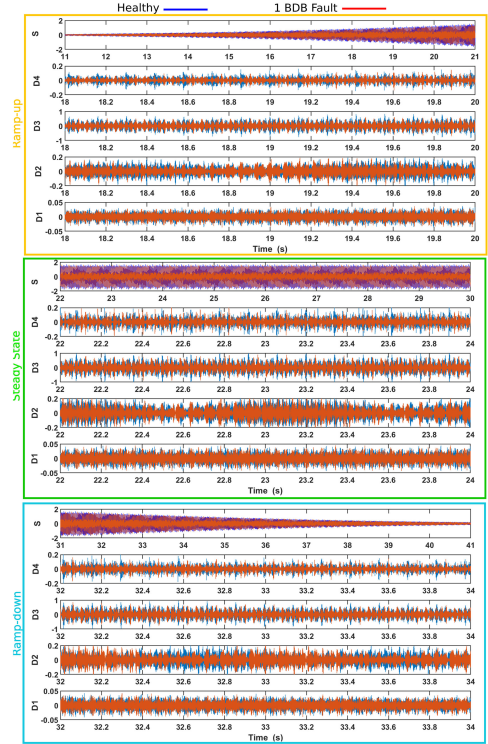

Fig. 11. Wavelet transform of the external measured magnetic field during no-load operation of the SPSG in healthy (blue) and with one BDB (red) in three cases: RU (top section), SS (middle section), and RD (lower section).

the modification due to the BDB fault is not only limited to the transient operation of the machine. Even during SS operation of the SPSG, the fault in the rotor bars alters the stray flux because the current is always passing through the damper bars, as shown in Fig. 5, due to the slot harmonics or the fractional winding configuration. BDB fault detection based on stray flux monitoring using the wavelet entropy is proposed since the computational complexity of the discrete wavelet transform is similar to fast Fourier transform, indicating that the proposed algorithm can be implemented online since the algorithm required computational time is limited to few seconds. The following sections describe the proposed algorithm as shown in Fig. 12.

A. Feature Extraction of a BDB Fault From Transient to SS Operation of the SPSG

Fig. 11 demonstrates the application of the discrete wavelet transform to the acquired stray flux field. The shape of the applied magnetization current to the rotor field winding is shown in Fig. 3, but the length of the signal for RU, SS, and RD is a total of 40 s in the experimental tests. The first rows in Fig. 11 are shown with the sign "S" to represent the acquired stray flux during the RU, SS, and RD periods, and this demonstrates
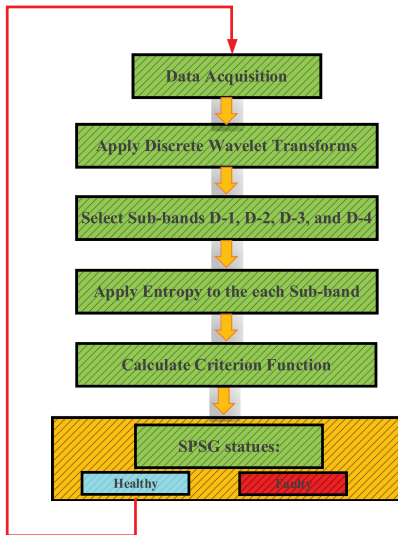
Fig. 12. Procedure of the BDB fault detection in an SPSG.

how the stray flux corresponds to the magnetization current. The healthy and faulty (one BDB) stray magnetic flux are colored in blue and red, respectively. Although some changes are evident in the waveform of the stray flux due to the appearance of the BDB fault, determining the degree of the fault is not possible. Therefore, the discrete wavelet transformed with the "Daubechies" mother wavelet is used to decompose the signal into eight subbands. A comprehensive comparison has been done between eight subbands of wavelet transform in healthy and under one BDB fault. However, only four subbands exhibit significant differences and are detailed as subbands one to four, with frequency components limited between 312.5 Hz and 5 kHz for a sampling frequency of 10 kHz. The frequency band of the wavelet subbands D1, D2, D3, and D4 are between 5000 and 2500 Hz, 2500 and 1250 Hz, 1250 and 625 Hz, and 625 and 312.5 Hz, respectively.

Since the variation in the stray flux under a BDB fault, in comparison to a healthy case, is noticeable, the value of the signal energy, and consequently, its entropy must be different. Thus, Shannon entropy is applied to the stray flux, which is decomposed by wavelet transform. The amplitudes of the wavelet entropy for subbands D4 and D3 under one BDB during the RU period are increased from 405 to 482 and 6 610 to 7 166, respectively. The magnitude of the wavelet entropy during the RD period is also increased for the D4 and D3 subbands, from 382 to 607 and from 6 397 to 8 355, respectively, under one BDB fault. Entropy applied to the stray flux of the detailed subbands of D4 and D3 during the SS operation exhibits significant changes. The magnitudes of the D4 and D3 subbands are increased from 959 to 1181 and from 10 403 to 11 473, respectively. Contrary to the assumption of a zero value for the current, and consequently, the magnetic field of the damper bars during SS, the obtained results questioned the proposed hypothesis.

In order to generalize the results, a new criterion function is proposed as follows:

$$\text{Criterion Function} = \frac{|\text{WEH}_{Di} - \text{WEF}_{Di}|}{\text{WEH}_{Di}} \times 100 \quad (13)$$

where WEH_{Di}, and WEF_{Di} are wavelet entropy of corresponding wavelet subband in the healthy and faulty cases, respectively. The introduced criterion function is normalized by dividing by the amplitude of the healthy wavelet entropy. The first row of Table III demonstrates the applied criterion function in the case of one BDB fault. The amplitude of the criterion function for each wavelet subband level differs depending on whether it occurs during transient or SS operation of the SPSG. The criterion function for subband D4 shows better sensitivity in comparison to the other subbands. In addition, the amplitude of the criterion function for one BDB during RD is higher than for RU and SS operation. Nevertheless, the result of applying the index to the stray flux during the SS operation also demonstrates the feasibility of the BDB detection during the SS operation.

B. Effect of the BDB Location on the Criterion Function

The rotor pole of an SPSG has a given shape in order to generate a flux waveform with minimized harmonics. Therefore, the distance of the rotor damper bars varies with respect to the stator inner diameter. The location of the damper bars imposes the magnitude of the current that should pass through them, since the reluctance of their pass differs and they encounter different flux density. The amplitude of the current is higher in the damper bars located on the rotor edges than in the damper bars embedded close to the center of the rotor pole. The amplitude of the damper bar current decreases closer to the center of the rotor pole. Hence, any breakage of damper bars other than the bars at the edges has less impact on the distortion of the stray flux. Consequently, the amplitude of the criterion function is decreased for these damper bars in comparison to the damper bars at the edge. In the case of a BDB fault for the damper #2, the amplitude of the criterion function becomes 13%, 7%, 5.1%, and 1.8% for wavelet subbands D4, D3, D2, and D1, respectively, during the RU period. The amplitude of the criterion function for BDB #2 is higher during RU than during the RD period. The magnitude of the criterion function for BDB #2 is also considerable during SS operation, which again shows the suitability of this approach for BDB detection during the SS period. The value of the criterion function during RU and RD should not be the same due to the saturation effect since the time constant during RU is higher and it requires more magnetizing current in order to reach a partly saturated point in a B–H curve while the magnetizing current reduces and the operating point of the generator changes from knee point to the linear part of a B–H curve indicating that more changes due to the BDB fault are expected in the RD period.

The trickiest BDB detection is for the bar located in the middle of the rotor pole for rotors with an odd number of damper bars. The reason is that the lowest amount of the current passes through this bar due to its location. Hence, its breakage has the least impact on the air-gap magnetic field distortion, and consequently, on the stray flux measured at the backside of the

<div align="center">

TABLE III
VALUE OF CRITERION FUNCTION FOR FOUR WAVELET SUBBANDS FOR DIFFERENT NUMBER OF BDB FAULTS IN THE SPSG OPERATING IN NO-LOAD CONDITION IN THREE TIME INTERVALS

</div>

Cases	Ramp-up interval				Steady-state interval				Ramp-down interval			
	D-4	D-3	D-2	D-1	D-4	D-3	D-2	D-1	D-4	D-3	D-2	D-1
1BDB #1	15.97%	7.75%	3.37%	7.4%	18.8%	9.3%	10.1%	7.9%	37%	23.4%	17.1%	15.9%
1BDB #2	13%	7%	5.1%	1.8%	7.1%	2.4%	2.5%	1.75%	6%	1.8%	1.1%	2.9%
1BDB #4	0.6%	0.4%	2.9%	1.8%	5.1%	3.1%	3.5%	3.5%	11.36%	7.6%	6.7%	8.7%
2BDB #1 & #2	31.7%	19.4%	7.2%	1.8%	15.3%	7.3%	6.3%	0.8%	20.4%	11.4%	0.4%	5.8%
2BDB #1 & #7	25.1%	12.1%	4.2%	5.5%	13.3%	4.1%	2.0%	6.1%	20.9%	9.4%	0	4.3%
3BDB #3 & #4 & #5	7.2%	3.6%	0.2%	1.8%	3.9%	3.1%	1.45%	0	7.5%	4.5%	2.1%	1.4%
7BDB #1 to #7	31.5%	18.1%	12.1%	5.5%	29.7%	15.1%	18.8%	18.4%	44.1%	28.4%	24.1%	23.1%

yoke. Table III demonstrates how the criterion function responds to one BDB fault in the middle of the rotor pole shoe (damper #4). As already stated, the detection during the RU period is challenging because the amplitude of the wavelet entropy for all four subbands is not considerable. However, detection during the RD and SS period is noticeable. For instance, the amplitudes of the criterion function become 11.36% and 5.1% for the subband D4 during the RD.

C. Multiple BDB Fault Detection

In the case of a single BDB, the majority of the BDB current passes through its neighboring bars, while the cross section of the damper bars is designed to carry the current that is designed for. Therefore, the additional current leads to a loss increment, and consequently, to a local hot spot. The result of this process in the long term is breakage of the adjacent bars. In the case of a BDB fault in two damper bars (#1 and #2), the criterion function is increased to 31.7%, 19.4%, 7.2%, and 1.8% for the D4, D3, D2, and D1 wavelet subbands, respectively, during RU. This shows that the amplitude of the criterion function is increased almost twofold in comparison to a single BDB fault. However, the amplitude of the criterion function is decreased for two BDB faults occurring during the SS and RD periods.

In the case of two BDB faults, each occurring at the corner of the same pole and exactly opposite to each other, the magnitude of the criterion function is decreased. The reason is that a symmetry exists in the nonuniform magnetic field due to the two BDB faults. As expected, the magnitude of the criterion function must be more than that for a single BDB, but less than two adjacent BDB faults. The criterion function during RU for subbands D4, D3, D2, and D1 is 25.1%, 12.1%, 4.2%, and 5.5%, respectively. The same trend is observed for the criterion function during the SS and RD periods.

Although increasing the number of BDBs leads to a criterion function increment, the criterion function in the case of three BDBs in the middle of the rotor pole is not considerable. The reason is that the amount of the current passing through the bars in the center and its adjacent bars is less than other damper bars current and the adjacent bars of the middle bar have a symmetry in the created nonuniform magnetic field, which reduces the asymmetry of the air-gap magnetic field and the stray flux. The BDB detection is possible during the RU, SS, and RD periods since a considerable increase occurs in the criterion function, especially in the D4 subband. In the worst case, where all damper bars of the same pole are broken, a significant increment

<div align="center">

TABLE IV
VALUE OF THE CRITERION FUNCTION FOR FOUR WAVELET SUBBANDS FOR ONE BDB FAULT IN A SYNCHRONOUS GENERATOR WITH SEPARATED SALIENT POLES DURING NO-LOAD OPERATION

</div>

Periods	Sub-band 4	Sub-band 3	Sub-band 2	Sub-band 1
Ramp-up	5.5%	1.9%	1%	3.4%
Steady-state	0.1%	0.3%	0.7%	0.5%
Ramp-down	4%	5.9%	5.5%	3.3%

occurs in the criterion function. The amplitude of the criterion function for all subbands during the RU, RD, and SS operation is increased significantly.

D. Interpole Connection Effect on BDB Index

In large SPSGs, the damper bars are connected at both sides of the machine, either by a continuous ring or by an interpole connection between each pole. In an SPSG with a large number of poles, the use of a continuous ring is preferable to having an interpole connection since the centrifugal force acting on them may result in mechanical deformation. Removing the interpole connection between the poles results in a subtransient salience (the difference between the subtransient reactance in the d- and q-axes), which in turn results in a huge short subtransient circuit current in the case of a phase-to-phase short-circuit fault. In addition, the induced open-phase voltage in a healthy winding may increase up to twice the maximum voltage. However, some cases occur where the rotor poles are isolated and the damper bars are short circuited by the end ring in each separate pole. Removing the interpole connections may reduce the cost and may also avoid any damage to the SPSG, since the centrifugal force causes deformation in the long run.

The proposed method and the criterion function have been applied to an SPSG without interpole connections. Table IV shows the result for a case of a single BDB fault (bar #1 was removed). The amplitude of the criterion function did not increase significantly, unlike the case of a rotor with a continuous ring. The amplitudes of the D4, D1, and D4 to D1 subbands during RU and RD were increased; however, their increments are similar to those of the BDB fault in bar #4 in a case with a continuous ring. The results obtained from an SS operation show that the detection of a BDB fault is almost impossible during this period. The reason is that the current in the damper bar circulates between the poles. In the case of isolated poles, no circulating current exists between the poles and the BDB fault cannot significantly distort the magnetic field, and correspondingly, the stray flux.
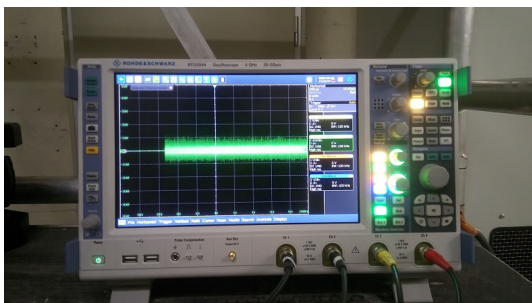
Fig. 13. Measured noise in a hydropower plant.

TABLE V
VARIATION IN THE CRITERION FUNCTION DURING SS OPERATION OF AN SPSG UNDER DIFFERENT DEGREES OF WHITE GAUSSIAN NOISE

Noise Level	Sub-band 4	Sub-band 3	Sub-band 2	Sub-band 1
No-noise	18.8%	9.3%	10.1%	7.9%
80 dB	18.6%	9.3%	10.1%	7.9%
60 dB	18.7%	10.2%	10%	7%
40 dB	19.9%	10.3%	9.9%	6.8%
20 dB	19.6%	9.6%	6.5%	0.4%

E. Noise Effect on Index

A desirable dataset without noise interference is preferable for signal processing of faulty electric machines, as noise may mask the fault indices or give a false positive fault signal. Various kinds of noise may exist in a power plant, with the most prevalent kind being white Gaussian noise. Fig. 13 shows the measured noise in a Norwegian hydropower plant. Therefore, the appearance of noise in the measured data is unavoidable, and its effect on the proposed feature criterion must be studied. An analysis of the measured data in the power plant demonstrates that the existing type of noise is white Gaussian noise with a signal-to-noise ratio of 75 dB.

The proposed criterion function was also investigated under impact of white Gaussian noise with different ratio levels of 80, 60, 40, and 20 dB. The proposed criterion function is not robust to the noise effect during the transient operation of the SPSG. The amplitude of the criterion function for the subband D4 during RU and RD changed from 15.9% and 37% in a no-noise situation to 33.4% and 20.7% with 20-dB noise. This result shows that the detection during RU and RD is impossible for an SPSG operating in environment with a noise ratio above 20 dB, even though the amplitude of the criterion function for the SS operation is unchanged. Table V shows the results for the criterion function under a noise effect during the SS operation. As seen in Table V, the amplitude of the index is almost unchanged.

VI. CONCLUSION

In this article, a novel approach was proposed for the diagnosis of BDB faults in an SPSG. A trapezoidal shape current was utilized as a rotor power source that included RU, SS, and RD regions that were symbols of transient and SS operation of the SPSG. The criterion function was introduced based on wavelet entropy analysis of the stray magnetic field for an accurate BDB detection. The detection was not limited to the transient operation of the SPSG, and it could diagnose a fault with a high sensitivity even during the SS operation. The obtained criterion function in RU, SS, and RD were complementary features for the BDB detection in the way that if the operator finds any increment in the criterion function in one of the operating regions, he should check the criterion function for the other operating conditions in order to avoid a false alarm. The location of the BDB fault had a significant impact on the magnitude of the criterion function since the amplitude of the current that passes in the damper bars depends on the location of the damper bar in the rotor pole shoe. The measurement in a power plant showed that the operating environment of synchronous generators was vulnerable to noise. Therefore, the efficacy of the proposed index was examined and was deemed robust to a high rate of noise that indicated the method's reliability.

The experimental results for a small-scaled 100-kVA salient pole synchronous generator running in a Norwegian hydropower plant verified the feasibility of using the proposed method for the BDB fault diagnosis. The method had no need for machine disassembly to install sensors inside the machine. The high sensitivity of the method was demonstrated, even for the detection of a middle broken bar. Detection was also possible during both transient and SS operation of the machine, demonstrating the superiority of the proposed method over the existing methods. The proposed method was based on the no-load operation of the SPSG. The BDB detection for a loaded SPSG was only possible during the SS operation since the generator cannot connect to the grid before it reaches the nominal voltage. The criterion function for a loaded SPSG must be performed in the same magnetization current in the healthy and faulty cases since the variation in the stray magnetic field was influenced by the loading condition.

REFERENCES

[1] D. P. Kothari and I. J. Nagrath, *Electric Machines. Tata McGraw-Hill Education*, 2004.
[2] *08583:Elektrisitetsbalanse (MWh) 2010M01–2019M09*. 2019. [Online]. Available: http://www.ssb.no/statbank/table/08583/
[3] G. Traxler-Samek, T. Lugand, and A. Schwery, "Additional losses in the damper winding of large hydrogenerators at open-circuit and load conditions," *IEEE Trans. Ind. Electron.*, vol. 57, no. 1, pp. 154–160, Jan. 2009.
[4] R. Wamkeue, I. Kamwa, and M. Chacha, "Line-to-line short-circuit-based finite-element performance and parameter predictions of large hydro-generators," *IEEE Trans. Energy Convers.*, vol. 18, no. 3, pp. 370–378, Sep. 2003.
[5] J. Machowski, J. Bialek, J. R. Bumby, and J. Bumby, *Power System Dynamics and Stability*. Hoboken, NJ, USA: Wiley, 1997.
[6] A. M. Knight, H. Karmaker, and K. Weeber, "Use of a permeance model to predict force harmonic components and damper winding effects in salient pole synchronous machines," in *Proc. IEEE Int. Elect. Mach. Drives Conf.*, 2001, pp. 179–184.
[7] J. Matsuki, T. Katagi, and T. Okada, "Effect of slot ripples on damper windings of synchronous machines," in *Proc. IEEE Int. Symp. Ind. Electron.*, 1992, pp. 864–865.
[8] C. Bruzzese and G. Joksimovic, "Harmonic signatures of static eccentricities in the stator voltages and in the rotor current of no-load salient-pole synchronous generators," *IEEE Trans. Ind. Electron.*, vol. 58, no. 5, pp. 1606–1624, May 2010.
[9] M. Ranlöf and U. Lundin, "The rotating field method applied to damper loss calculation in large hydrogenerators," in *Proc. Int. Conf. Elect. Mach.*, 2010, pp. 1–6.

[10] H. C. Karmaker, "Broken damper bar detection studies using flux probe measurements and time-stepping finite element analysis for salient-pole synchronous machines," in *Proc. 4th IEEE Int. Symp. Diagnostics Elect. Mach., Power Electron. Drives*, 2003, pp. 193–197.

[11] P. J. Berry and E. S. Hamdi, "An investigation into damper winding failure in a large synchronous motor," in *Proc. 50th Int. Univ. Power Eng. Conf.*, 2015, pp. 1–4.

[12] S. K. Sahoo, P. Rodriguez, and M. Sulowicz, "Comparative investigation of fault indicators for synchronous machine failures," in *Proc. Int. Conf. Elect. Mach.*, 2014, pp. 1503–1509.

[13] J. Bacher, "Detection of broken damper bars of a turbo generator by the field winding," *Renewable Energy Power Quality J.*, vol. 1, pp. 199–203, 2004.

[14] J. A. Antonino-Daviu, M. Riera-Guasp, J. Pons-Llinares, J. Roger-Folch, R. B. Perez, and C. Charlton-Perez, "Toward condition monitoring of damper windings in synchronous motors via EMD analysis," *IEEE Trans. Energy Convers.*, vol. 27, no. 2, pp. 432–439, Jun. 2012.

[15] H. Karmaker and C. Mi, "Improving the starting performance of large salient-pole synchronous machines," *IEEE Trans. Magn.*, vol. 40, no. 4, pp. 1920–1928, Jul. 2004.

[16] J. Yun *et al.*, "Airgap search coil-based detection of damper bar failures in salient pole synchronous motors," *IEEE Trans. Ind. Appl.*, vol. 55, no. 4, pp. 3640–3648, Jul./Aug. 2019.

[17] J. Antonino-Daviu *et al.*, "Electrical monitoring of damper bar condition in salient-pole synchronous motors without motor disassembly," *IEEE Trans. Ind. Appl.*, vol. 56, no. 2, pp. 1423–1431, Mar./Apr. 2020.

[18] Y. Park, S. B. Lee, J. Yun, M. Sasic, and G. C. Stone, "Air gap flux-based detection and classification of damper bar and field winding faults in salient pole synchronous motors," *IEEE Trans. Ind. Appl.*, vol. 56, no. 4, pp. 3506–3515, Jul./Aug. 2020.

[19] P. Neti, A. B. Dehkordi, and A. M. Gole, "A new robust method to detect rotor faults in salient-pole synchronous machines using structural asymmetries," in *Proc. IEEE Ind. Appl. Soc. Annu. Meeting*, 2008, pp. 1–8.

[20] F. Holmgren, "Damper winding fault detection in synchronous machines," Master thesis, Univ. Uppsala, Uppsala, Sweden, p. 54, Nov. 2016.

[21] P. Rodriguez, "Method and a diagnostics device for determining a fault condition in a synchronous motor," *Euro Patent EP3401693*, Nov. 2018.

[22] H. Ehya, A. Nysveen, R. Nilssen, and U. Lundin, "Time domain signature analysis of synchronous generator under broken damper bar fault," in *Proc. 45th Annu. Conf. IEEE Ind. Electron. Soc.*, 2019, vol. 1, pp. 1423–1428.

[23] *Academic Research Electronics Desktop, ANSYS Release R2.4.* 2020.

[24] O. A. Rosso *et al.*, "Wavelet entropy: A new tool for analysis of short duration brain electrical signals," *J. Neurosci. Methods*, vol. 105, no. 1, pp. 65–75, 2001. [Online]. Available: http://www.sciencedirect.com/science/article/pii/S0165027000003563

[25] I. Zamudio-Ramirez, R. A. Osornio-Rios, R. d. J. Romero-Troncoso, and J. A. Antonino-Daviu, "Wavelet entropy to estimate the winding insulation healthiness in induction motors," in *Proc. 45th Annu. Conf. IEEE Ind. Electron. Soc.*, 2019, vol. 1, pp. 3716–3722.

[26] H. Zheng-you, C. Xiaoqing, and F. Ling, "Wavelet entropy measure definition and its application for transmission line fault detection and identification; (Part II: Fault detection in transmission line)," in *Proc. Int. Conf. Power Syst. Technol.*, 2006, pp. 1–5.

Hossein Ehya (Student Member, IEEE) received the M.Sc. degree in electrical engineering from the Department of Electrical and Computer Engineering, University of Tehran, Tehran, Iran, in 2013. He is currently working toward the Ph.D. degree in electrical engineering with the Norwegian University of Science and Technology, Trondheim, Norway.

From 2013 to 2018, he worked as an Electrical Machine Design Engineer in electrical machine companies. His research interests include the design and condition monitoring of electrical machines, signal processing, pattern recognition, and machine learning.

Mr. Ehya was the recipient of the ICEM Jorma Luomi Award in Gothenburg, Sweden, in 2020.

Arne Nysveen (Senior Member, IEEE) received the M.Sc. degree and Dr.ing. degree (Ph.D.) from the Norwegian Institute of Technology (now Norwegian University of Science and Technology), Trondheim, Norway, in 1988 and 1994, respectively, both in electric power engineering.

From 1995 to 2002, he was a Senior Scientist with ABB Corporate Research, Oslo, Norway. Since 2002, he has been a Professor with the Norwegian University of Science and Technology. He is currently a Manager for the research on Turbine and Generator Technologies, Norwegian Research Center for Hydropower Technology (HydroCen). His current research interests include design, modeling, and monitoring of hydroelectric generators.

Paper VIII

Paper VIII

Performance Evaluation of Signal Processing Tools Used for Fault Detection of Hydrogenerators Operating in Noisy Environments

Hossein Ehya ⓘ, *Student Member, IEEE*, Arne Nysveen ⓘ, *Senior Member, IEEE*, and Tarjei N. Skreien ⓘ

Abstract—Signal processing plays a crucial role in addressing failures in electrical machines. Experimental data are never perfect due to the intrusion of undesirable fluctuations unrelated to the investigated phenomenon, namely so-called noise. Noise has disturbing effects on the measurement data and, in the same way, could diminish or mask the fault patterns in feature extraction using different signal processors. This article introduces various types of noise occurring in an industrial environment. Several measurements are performed in the laboratory and power plants to identify the dominant type of noise. Fault detection in a custom-made 100-kVA synchronous generator under an interturn short-circuit fault is also studied using measurements of the air-gap magnetic field. Signal processing tools such as fast Fourier transform, short-time Fourier transform (STFT), discrete wavelet transform, continuous wavelet transform (CWT), and time-series data mining are used to diagnose the faults, with a central focus on additive noise impacts on processed data. Two novel patterns are introduced based on STFT and CWT for interturn short-circuit fault detection of synchronous generators that do not need *a priori* knowledge of a healthy machine. Useful methods are presented for hardware noise rejection.

Index Terms—Fault diagnosis, interturn short circuit (ITSC), noise rejection, salient pole synchronous generator, short-time Fourier transform (STFT), signal processing, time-domain analysis, wavelet transforms.

I. INTRODUCTION

EARLY-STAGE diagnosis of incipient faults in electrical machines can limit the progressive damage that leads to substantial economic losses. Over the past two decades, sustained research activity has been conducted in the field of fault detection of electrical machines. Faults in hydrogenerators are divided into two categories: electrical faults, such as short-circuit faults of stator windings or interturn short-circuit (ITSC) faults in rotor field windings, and mechanical faults, such as static or dynamic eccentricity, broken damper bars, broken end rings, and misalignment. Each type of fault in an electrical machine can give rise to a specific symptom, which may be observed in a measured signal [1].

The working environment of electrical machines in the industries and power plants is susceptible to various kinds of noise that may have considerable consequences on the measured signals [2]. The working environment of synchronous generators in hydropower plants is vulnerable to noise emitted from power transformers, power station busbars and switchgear, the turbine, and the machine itself. In addition, industrial induction motors controlled by a static converter may create interfering noise [3]–[5]. The amplitude and frequency of the emitted noise by the converter depend on the modulation techniques used in the power converter [6].

Previous studies [7] have shown that the majority of industries are subjected to a high degree of complex noise, which is the combination of white Gaussian noise and impulsive noise. The amplitude of the noise in the working environment of the industry depends on various criteria [8], and the noise profile varies from case to case. In addition to noise emitted from the equipment used in the industry, faulty electrical machines also cause some degree of noise [9], and the noise level is increased with the increasing severity of the fault.

Feature extraction and signal processing is the central part of a fault detection procedure. Numerous indices are proposed based on the various signal processing tools capable of detecting different types of fault in electrical machines. The main component of fault detection is a measured signal from the faulty machine in the form of an air-gap magnetic field, stator or rotor current, voltage, stray magnetic field, or torque. If the working environment is vulnerable to noise, having a signal not contaminated by noise is almost impossible, indicating that the noise effect on the measured signal must be considered. In addition, the noise might affect the fault signature extracted by signal processing tools and result in a false alarm, since various signal processing tools might respond differently to the noise presence.

The fast Fourier transform (FFT) is the most commonly applied signal processing tool in the fault detection of electrical machines. The FFT is applied to the stator current and voltage, torque, air-gap magnetic field, and stray magnetic

flux of different electrical machines, such as induction motors, permanent magnetic machines, and salient pole synchronous machines, to detect a fault [1], [10]–[14]. Although the FFT is simple and has low computational complexity, it does not show clear changes in the spectrum plot for a fault with low severity nor does it determine the type of fault. Moreover, the FFT only depicts the frequency contents of the signal, whereas it lacks time representation. Therefore, the demand for methods that could overcome these shortcomings has resulted in advanced signal processing tools, such as short-time Fourier transform (STFT), continuous wavelet transform (CWT), and discrete wavelet transform (DWT).

Application of these advanced signal processing tools to fault detection problems has indicated that they could meticulously identify a certain pattern due to the specific type of fault in electrical machines. For instance, the STFT is used to detect broken bars and ITSC faults in salient pole synchronous generators [15]–[17] and was able to provide a unique pattern for each type of fault. In [18] and [19], the CWT was used to identify broken bars and eccentricity faults in induction motors. Unlike the STFT and the CWT, which provide a qualitative representation of a measured signal, the DWT classifies the signal into different frequency bands. The DWT has been used to diagnose different kinds of fault in induction motors [18], [19], salient pole synchronous generators [20], and permanent magnet machines [21]. These advanced signal processing tools have been widely used for fault detection in electrical machines, but they have not considered the noise effect, although some attempts have been made to address this issue in [22] and [23].

The present work is a detailed study of the noise impact on the signal processing tools used in the fault diagnosis of hydroelectric synchronous generators and how noise impact must be considered in the fault detection procedure, as depicted in Fig. 1. The Hall effect sensor is used to measure the air-gap magnetic field since it is exposed to both internal noise generated by the machine and external noise in the environment. A custom-made 100-kVA synchronous generator is used to conduct the ITSC fault and provide the required data. Section II presents a definition of signal and noise. It also thoroughly presents a source of noise in a power plant and industry. Various types of noise are introduced to provide a perspective for characterizing the existing types of noise in a power plant. In Section III, the experimental setup used to measure the air-gap magnetic field is explained. The results of two field tests are discussed to show the existence of noise in the hydropower plants. In Section IV, the effects of noise on signal processing tools, such as FFT, STFT, CWT, DWT, and time-series data mining (TSDM), are investigated. The impacts of noise on the extracted signature by the signal processing tools are discussed. The obtained results demonstrate how a certain level of noise can deteriorate the fault signatures.

II. SIGNAL AND NOISE

A. Definition

The term "signal" in the field of condition monitoring means only the desirable data that are measured. However, signals are vulnerable to noise during the process of acquisition, storage,
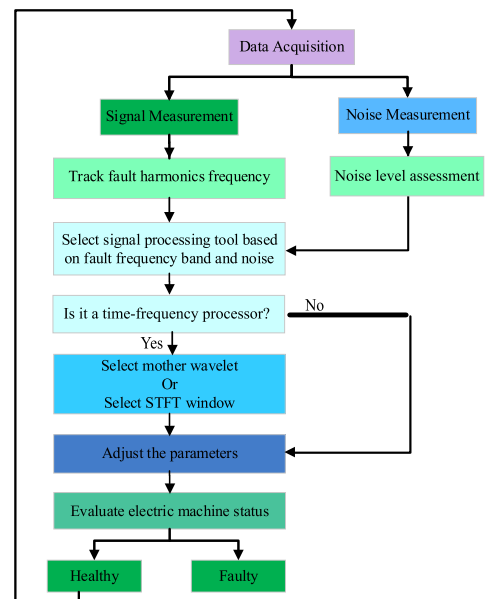

Fig. 1. Flowchart for fault detection.

or conversion. Noise is an unwanted signal that may disrupt the quality of the main signal. Every device in the power plant or industry that works based on the electromagnetic law may act as a noise source. The noise generated by each electric device has its own unique characteristics that fall into a specific category of noise. The noise level can be expressed as a ratio of the power in 1 Hz of bandwidth (dBm/Hz), where power is expressed in units of dBm. The quality of the signal is quantified by the expression of the signal-to-noise ratio (SNR). It represents the ratio of the signal amplitude to the standard deviation of the noise [2].

B. Source of Noise in Industries

The noise radiated from electric equipment is generally limited to a discrete low-frequency signal. However, an electrical machine, whether stationary (e.g., transformers) or rotating (e.g., electric motors or generators), generates a broadband noise component due to its cooling systems. The net noise is superimposed on the electromagnetic and cooling system components. The noise in an electric machine can be represented as follows [2], [5].

1) The magnetic source of noise in the electrical machine is due to the radial force created by the interaction of the stator and rotor magnetic field. When magnetic flux inside the air gap passes in a radial direction, a radial component of the force creates vibration and noise. A severe resonance happens if a frequency of the radial force components coincides with a natural frequency of the machine. Acoustic noise is one of the consequences of the resonance in the machine. The structure of the rotor and the slot harmonics cause high-frequency components
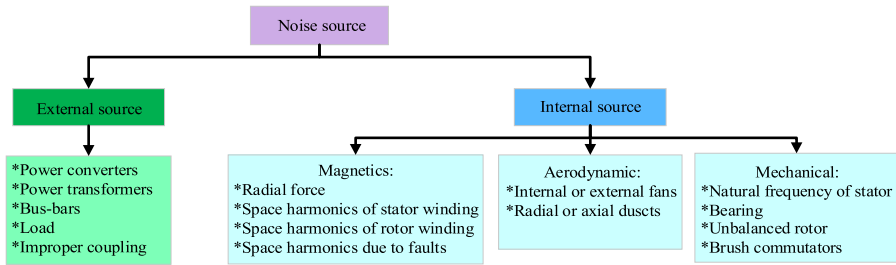
Fig. 2.   Sources of noise in the industries and power plants.

that, in turn, lead to force and noise inside the machine. Moreover, there exist some other sources of magnetic noise including the product of the space harmonics of stator and rotor winding, the product of space harmonics of the stator winding and the eccentricity fault, and the product of stator space harmonics and the rotor saturation harmonics.

2) The aerodynamic source of noise has a broad frequency band (100 Hz–10 kHz) that is generated due to the flow of the air at the inlet or outlet of the machine cooling system. The fans either inside the machine driven by the shaft or the external can generate acoustic noise. The axial or radial ventilation ducts inside the stator core also contribute to the noise.

3) The mechanical source of noise arises due to the natural frequency of the stator, improper installation of the machine, shaft, and bearing vibration. If the exciting frequency of the machine coincides with the stator's natural frequency, a strong noise will be created. The improper coupling between the shaft of the synchronous machine and the driving component or the load is also accounted as a mechanical source of the noise. There exist three main factors that result in a mechanical noise due to bearings, brush commutators, and the unbalanced rotor during manufacturing. The sleeve bearing compared with the rolling bearing contributes to less noise; however, the rolling bearing is preferred due to low cost especially in low-power electric machines.

The amount of noise created by transformers is significant in comparison to the noise in rotating electrical machines. The source of the noise in power transformers is divided into magnetic noise, which is due to the magnetic field of the core, and the load noise, which is caused due to interaction of the leakage flux and the current passing through the coils [3]. However, the metallic body of the transformer may shield the emitted noise from the working environment, even if the generated noise is unavoidable. The power transformers in power plants are also placed in a separate room for safety reasons, and this further reduces their effect on the measured signal from the synchronous generator. Busbars that carry large current from the generator to the transformer are another source of noise in power plants.

Many electrical motors use solid-state converter drives to feed power sources into the windings. The power supply is not entirely sinusoidal and contains numerous harmonics and subharmonics. The most important harmonics created are 5th, 7th, and 11th, which become critical if these harmonics coincide with a natural frequency of the stator [4]. The net forces due to the power electronics harmonic components result in significant noise. Fig. 2 shows the different sources of noise.

C. Various Types of Noise

Various types of noise, based on their properties, have different effects on the measured signal. The signal from the noise can be discriminated based on the frequency components. The signal may contain mostly low-frequency components, whereas the noise may spread out over the wide frequency range or the noise may only contain high-frequency components. The noise is characterized based on its frequency spectrum, which is commonly described in terms of noise color. The noise is categorized as white noise, pink noise, Brownian noise, blue noise, and violet noise. Each type of noise is specified according to the frequency distribution of its power spectral density, as shown in Fig. 3.

1) White noise is a random noise that has equal power over the entire frequency range.
2) Pink noise is characterized by high power at low frequencies, and its power is diminished by increasing the frequency.
3) Brownian noise's amplitude is proportional to the square of the frequency over a frequency range.
4) Blue noise has strong power at high frequency and is not common in experimental measurements.
5) Violet noise, which is a differentiation of white noise, has a power spectral density that is proportional to the square of the frequency over the finite range.

III. LABORATORY AND FIELD TESTS

A. Experimental Setup

Fig. 4 shows the experimental setup used in this article with a detailed specification, as shown in Table I. A custom-made 100-kVA, 400-V, synchronous generator with 14 salient poles is used to investigate the noise effect on an air-gap magnetic field signal under an ITSC fault. A 90-kW four-pole induction motor is used to rotate the coupled synchronous generator. The induction motor shaft is connected to the generator by a gearbox with a gear ratio of 1/3. A programmable converter is used to
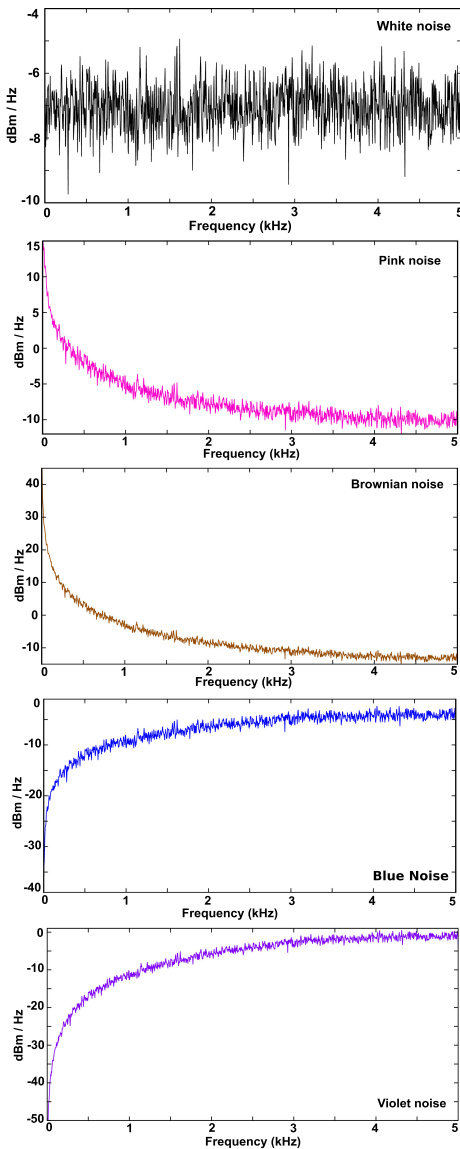
Fig. 3. Prevalent type of noise based on their color definition: white Gaussian noise, pink noise, Brownian noise, blue noise, and violet noise.
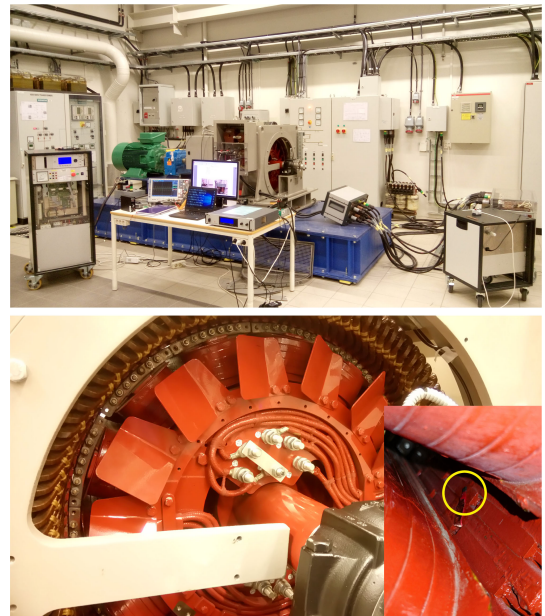

Fig. 4. Laboratory setup of a 100-kVA salient pole synchronous generator (top). The copper plate is used to apply the ITSC fault on one of the rotor field windings; the installed Hall effect sensor on the stator tooth of a laboratory setup (bottom).

TABLE I
100-KVA, 50-HZ, SYNCHRONOUS GENERATOR TOPOLOGY SPECIFICATION AND NAMEPLATE DATA

Quantity	Values	Quantity	Values
Winding connection	Wye	Number of poles	14
No. of stator turns	8	No. of rotor turns / pole	35
Nominal speed	428 rpm	Power factor	0.90
Nominal voltage	400 V	Nominal current	144.3 A
Nominal exc. current	103 A	No-load exc. current	53.2 A

feed the induction motor. The field winding of the generator is supplied by a dc power supply. A copper plate is used to create the ITSC fault on one of the rotor field windings, as shown in Fig. 4. A Hall effect sensor (AST244), with a ratio of the induced voltage to the magnetic field equal to 2.54 T/V, is installed on the stator tooth to acquire the air-gap magnetic field (see Fig. 4). The data sheet specifies that the sensor should be supplied by a 2-mA dc current source. However, due to considerable electromagnetic interference, the magnitude of the current power supply is increased to 4 mA to increase the SNR. A high-resolution (16-bit) oscilloscope is used to sample the data at 10 kHz.

The test procedure for the experimental setup is as follows: tests were conducted in both a healthy state and under the ITSC fault at different degrees of severity. The synchronous generator is accelerated using an induction motor until it reaches its nominal speed. The nominal magnetizing current is applied to the rotor field winding to achieve a nominal voltage in the stator terminals. The ITSC fault is conducted at a standstill by removing the desired number of turns from the rotor field winding using a copper plate. Fig. 5 represents the measured air-gap magnetic field in the presence of noise. The signal is analyzed to recognize the type of noise that leaked into the signal. The separated power spectrum of the noise from the measured air-gap magnetic field shows that its behavior resembles that of white Gaussian noise.
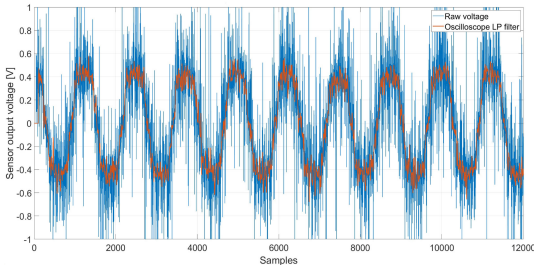
Fig. 5. Measured air-gap magnetic field of the synchronous generator in the laboratory in the presence of a significant noise impact (blue waveform) and the applied low-pass filter of the oscilloscope to diminish the noise impact (red waveform).
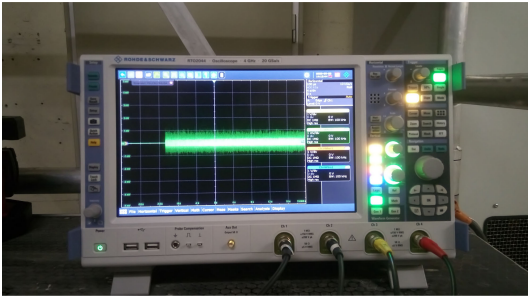

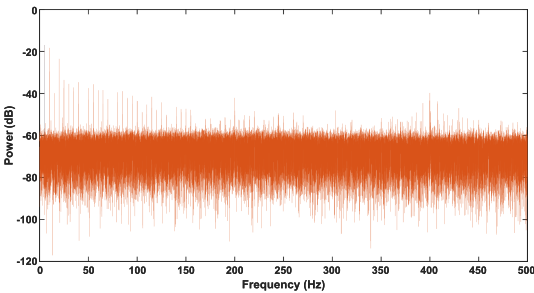Fig. 6. Measured noise in hydropower plant.

Fig. 7. Spectrum density of a measured noise in a hydropower plant.

B. Field Tests

Field tests were conducted in two power plants: a power plant with a single unit generator and another power plant with four units. Hall effect sensors were installed on the stator tooth, and the data were measured while the generator was at standstill. Therefore, the measured data, as shown in Fig. 6, represent the noise in the working environment of the hydrogenerator. The power spectrum of a measured noise is depicted in Fig. 7, which indicates that a white Gaussian noise exists with a 70-dB SNR. The measured noise for a power plant with only one unit shows a lower SNR, thereby showing the impact of electric power equipment on the generated level of noise.

IV. SIGNAL PROCESSING

Signal processing is a core part of the fault detection procedure. Although the measured signals from the electrical machines, whether in a healthy or faulty state, contain useful data, they must be analyzed using signal processing tools. The signal processing tools are categorized into the following three domains:

1) time domain;
2) frequency domain; and
3) time–frequency domain.

Several methods are available, based on time, frequency, and time–frequency domains. In this article, TSDM is used as a time-domain processor. The FFT, which is a frequency-domain processor, is used to obtain the frequency spectrum density of the signal. The wide range of time–frequency processors is limited in this article to STFT, CWT, and DWT.

A. Fast Fourier Transform

The Fourier transform represents the desired function as its constituent harmonic components, and the Fourier transform is a convolution operation. A Fourier series is a periodic function, and it requires that the processed signal must be periodic. Since the majority of the measured time series are not periodic, it assumes that the entire measured data series is one periodic function. A discrete Fourier transform is formulated for a discrete signal that represents the frequency contents of the time data series, and the FFT is a commonly applied approach to achieve a discrete Fourier transform [24]. The FFT is computationally efficient, and it reduces the computational complexity of the discrete Fourier transform from $O(m^2)$ to $O(m\log(m))$, where m is the total number of samples. The spectral representation of the time signal consists of periodic components in the frequency domain that each has a specific frequency, phase angle, and amplitude. The FFT can provide a general representation of the frequency contents of the signal. The amplitude of the frequency spectrum is increased if a signal changes. Indicating that the FFT can track the faulty signal variation in the frequency spectrum, the provided information based on the frequency spectrum is not informative unless the fault frequency is known. Moreover, the accuracy and precision of the spectrum density of the signal depends on the amount of sampled data and the sampling frequency of the signal.

The distorted magnetic field caused by an ITSC fault contains subharmonics that can be distinguished using the FFT based on the following features:

$$f_{\text{subharmonic}} = \frac{(p \pm k)f_s}{p} \qquad (1)$$

where f_s is the stator terminal frequency, p is the number of poles, and k is an integer. Fig. 8 depicts the spectral density of the air-gap magnetic field in the healthy state and under a ten-ITSC fault in one of the rotor poles, as obtained by the FFT processor. Increasing the number of shorted turns in the rotor field winding also increases the amplitude of the sideband components. For instance, the amplitude of the sidebands for a ten-ITSC fault at frequencies of 7.15, 14.3, 28.6, and 35.7 Hz increased from
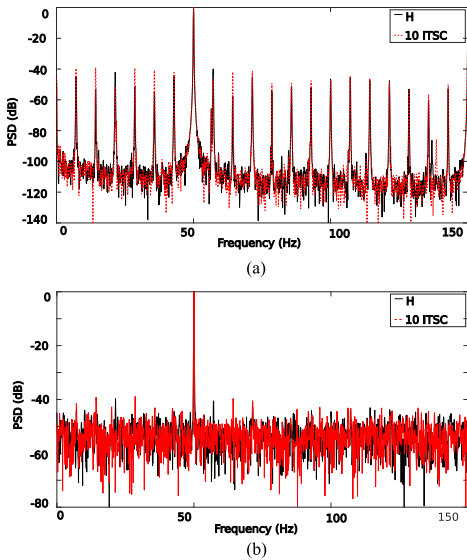
Fig. 8. Spectrum density of an air-gap magnetic field in a healthy state and under a ten-ITSC fault, without noise interference (top), and with 20-dB SNR (bottom).

TABLE II
EFFECT OF VARIOUS SNRs ON THE NOMINATED SIGNATURE IN A HEALTHY
STATE AND UNDER AN ITSC FAULT (GRAY COLORS)

Noise Level	7.15 Hz	14.3 Hz	28.6 Hz	35.7 Hz	64.3 Hz
No-Noise	-44.6	-53.1	-51.3	-54.9	-57.4
60 dB	-44.6	-52.9	-51.2	-55.0	-57.6
50 dB	-44.8	-53.1	-51.4	-54.1	-57.8
40 dB	-45.1	-53.0	-51.1	-55.3	-58.2
30 dB	-45.3	-55.1	-51.5	-54.8	-57.3
No-Noise	-39.6	-38.9	-39.4	-40.8	-41.8
60 dB	-39.6	-38.9	-39.4	-40.8	-41.8
50 dB	-39.5	-38.9	-39.4	-40.8	-41.9
40 dB	-39.8	-39.1	-39.2	-40.6	-42.1
30 dB	-40.3	-39.1	-39.9	-40.2	-41.8

-44.6, -53.1, -51.3, and -54.9 dB to -36.6, -38.9, -39.4, and -40.8 dB, respectively.

Fig. 8 demonstrates the effect of 20-dB white Gaussian noise on the spectral density of the air-gap magnetic field in a healthy state and under a ten-ITSC fault. The noise level of the frequency spectrum is increased from -100 to -50 dB by decreasing the SNR. Therefore, the magnitude of the introduced feature for ITSC detection is simply masked in the case of high-level noise interference. Hence, the ITSC diagnosis under a 30-dB SNR is almost impossible.

Table II presents the effect of various SNRs on the nominated feature under an ITSC fault. The amplitude of the index for a low degree of SNR is acceptable, since the ITSC fault can be identified. However, the SNR of 20 dB is the borderline for accurate fault detection. By decreasing the SNR, the amplitudes of the sidebands in both the healthy and faulty cases are masked, and the faulty sideband components cannot be identified. The sideband component of the healthy case is also increased, and its

amplitude is similar to that of a faulty case without noise impact and may result in a false alarm indication of a fault.

B. Short-Time Fourier Transform

The STFT performs a time–frequency analysis that represents both the frequency and time contents of a signal. The STFT uses a fixed basis function, like FFT. In addition, the signal transformation is performed by sweeping a fixed window function over a signal. The STFT, compared with the FFT, provides a better temporal and frequency localization. However, according to the uncertainty principle, the product of temporal and frequency resolution is constant; therefore, achieving an acceptable time and frequency resolution at the same time is impossible. Moreover, the STFT has a superiority over the FFT since it can analyze the nonstationary signals. The mathematical representation of the STFT is shown as follows:

$$\text{STFT}(f,t) = \frac{1}{2\pi} \int_{-\infty}^{\infty} x(t)h(t-\tau)e^{-i2\pi f\tau}d\tau \qquad (2)$$

where $h(t)$ is the window function. There exist numerous types of window function, which must be selected according to the signal characteristics for optimal result. The end effect must be considered since it may result in a false decision of fault, and it can be mitigated using a proper window function including flat top, Nuttall, Dirichlet, Bartlett–Hann, Parzen, Blackman, Blackman–Harris, Chebwin, exponential, triangular, Hamming, Hann, Gaussian, Bartlett, Bohman, Kaiser, and Slepian. There exists no straightforward rule to find an appropriate window function, indicating that several window functions must be performed. The length of the data in addition to the window length is also the main factor that must be considered during parameter adjustment. The time resolution of the STFT is inversely proportional to the length of the time window, while the frequency resolution of the STFT has a direct relationship with the length of the window function. The computational complexity of the STFT compared with the FFT is negligible since the computational complexity of the STFT is $O(n.m\log(m))$, where n is the window length, indicating that the FFT is performed n times. The percentage of the window overlapping when the window function sweeps across the data is a key point since window overlap can give a more analysis point and higher resolution across time, but the computational cost becomes higher. Therefore, a tradeoff must settle down to have adequate analysis points to achieve a smooth result across time, while the computational cost does not increase significantly.

Nevertheless, the STFT is widely used in feature extraction for fault detection of electrical machines. Figs. 9 and 10 present the application of the STFT to the measured air-gap magnetic field in a healthy state and a ten-ITSC fault without a noise effect and with white additive Gaussian noise with SNRs of 40 and 20 dB. The STFT is performed with a window length of one electric period. A novel index using the STFT is introduced that does not require *a priori* knowledge of the healthy machine. A comparison between the healthy and faulty STFTs reveals that the fault has a significant impact on a frequency band of the STFT between 50 and 75 Hz. In a case of a healthy machine, there is
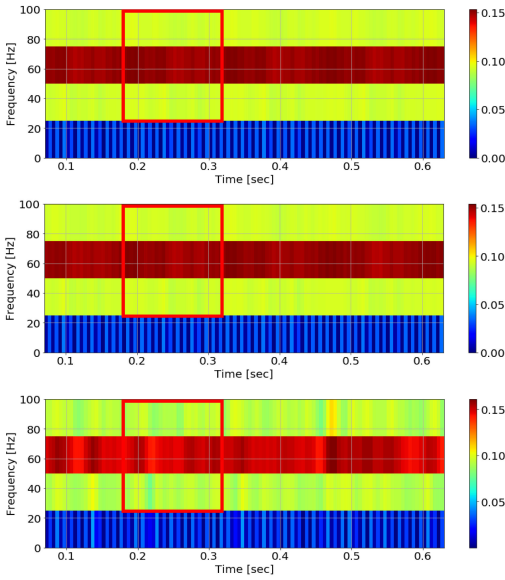
Fig. 9. Applied STFT to an air-gap magnetic field in the healthy case, without noise impact (first row), 40-dB SNR (second row), and 20-dB SNR (third row).
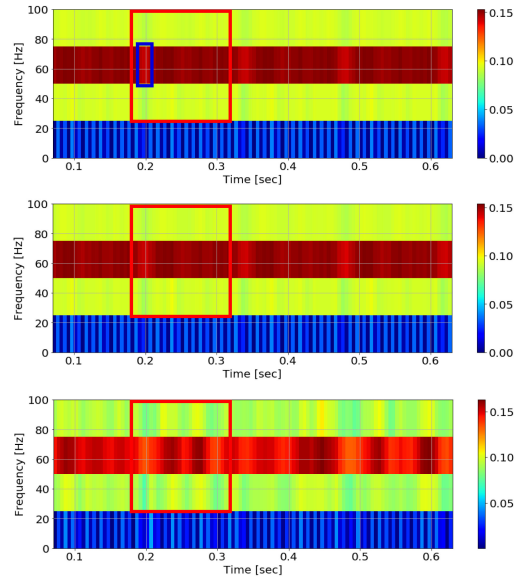

Fig. 10. Applied STFT to an air-gap magnetic field under a ten-ITSC fault, without noise impact (first row), 40-dB SNR (second row), and 20-dB SNR (third row).

a uniform pattern with the same intensity pattern along with the mentioned frequency band. Having a ten-ITSC fault in one of the rotor field winding results in a clear periodic intensity reduction in a frequency band between 50 and 75 Hz. The width of a red window in an STFT plot is equal to 140 ms, which represents one mechanical revolution of the synchronous generator, and the widths of a faulty pole are equal to 10 ms, which is shown with a blue window. The blue window with a reduced intensity is periodic, which shows a faulty pole in the time–frequency plot. Conclusively, the frequency pattern of the desired frequency band in a healthy operation is uniform, while having a fault results in a periodic window with widths equal to a rotor pole.

The demonstration that the STFT applied to an air-gap magnetic field signal interfered with a 40-dB SNR in healthy and faulty cases shows that detection of the fault is possible, since noise does not change the available pattern. By contrast, the STFT plot of the signal with 20-dB white Gaussian noise disturbs the fault pattern, and fault detection is not possible. A qualitative comparison of the healthy and faulty signals by the introduction of noise implies that noise does not mask the frequency band and fault feature to a great extent up to 40 dB of noise, and this likely reflects the long window length. Therefore, noise with a higher ratio may lead to false fault identification. A caveat of STFT analysis in the presence of noise is that increasing the window length to reject noise will reduce the temporal resolution and limit its usefulness.

C. Continuous Wavelet Transform

The wavelet transform is a signal processing method that decomposes a signal into a set of primary waveforms that, by analyzing the wavelet coefficients of waveforms, may provide some insight. Wavelet transform tries to alleviate the constraints of the STFT by defining a mother wavelet as a basis function. The wavelet transform includes numerous mother wavelets, unlike STFT that has a single basis function. The wavelet transform divides a time–frequency space from coarse to fine sizes, while the STFT divides a time–frequency space into equal sizes. Moreover, the transform convolutes the signal to the mother wavelet, while in the STFT, the window function is dilated over the entire time series to perform the FFT [25].

Different frequencies in the signal can be tracked by compressing or stretching the wavelet using the wavelet scaling factor. The convolution computation is applied as (3) to the signal, and the obtained result is depicted in the time–frequency plot.

$$X(a,b) = \frac{1}{\sqrt{a}} \int_{-\infty}^{\infty} x(t)\Psi^*\left(\frac{t-b}{a}\right)dt. \qquad (3)$$

The analyzed signal is denoted by $x(t)$, and Ψ represents the mother wavelet. The scaling factor and the temporal center of the wavelet are adjusted by a and b. The type of mother wavelet must be chosen depending on the type of signal, the frequency of interests, and the investigated properties in the signal, indicating that there exists no clear rule of thumb to select the mother wavelet, and it must be selected by trial and error. However, a general rule indicates that a mother wavelet must be used that is similar to the measured signal. For instance, a Haar wavelet can be utilized if the signal has a sudden transition, while a Morlet mother wavelet is suitable when the signal has a smooth variation [26]. The computational complexity of the
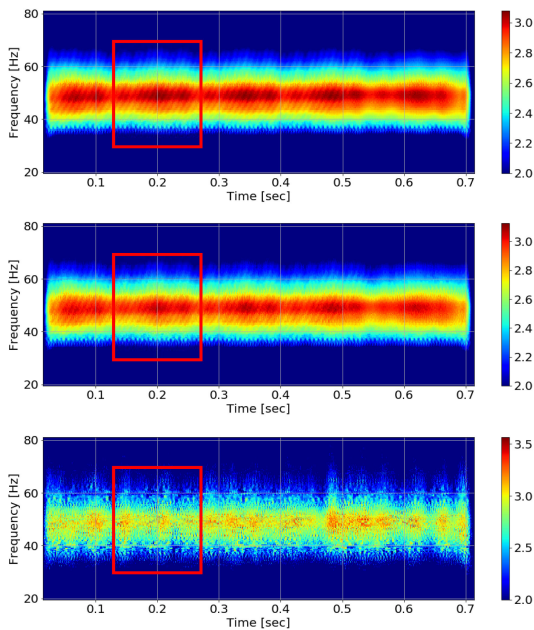
Fig. 11. Applied CWT to an air-gap magnetic field in the healthy case in no noise (first row), 40-dB SNR (second row), and 20-dB SNR (third row).
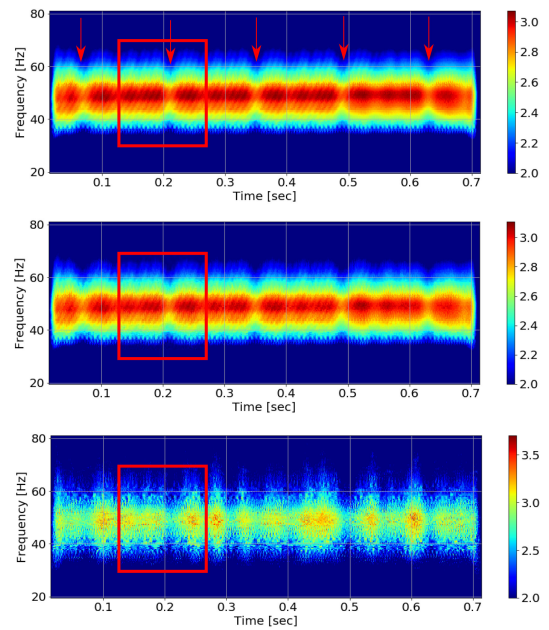

Fig. 12. Applied CWT to an air-gap magnetic field in a ten-ITSC fault case in no noise (first row), 40-dB SNR (second row), and 20-dB SNR (third row).

CWT is $(O(m))$, where m is the length of data. A comparison between the computational complexity of the CWT and the FFT indicates that the FFT performs slower than the CWT. Conclusively, the CWT also outperforms faster than the STFT since the computational complexity of the STFT is n times the computational complexity of the FFT. The data interpretation of the processed signal by the CWT is arduous since it must be analyzed by a convolutional neural network or an image processing expert, which makes its application difficult.

The CWT is a qualitative signal processing tool that is widely used in fault detection of electrical machines [13]. A novel index using the frequency B-spline mother wavelet is introduced to diagnose the ITSC in the rotor field winding based on the CWT. Finding healthy state data of a synchronous generator that operates for decades in a power plant is almost impossible, indicating that a method that can independently indicate the health status of the generator is required. Application of fault detection algorithm based on the CWT to the air-gap magnetic field, as shown in Fig. 11, generates a uniform frequency band with a map of various intensities. Having a short-circuit fault in the rotor field winding result is an appearance of a periodic notch in the time–frequency response. A periodic notch pattern is repeated when a faulty pole passes over the installed sensor in the air gap. Figs. 11 and 12 depict the application of the CWT to measured air-gap magnetic fields of healthy and faulty machines, respectively. A comparison between the healthy state and a ten-ITSC fault between the frequency bands of 40–60 Hz indicates that the presence of a fault changes the CWT profile by introducing a periodic notch.

The effect of white Gaussian noise on the CWT is studied by adding different amounts of noise. Figs. 11 and 12 show the impact of 40- and 20-dB noise on CWT plots in both healthy and faulty cases. A signal with an SNR up to 40-dB noise does not show significant changes, and identifying the changes due to ITSC fault is still possible, while the intensity of the CWT is reduced by decreasing SNR level. Moreover, a signal with an SNR equal to 20 dB completely destroys the shape of pattern in both healthy and ITSC fault cases. The CWT is affected uniformly across frequencies, unlike the STFT, due to its greater time–frequency resolution. This effect will vary among wavelets. Some of the noise-rejecting qualities of the STFT could be achieved in the CWT by selecting wavelets with a greater number of oscillations, such as the Shannon mother wavelet.

D. Discrete Wavelet Transform

The DWT is based on the same principle as the CWT since the DWT is commonly implemented based on filter banks. Each level of the filter consists of a low-pass filter and a high-pass filter, in which the output is downsampled by a factor of 2 at each level. The output of the high-pass filter plus the downsampling is known as a detailed signal ($h(n)$), while the output of the low-pass filter plus downsampling is called an approximate signal ($g(n)$). The output of the detail coefficient is saved, while the output of the approximate coefficient is fed to the next level of the DWT. This process continues until the desired number of decomposition is achieved. Fig. 13 shows one level of the DWT.
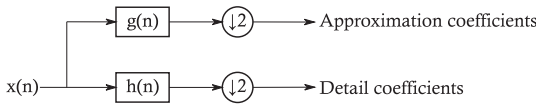
Fig. 13.   One level DWT including the filtering and the downsampling procedures.

The decomposed signal by the DWT depends on the type of selected mother wavelet. Daubechies and Haar wavelets are two commonly applied mother wavelets in the DWT. The computational complexity of the DWT is similar to that of the CWT, while, in practice, it is faster than the CWT since the data are downsampled in each level. A better temporal resolution can be achieved by the CWT compared with the DWT since it can shift the filter only by one sample, but higher storage is required in the CWT. A frequency tracking of the DWT compared with the CWT and the STFT is simpler since the mother wavelets are limited. The frequency of interest must be determined, and based on that, the number of DWT levels must be picked out, if not the frequency of interest appears in two different detailed subbands. In this article, Daubechies 8 is used to decompose the air-gap magnetic field into various frequency subbands. Since the sampling frequency is 10 kHz, the first and second detailed subbands are between 5000 and 2500 Hz and 2500 and 1250 Hz, respectively.

The DWT is a useful signal processing tool for feature extraction of an electrical machine under a faulty condition. Various features can be extracted from detailed subbands of the DWT such as standard deviation, median, mean, entropy, skewness, kurtosis, variance, and various energies. In this article, the energy of each subband level is introduced as a proper signature to diagnose the occurrence of the ITSC fault. The energy of the signal is as follows:

$$E = \int_{-\infty}^{\infty} |D_n|^2 dt \qquad (4)$$

where D_n is the magnitude of each DWT subbands. The occurrence of a ten-ITSC fault in one of rotor poles leads to an increment of the energy of D1–D6 from 1.35, 1.06, 1, 0.97, 0.94, and 0.83 to 0.65, 0.72, 0.79, 0.83, 0.88, and 0.81, respectively. A comparison between the energy variation of the different wavelet subbands in healthy and faulty cases provides an accurate indication of the occurrence of an ITSC fault.

Having an air-gap magnetic field signal with an SNR up to 40 dB does not disturb the introduced feature, whereas the signal with an SNR equal to 20 dB changes the results significantly. Fig. 14 shows the DWT of the air-gap magnetic field in a healthy case without a white Gaussian noise effect and under a noisy condition with a 20-dB SNR. As shown in Fig. 14, the 20-dB noise significantly changes the amplitude and shape of some of the subbands, like D5, D4, D3, D2, and D1 even in a healthy case, while it does not change the subbands level of D6–D8. However, the energy of wavelet subbands of the healthy generator with 20-dB white Gaussian noise is equal to the energy level of the corresponding wavelet subbands under a ten-ITSC fault. For instance, the amplitude of the energy of the subbands of D3, D2,
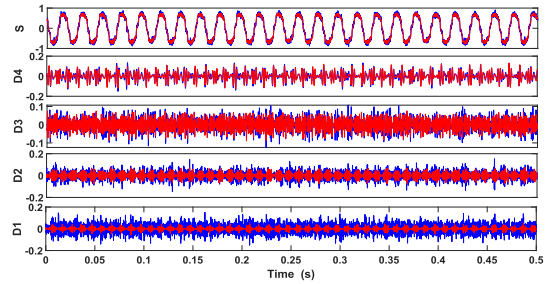

Fig. 14.   DWT of air-gap magnetic field in a healthy case without noise impact (red) and with 20-dB SNR (blue).

TABLE III
ENERGY OF VARIOUS DWT SUBBANDS APPLIED TO AIR-GAP MAGNETIC FIELD SIGNAL IN A HEALTHY STATE AND UNDER ITSC FAULT

	D6	D5	D4	D3	D2	D1
Healthy - No-Noise	0.83	0.94	0.97	1.0	1.06	1.35
Faulty - No-Noise	0.81	0.88	0.83	0.79	0.72	0.65
Healthy - 20 dB	0.81	0.88	0.83	0.79	0.72	0.65

and D1 for the healthy generator with a 20-dB SNR is decreased to 0.79, 0.72, and 0.65, while the energy of the same subbands for a ten-ITSC fault is also the same. Consequently, the noisy environment leads to a false alarm of a fault occurrence in a healthy generator. Table III shows the result of DWT applied to the healthy and faulty generators. The application of the DWT for fault detection of the electric machines in a noisy environment must be evaluated based on a subband level, on which the signature is defined, since some of the low-frequency subbands do not undergo any changes even with 20-dB noise.

E. Time-Series Data Mining

TSDM is a time-domain nonlinear signal processing tool that is developed based on discrete stochastic models of the reconstructed phase space using the dynamical system theory [27]. A single sampled state variable can generate a metrically equivalent state space; in addition, a dynamical invariant is also preserved in the reconstructed state space. If the trend of time variation of the signal is high, its average value for the different operating points may be utilized to extract a feature. The air-gap magnetic field signal is considered as a state variable to create the state space of the generator.

The reconstructed state space can be developed using time-delay embedding and derivative embedding approaches. The method based on derivative embedding includes higher order derivates that make its application impractical in noisy environments indicating that time-delay embedding is the proper approach for TSDM development. The invariant of the dynamical system in the time-delay embedding method is found by transforming scalar points into a vector form [28]–[30].

For a given time series of the magnetic field of the air gap, we have:

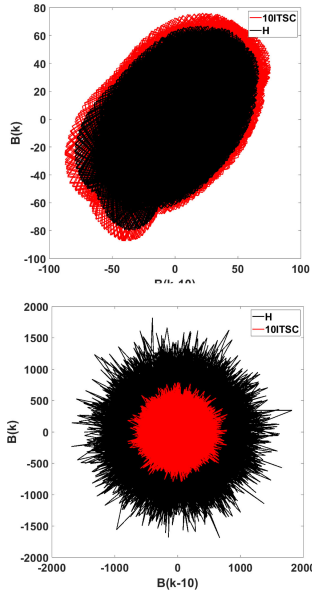$$B = \{B(k) - B(k-1)\}, \quad k = 2, 3, \ldots, j \qquad (5)$$

Fig. 15. Gyration radius of the air-gap magnetic field in a healthy state and a ten-ITSC fault without noise impact (top) and with a 20-dB SNR (bottom).

where j is the number of the sampled signal and k is the time index. The reconstructed phase space for k equal to 10 is shown in Fig. 15. A TDSM is used to generate the mass (gyration) based on variation in the magnetic field time series. The variation in a radius of gyration (RG) is a suitable tool for feature extraction from the air-gap magnetic field of a faulty machine. The RG is calculated from the generated mass to quantify the rate of changes due to ITSC fault, as follows [31]:

$$\text{RG} = \sqrt{\frac{\sum_{k=l+1}^{j}(B(k-\mu_0)^2 + (B(k-l)-\mu_l)^2}{j-l}} \quad (6)$$

where μ_0 and μ_l are the center of gyration for their respective dimension, and l is the time lag of the phase space. The TSDM is able to point out the variation in the signal that is changed due to fault. However, the fault detection based on TSDM requires *a priori* knowledge of the healthy state of the machine for comparison. Although the processed signal by TSDM indicates the fault sign in the machine, the extracted feature is not informative to provide more insight into the fault-type recognition.

As shown in Fig. 15, the fault leads to distortion of the magnetic field, which results in an increment in the RG. The calculated RG to magnetic flux density in the healthy state and under a ten-ITSC fault is 61 and 78, respectively. Fig. 15 represents the application of TSDM to the healthy and faulty air-gap magnetic field in a presence of 20-dB white Gaussian noise. The magnitude of the RG is increased considerably compared with the signal without the noise effect. Moreover, the area of the mass and, correspondingly, the RG in healthy cases is enormously larger than in the faulty case. This results in false identification of

a fault and indicates that the signal input to the TSDM algorithm must be noiseless; otherwise, it leads to an inaccurate feature.

V. HARDWARE NOISE REJECTION

Every wire in the electrical instrument behaves like an antenna that absorbs the electromagnetic energy emitted from electrical equipment in the environment and converts it into an electrical signal with low amplitude. Therefore, rejecting this noise or reducing its impact on the measured signal is essential. A couple of simple solutions are shown as follows:

1) grounding the machine frame diminishes the environmental noise effect;
2) protecting a circuit or wires, which are exposed to noise with a conducting material like a copper foil;
3) reducing the length of wire used for data transmission or preferably using a coaxial cable; and
4) using the low-pass filter implemented in the measurement instrument.

Since the air-gap magnetic field measured in the laboratory is vulnerable to noise, copper foil is used to shield the sensor wires all the way to the dc power supply. The connection between the dc power supply to the oscilloscope is made with a coaxial cable. In addition, the SNR of the measured air-gap magnetic field is increased by increasing the magnitude of the current feeding into the Hall effect sensor. The body of the generator is grounded in to avoid additional noise leaking into the sensor.

VI. CONCLUSION

This article discussed thoroughly the various kinds of noise that may exist in the industrial environment and demonstrated how it can negatively affect the measured data. A detailed investigation of the frequency component of the measured noisy data in both laboratory and hydropower plants revealed that white Gaussian noise exists and is the most prevalent type of noise in power industries.

Signal processing tools are key to fault detection procedures for electrical machines. Based on the level of leaked noise into the signal, the processed data may indicate a false result, indicating that noise must be measured in industry and power plants during data acquisition. Although the main criterion to select a proper signal processing tool is its ability to track the fault frequency and performing algorithm in real time with low computational burden, the level of noise must also be considered during the fault detection procedure. In order to show how signal processing tools work in a noisy environment, the air-gap magnetic field of a 100-kVA salient pole synchronous generator in a healthy state and under ITSC fault is measured. The Hall effect sensor is used to measure the air-gap magnetic field, since it is susceptible to the magnetic noise from inside the generator and noise from the working environment of the generator. Different signal processing tools, such as FFT, STFT, CWT, DWT, and TSDM, are used for ITSC fault detection. Suitable features were introduced, and their performance in the presence of noise are evaluated and summarized as follows.

1) *FFT:* The FFT can provide a general picture of the health state of the machine since it cannot reveal the fault type.

Moreover, fault detection based on the FFT requires *a priori* data of a healthy machine for comparison. The FFT is only sensitive to high-level noise, and sidebands are masked if the SNR is higher than 20 dB.

2) *STFT:* The STFT can indicate the fault harmonics if a proper window function is selected, and the parameters are adjusted precisely. The computational complexity of the STFT is n times an FFT; however, it can be used in real-time fault detection. Its sensitivity to noise and resolution of the frequency bands depend on the length of the window and may result in a false alarm for the SNR below 40 dB.

3) *CWT:* Application of CWT in fault detection provides a pattern that indicates the harmonics variation both in time and frequency. The selection of a proper mother wavelet is a key factor to track the fault harmonics. The computational complexity of the CWT compared with the STFT and the FFT is lower that makes its real-time implementation easier. The CWT works fine with an SNR up to 40 dB, although its time–frequency plot becomes blurry. However, fault identification is still possible. The CWT generates a chaotic representation of a signal with the SNR above 40 dB, and interpreting the plot is impossible.

4) *DWT:* Selection of a proper number of subbands plays a key role in precise fault harmonic track. A proper mathematical tool based on the signal property must be applied to the signal to indicate the effect of fault harmonic in the selected subband. The computational complexity of the DWT is similar to that of the CWT. It depends on a frequency subband, which is utilized for feature extraction. If a feature is defined based on low-frequency subbands, such as D6–D8, even a signal with the SNR above 20 dB could not disturb the data.

5) *TDSM:* Although extracted feature based on the variation in the RG shows a fault harmonic impact on the measured signal, it is highly sensitive to noisy data, and it is not a useful tool if a signal is measured in a noisy environment.

REFERENCES

[1] H. Ehya, I. Sadeghi, and J. Faiz, "Online condition monitoring of large synchronous generator under eccentricity fault," in *Proc. 12th IEEE Conf. Ind. Electron. Appl.*, 2017, pp. 19–24.

[2] P. Vijayraghavan and R. Krishnan, "Noise in electric machines: A review," *IEEE Trans. Ind. Appl.*, vol. 35, no. 5, pp. 1007–1013, Sep./Oct. 1999.

[3] R. S. Girgis, M. Bernesjo, and J. Anger, "Comprehensive analysis of load noise of power transformers," in *Proc. IEEE Power Energy Soc. Gen. Meeting*, 2009, pp. 1–7.

[4] S. Yang, "Effects of voltage/current harmonics on noise emission from induction motors," in *Vibrations and Audible Noise in Alternating Current Machines*. New York, NY, USA: Springer, 1988, pp. 457–468.

[5] H. Tischmacher, I. P. Tsoumas, B. Eichinger, and U. Werner, "Case studies of acoustic noise emission from inverter-fed asynchronous machines," *IEEE Trans. Ind. Appl.*, vol. 47, no. 5, pp. 2013–2022, Sep./Oct. 2011.

[6] I. P. Tsoumas and H. Tischmacher, "Influence of the inverter's modulation technique on the audible noise of electric motors," *IEEE Trans. Ind. Appl.*, vol. 50, no. 1, pp. 269–278, Jan./Feb. 2014.

[7] J. Qin, P. Sun, and J. Walker, "Measurement of field complex noise using a novel acoustic detection system," in *Proc. IEEE AUTOTEST*, 2014, pp. 177–182.

[8] S. M. J. Ali, "Measurement of vibration and noise level at power plant and refinery companies that represents a condition monitory for the health of machines," in *Proc. Int. Conf. Environ. Impacts Oil Gas Ind.: Kurdistan Region Iraq Case Study*, 2017, pp. 85–87.

[9] D. P. Martins and M. S. Alencar, "A new approach to noise measurement and analysis in an industrial facility," in *Proc. IEEE Int. Instrum. Meas. Technol. Conf.*, 2014, pp. 964–967.

[10] V. Ghorbanian and J. Faiz, "A survey on time and frequency characteristics of induction motors with broken rotor bars in line-start and inverter-fed modes," *Mech. Syst. Signal Process.*, vol. 54/55, pp. 427–456, Mar. 2015.

[11] J. Faiz and H. Nejadi-Koti, "Demagnetization fault indexes in permanent magnet synchronous motors-an overview," *IEEE Trans. Magn.*, vol. 52, no. 4, pp. 1–11, Apr. 2016.

[12] J. Faiz, H. Nejadi-Koti, and Z. Valipour, "Comprehensive review on inter-turn fault indexes in permanent magnet motors," *IET Electr. Power Appl.*, vol. 11, no. 1, pp. 142–156, Jan. 2017.

[13] M. Riera-Guasp, J. A. Antonino-Daviu, and G. Capolino, "Advances in electrical machine, power electronic, and drive condition monitoring and fault detection: State of the art," *IEEE Trans. Ind. Electron.*, vol. 62, no. 3, pp. 1746–1759, Mar. 2015.

[14] I. Sadeghi, H. Ehya, J. Faiz, and A. A. S. Akmal, "Online condition monitoring of large synchronous generator under short circuit fault—A review," in *Proc. IEEE Int. Conf. Ind. Technol.*, 2018, pp. 1843–1848.

[15] J. Antonino-Daviu *et al.*, "Electrical monitoring of damper bar condition in salient-pole synchronous motors without motor disassembly," *IEEE Trans. Ind. Appl.*, vol. 56, no. 2, pp. 1423–1431, Mar./Apr. 2020.

[16] J. Yun *et al.*, "Airgap search coil-based detection of damper bar failures in salient pole synchronous motors," *IEEE Trans. Ind. Appl.*, vol. 55, no. 4, pp. 3640–3648, Jul./Aug. 2019.

[17] Y. Park, S. B. Lee, J. Yun, M. Sasic, and G. C. Stone, "Air gap flux-based detection and classification of damper bar and field winding faults in salient pole synchronous motors," *IEEE Trans. Ind. Appl.*, vol. 56, no. 4, pp. 3506–3515, Jul./Aug. 2020.

[18] G. Georgoulas *et al.*, "The use of a multilabel classification framework for the detection of broken bars and mixed eccentricity faults based on the start-up transient," *IEEE Trans. Ind. Informat.*, vol. 13, no. 2, pp. 625–634, Apr. 2017.

[19] J. Pons-Llinares, J. A. Antonino-Daviu, M. Riera-Guasp, S. B. Lee, T. Kang, and C. Yang, "Advanced induction motor rotor fault diagnosis via continuous and discrete time-frequency tools," *IEEE Trans. Ind. Electron.*, vol. 62, no. 3, pp. 1791–1802, Mar. 2015.

[20] H. Ehya, A. Nysveen, R. Nilssen, and Y. Liu, "Static and dynamic eccentricity fault diagnosis of large salient pole synchronous generators by means of external magnetic field," *IET Elect. Power Appl.*, 2021, DOI: doi.org/10.1049/elp2.12068

[21] M. Heydarzadeh, M. Zafarani, M. Nourani, and B. Akin, "A wavelet-based fault diagnosis approach for permanent magnet synchronous motors," *IEEE Trans. Energy Convers.*, vol. 34, no. 2, pp. 761–772, Jun. 2019.

[22] B. M. Ebrahimi, J. Faiz, and M. J. Roshtkhari, "Static-, dynamic-, and mixed-eccentricity fault diagnoses in permanent-magnet synchronous motors," *IEEE Trans. Ind. Electron.*, vol. 56, no. 11, pp. 4727–4739, Nov. 2009.

[23] H. Ehya, T. N. Skreien, A. Nysveen, and R. Nilssen, "The noise effects on signal processors used for fault detection purpose," in *Proc. 23rd Int. Conf. Elect. Mach. Syst.*, Nov. 2020, pp. 183–188.

[24] E. O. Brigham, *The Fast Fourier Transform and its Applications*. Englewood Cliffs, NJ, USA: Prentice-Hall, 1988.

[25] C. Torrence and G. P. Compo, "A practical guide to wavelet analysis," *Bull. Amer. Meteorol. Soc.*, vol. 79, no. 1, pp. 61–78, Jan. 1998.

[26] B. Y. Lee and Y. S. Tarng, "Application of the discrete wavelet transform to the monitoring of tool failure in end milling using the spindle motor current," *Int. J. Adv. Manuf. Technol.*, vol. 15, no. 4, pp. 238–243, Apr. 1999.

[27] D. A. Rand and L.-S. Young, *Dynamical Systems and Turbulence, Warwick 1980: Proceedings of a Symposium Held at the University of Warwick 1979/80*, vol. 898. New York, NY, USA: Springer, 2006.

[28] H. Ehya, A. Nysveen, R. Nilssen, and U. Lundin, "Time domain signature analysis of synchronous generator under broken damper bar fault," in *Proc. 45th Annu. Conf. IEEE Ind. Electron. Soc.*, 2019, pp. 1423–1428.

[29] F. Takens, "Detecting strange attractors in turbulence," in *Dynamical Systems and Turbulence, Warwick1980*. New York, NY, USA: Springer, 1981, pp. 366–381.

[30] A. R. Webb, *Statistical Pattern Recognition*. Hoboken, NJ, USA: Wiley, 2003.

[31] R. J. Povinelli, J. F. Bangura, N. A. O. Demerdash, and R. H. Brown, "Diagnostics of bar and end-ring connector breakage faults in polyphase induction motors through a novel dual track of time-series data mining and time-stepping coupled Fe-state space modeling," *IEEE Trans. Energy Convers.*, vol. 17, no. 1, pp. 39–46, Mar. 2002.

Hossein Ehya (Student Member, IEEE) received the M.Sc. degree in electrical and computer engineering from the University of Tehran, Tehran, Iran, in 2013. He is currently working toward the Ph.D. degree in electrical engineering with the Norwegian University of Science and Technology, Trondheim, Norway.

From 2013 to 2018, he was an Electrical Machine Design Engineer with Electrical Machine Companies. His research interests include the design and condition monitoring of electrical machines, signal processing, pattern recognition, and machine learning.

Mr. Ehya received the ICEM Jorma Luomi Award in Gothenburg, Sweden, in 2020.

Tarjei Nesbø Skreien is a master student graduate in electric power engineering from The Norwegian University of Technology and Science in Trondheim, Norway.

His research interests include synchronous machine fault detection, machine learning and sampling noise mitigation.

Arne Nysveen (Senior Member, IEEE) received the M.Sc. and Dr.Ing. (Ph.D.) degrees in electric power engineering from the Norwegian University of Science and Technology (NTNU), Trondheim, Norway, in 1988 and 1994, respectively.

From 1995 to 2002, he was a Senior Scientist with ABB Corporate Research, Oslo, Norway. Since 2002, he has been a Professor with NTNU. He is currently a Manager for the research on Turbine and Generator Technologies with the Norwegian Research Center for Hydropower Technology. His current research interests include design, modeling, and monitoring of hydroelectric generators.

Paper IX

Paper IX

Intelligent Data-Driven Diagnosis of Incipient Interturn Short Circuit Fault in Field Winding of Salient Pole Synchronous Generators

Hossein Ehya ©, *Graduate Student Member, IEEE*, Tarjei N. Skreien ©,
and Arne Nysveen ©, *Senior Member, IEEE*

Abstract—**This article examines if machine learning (ML) and signal processing can be used for online condition monitoring to reveal interturn short circuit (ITSC) fault in the field winding of salient pole synchronous generators (SPSG). This was done by creating several ML classifiers to detect ITSC faults. A dataset for ML was built using power spectral density of the air-gap magnetic field extracted by fast Fourier transform, discrete wavelet transform energies, and Time Series FeatuRe Extraction based on Scalable Hypothesis tests (TSFRESH) to extract features from measurements of SPSG operated under several different severities of ITSC fault. Using this dataset, a wide range of classifiers were trained to detect the presence of ITSC faults. The classifiers evaluated were logistic regression, *K*-nearest neighbors, radial basis function support vector machine (SVM), linear SVM, XGBoost decision tree forest, multilayer perceptron, and a stacking ensemble classifier including all of the aforementioned. The classifiers were optimized using hyperparameter grid searches. In addition, some feature selection and reduction algorithms were assessed such as random forest feature selection, TSFRESH feature selection, and principal component analysis. This resulted in a classifier capable of detecting 84.5% of samples containing ITSC fault, with a 92.7% chance that fault detections are correct.**

Index Terms—**Air-gap magnetic field, fault diagnosis, feature extraction, machine learning (ML), salient pole synchronous generator (SPSG), signal processing.**

I. INTRODUCTION

SALIENT pole synchronous machines are the machines most commonly used in hydroelectric plants [1] and, so, are ubiquitous throughout the Norwegian power system. In fact, hydroelectric generation accounted for 95% of the total electric energy produced in Norway in 2018 [2]. Failure of

the synchronous generators that generate the electricity that the Norwegian society is run on can incur not only a great expense in restoring power plants but also a large cost to society. These machines are under ever-increasing operational demands as intermittent power sources enter the power system. The proper running and maintenance of synchronous machines, and, by extension, the timely detection and diagnosis of their faults, are more important than ever. Hydroelectric generators can suffer failure as a result of undetected incipient faults that induce larger faults. The state of the art in online fault detection in salient pole synchronous generators (SPSGs) is still lacking in this respect [3], [4].

In the transition from reactive to predictive maintenance, it is vital with accurate estimations of machine states. This involves integrating sensors, signal analysis, and decision-making algorithms. The potential benefits to society are immense, estimated by McKinsey Digital to reach a total potential economic value of 11 trillion USD in 2025 [5], and the power generation sector is no exception. By applying online condition monitoring, incipient machine faults can be detected in real time and faults can be detected before they cause unscheduled stops and further damage to the machine.

The rotor winding interturn short circuit (ITSC) is the failure of insulation between turns in the rotor winding coil so that the number of turns in the coil is effectively reduced [1]. This can be due to overheating, causing damage to the insulation, thermal deformation, or mechanical stresses [6]. The fault can then propagate to cause the rotor winding to be further short-circuited and eventually a short to ground [6]. Another issue that could arise from the uneven magnetic field is uneven mechanical stresses that further compromise other machine components [6].

The pole-drop test is the most commonly applied offline test to detect short-circuited turns in the field winding [6]. It is done by applying low-voltage ac to terminals of the field winding and measuring the voltage across each pole. A faulty pole will have a lower voltage across it compared to the other poles [6]. The disadvantage of this test is that it requires the machine to be taken offline. Offline tests require the shut-down of the machine and are, therefore, expensive. They also occur while the machine is at a standstill, and, therefore, faults that are induced due to rotational forces can become invisible [6]. To find the faults present during operation, it is necessary to conduct online monitoring and tests [6]. Online condition monitoring for

diagnosing rotor winding ITSC is often done using flux probe measurements, where the magnetic field registered by a flux probe placed on a stator tooth in the air gap of the machine is analyzed by comparison to a healthy case [7]. The extracted feature for ITSC fault based on measured air-gap magnetic field is done either in steady-state [7] or transient operation of the synchronous machine [8].

Numerous noninvasive approaches exist to diagnose ITSC fault in SPSG based on stray flux analysis [9], harmonics of stator current and voltage [10], and unbalanced circulating current in the stator winding [11]. In [12], a sensorless method based on measurements of the induced voltage in the screw located in the stator core was proposed. Although the induced voltage in the screw is mirrored in the air-gap magnetic field of the synchronous generator, the method is not sensitive to a low degree of ITSC. The magnetic field of the rotor shaft, shaft voltage, and its current are also proposed in [13], where it does not have adequate sensitivity to less severe ITSC faults in synchronous generator rotor poles.

Numerous signal processing tools based on a frequency domain or joint time-frequency domain were applied to the aforementioned signals and different features were extracted to identify the ITSC fault. However, interpretation of the data requires an expert in the field. Therefore, data-driven methods may exclude prior knowledge that is suitable for fault detection. Artificial intelligence has become a useful technique which may be employed in data-driven fault detection of electrical machines. Both supervised and unsupervised machine learning (ML) approaches have demonstrated their effectiveness in fault diagnosis [14]. Unsupervised methods are trained on unlabeled data and are frequently used in fault classification. *K*-means and self-organizing neural networks such as ART networks in combination with wavelet are used for fault detection purposes [15]–[17]. Support vector machine (SVM) [18]–[20], K-nearest neighbor (KNN) and artificial neural networks [17], [21]–[23], fuzzy logic network [24], principal component analysis (PCA) [25], [26], convolutional neural network [20], and XGBoost [27] are widely used as supervised ML classifiers for fault diagnosis of electric machines. Although the mentioned methods showed their ability in classification of fault in electrical machine, accuracy and classifier robustness are increased by integration of various base learners in order to form an ensemble learner [28], [29].

This article applies ensemble stacking classifiers in combination with a sparse sensor application of a single air-gap magnetic flux sensor to detect ITSC faults. This combination of several ML algorithms into one improves predictive performance, while the single sensor is minimally invasive. Previous applications have used solitary ML models, whereas, in this article, it is shown that a superior result can be achieved by *combining* ML models. Furthermore, generating feature-rich datasets using automatic feature generation algorithms makes the procedure nearly sensor agnostic. This system is applied on data that is preprocessed to resemble samples likely to be found in industry to avoid overconfident performance assertions.

In order to investigate which ML models perform the best, and if a single air-gap magnetic field sensor is sufficient for
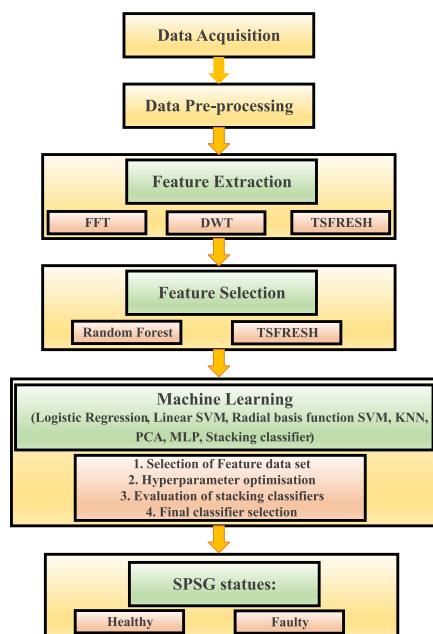

Fig. 1. Procedure of health statues determination of SPSG based on intelligent data-driven approach.

reliable ITSC fault diagnosis or not, a fault classification system as shown in Fig. 1 has been created in this article that includes the following:

1) automatic sample processing and segmentation from longer sample series;
2) a feature extraction process capable of processing and organizing an arbitrary number of samples;
3) a feature selection process that employs several feature selection methods;
4) a process to assess the usefulness of feature selection, select the best ML model among several, and assess the performance of the final model;
5) a final ensemble classifier to detect ITSC faults.

II. Laboratory Test

A. Experimental Setup

The dataset is composed of two concurrent Hall-effect sensor readings taken of a SPSG running at synchronous speed in no-load and full-load with several different ITSC fault severities induced. The machine, the sensors attached, and the measurements are described as follows.

1) A 100 kVA, 400 V, synchronous generator with 14 salient poles constructed to resemble generators commonly situated in Norwegian hydroelectric power plants. It is shown in Fig. 2. Its nameplate value and some defining features of its topology are given in Table I.
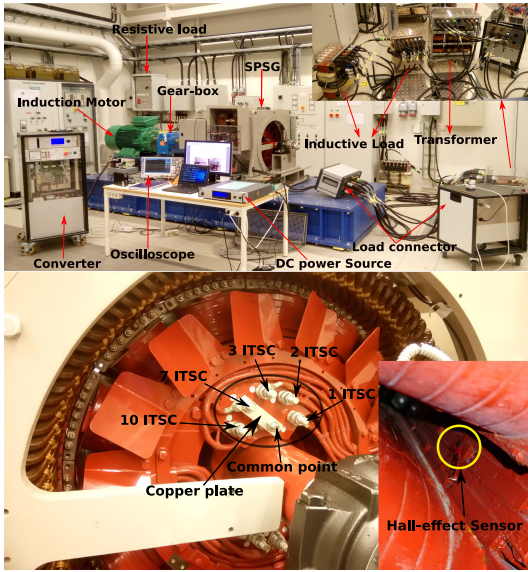
Fig. 2. Experimental test rig of a 100 kVA synchronous generator (top). A copper shunt utilized to short circuit the field winding of SPSG. The location of installed Hall-effect sensor on a stator tooth in yellow circle (bottom).

TABLE I
SPECIFICATION OF 100 kVA, 50 Hz, SYNCHRONOUS GENERATOR

Quantity	Values	Quantity	Values
No. of slots	114	No. of damper bars/pole	7
Winding connection	Wye	Number of poles	14
No. of stator turns	8	No. of rotor turns / pole	35
Nominal speed	428 rpm	Power factor	0.90
Nominal voltage	400 V	Nominal current	144.3 A
Nominal exc. current	103 A	No-load exc. current	53.2 A
Nominal exc. voltage	20 V	No-load exc. Voltage	10.5 V

2) The generator was driven by a 90 kW, 400 V induction motor with four poles and rated speed of 1482 rpm supplied by a three-phase converter. The speed of the induction motor during all tests was set so that the frequency of the generator's electrical output was 50.004 Hz.

3) A gearbox was used to connect the shaft of the induction motor to the synchronous generator.

4) A programmable converter was employed to control the operation of the induction motor. The converter is supplied by an external rectifier connected to the grid.

5) A 20 kW (LAB-HP/E2020) dc power source was utilized to magnetize the field winding.

6) Two Hall-effect sensors (AST244) were placed into the air gap and glued onto stator teeth at diametrically opposing ends of the stator as shown in Fig. 2. The dimensions of the sensors were $(3.0 \times 5.0 \times 0.8)$ mm with a flux density to a voltage ratio of 2.54 T/V. The constant dc current supply is used to feed 4.75 mA into the Hall-effect sensors. The data sheet specifies that
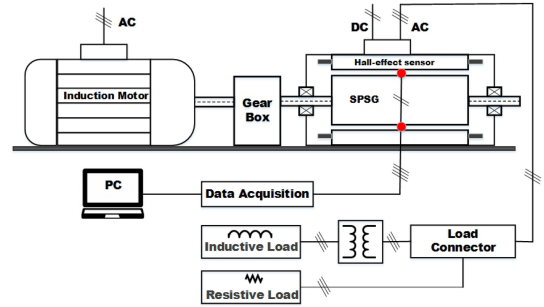

Fig. 3. Connection diagram of experimental setup.

TABLE II
SPECIFICATION OF GENERATOR FROM NO-LOAD TO FULL-LOAD IN FOUR DIFFERENT CASES IN THE HEALTHY OPERATION OF SPSG

Characteristics	No-load	Load 1	Load 2	Load 3
Output Power	-	30 kVA	40 kVA	65 kVA
Power Factor	-	1.0	0.79	0.93
Exc. Current	56 A	60 A	77 A	84 A
Exc. Voltage	10.5 V	11.1 V	13.9 V	14.7 V
I_R	0 A	43 A	43 A	84 A
I_L	0 A	0 A	36 A	33 A

the sensor should be supplied by a 2 mA dc current source. However, due to considerable electromagnetic interference, the magnitude of the current power supply was increased to 4 mA to increase the signal-to-noise ratio.

7) A high-resolution oscilloscope (16-bit Tektronix MSO 3014), with sampling frequencies of 10 and 50 kHz, was used for data acquisition.

8) A water-cooled resistor composed of two parallel sets of resistors, where the total resistance can be controlled and adjusted in steps by contactors and relays in a separate control panel. The per-phase resistance could be varied from a maximum of 160 Ω to a minimum of about 2.78 Ω. At the maximum load setting, the dissipated power of the resistors amounts to about 57 kW.

9) Two inductive loads, in which each phase is connected in series, are connected to the generator by a three-phase transformer. The approximate value of the inductance in each phase based on the turn ratio of the transformer is equal to 22 mH.

10) A copper plate was used to make an ITSC fault on one of the rotor field windings by short circuiting 1, 2, 3, 7, or/10 turns as shown in Fig. 2.

B. Test Procedure

Fig. 3 presents a connection diagram of the experimental test rig. The procedure of experimental tests is as follows: Tests were performed in healthy and faulty cases in no-load, fully resistive, and resistive–inductive load according to Table II. The SPSG which was coupled to an induction motor with the help of a gearbox is accelerated until it reaches its nominal synchronous

speed. The magnetizing current is increased until the stator voltage reaches its nominal value. The magnetizing current is increased by increasing the load to maintain the stator voltage in its nominal value. ITSC fault is conducted at standstill by removing a certain desired number of turns from the rotor field winding with the help of a copper plate. As shown in Fig. 2, there exists a common tap on a rotor field winding connected to a bolt located at the rotor which is called a common point. There are five taps on the rotor field winding that is connected to the bolts that enable to apply ITSC fault by removing 1, 2, 3, 7, and 10 turns. For instance, by connecting a common point and tap (7 ITSC) as shown in Fig. 2 by using the copper plate, seven turns are removed. In total, 48 experiments were conducted, each of which sampled with two sensors and two sampling frequencies. The temperature effects on tests were examined by comparing the results in the cold and warm operation of SPSG. Analysis shows that temperature does not have an impact on the acquired signal.

III. METHOD AND RESULTS

A. Data Preprocessing

The data was processed to appear similar to something one would sample in a production environment. In a production deployment of the fault detection system, the measurement series would need to be windowed with the classification run on a sliding window of the last electrical periods to be able to detect faults in near real time. Since incipient faults are not critical, a long window length of several mechanical periods is possible. The minimum viable window length is one mechanical period, as this is the window length necessary to ensure that any fault will pass the sensors. An excessively long window length is prohibitive since it will add little new information and slow down feature extraction. However, the window length should be long enough to remediate end effects in signal processing tools that suffer from them. End effects can be alleviated by analyzing a concatenated series if the signal is assumed to be periodic. Since the machine has seven pole pairs, seven electrical periods will capture one complete mechanical period. The reduced sample series (RSS) extracted from original sample series (OSS) are cut at rising zero-crossing to have integer electrical periods in each RSS as shown in Fig. 4. Each RSS represents a dataset, indicating that the total number of RSS used for ML purposes in this article by performing 48 experiments (8 healthy cases and 40 faulty cases) under different load conditions and fault severity is approximately equal to 2500.

B. Feature Extraction

To generate features, signal processing methods can be used in concert with discipline knowledge. From a frequency spectrum generated by a signal processing method, one would select the frequencies of the signal that are most informative and generate some features from that. This could be the energy spectrum of a certain decomposition level in discrete wavelet transform (DWT), the intensity of some side-band frequencies relative to
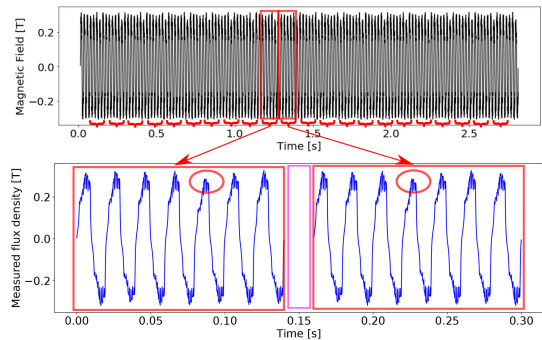

Fig. 4. Two consecutive RSSs that each of them represents one dataset cut from the same OSS. They are each of seven electrical periods, with one electrical period between the two. Note the smaller negative peak occurring in periods 4 and 3 of the first and second RSSs, respectively. The one-period shift between each RSS makes the fault indication appear one position earlier.

a harmonic frequency, or any other property of the signal or its transforms.

Raw time series are very sensitive to small perturbations and thus not suited to be used directly as tabular training data. Features are, therefore, extracted from each RSS that are then used as a basis for feature selection and, finally, as training data. The feature extraction methods used were fast Fourier transform (FFT), DWT energies, and Time Series FeatuRe Extraction based on Scalable Hypothesis tests (TSFRESH). In total, 475 distinct features were extracted.

1) Fast Fourier Transform: The frequency content of each RSS was extracted by FFT. FFTs of healthy and faulty signals showed that the faulty signal had a marked increase in harmonic frequency components at intervals of $f_m = \frac{50}{7}$ Hz, the mechanical frequency of the generator, outside of the odd multiples of fundamental frequency compared to the healthy case. The frequency components of integer multiples of f_m up to 500 Hz were extracted as features; see the following equation:

$$f_{k,\text{extracted}} = k \cdot f_m = k \cdot \frac{2f_{\text{sync}}}{p}, k = 0, 1, 3, \dots . \quad (1)$$

2) DWT Wavelet Energies: A 12-level decomposition, Haar wavelet DWT was taken of each RSS and instantaneous, Teager, hierarchical, and relative wavelet energies were computed for each decomposition level. An issue with DWT is its end effects, which are worsened substantially in each decomposition level since the length of the data series that is transformed is effectively halved in each decomposition level with the Haar wavelet. The adverse effects are diminished as the length of the data series increases since the portions affected by end effects are proportionally smaller. Therefore, each RSS was concatenated to 4 times its length before the DWT was taken. This exploits the assumption that the generator behavior is stationary.

3) TSFRESH: An algorithm to extract features from time series, called FeatuRe Extraction based on Scalable Hypothesis

TABLE III
THREE DATASETS TAKEN INTO MACHINE LEARNING

Set	Selection method	Num. features
A	None	417
B	Random forest	81
C	TSFRESH	301

tests (FRESH), is proposed in [30]. Its intent is to automate time series feature extraction while implementing feature selection. The FRESH algorithm was integrated into a algorithmic feature generation package, called Time Series FeatuRe Extraction based on Scalable Hypothesis tests [31]. TSFRESH is able to generate a total of 794 time series features, using 63 time series characterization methods as well as applying feature selection methods. A comprehensive feature extraction was done using TSFRESH. TSFRESH's FFT features were not included because TSFRESH did not offer the ability to select frequencies of interest.

IV. FEATURE SELECTION

Two feature selection methods, random forest feature selection and TSFRESH, were applied to the feature dataset. Before any feature selection was undertaken, a hold-out dataset was extracted from it to prevent any target leakage.

A. Random Forest Feature Selection

The random forest feature selection was done using a forest of 1000 decision tree estimators, which were trained on the training set using Gini impurity as the splitting criterion. During training, every feature is assigned an importance based on its impurity. All features of greater than mean importance were selected, the remainder discarded. This resulted in a feature reduction from 417 to 81 features.

B. Time Series Feature Extraction Based on TSFRESH

Using the feature extraction module included in TSFRESH, a subset of features deemed relevant was extracted. TS-FRESH was configured to assume dependent features. False discovery rates in the interval 0.001, 0.01, 0.05, and 0.1 were tried; this resulted in a similar amount of features. The false discovery rate settled upon was 0.05, the rate used in [32]. This resulted in a feature reduction from 417 to 301 features.

C. Selected Datasets

The three versions of the feature dataset, hereby termed feature data sets A, B, and C, are summarized in Table III. By comparing the performance of classifiers trained upon the different collections of features, some insights into which features are most useful for classifying the fault can be gleaned and which feature selection algorithms are most useful with this data. In a final version of the fault detection system, this knowledge could be used to selectively compute only the most useful features.

V. MACHINE LEARNING

The following section details the development of a classifier intended to detect the presence of ITSCs using the datasets previously created. This is done in the following four phases:

1) selection of the feature dataset;
2) hyperparameter optimization of single ML models;
3) evaluation of stacking classifiers;
4) final classifier selection and evaluation on hold-out dataset.

The first objective, selection of the feature dataset, was accomplished by evaluating the results of training a host of different classifiers on each dataset. The classifiers chosen were the following:

1) logistic regression with and without PCA;
2) KNN with and without PCA;
3) radial basis function SVM with and without PCA;
4) linear SVM with and without PCA;
5) XGBoost;
6) multilayer perceptron (MLP);
7) stacking classifier.

By implementing logistic regression, SVM and KNN with and without a PCA, the effectiveness of PCA in this application can be gauged as well. PCA was not combined with XGBoost because PCA reduces the interpretability of the model, a key strength of decision trees. The PCA was identically executed in all four applications.

1) Evaluation Metrics: There are several ways to evaluate the performance of classifiers, and they give differing results. Perhaps, the simplest method is to count the number of correct classifications and divide by the total number of samples. This is what is called the *accuracy* of the classifier, as shown in (2). It says something about the performance of the classifier but has trouble with unbalanced datasets. Given an unbalanced electric machine measurement dataset containing 99% of samples of healthy machines and 1% of samples of faulty machines, a classifier that always classifies a sample to be healthy would have a 99% accuracy. This is obviously a poor classifier as it would never correctly classify a single faulty machine. This is addressed by including other measurements that also emphasize the misclassified samples. A popular metric that does this is the *F-score*. It works by combining *sensitivity and precision*

$$\text{accuracy} = \frac{\text{TP} + \text{TN}}{\text{TP} + \text{FP} + \text{FN} + \text{TN}}. \tag{2}$$

A useful tool to talk about these measures is the confusion matrix for a binary classifier that classifies samples as belonging to the class, true, or not belonging to the class, false. The confusion matrix contains the number of samples that are: correctly classified as belonging to the class, true positive (TP); incorrectly classified as belonging to the class, false positive (FP); incorrectly classified as not belonging to the class, false negative (FN); and correctly classified as not belonging to the class, true negative (TN).

Sensitivity, as shown in (3), is a measure of how well the model picks up on the class, essentially the probability that the
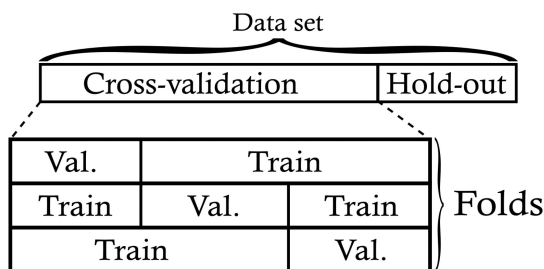
Fig. 5. Threefold cross-validation. Each fold is composed of a training and validation set.

class is detected

$$\text{sensitivity} = \frac{\text{TP}}{\text{TP} + \text{FN}}. \tag{3}$$

Specificity, as shown in (4), gives an impression of the model's capacity to correctly classify false samples

$$\text{specificity} = \frac{\text{TN}}{\text{TN} + \text{FP}}. \tag{4}$$

Precision, as shown in (5), is the ratio of true positives divided by the total number of samples classified as true. A high precision gives confidence that the classifier has made a correct prediction when it returns true

$$\text{precision} = \frac{\text{TP}}{\text{TP} + \text{FP}}. \tag{5}$$

Each of these has pit-falls when faced with unbalanced datasets and classifiers that classify all samples as either true or false. To balance the possible pitfalls, the *F*-score is especially good for unbalanced classes. The *F*-score is defined as the harmonic mean of precision and sensitivity; it weighs the reliability of a classification together with its chance of detecting the class [33]. The *F*1-score is shown in the following equation:

$$F_1 - \text{score} = 2 \cdot \frac{\text{precision} \cdot \text{sensitivity}}{\text{precision} + \text{sensitivity}}. \tag{6}$$

2) Cross-Validation: Since datasets are not entirely uniform, the results of the train/test procedure are affected by the way the data is split. One split may, by chance, give very good test results, while another does the opposite. This could result in selecting a model that generalizes poorly even though it performs well on the test set. To counter this, *k*-fold cross-validation can be used [34]. *k*-fold cross-validation takes in a dataset and splits it into *k* folds. Each fold is composed of a training set and a validation set. For each fold, the model is trained on the training set and its performance measured on the validation set. The model's performance is then the average performance across all the folds, and the performance is more likely to reflect the true performance of the model on unseen data.

Since what is of interest when testing a new model is its performance on *new and unseen data*, a part of the dataset should be set aside to be used only to assess the performance of the model. This is known as a *hold-out dataset* (as shown in Fig. 5) that includes 20% of the dataset. The datasets were previously, during the

Data set	Classifier	Sensitivity	Precision
A	Logistic Regression	0.8853	0.7722
	Logistic Reg. with PCA	0.8622	0.8131
	KNN	0.8269	0.6747
	KNN with PCA	0.8201	0.6775
	SVM (rbf)	0.8492	0.7050
	SVM (rbf) with PCA	0.8538	0.6312
	SVM (linear)	0.8859	0.7612
	SVM (linear) with PCA	0.8576	0.8176
	XGBoost	0.8518	0.7766
	Multi-layer Perceptron	0.8833	0.7390
	Stack	0.8652	0.8191
	Average classifier score	0.8583	0.7443
B	Logistic Regression	0.8675	0.7772
	Logistic Reg. with PCA	0.8140	0.7394
	KNN	0.8074	0.7237
	KNN with PCA	0.8392	0.7207
	SVM (rbf)	0.8117	0.7029
	SVM (rbf) with PCA	0.8149	0.6453
	SVM (linear)	0.8790	0.7925
	SVM (linear) with PCA	0.7878	0.7392
	XGBoost	0.8407	0.7193
	Multi-layer Perceptron	0.8702	0.7322
	Stack	0.8712	0.7981
	Average classifier score	0.8367	0.7355
C	Logistic Regression	0.8966	0.7998
	Logistic Reg. with PCA	0.8663	0.8082
	KNN	0.8282	0.6743
	KNN with PCA	0.8222	0.6756
	SVM (rbf)	0.8531	0.7226
	SVM (rbf) with PCA	0.8492	0.6327
	SVM (linear)	0.8972	0.8106
	SVM (linear) with PCA	0.8615	0.8162
	XGBoost	0.8313	0.7816
	Multi-layer Perceptron	0.8859	0.7643
	Stack	0.8714	0.8485
	Average classifier score	0.8603	0.7577

feature selection process, split into a hold-out test dataset and a remainder dataset. Since the results of a single train/test cycle can be very dependent upon the split of the samples, the classifiers were evaluated by their average performance across a fivefold CV. This produces five folds of CV-train and CV-validation sets drawn from the remainder dataset of the initial split. The folds are identical across all classifiers and feature datasets.

3) Standardisation: Logistic regression, KNN, and SVM are sensitive to the variance of the samples; this is addressed by applying standardization. Each cross-validation split was standardized to zero-mean and unity variance. The mean and variance of every feature was calculated from the CV-train set. Both CV-test and CV-validation sets were standardized using the CV-train means and variances.

4) Results: This procedure was repeated for every classifier on every feature dataset and performance metrics were gathered. The results are presented in Table IV. This method of model fitting was used for every classifier evaluation at later stages of the classifier development.

A. Feature Selection and Reduction Performance

It appears that the choice of dataset does not greatly affect the performance of the classifiers, and the variance of the results is large. However, feature dataset C, the TSFRESH feature

TABLE V
HYPERPARAMETER SEARCH GRIDS FOR LOGISTIC REGRESSION, KNN, SVM, AND XGBOOST CLASSIFIERS

Classifier	Hyperparameter	Values	Final Value	Description
Log. Reg.	C	10^k, $k = -10, -9.5, ..., 10$	$10^{8.5}$	Inverse of regularisation strength
	penalty	"l1", "l2"	l2	Penalisation norm
KNN	n_neighbors	$1, 3, 5, ..., 351$	1	Number of nearest neighbours
SVM	C	10^k, $k = -1, 0, 1, 2, 3$	10	Inverse of regularisation strength
	gamma	10^k, $k = 0, -1, -2, -3, -4$	1	Inverse of regularisation strength
	kernel	"rbf", "linear"	linear	Kernel type
XGBoost	learning_rate	0.01, 0.2, 0.3, 0.5	0.5	Learning rate
	n_estimators	100, 400, 700, 1000	100	Number of trees in ensemble
	max_depth	3, 10, 15, 25	3	Maximum tree depth
	col_sample_bytree	0.8, 1	0.8	Per tree column subsampling ratio
	subsample	0.6, 0.8, 1	1	Sample subsampling ratio
	reg_alpha	0.7, 1, 1.3	1.3	Lasso regularisation term on weights
	reg_lambda	0, 0.5, 1	0	Ridge regularisation term on weights
MLP	activation	'identity', 'logistic', 'tanh', 'relu'	identity	The activation function
	batch_size	200, 133, 66, 32	200	Size of minibatches
	max_iter	200, 500, 1000, 1200	200	The maximum number of epochs
	hidden_layer_sizes	(50,25,3), (100,50,7), (200,100,14), (300,150,21)	(50, 25, 3)	Size and number of hidden layers

selection dataset, slightly outperforms the rest on every averaged metric. Dataset C is thus preferred and will be utilized from this point onward.

As for feature reduction, i.e., application of PCA, every classifier suffered a drop in performance in nearly every metric when PCA was applied. Of special note is that radial basis function SVM with PCA had an receiver operating characteristic (ROC) area under the curve (AUC) consistently lower than 0.5, which indicates that it performed worse than chance. Due to this, PCA was abandoned. It might still have been justified on grounds of reducing training and prediction time if there were more features or an extremely large number of samples, but no such considerations were necessary.

B. Hyperparameter Optimization and Selection

Since a classifier's performance is heavily dependent upon its hyperparameters, all the candidate classifiers were optimized before selecting among them. The optimization procedure was a fivefold cross-validating grid search. In this procedure, a hyperparameter grid is defined that contains a range of values for each of the hyperparameters to be optimized. The grid search algorithm then executes a cross-validation of the classifier for every possible combination of these hyperparameters. The mean cross-validation performance is calculated for each hyperparameter combination, and the hyperparameter combination that yields the best performance on the chosen performance metric is selected. The performance metric used is $F1$-score because it combines sensitivity and precision.

The hyperparameter sets with the greatest mean performance across fivefold cross-validation for each classifier are presented as final value in Table V. Table VI shows the scores of these classifiers across several metrics. Of the optimized classifiers, the XGBoost and KNN models are outperformed by the others. KNN's accuracy was 64.0% in an imbalanced dataset of 65.9% majority class. This performance is worse than that of a dummy classifier that classifies randomly or always classifying samples as the majority class. Furthermore, KNN is entirely

TABLE VI
ACCURACY, SENSITIVITY, PRECISION, AND $F1$-SCORE OF THE BEST MODELS FOUND IN THE HYPERPARAMETER GRID SEARCH

Classifier	Accuracy	Sensitivity	Precision	F1-score
Logistic Regression	0.7986	0.8740	0.8376	0.8506
KNN	0.6395	0.8350	0.6990	0.7501
SVM	0.7940	0.8854	0.8247	0.8501
XGBoost	0.7438	0.8576	0.7846	0.8142
MLP	0.7958	0.9022	0.8170	0.8542

nongeneralizing with a $k = 1$, indicating that the algorithm is not well-suited for this problem.

C. Ensemble Learners

Ensemble learners are learners that combine several weak learners that may have poor performance to create a stronger learner with better performance. There are a few methods of accomplishing this, mainly *bagging, boosting, and stacking*. Stacking is to train a metalearner, a model that is trained to interpret the outputs of several other models to make a prediction based on the predictions of the other learners. The learners that provide predictions to the metalearner are termed base-learners. It usually outperforms the base-learners it is trained upon. Each of the base-learners are first fitted to the training set, and their predictions upon the training set are used as the training set for the metalearner. The base-learners can be any ML model that returns predictions. This provides a benefit in that by including different models as base-learners, the weaknesses of one model can be remedied by another.

Since a stacking classifier improved the performance during the feature dataset selection, the same approach is made again using the optimized classifiers. Four stacking classifiers were made with different metaclassifiers, logistic regression, MLP, gradient boosting forest, and a random forest classifier. The gradient boosting forest classifier was chosen over XGBoost as a metaclassifier due to greater compatibility with Sci-kit Learn's stacking framework. Since XGBoost is also a variant of gradient boosting forest, it should return similar results at the expense
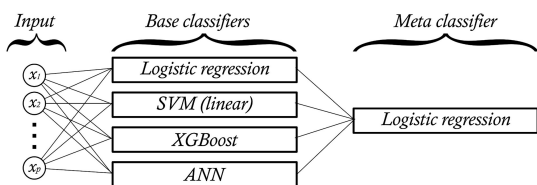
Fig. 6. Stacking classifier with logistic regression as its metaclassifier.

TABLE VII
RESULTS FROM THE STACKING CLASSIFIER COMPARISON

Meta-classifier	Accuracy	Sensitivity	Precision	F1-score
Logistic Regression	0.7840	0.8701	0.8260	0.8432
Multi-layer Perceptron	0.7479	0.8057	0.8276	0.8107
Gradient boosting forest	0.7663	0.8268	0.8304	0.8255
Random Forest	0.7704	0.8216	0.8388	0.8265

TABLE VIII
RESULTS OF THE BEST OF THE SINGLE AND STACKING CLASSIFIERS ON THE
HOLD-OUT DATA SAMPLES

Classifier	Accuracy	Sensitivity	Precision	F1-score
Logistic Regression	0.7569	0.6961	0.9435	0.8011
Logistic Reg. stack	0.8448	0.8456	0.9274	0.8846

of computing power. The stacks all include the optimized logistic regression, SVM, MLP, and XGBoost classifiers as base classifiers (Fig. 6). KNN was again excluded due to its poor performance and slow prediction time. Results are shown in Table VII. Of the stacking classifiers, the logistic regression stacking classifier outperformed the others by a large margin.

Comparing the performance of the best stacking classifier with that of the best nonensemble classifier, a somewhat surprising result surfaces. The logistic regression classifier alone on average slightly outperforms the stacking classifier of which it is a part of across the cross-validation folds.

An advantage of stacking classifiers is that they often generalize better than single classifiers, and they usually outperform their base classifiers. However, the hyperparameters of the metaclassifier have not been optimized on the training set as is the case with the simple logistic regression classifier. To gauge their performance on unseen samples, both are trained on the entire training set and tested on the hold-out dataset. The results are presented in Table VIII.

On the hold-out set, the stacking classifier outperforms the simple logistic regression classifier. The stacking classifier could likely be further improved by running a grid search for the optimal hyperparameters of the logistic regression metaclassifier.

VI. CONCLUSION

This article investigated how signal processing and ML tools can be used to detect ITSCs in rotor field windings. This was done in three stages, data preprocessing, feature extraction and selection, and classifier development as described in the following.

1) Signal partitioning was used to achieve a sufficient number of datasets to train the intelligent system.

2) The features extracted were power spectral density of integer multiples of the generator's mechanical frequency extracted by FFT, DWT wavelet energies, and the entire TSFRESH feature extraction suite. The most useful features were the wavelet energy features and some of the TSFRESH features.

3) Linear ML models were best suited for fault detection on this dataset, especially the logistic regression and linear SVM classifiers. The best classifier was an ensemble stacking classifier with logistic regression as the metaclassifier taking inputs from logistic regression, XGBoost, linear SVM, and MLP classifiers as base-classifiers.

The results indicated that ITSC fault classification using ML on air-gap magnetic field measurements from a single sensor can yield good results. The logistic regression stacking classifier had an accuracy of 0.8448, a sensitivity of 0.8456, and a precision of 0.9274. This means that the classifier correctly classified 84.48% of all the samples in the hold-out dataset, and 84.56% of the faulty samples present were correctly classified as such. Of the samples that were classified as faulty, 92.74% were correctly classified. Since a large portion of faults go undetected, this fault detection system should therefore not be relied upon as the only detection system. However, if the system alerts of a fault, it would warrant investigation since it is likely to be correct.

A general trend during optimization was that linear ML models performed well and that the performance of nonensemble classifiers *increased* as the complexity *decreased*. The worst performance was exhibited by the KNN classifier, performing worse than random chance.

Future work in this research includes the following:

1) using a combination of various sources of signals such as vibration and stray magnetic field to achieve higher accuracy and sensitivity in a classifier;

2) ITSC fault severity assessment using some of the same methodology mentioned in this article;

3) application of ensemble stacking classifier in different kinds of faults in synchronous generators such as eccentricity fault and broken damper fault.

REFERENCES

[1] D. P. Kothari and I. J. Nagrath, *Electric Machines*. New York, NY, USA: Tata McGraw-Hill Education, 2004. google-Books-ID: axGw7r3SOEMC.

[2] "08583: Elektrisitetsbalanse (MWh) 2010m01-2019m09." [Online]. Available: http://www.ssb.no/statbank/table/08583/

[3] H. Ehya, I. Sadeghi, and J. Faiz, "Online condition monitoring of large synchronous generator under eccentricity fault," in *Proc. 12th IEEE Conf. Ind. Electron. Appl.*, 2017, pp. 19–24.

[4] I. Sadeghi, H. Ehya, J. Faiz, and A. A. S. Akmal, "Online condition monitoring of large synchronous generator under short circuit fault—A review," in *Proc. IEEE Int. Conf. Ind. Technol.*, 2018, pp. 1843–1848.

[5] J. Manyika *et al.*, *Unlocking the Potential of the Internet of Things*. New York, NY, USA: McKinsey. Library Catalog: www.mckinsey.com. [Online]. Available: https://www.mckinsey.com/business-functions/mckinsey-digital/our-insights/the-internet-of-things-the-value-of-digitizing-the-physical-world

[6] J. Yun *et al.*, "Comprehensive monitoring of field winding short circuits for salient pole synchronous motors," *IEEE Trans. Energy Convers.*, vol. 34, no. 3, pp. 1686–1694, Sep. 2019.

[7] J. A. Antonino-Daviu, M. Riera-Guasp, J. Pons-Llinares, J. Roger-Folch, R. B. Pérez, and C. Charlton-Pérez, "Toward condition monitoring of damper windings in synchronous motors via EMD analysis," *IEEE Trans. Energy Convers.*, vol. 27, no. 2, pp. 432–439, Jun. 2012.

[8] Y. Park, S. B. Lee, J. Yun, M. Sasic, and G. C. Stone, "Air gap flux-based detection and classification of damper bar and field winding faults in salient pole synchronous motors," *IEEE Trans. Ind. Appl.*, vol. 56, no. 4, pp. 3506–3515, Jul./Aug. 2020.

[9] M. Cuevas, R. Romary, J. Lecointe, F. Morganti, and T. Jacq, "Noninvasive detection of winding short-circuit faults in salient pole synchronous machine with squirrel-cage damper," *IEEE Trans. Ind. Appl.*, vol. 54, no. 6, pp. 5988–5997, Nov./Dec. 2018.

[10] M. Valavi, K. G. Jørstad, and A. Nysveen, "Electromagnetic analysis and electrical signature-based detection of rotor inter-turn faults in salient-pole synchronous machine," *IEEE Trans. Magn.*, vol. 54, no. 9, pp. 1–9, Sep. 2018.

[11] L. Hao, Y. Sun, A. Qiu, and X. Wang, "Steady-state calculation and online monitoring of interturn short circuit of field windings in synchronous machines," *IEEE Trans. Energy Convers.*, vol. 27, no. 1, pp. 128–138, Mar. 2012.

[12] W. Yucai, M. Qianqian, and C. Bochong, "Fault diagnosis of rotor winding inter-turn short circuit for sensorless synchronous generator through screw," *IET Elect. Power Appl.*, vol. 11, no. 8, pp. 1475–1482, 2017.

[13] J. S. Hsu and J. Stein, "Shaft signals of salient-pole synchronous machines for eccentricity and shorted-field-coil detections," *IEEE Trans. Energy Convers.*, vol. 9, no. 3, pp. 572–578, Sep. 1994.

[14] X. Dai and Z. Gao, "From model, signal to knowledge: A data-driven perspective of fault detection and diagnosis," *IEEE Trans. Ind. Informat.*, vol. 9, no. 4, pp. 2226–2238, Nov. 2013.

[15] B. Chen, X. Wang, S. Yang, and C. McGreavy, "Application of wavelets and neural networks to diagnostic system development, 1, feature extraction," *Comput. Chem. Eng.*, vol. 23, no. 7, pp. 899–906, 1999.

[16] S. M. Cruz and A. M. Cardoso, "Multiple reference frames theory: A new method for the diagnosis of stator faults in three-phase induction motors," *IEEE Trans. Energy Convers.*, vol. 20, no. 3, pp. 611–619, Sep. 2005.

[17] A. Glowacz and Z. Glowacz, "Diagnosis of the three-phase induction motor using thermal imaging," *Infrared Phys. Technol.*, vol. 81, pp. 7–16, 2017.

[18] B. M. Ebrahimi, M. Javan Roshtkhari, J. Faiz, and S. V. Khatami, "Advanced eccentricity fault recognition in permanent magnet synchronous motors using stator current signature analysis," *IEEE Trans. Ind. Electron.*, vol. 61, no. 4, pp. 2041–2052, Apr. 2014.

[19] A. Widodo and B.-S. Yang, "Support vector machine in machine condition monitoring and fault diagnosis," *Mech. Syst. Signal Process.*, vol. 21, no. 6, pp. 2560–2574, 2007.

[20] S. Munikoti, L. Das, B. Natarajan, and B. Srinivasan, "Data-driven approaches for diagnosis of incipient faults in DC motors," *IEEE Trans. Ind. Informat.*, vol. 15, no. 9, pp. 5299–5308, Sep. 2019.

[21] P. Janik and T. Lobos, "Automated classification of power-quality disturbances using SVM and RBF networks," *IEEE Trans. Power Del.*, vol. 21, no. 3, pp. 1663–1669, Jul. 2006.

[22] A. Glowacz, "Fault diagnostics of acoustic signals of loaded synchronous motor using smofs-25-expanded and selected classifiers," *Tehnički Vjesnik*, vol. 23, no. 5, pp. 1365–1372, 2016.

[23] A. Glowacz, W. Glowacz, Z. Glowacz, and J. Kozik, "Early fault diagnosis of bearing and stator faults of the single-phase induction motor using acoustic signals," *Measurement*, vol. 113, pp. 1–9, 2018.

[24] F. Zidani, D. Diallo, M. E. H. Benbouzid, and R. Nait-Said, "A fuzzy-based approach for the diagnosis of fault modes in a voltage-fed PWM inverter induction motor drive," *IEEE Trans. Ind. Electron.*, vol. 55, no. 2, pp. 586–593, Feb. 2008.

[25] A. Stief, J. R. Ottewill, J. Baranowski, and M. Orkisz, "A PCA and two-stage Bayesian sensor fusion approach for diagnosing electrical and mechanical faults in induction motors," *IEEE Trans. Ind. Electron.*, vol. 66, no. 12, pp. 9510–9520, Dec. 2019.

[26] W. Zhao and L. Wang, "Multiple-kernel MRVM with LBFO algorithm for fault diagnosis of broken rotor bar in induction motor," *IEEE Access*, vol. 7, pp. 182173–182184, 2019.

[27] D. Zhang, L. Qian, B. Mao, C. Huang, B. Huang, and Y. Si, "A data-driven design for fault detection of wind turbines using random forests and XGBoost," *IEEE Access*, vol. 6, pp. 21020–21031, 2018.

[28] Z. Xu *et al.*, "Data-driven inter-turn short circuit fault detection in induction machines," *IEEE Access*, vol. 5, pp. 25055–25068, 2017.

[29] M. Seera, C. P. Lim, S. Nahavandi, and C. K. Loo, "Condition monitoring of induction motors: A review and an application of an ensemble of hybrid intelligent models," *Expert Syst. With Appl.*, vol. 41, no. 10, pp. 4891–4903, 2014.

[30] M. Christ, A. W. Kempa-Liehr, and M. Feindt, "Distributed and parallel time series feature extraction for industrial Big Data applications," May 2017, *arXiv:1610.07717*. [Online]. Available: http://arxiv.org/abs/1610.07717

[31] M. Christ, N. Braun, J. Neuffer, and A. W. Kempa-Liehr, "Time series FeatuRe extraction on basis of scalable hypothesis tests (TSFRESH - a python package)," *Neurocomputing*, vol. 307, pp. 72–77, Sep. 2018.

[32] Y. Benjamini and Y. Hochberg, "Controlling the false discovery rate: A practical and powerful approach to multiple testing," vol. 57, no. 1, pp. 289–300. [Online]. Available: https://rss.onlinelibrary.wiley.com/doi/abs/10.1111/j.2517-6161.1995.tb02031.x

[33] D. D. Lewis, R. E. Schapire, J. P. Callan, and R. Papka, "Training algorithms for linear text classifiers," in *Proc. 19th Annu. Int. ACM SIGIR Conf. Res. Develop. Inform. Retrieval*, 1996, pp. 298–306.

[34] R. R. Picard and R. D. Cook, *Cross-Validation of Regression Models*, vol. 79, no. 387. New York, NY, USA: Taylor & Francis Group, 1984, pp. 575–583.

Hossein Ehya (Graduate Student Member, IEEE) received the M.Sc. degree in electrical engineering from the Department of Electrical and Computer Engineering, University of Tehran, Tehran, Iran, in 2013. He is currently working toward the Ph.D. degree in electrical engineering at the Norwegian University of Science and Technology (NTNU), Trondheim, Norway.

From 2013 to 2018, he was an Electrical Machine Design Engineer with electrical machine companies. His research interests include the design and condition monitoring of electrical machines, signal processing, pattern recognition, and machine learning.

In 2020, he was awarded with the ICEM Jorma Luomi Award in Gothenburg, Sweden.

Tarjei Nesbø Skreien is currently working toward the master's degree at The Norwegian University of Technology and Science, Trondheim, Norway, in 2020.

His research interests include synchronous machine fault detection, machine learning, and sampling noise mitigation.

Arne Nysveen (Senior Member, IEEE) received the Dr.ing. (Ph.D.) and the M.Sc. degrees in electric power engineering from the Norwegian Institute of Technology (now NTNU), Trondheim, Norway, in 1994 and 1988, respectively.

From 1995 to 2002, he was a Senior Scientist with ABB Corporate Research, Oslo, Norway. Since 2002, he has been a Professor with the Norwegian University of Science and Technology (NTNU), Trondheim. He is currently the Manager for the research on Turbine and Generator Technologies at the Norwegian Research Center for Hydropower Technology (HydroCen). His current research activities are on design, modeling, and monitoring of hydroelectric generators.

Patent

H. Ehya, and A. Nysveen, "Fault Detection in Synchronous Machines," UK. Patent Office, WO2021/074248, October 2019.

(12) INTERNATIONAL APPLICATION PUBLISHED UNDER THE PATENT COOPERATION TREATY (PCT)

(54) **Title:** FAULT DETECTION IN SYNCHRONOUS MACHINES

(57) **Abstract:** A method of fault detection in synchronous machines includes using at least one sensor to determine parameters linked to the magnetic field generated within the synchronous machine including parameters based on one or more of magnetic field strength, rotor current or voltage, stator current or voltage, and vibration. The sensor measurements are processed to identify data artefacts linked to the magnetic field, wherein the processing includes one or more signal processing techniques based on time, frequency, and both time and frequency. Subsequently, the output of the signal processing is analysed in order to identify and categorise irregularities in the magnetic field that are indicative of a fault in the synchronous machine. The analysing step includes recognising patterns in the processed sensor measurements, via use of computer aided pattern recognition techniques such as via machine learning algorithms.

NTNU
Norwegian University of
Science and Technology